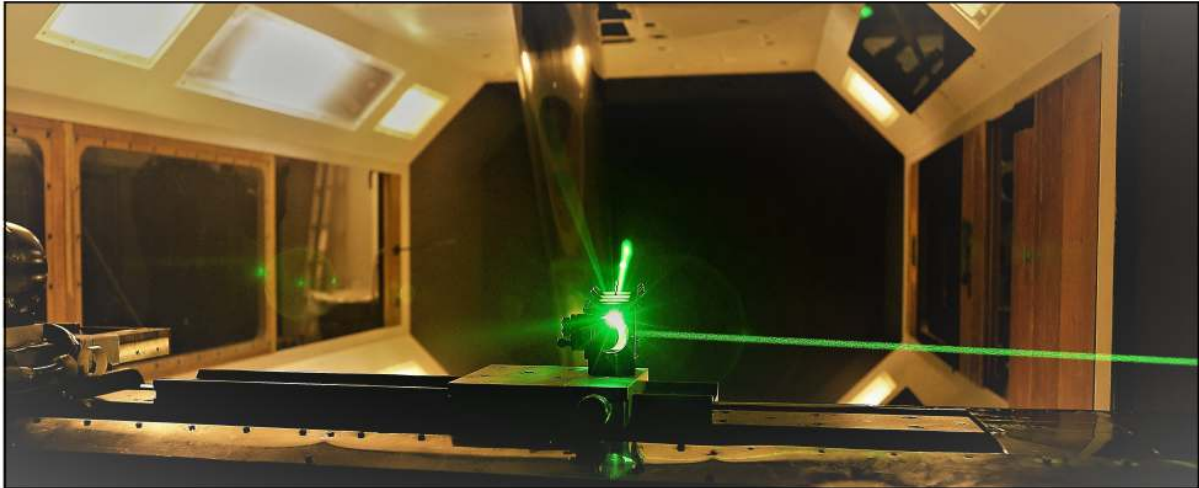


Master of Science Thesis



Mechanisms of boundary layer transition due to isolated roughness on swept wings

An experimental study

Filippo Munaro

September 15, 2017

**Mechanisms of boundary layer
transition due to isolated roughness on
swept wings**
An experimental study

Master of Science Thesis

For obtaining the degree of Master of Science in Aerospace Engineering
at Delft University of Technology

Filippo Munaro

September 15, 2017



Delft University of Technology

Copyright © Aerospace Engineering, Delft University of Technology
All rights reserved.

DELFT UNIVERSITY OF TECHNOLOGY
DEPARTMENT OF AERODYNAMICS

The undersigned hereby certify that they have read and recommend to the Faculty of Aerospace Engineering for acceptance the thesis entitled “**Mechanisms of boundary layer transition due to isolated roughness on swept wings**” by **Filippo Munaro** in fulfillment of the requirements for the degree of **Master of Science**.

Dated: September 15, 2017

Supervisors:

Dr. Marios Kotsonis & Jacopo Serpieri

Prof. Dr. Fulvio Scarano

Dr. Qingqing Ye

Dr. Francesco Avallone

Acknowledgment

This thesis is the final step of a wonderful journey, the most amazing of my life. It is almost impossible to describe how much I lived, learned and grew, since the day I walked away from home, leaving for a new adventure. I just want everyone to know how grateful I am to all those fantastic people I met along the way - to those ones who were with me since day one and to the friends that shared with me only part of the journey. Thank you.

First of all, I want to thank Jacopo Serpieri for everything he did for me. He has been a great supervisor and an even better mentor. He supported me and challenged me to do my best every day, with patience, wisdom and positiveness. I could not have asked for a better person to work with. I want to thank Dr. Marios Kotsonis, for his intelligence and sensitivity in really understanding who I am: with my weaknesses and my strengths. This way, he knew how to make me perform at the best of my possibilities and helped me through this process. I also would like to thank some of the people from TU Delft, that gave contribution to my thesis during these months. Thanks to Koen, Beppe, Srikar, Alberto and Theo for the help and the suggestions, and to Dr. Ye, Dr. Ragni and Dr. Avallone for their help during the experimental campaign and the analysis of my results. Many thanks also to Stefan and Leo, for all the times they helped me in the laboratory.

I really want to thank Dani for being an older brother to me, for the last three years. He is one of the most generous people that I have ever met. I wish him nothing but the best. I could fill in hundreds of pages with the things he did for me, but I will pick the most important one: he transmitted me his passion and love for what we do. I want to thank Edgar, Argi, Tom, Tea, Andre, Dario, Anton, Eirini, Reynard, Fra, Faggio, Lotfi, Fer and all those friends that have become my family in The Netherlands. I would have never made it without you. A special thanksgiving to Angelica, for her love and her support during the last year. I want to thank her for never leaving me alone, for taking care of me every day, and for all the moments spent together that were giving me happiness and motivation. I want to thank all my friends in Italy: those that have always been next to me. Those that supported me, regardless of my decisions. Those that have always given to me all the happiness that I need in my life. Leo, Ema, Teo, Ale, Puppo, Matte, Doz, Canta, Simo, Michi, Cepi, Vale and all the others, from Milan to Tuscany.

Finally, my family. Thanks to my grandmother Franca, for loving me more than anyone could ever do. For believing in me more than anyone else, even more than myself. Thank you for making me believe there is nothing that I cannot do. Thank you Benedetta, because your smiles put everything in perspective and remind me what the important things in life are, every day. Please, don't grow up too fast. Thanks to my brother Pietro. I wish I told you before that every time I leave, you are the one that I miss the most. I want you to know that I am proud of you, always. The strength that I need to go through hard times, I find it in the desire of being an example for you. Thanks to my sister Lucia, for being the only person that I accept suggestions from. Because your opinion is worth more than the ones of anyone else. Because you are my best friend, and will always be. Thanks to my father Oscar, none of my achievements would have been possible without him. His courage, his strength, his efforts and his positiveness makes my successes possible. Thanks for teaching me to be strong and positive, and to "give the right value to things". Thanks because I never told you that every time I look at you, I see the man I wish to become. Thanks to my mother Marta, the most important person of my life, the most precious thing I have in this world. My words cannot explain how much I love you, and I will never be able to pay you back for all the things you did for me. Thank you for your love, for your wisdom and your sensitivity. Thank you for dedicating your life to us. You made me who I am today.

Summary

In the context of the ongoing research regarding boundary layer transition, this project aims to study the effects of isolated cylindrical roughness elements on the transition from laminar to turbulent flow in a swept wing boundary layer. The project entails experimental campaigns: the 45° swept wing model is placed inside the test section of the Low Turbulence Tunnel (LTT) and millimeter-sized roughness elements are attached to it, so that their interference with the boundary layer flow can be studied. The main goal is to investigate the flow features generating aft the roughness elements and their development into turbulent streaks. Moreover, this project aims to understand and quantify the effects of different roughness sizes on transition mechanisms, in the specific case of a three-dimensional boundary layer. This is achieved by means of different experimental techniques, such as PIV, HWA and thermographic flow visualization.

The obtained results lead to a comprehensive description of this type of flows, with several phenomena changing their characteristics due to a change in parameters (freestream speed, roughness diameter and roughness height). Velocity field, spectral analysis of the signal, wedge width evolution, instability modes and velocity fluctuations in time were investigated with different parametric conditions, in order to understand how the flow was affected by them. Furthermore, the study allowed to evaluate the use of non-dimensional parameters such as roughness Reynolds number and aspect ratio for the prediction of the flow topology. The complexity of the phenomena involved is underlined in the conclusions of this research, with the interaction of several flow features making it a broad and interdisciplinary field of research.

Table of Contents

Acknowledgment	v
Summary	vii
List of Figures	xiii
List of Tables	xxv
List of Symbols	xxvii
1 Introduction	1
2 Literature Review	3
2.1 Crossflow Instability	3
2.2 Fundamentals of Isolated Roughness Induced Transition	6
2.3 Distributed Roughness Induced Transition	13
2.3.1 Isolated Roughness Induced Transition	17
2.4 Research questions, objectives and outline	36
3 Methodology	39
3.1 Experimental facilities	39
3.1.1 Wind tunnel and airfoil model	39

3.1.2	Coordinate system	41
3.2	Experimental techniques	41
3.2.1	Infrared thermography	41
3.2.2	Hot wire anemometry	45
3.2.3	Particle image velocimetry	47
3.2.4	Roughness elements	51
3.2.5	Experimental matrix	52
4	Results	55
4.1	Parametric Study of Transition with IR Thermography	55
4.1.1	The Turbulent Wedge Opening	55
4.1.2	Thermographic Results	56
4.2	Flow Physics & Variation of Parameters	62
4.2.1	Central Element: $U = 8$ m/s, $D = 4$ mm, $k = 1.5$ mm	62
4.2.2	Effects of Height Variation	83
4.2.3	Effects of Freestream Velocity Variation	95
4.2.4	Effects of Diameter Variation	101
4.3	Aspect Ratio Outliers	117
4.3.1	Scaling of the Metrics	117
4.3.2	Analysis of Sinuous Instability	119
4.3.3	Analysis of Low Aspect Ratio k/D	121
5	Conclusions and Recommendations	127
5.1	Conclusions	127
5.2	Recommendations	128
	Bibliography	131
	A Tomographic PIV	135

A.1	Methodology	135
A.2	Results	137
A.2.1	Central Element: $U = 8$ m/s, $D = 4$ mm, $k = 1.5$ mm	137
A.2.2	Diameter increase: $U = 8$ m/s, $D = 10$ mm, $k = 1.5$ mm	140
B	Clean Boundary Layers	143

List of Figures

2.1	Velocity profiles of a swept wing boundary layer. Reproduced from Saric et al. (2003)	4
2.2	Oil flow visualization of crossflow stationary vortices over a swept wing. Reproduced from Serpieri and Kotsonis (2016)	5
2.3	Tomographic PIV reconstruction of crossflow vortices. Reproduced from Serpieri and Kotsonis (2016)	5
2.4	Spatial growth of steady and unsteady instability modes: $Tu = 0.15\%$. From Deyhle and Bippes (1996)	6
2.5	Spatial growth of steady and unsteady instability modes: $Tu = 0.27\%$. From Deyhle and Bippes (1996)	6
2.6	Spatial growth of steady and unsteady instability modes: $Tu = 0.57\%$. From Deyhle and Bippes (1996)	6
2.7	Transition scheme with varying disturbance intensity. From Downs et al. (2008)	7
2.8	Transition Reynolds number vs. critical Reynolds number for elements of $k/D = 1$ and zero pressure gradient. From Tani (1969), collecting data from Klebanoff et al. (1955); Tani et al. (1962); Mochizuki (1961)	8
2.9	Displacement thickness Str vs. Re_k . From Klebanoff et al. (1992). Squares: hemisphere. Diamonds: cylinders.	9
2.10	Cylinder height Str vs. Re_k . From Klebanoff et al. (1992)	9
2.11	Experimental setup. From Acarlar and Smith (1987)	10
2.12	Hairpin representation. The formation process, as well as the standing vortices are visible. From Acarlar and Smith (1987)	10
2.13	Strouhal number variation with Re_k : different symbols represent different radii, the full or empty filling stands for different hemispherical roughness and locations. From Acarlar and Smith (1987)	11

2.14	Scheme for the development of an hairpin vortex. Legs moving up from the surface (b) and tilting outside the BL. From Acarlar and Smith (1987)	12
2.15	Secondary lateral vortices formation. From Acarlar and Smith (1987)	12
2.16	Horseshoe vortex PSD spectra, $x/D = -0.82$, $y/D = 0.063$, $z/D = 0$. $D/\delta^* = 33.8$ and $UD/\nu = 4720$. From Baker (1979)	13
2.17	Horseshoe vortex PSD spectra, $x/D = -0.82$, $y/D = 0.063$, $z/D = 0$. $D/\delta^* = 34.2$ and $UD/\nu = 4780$. From Baker (1979)	13
2.18	Spanwise frequency spectra. From Rizzetta et al. (2010)	15
2.19	$Re_k = 301$: steady (increments of $0.1U_\infty$) and unsteady (colors) velocity contours. All the contours refer to the plot on the bottom right corner. From Downs et al. (2008)	16
2.20	$Re_k = 334$: steady (increments of $0.1U_\infty$) and unsteady (exponentially distributed color levels) velocity contours. From Ergin and White (2006)	16
2.21	Streamlines of the in-plane velocity and time-averaged velocity contour of u/u_∞ : a) cylinder, b) square, c) hemisphere, d) micro-ramp. From Ye et al. (2016b)	18
2.22	Wake topologies: lines represent streamwise vortices, grey and yellow areas represent low- and high-speed streaks respectively. From Ye et al. (2016b)	19
2.23	Conceptual representation of the wake formation of vortical structures. From Ye et al. (2016b)	19
2.24	Streaks amplitude along streamwise coordinate. From Ye et al. (2016b)	20
2.25	Instability modes along the xz plane. High-speed streaks: dashed lines. Low-speed streaks: solid lines. From Andersson et al. (2001)	20
2.26	Simmetry plane view of the near wake under the effects of different Re : contours from $U = 0.1$ to $U = 0.99$. a) $(Re, \eta) = (600, 1)$, b) $(Re, \eta) = (1250, 1)$. From Loiseau et al. (2014)	21
2.27	Top view of streaky structures aft the roughness element under the effects of different Re : white and black are respectively low- and high-speed streaks. a) $(Re, \eta) = (600, 1)$, b) $(Re, \eta) = (1250, 1)$. From Loiseau et al. (2014)	21
2.28	Simmetry plane view of the near wake under the effects of different η : contours from $U = 0.1$ to $U = 0.99$. a) $(Re, \eta) = (600, 2)$, b) $(Re, \eta) = (600, 3)$. From Loiseau et al. (2014)	22
2.29	Top view of streaky structures aft the roughness element under the effects of different Re : white and black are respectively low- and high-speed streaks. a) $(Re, \eta) = (600, 2)$, b) $(Re, \eta) = (600, 3)$. From Loiseau et al. (2014)	22

2.30	Main instability modes of the streamwise component of the velocity under the effect of different aspect ratio: a) $\eta = 0.85$, b) $\eta = 1$, c) $\eta = 2$, d) $\eta = 3$. From Loiseau et al. (2014)	23
2.31	Flow velocity signal for a varicose instability dominated type of flow. From Loiseau et al. (2014)	24
2.32	Lambda criterion visualization of hairpin vortex generation, in a varicose instability dominated type of flow. From Loiseau et al. (2014)	24
2.33	Flow velocity signal for a sinuous instability dominated type of flow. From Loiseau et al. (2014)	24
2.34	Lambda criterion visualization of hairpin vortex generation, in a sinuous instability dominated type of flow. From Loiseau et al. (2014)	24
2.35	Reproduction of the transition diagram by Doenhoff and Braslow (1961), taken from Loiseau et al. (2014). Red and green markers respectively indicate varicose and sinuous instabilities limits.	25
2.36	Streaks of positive (yellow) and negative (blue) velocity variation with respect to the average of the base flow. Reynolds values and heights reported on the figure. From Cherubini et al. (2013)	25
2.37	Evolution of varicose perturbation in time: a,b) streamwise vorticity perturbations, c,d) streamwise velocity perturbations. From Cherubini et al. (2013)	26
2.38	Evolution of sinuous perturbation in time: a,b) streamwise vorticity perturbations, c,d) streamwise velocity perturbations. From Cherubini et al. (2013)	26
2.39	Transition Re vs. roughness position ($D=3.7\text{mm}$ and $k=6\mu\text{m}$). From Radeztsky et al. (1999)	28
2.40	Transition location vs. roughness height and diameter ($x/c=0.023$ and $Re_c = 2.6 \times 10^6$). From Radeztsky et al. (1999)	28
2.41	Transition Re vs. roughness diameter and Reynolds number ($x/c=0.023$). From Radeztsky et al. (1999)	28
2.42	Spanwise hot-wire measurement of the streamwise velocity component ($y = y \bar{u}/U_e = 0.5$, $k = 6\mu\text{m}$, $D = 3.7\text{mm}$, $x/c = 0.23$, $Re_c = 2.6 \times 10^6$). From Radeztsky et al. (1999)	29
2.43	Evolution of the wake of a subcritical roughness element. From Brynjell-Rahkola et al. (2015)	29
2.44	Evolution of the wake of a supercritical roughness element. From Brynjell-Rahkola et al. (2015)	29
2.45	Upper view of the roughness element near wake: velocity magnitude ($y=0.4$). From Brynjell-Rahkola et al. (2015)	30

2.46	Eigenfunction of the most unstable mode in the supercritical roughness element. From Brynjell-Rahkola et al. (2015)	30
2.47	Experimenta scheme of the model. From Chernoray et al. (2005)	31
2.48	Stationary disturbances evolution: isosurfaces. From Chernoray et al. (2005)	32
2.49	Forced perturbation modes. From Chernoray et al. (2005)	32
2.50	Backflow region in the near wake of the element, under the effects of a 2D and a 3D flow. The isosurface represents a $u = -1 \times 10^{-4}$. From Kurz and Kloker (2016)	32
2.51	Isosurfaces of streamwise vorticity in the near wake of the element, under the effects of a 2D and a 3D flow. From Kurz and Kloker (2016)	33
2.52	Two-dimensional flow: lambda criterion isocontours (lines) and shading of streamwise vorticity. From Kurz and Kloker (2016)	33
2.53	Three-dimensional flow: lambda criterion isocontours (lines) and shading of streamwise vorticity. From Kurz and Kloker (2016)	33
2.54	Snapshots of the wake evolution. From Kurz and Kloker (2016)	34
2.55	Global pertubation modes for $k = 1.5$ and $Re_k = 564$. From Kurz and Kloker (2016)	35
2.56	Global pertubation modes for $k = 2$ and $Re_k = 881$. From Kurz and Kloker (2016)	35
3.1	Comparison between NACA 66018 and 66018M3J airfoil. Profiles taken as perpendicular to the leading edge. From Serpieri and Kotsonis (2016)	40
3.2	Airfoil model scheme with the representation of used reference systems. From Serpieri and Kotsonis (2016)	40
3.3	Schematic representation of the IR thermography experimental setup. From Serpieri et al. (2017)	43
3.4	Experimental setup for the infrared thermography test	44
3.5	Close-up of the infrared camera setup	44
3.6	Illumination system for the infrared thermography experiment. View from inside the wind tunnel.	45
3.7	Schematic representation of the hot wire anemometry experimental setup. From Serpieri and Kotsonis (2016)	47
3.8	Schematic representation of the particle image velocimetry experimental setup. From Serpieri et al. (2017)	48
3.9	Close-up of the PIV setup: double camera arrangement for the	48

3.10	PIV laser sheet pointing at the investigation volume	49
3.11	Side view of the roughness elements ($D = 10mm$) attached to the wing model	50
3.12	Front view of the roughness elements ($D = 10mm$) attached to the wing model	50
3.13	Schematic drawing of the element investigated in detail: the central element is painted in red	54
4.1	Spreading of the wedge angle and its streamwise velocity fluctuations (xz view). From Ye et al. (2016a)	56
4.2	Visual legend for the thermography wedge opening. Red lines are the boundaries of a turbulent wedge. Black lines show the initial disturbance/horseshoe vortex traces.	57
4.3	$D = 6mm$: position of wedge opening vs. freestream speed	58
4.4	$D = 4mm$: position of wedge opening vs. freestream speed	58
4.5	$D = 6mm$: position of wedge opening vs. Re_k	59
4.6	$D = 4mm$: position of wedge opening vs. Re_k	59
4.7	$k = 1.5mm$: position of wedge opening vs. Re_k	60
4.8	Matching of data for elements with same aspect ratio k/D	61
4.9	Boundary layer U profiles from the Matlab [®] code. The $U_\infty = 8m/s$ case is compared with the HWA results.	62
4.10	Central element: time averaged velocity field	63
4.11	Central element: freestream and orthogonal velocity displacement from the clean BL	63
4.12	Central element: zy plane of time averaged velocity at $X = 6mm$	65
4.13	Central element: zy plane of time averaged velocity at $X = 12mm$	65
4.14	Central element: zy plane of time averaged velocity at $X = 18mm$	65
4.15	Central element: zy plane of time averaged velocity at $X = 24mm$	66
4.16	Central element: zy plane of time averaged velocity at $X = 30mm$	66
4.17	Central element: zy plane of time averaged velocity at $X = 42mm$	66
4.18	Central element: zy plane of time averaged velocity at $X = 54mm$	67
4.19	Central element: zy plane of time averaged velocity at $X = 66mm$	67

4.20 Central element: zy plane of time averaged velocity at $X = 90mm$	67
4.21 Central element: zy plane of time averaged velocity at $X = 114mm$	68
4.22 HWA and PIV comparison at $X = 24mm$: $y = 1.68mm$	68
4.23 HWA and PIV comparison at $X = 24mm$: $y = 1.8mm$	68
4.24 HWA and PIV comparison at $X = 54mm$: $y = 1.44mm$	68
4.25 HWA and PIV comparison at $X = 54mm$: $y = 1.56mm$	68
4.26 Central element: velocity fluctuations field	70
4.27 Central element: zy plane of velocity fluctuations at $X = 6mm$	70
4.28 Central element: zy plane of velocity fluctuations at $X = 12mm$	70
4.29 Central element: zy plane of velocity fluctuations at $X = 18mm$	71
4.30 Central element: zy plane of velocity fluctuations at $X = 24mm$	71
4.31 Central element: zy plane of velocity fluctuations at $X = 30mm$	71
4.32 Central element: zy plane of velocity fluctuations at $X = 42mm$	72
4.33 Central element: zy plane of velocity fluctuations at $X = 54mm$	72
4.34 Central element: zy plane of velocity fluctuations at $X = 66mm$	72
4.35 Central element: zy plane of velocity fluctuations at $X = 90mm$	73
4.36 Central element: zy plane of velocity fluctuations at $X = 114mm$	73
4.37 Example of a frequency spectrum and its filtering	74
4.38 Central element, $X = 24mm$: frequency spectra along $y = \delta_{0.99}/2$	75
4.39 Central element, $X = 24mm$: frequency spectra along $y = 2.5mm$	75
4.40 Central element, $X = 54mm$: frequency spectra along $y = \delta_{0.99}/2$	77
4.41 Central element, $X = 66mm$: frequency spectra along $y = \delta_{0.99}/2$	77
4.42 Central element, $X = 90mm$: frequency spectra along $y = \delta_{0.99}/2$	78
4.43 Central element, $X = 114mm$: frequency spectra along $y = \delta_{0.99}/2$	78
4.44 Central element: zy plane of filtered velocity fluctuations at $X = 24mm$	79
4.45 Central element: zy plane of filtered velocity fluctuations at $X = 54mm$	79

4.46	Central element: zy plane of filtered velocity fluctuations at $X = 66mm$	79
4.47	Central element: zy plane of filtered velocity fluctuations at $X = 90mm$	80
4.48	Central element: zy plane of filtered velocity fluctuations at $X = 114mm$	80
4.49	Central element: U component, POD mode 1	81
4.50	Central element: U component, POD mode 3	81
4.51	Central element: Recorded signal of HWA in the position of highest fluctuations .	82
4.52	Central element: instantaneous Y -vorticity field	83
4.53	Visual map for the identification of the wedges	84
4.54	$D = 4mm, k = 0.75mm$: time averaged velocity field	85
4.55	$D = 4mm, k = 2.1mm$: time averaged velocity field	85
4.56	$k = 0.75mm$: zy plane of time averaged velocity at $X = 6mm$	86
4.57	$k = 1.5mm$: zy plane of time averaged velocity at $X = 6mm$	86
4.58	$k = 2.1mm$: zy plane of time averaged velocity at $X = 6mm$	86
4.59	$k = 0.75mm$: zy plane of time averaged velocity at $X = 24mm$	87
4.60	$k = 1.5mm$: zy plane of time averaged velocity at $X = 24mm$	87
4.61	$k = 2.1mm$: zy plane of time averaged velocity at $X = 24mm$	87
4.62	$k = 1.5mm$: zy plane of time averaged velocity at $X = 54mm$	88
4.63	$k = 2.1mm$: zy plane of time averaged velocity at $X = 54mm$	88
4.64	k variation: time averaged metrics	89
4.65	k variation: time averaged metrics (normalized)	89
4.66	k variation: fluctuation metrics	90
4.67	k variation: fluctuation metrics (normalized)	90
4.68	$D = 4mm, k = 0.75mm$: velocity fluctuations field.	90
4.69	$D = 4mm, k = 2.1mm$: velocity fluctuations field.	91
4.70	$k = 0.75mm$: zy plane of velocity fluctuations at $X = 24mm$	92
4.71	$k = 1.5mm$: zy plane of velocity fluctuations at $X = 24mm$	92

4.72	$k = 2.1mm$: zy plane of velocity fluctuations at $X = 24mm$	92
4.73	$k = 1.5mm$: zy plane of velocity fluctuations at $X = 54mm$	93
4.74	$k = 2.1mm$: zy plane of velocity fluctuations at $X = 54mm$	93
4.75	$k = 1.5mm$: zy plane of velocity fluctuations at $X = 114mm$	93
4.76	$D = 4mm$ and $k = 2.1mm$. $X = 24mm$: frequency spectra along $y = \delta_{0.99}/2$.	94
4.77	$D = 4mm, k = 2.1mm$: U component, POD mode 1	95
4.78	Central element at $U_\infty = 6m/s$: time averaged velocity field	96
4.79	Central element at $U_\infty = 12m/s$: time averaged velocity field	96
4.80	U variation: fluctuation metrics	97
4.81	U variation: fluctuation metrics (normalized)	97
4.82	Central element at $U_\infty = 6m/s$: velocity fluctuations field	98
4.83	Central element at $U_\infty = 12m/s$: velocity fluctuations field	98
4.84	Central element at $U_\infty = 6m/s$: U POD mode 1	100
4.85	Central element at $U_\infty = 12m/s$: U POD mode 1	100
4.86	$D = 2.5mm$: time averaged velocity field	101
4.87	$D = 10mm$: time averaged velocity field	102
4.88	$D = 2.5mm$: zy plane of time averaged velocity at $X = 6mm$	102
4.89	$D = 4mm$: zy plane of time averaged velocity at $X = 6mm$	102
4.90	$D = 2.5mm$: zy plane of time averaged velocity at $X = 24mm$	103
4.91	$D = 4mm$: zy plane of time averaged velocity at $X = 24mm$	103
4.92	$D = 2.5mm$: zy plane of time averaged velocity at $X = 54mm$	104
4.93	$D = 4mm$: zy plane of time averaged velocity at $X = 54mm$	104
4.94	$D = 10mm$: zy plane of time averaged velocity at $X = 12mm$	105
4.95	$D = 10mm$: zy plane of time averaged velocity at $X = 24mm$	105
4.96	$D = 10mm$: zy plane of time averaged velocity at $X = 42mm$	105
4.97	$D = 10mm$: zy plane of time averaged velocity at $X = 54mm$	106

4.98 $D = 10mm$: zy plane of time averaged velocity at $X = 90mm$	106
4.99 D variation: velocity displacement metrics	106
4.100 D variation: fluctuation metrics	106
4.101 $D = 2.5mm$: velocity fluctuations field	107
4.102 $D = 10mm$: velocity fluctuations field	107
4.103 $D = 2.5mm$: zy plane of velocity fluctuations at $X = 24mm$	109
4.104 $D = 4mm$: zy plane of velocity fluctuations at $X = 24mm$	109
4.105 $D = 10mm$: zy plane of velocity fluctuations at $X = 24mm$	109
4.106 $D = 2.5mm$: zy plane of velocity fluctuations at $X = 54mm$	110
4.107 $D = 4mm$: zy plane of velocity fluctuations at $X = 54mm$	110
4.108 $D = 10mm$: zy plane of velocity fluctuations at $X = 54mm$	110
4.109 $D = 10mm$ and $k = 1.5mm$. $X = 24mm$: frequency spectra along $y = \delta_{0.99}/2$.	111
4.110 $D = 10mm$: : U POD mode 1	112
4.111 $D = 10mm$: U POD mode 3	112
4.112 $D = 2.5mm$: Recorded signal of HWA in the position of highest fluctuations . .	114
4.113 $D = 2.5mm$: instantaneous Y -vorticity field	114
4.114 $D = 2.5mm$: U POD mode 1	115
4.115 $D = 2.5mm$: U POD mode 3	115
4.116 $D = 2.5mm$: U POD mode 5	116
4.117 $D = 2.5mm$: U POD mode 7	116
4.118 Wedge size along their downstream evolution. Legend on figure 4.119	118
4.119 Wedge size along their downstream evolution, scaled with C_W	118
4.120 Velocity displacement metrics, scaled with C_{met}	119
4.121 Fluctuation metrics of the elements displaying a POD mode structure (either vari- cose or sinuous), scaled with C_{met}	120
4.122 $D = 4mm, k = 1.5mm$ and $D = 2.5mm, k = 1.5mm$: position of wedge opening vs. Re_k	121
4.123 Wedge size along their downstream evolution, for elements with $D = 10mm$. . .	122

4.124	Wedge size along their downstream evolution scaled with C_W , for elements with $D = 10mm$	122
4.125	$k = 1mm$, different diameters: position of wedge opening vs. Re_k	123
4.126	$k = 0.5mm$, different diameters: position of wedge opening vs. Re_k	123
4.127	$k = 0.5mm$ and $k = 1.5mm$, different diameters: position of wedge opening vs. U_∞	124
4.128	$D = 10mm$, $k = 0.5mm$, $U_\infty = 8m/s$: U time averaged field.	125
4.129	$D = 6mm$ and $U_\infty = 15m/s$	126
4.130	$D = 10mm$ and $U_\infty = 22.5m/s$	126
A.1	Tomographic PIV setup, inclusive of the thermographic camera	136
A.2	Tomographic PIV setup. In the background the laser sheet along the FOV	136
A.3	Tomographic PIV results: wall parallel planes for $U = 8m/s$, $D = 4mm$, $k = 1.5mm$, $y = 0.98mm$	137
A.4	Tomographic PIV results: wall parallel planes for $U = 8m/s$, $D = 4mm$, $k = 1.5mm$, $y = 1.09mm$	138
A.5	Tomographic PIV results: wall parallel planes for $U = 8m/s$, $D = 4mm$, $k = 1.5mm$, $y = 1.2mm$	138
A.6	Tomographic PIV results: wall parallel planes for $U = 8m/s$, $D = 4mm$, $k = 1.5mm$, $y = 1.32mm$	139
A.7	Tomographic PIV results: wall normal planes for $U = 8m/s$, $D = 4mm$, $k = 1.5mm$	139
A.8	Tomographic PIV results: wall parallel planes for $U = 8m/s$, $D = 10mm$, $k = 1.5mm$, $y = 0.98mm$	140
A.9	Tomographic PIV results: wall parallel planes for $U = 8m/s$, $D = 10mm$, $k = 1.5mm$, $y = 1.09mm$	140
A.10	Tomographic PIV results: wall parallel planes for $U = 8m/s$, $D = 10mm$, $k = 1.5mm$, $y = 1.2mm$	141
A.11	Tomographic PIV results: wall parallel planes for $U = 8m/s$, $D = 10mm$, $k = 1.5mm$, $y = 1.32mm$	141
A.12	Tomographic PIV results: wall normal planes for $U = 8m/s$, $D = 10mm$, $k = 1.5mm$	142
B.1	$U_\infty = 8m/s$: clean boundary layer	143

B.2 $U_\infty = 6m/s$: clean boundary layer	144
B.3 $U_\infty = 12m/s$: clean boundary layer	144

List of Tables

3.1	List of all the elements produced and tested during this project	51
3.2	Hot wire anemometry experimental matrix	52
3.3	List of all the elements tested with PIV	53
3.4	Transition regime of the main elements: nominal and critical Re_k	54
4.1	Frequencies and Strouhal numbers: variation of diameter	111

List of Symbols

D	Roughness diameter
f	Frequency
k	Roughness height
Re_c	Chord Reynolds number
Re_k	Roughness Reynolds number
$Re_{k,crit}$	Critical roughness Reynolds number
Str	Strouhal number
U_{Avg}^{HWA}	Time-averaged streamwise velocity measured by HWA
U_{Std}^{HWA}	Fluctuations of streamwise velocity measured by HWA
U_{Avg}^{PIV}	Time-averaged streamwise velocity measured by PIV
U_{Std}^{PIV}	Fluctuations of streamwise velocity measured by PIV
U_k	Undisturbed boundary layer speed at the roughness top
U_∞	Freestream velocity
UVW	Velocities along XYZ
$\Delta U, \Delta W$	Displacement from the the undisturbed BL velocity
W_w	Wedge width
X_{wo}	Streamwise location of wedge opening
XYZ	Wind tunnel coordinate system
δ_*	Boundary layer displacement thickness
η	Aspect ratio D/k
BL	Boundary layer
FOV	Field of view
HWA	Hot wire anemometry
LTT	Low turbulence tunnel
PIV	Particle image velocimetry
POD	Proper orthogonal decomposition

Chapter 1

Introduction

Ever since the groundbreaking publication of Ludwig Prandtl (1905), boundary layer transition has been one of the main topics of research in the field of fluid dynamics. Due to the complexity of the physics involved, the scientific interest around this phenomenon remains unchanged, as many more steps are still to be taken in the direction of a deep and thorough understanding. Nevertheless, purely scientific relevance is not the only reason behind the appeal of this topic. Aeronautical engineering and industry focus their attention in the increase in skin friction drag generated by the transition from a laminar to a turbulent boundary layer. As reported by Saric et al. (2011), in a modern transport aircraft such as Airbus A320, about half of the total drag force is caused by the turbulent skin friction, and 40% of it comes from aerodynamic appendices: wing, tail and fin. Hence, the possibility to increase the amount of wing surface undergoing a laminar boundary layer could be crucial, both in terms of fuel consumption and aerodynamic performances. Higher economic competitiveness and inferior environmental impact are among the consequential aspects of this potential enhancement. These are expected to be the main goals of the next decades of aviation. Furthermore, the almost complete exploitation of other technologies (i.e. propulsive and structural improvements) seems to suggest this as a promising direction, although extremely intricate (Green, 2008).

Among the several different facets of boundary layer transition, one of the most commonly investigated is the influence of surface roughness. This can be either a distributed roughness, characteristic of the aerodynamic surface, or an isolated element of disturbance. The latter is the main protagonist of this research. More specifically, the effects of millimeter-sized cylinders on a three-dimensional boundary layer were investigated. This last sentence contains the two identification characteristics of this work: the type of boundary layer and the specific disturbance it undergoes.

Swept wings are one of the most commonly used aerodynamic solutions in aeronautic. Boundary layers along these wings are characterized by a velocity component called crossflow, normal to the direction of the inviscid streamlines and generated by a perpendicular pressure gradient

(Malik et al., 1994). Due to the no-slip condition at the wall and to the inviscid force balance in the outer border of the boundary layer, this velocity profiles show a point of inflection: inception for the propagation of instabilities (Tani, 1969). The most characterizing feature of these instabilities is the generation of stationary co-rotating vortices (under low freestream turbulence condition (Deyhle and Bippes, 1996), whose breakdown is often preceded by arising secondary instabilities (Serpieri and Kotsonis, 2016).

Over the years, single millimeter-sized roughness elements have been largely used for experimental study of the most fundamental phenomena occurring inside boundary layers (Acarlar and Smith, 1987; Klebanoff et al., 1992). Furthermore, distributed arrays of cylinders have been exploited for the conditioning of three-dimensional boundary layer, by forcing the cross-flow disturbances at given wavelength (Saric et al., 1998; Bippes, 1999). On a general basis, several researches have been carried out in order to assess the effects of different types of disturbances on the development of two-dimensional and three-dimensional boundary layers. However, the available literature concerning isolated roughness elements inside a crossflow dominated boundary layer is minimal (Kurz and Kloker, 2016), especially in terms of experimental investigations. This research is believed to fill a blank space in the current knowledge of a scientifically relevant phenomenon, whose physical mechanisms are still to be fully comprehended (Reshotko and Tumin, 2004). By doing this, the author carried out a state-of-the-art wind tunnel experiment concerning three-dimensional boundary layer. In fact, the particle image velocimetry test was upgraded by the inclusion of hot wire anemometry and infrared thermography, and by the combination of all these techniques. Moreover, the choice of isolated elements over a distribution of roughness is related to the importance of understanding the phenomena playing a main role in this transition mechanism. This process is crucial to continue the research towards the study of more chaotic sources of disturbance, such as surface roughness. Finally, the millimeter-sized elements could be used to model the presence of protuberances of any sort, pointing out the industry level relevance of this research. In fact, these cylinders could model accumulation of external residues (Suryanarayanan et al., 2017), imperfections in manufacturing, fasteners or mechanical junctures. Other than a physical description, interpretation and analysis of the obtained data, the results led to a detailed study of the effects of different roughness sizes. In fact, the experiments were repeated with cylinders of different diameter and height, and under the influence of different freestream speeds of the wind tunnel.

Chapter 2

Literature Review

This chapter is dedicated to a comprehensive review of the relevant literature for the studied topic. The first section describes the crossflow instability, which is the main feature of the investigated boundary layer. After this, a review around roughness induced transition is reported, starting with distributed roughness on swept wings, used for the conditioning of crossflow dominated boundary layers. Finally, isolated roughness transition is treated, with focus towards both two-dimensional and three-dimensional boundary layers.

2.1 Crossflow Instability

After the short description provided in chapter 1, it is important to get deeper into the topic of crossflow instability, in order to put into context this research project. Fundamental contributions to the experimental study of three-dimensional boundary layer have been brought by the ASU (Arizona State University) group, led by William Saric and by the DLR team of research with Bippes and coworkers. [Saric et al. \(2003\)](#) and [Bippes \(1999\)](#) are fully comprehensive reviews of the topic. Flow over swept wings is characterized by curved streamlines, related to the aforementioned perpendicular pressure gradient. The balance between this pressure force and the centripetal force (strictly related to the flow speed) is in equilibrium in the inviscid field. However, the same cannot be said for the boundary layer region. As the flow momentum gets lower inside this region, the particles would tend to move in the direction perpendicular to the streamline (see figure 2.1), generating a secondary flow: the crossflow ([Serpieri and Kotsonis, 2016](#); [Saric et al., 2003](#)).

The inflectional point of this velocity component generates both unsteady and steady instability modes, where the latter dominate in low turbulence environment, whereas the traveling modes (unsteady) prevaricate in case of medium-high level of turbulence ([Deyhle and Bippes, 1996](#); [Bippes, 1999](#)]. This is visible from figure 2.4 from [Deyhle and Bippes \(1996\)](#): the stationary mode, indicated with \bar{u}_s prevaricates over the traveling mode (u_{rms}), when the

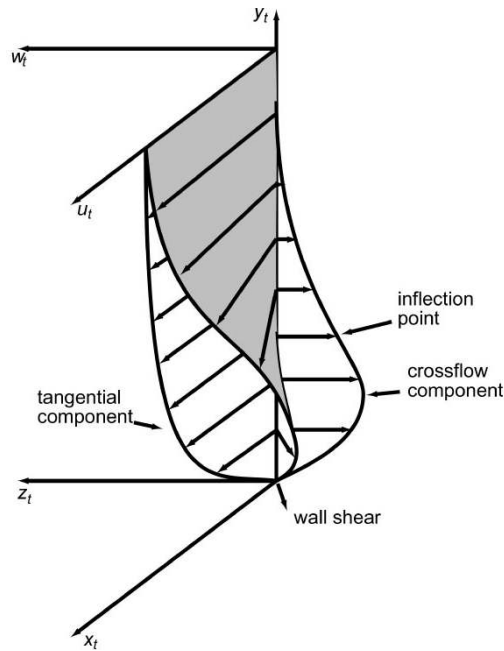


Figure 2.1: Velocity profiles of a swept wing boundary layer. Reproduced from Saric et al. (2003)

turbulence level is $Tu = 0.15\%$. On the other hand, a level of turbulence of $Tu = 0.57\%$ sees the domination of unsteady modes 2.6, whose occurrence is less evident but already present on figure 2.5. The authors also describe the effects of other environmental conditions on the crossflow instability behaviour, during the receptivity phase. They found that the most influencing external disturbance is the surface roughness, especially in terms of transition location. Two-dimensional roughness elements and sound sources do not influence to the same extent. On the other hand, the increase in turbulence level of the flow is a transition delaying feature up to $Tu > 0.2\%$, damping the growth of steady vortices. However, if combined to a proper roughness level, it reinforces the traveling modes up to the point they become the leading mechanism, canceling the positive influence of freestream turbulence.

The case of interest for this project concerns low turbulence levels, valid for both wind tunnel environment and free flight circumstances (Reibert et al., 1996; Carpenter et al., 2008). Under these conditions, the boundary layer experiences the so-called crossflow vortices: flow structures approximately aligned with the flow direction (Serpieri and Kotsonis, 2016). The development of these structures leads to transition of the boundary layer after three stages, as exhaustively explained by White et al. (2001). The first is the so-called receptivity stage (Tempelmann et al., 2012a,b; Schrader et al., 2009), when the environmental features such as flow turbulence, surface roughness and acoustic disturbance are internalized by the boundary layer in the shape of primary instabilities. The second phase starts with an amplitude growth of these structures, which is initially complying with the linear stability theory (Saric et al., 2003). However, the saturation of this initial disturbances eventually leads to the birth of high frequency secondary instabilities, associated to the velocity shears (Serpieri and Kotsonis, 2016). These secondary modes have been proven to be the cause of the crossflow vortices breakdown (White et al., 2001), which occur farther downstream of the primary instability saturation (Saric et al., 2003). They have been extensively investigated with several different

flow measurement techniques by [Serpieri and Kotsonis \(2016\)](#), with the intention to provide a complete description of the three-dimensional organization of these structures. Some of the results of their research are displayed in figure 2.2 and 2.3, where an oil flow visualization and a tomographic PIV flow field are shown, respectively. One could notice the slightly inclined path followed by these structures, distributed all over the swept wing. Furthermore, the breakdown zone is visible in the bottom left corner, where the structures start losing coherence and develop in a turbulent boundary layer.

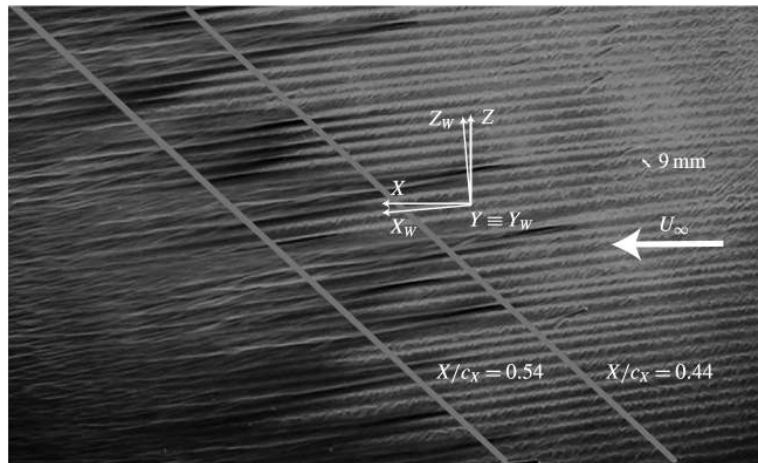


Figure 2.2: Oil flow visualization of crossflow stationary vortices over a swept wing. Reproduced from [Serpieri and Kotsonis \(2016\)](#)

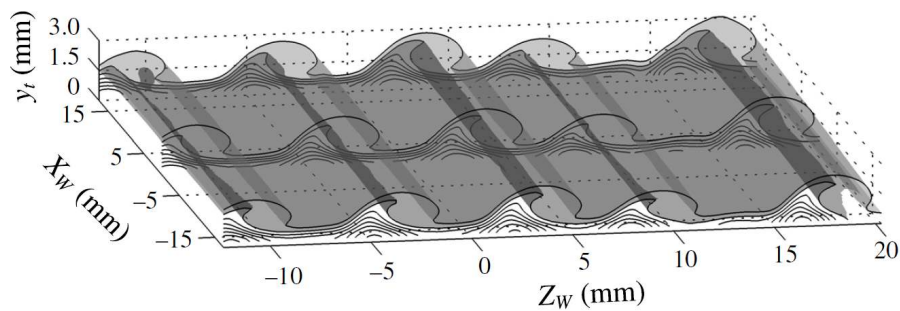


Figure 2.3: Tomographic PIV reconstruction of crossflow vortices. Reproduced from [Serpieri and Kotsonis \(2016\)](#)

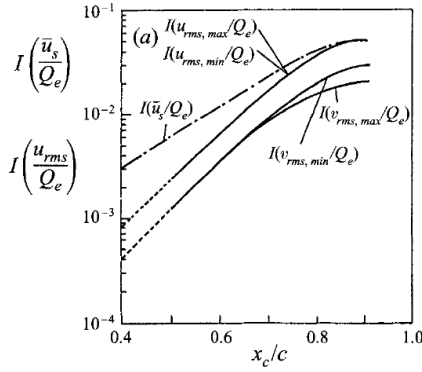


Figure 2.4: Spatial growth of steady and unsteady instability modes: $Tu = 0.15\%$. From Deyhle and Bippes (1996)

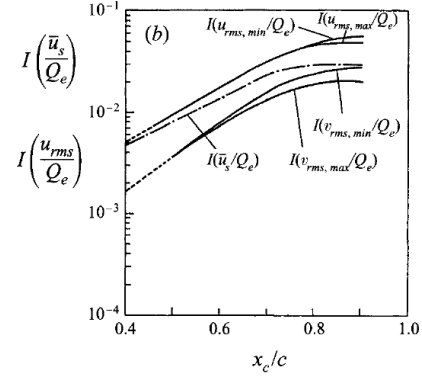


Figure 2.5: Spatial growth of steady and unsteady instability modes: $Tu = 0.27\%$. From Deyhle and Bippes (1996)

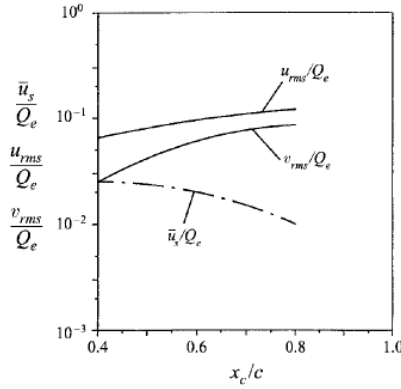


Figure 2.6: Spatial growth of steady and unsteady instability modes: $Tu = 0.57\%$. From Deyhle and Bippes (1996)

2.2 Fundamentals of Isolated Roughness Induced Transition

The topic of roughness induced transition must start with an introduction to the mechanisms involved in this process. Roughness induced transition could occur in many different variations, meaning that the level of introduced disturbances modifies the nature of the phenomenon. A conceptual map is shown in figure 2.7, whose contents were initially introduced by Morkovin (1969) and subsequently reorganized by Morkovin et al. (1994). Depending on the intensity and the typology of the disturbance perceived, boundary layer could develop primary growth modes, transient growth or secondary growth modes. It is possible to observe the so-called bypass transition mechanism, leading to the immediate occurrence of transition.

The concept of bypass transition is well explained by [Henningson et al. \(1993\)](#), who refer once again to the words of [Morkovin \(1969\)](#). When transition occurs more rapidly than a classic Tollmien-Schlichting dominated scenario, the growth of two dimensional instabilities is bypassed. This is the reason for which transition due to generation of finite amplitude oscillation can be observed not far downstream of the roughness elements, in a supercritical condition.

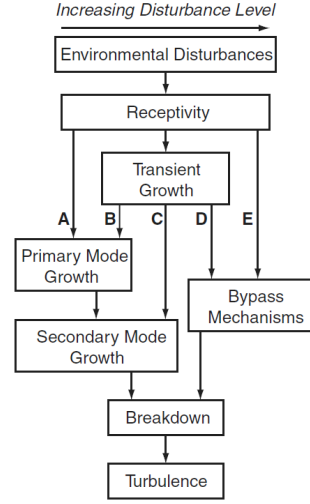


Figure 2.7: Transition scheme with varying disturbance intensity. From [Downs et al. \(2008\)](#)

Geometry and dimensions of the roughness elements plays a crucial role for the determination of the perturbation intensity, especially for isolated roughness elements. In fact, starting from the late 1950's, the research around isolated roughness transition focused on the effect of element height. It was found that the behaviour of this phenomenon is much more critical than for two-dimensional roughness elements (such as trip wire) and distributed surface roughness. This means that the transition location moves brusquely towards the roughness position after the critical level of velocity or roughness height is reached, with only slight variation when these two parameters are increased within critical limits ([Tani, 1969](#); [Klebanoff et al., 1992](#)). Typically, the parameter in use for the criticality identification of the roughness element is the Reynolds number Re_k ([Redford et al., 2010](#)), shown by equation 2.1, where U_k is the speed at the roughness height in the undisturbed boundary layer and k is the height of the element itself.

$$Re_k = \frac{U_k k}{\nu} \quad (2.1)$$

It is clear from this equation that both an increase in freestream speed and element height could move this value towards a critical value. This last is defined as the lowest Re_k that is capable of triggering transition by means of a bypass transition mechanism, downstream of the element ([Downs et al., 2008](#); [Klebanoff et al., 1955](#); [Doenhoff and Braslow, 1961](#)). In these regards, one of the main reference is [Tani \(1969\)](#). The author splendidly reviews all

the phenomena affecting transition inside boundary layers, with a detailed section on isolated roughness related phenomena. He states that the behaviour of the critical Reynolds number scales according to $k/D^{2/5}$, starting from a value between 600 and 900, for those elements with unity aspect ratio (Ergin and White, 2006; Klebanoff et al., 1992, 1955). Furthermore, this information is also displayed by the author in shape of a graph, including data from three different pieces of work (Klebanoff et al., 1955; Tani et al., 1962; Mochizuki, 1961), visible in figure 2.8.

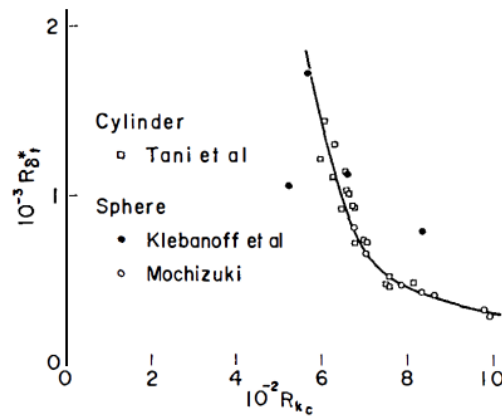


Figure 2.8: Transition Reynolds number vs. critical Reynolds number for elements of $k/D = 1$ and zero pressure gradient. From Tani (1969), collecting data from Klebanoff et al. (1955); Tani et al. (1962); Mochizuki (1961)

This figure shows elements that were placed in a zero pressure gradient boundary layer. Nevertheless, Tani affirms that the pressure gradient on the boundary layer is not a relevant variable for the transition location change.

The second pivotal research was carried out by Klebanoff et al. (1992). Among the various aspects evaluated in this work, one of the most interesting is the variation of Reynolds of transition under the effects of several different Re_k values, roughness dimensions and element locations. The target of this work was to increase the available data around isolated roughness induced transition, by means of hot wire anemometry measurements and oscillograms. Both hemispherical elements ($D = 3.18mm$ and $D = 6.36mm$) and cylindrical elements ($D = 3.18mm$ and $k/D = 1$) were tested, and a large set of data was collected. Moreover, the fundamental processes involved in this phenomenon were studied in order to investigate the relation between large scale structures and small scale structures. In fact, most of the previous researches tended to either focus on the study of small scale phenomena, such as hairpin vortices shed by the element, or visualize and measure the macro-structures generating aft the element, such as horseshoe vortices. The authors stand against this dualism in the approach and in the physical interpretation, supporting the idea of two complementary views to deeply understand the transition mechanisms. In fact, the boundary layer is modeled by means of a two regions simplification: outer (far from the wall) region and inner region, with the latter having as a protagonist the interaction between hairpin eddies and stationary structures. This is believed to sustain the generation of turbulence towards a fully developed turbulent boundary layer, as also confirmed by Citro et al. (2015). In the outer region, the hairpin

vortices deformation leads to the creation of large vortex rings. One of the most remarkable results of this research comes from the review of the shedding behaviour of these roughness elements. Figure 2.9 shows the Strouhal number trend of all the elements, calculated with the boundary layer scaling; i.e. $Str = f\delta_k^*/U_k$ where f is the shedding frequency δ_k^* is the boundary layer displacement thickness, and U_k the boundary layer velocity at the tip of the roughness position in the undisturbed boundary layer. Finally, figure 2.10 displays the Strouhal number computed from the roughness height $Str = fk/U_k$.

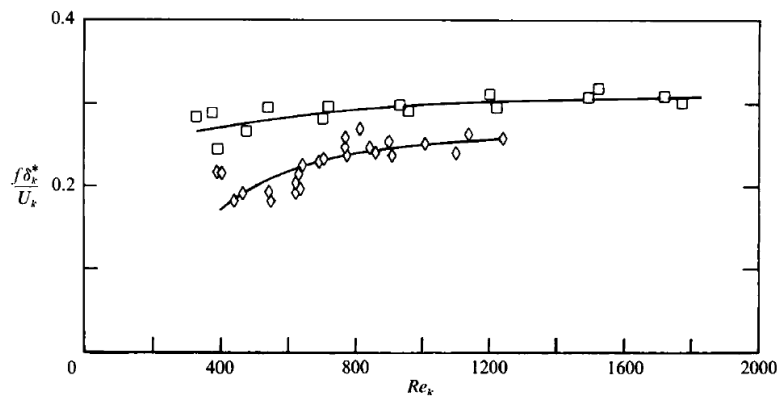


Figure 2.9: Displacement thickness Str vs. Re_k . From Klebanoff et al. (1992). Squares: hemisphere. Diamonds: cylinders.

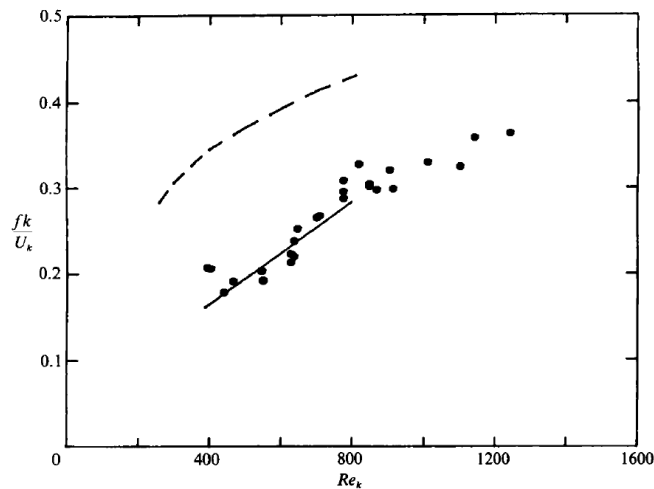


Figure 2.10: Cylinder height Str vs. Re_k . From Klebanoff et al. (1992)

The results of this research are often compared with the data available from Acarlar and Smith (1987), which cannot be omitted when studying the topic of isolated roughness transition mechanisms. The purpose of this research was to investigate the role of hairpin vortices in sustaining and generating turbulence inside a boundary layer. Furthermore, the study of shedding behaviour and structure topology has been carried out, leading to a complete and thorough overview of the phenomenon.

The authors accomplished their purposes by experimentally studying the effects of an hemispherical (and half-teardrops) elements on the boundary layer of a flat plate. The experiments were carried out in a Plexiglas water channel and the flow past the elements was visualized by means of dye and hydrogen-bubble wire. The experimental setup is displayed in figure 2.11, where three sets of dye injection positions allow the visualization of the structures in different wake's locations and help describing the hairpin vortex creation mechanism. As for the shedding frequency behaviour, hot film anemometry has been exploited.

The results obtained by this investigation display the values of the Strouhal number with a range of roughness radii from 3 to 18 mm and free stream velocities from 3 to 30 m/s, with the characteristic frequency in the position of maximum velocity oscillation with the probe. Therefore, the roughness Reynolds number was increased from $Re_k = 30$ to $Re_k = 3400$, after which the wake becomes irregular. It is worth mentioning the range of δ_* varying between 1.8 and 10.5 mm, as well as the boundary layer thickness spectrum: from 5 to 30.6 mm. The results indicate how Str starts from a minimum of 0.05 when Reynolds fall under $Re_k = 120$ up to a maximum value oscillating between 0.38 and 0.41 depending on the streamwise location of the roughness element. The mentioned $Re_k = 120$ sets the beginning of the regular shedding of the hairpin structures, whereas $Re_k = 1400$ represents the first value for which the frequency spectra show multiple peaks (therefore the first harmonic was selected as representative). All these data are reported in figure 2.13. What is interesting to notice is the absence of a monotonic behaviour with respect to Re_k growth when passing the value of about $Re_k = 1000$.

As for the topological study, the first step was taken in the direction of the near wake flow description. Consequently, the physics behind the generation of haripin vorteces is widely investigated. As visible from figure 2.12, the standing vortex, i.e. the horseshoe vortex, wraps around the element and its legs propagatate downstream. This is characterized by a typical steady behaviour, differently from the hairpin structures which are shed right downstream the roughness disturbance. Both these two types of structures are connected to the concentration of vortex lines, but in a slight different manner, as explained by the authors. In the hairpin vortex shedding, the low pressure area aft of the roughness is of fundamental importance, causing an inward curvature of the streamlines pass the element. Due to this phenomenon,

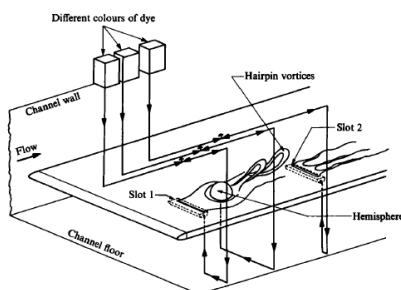


Figure 2.11: Experimental setup. From Acarlar and Smith (1987)

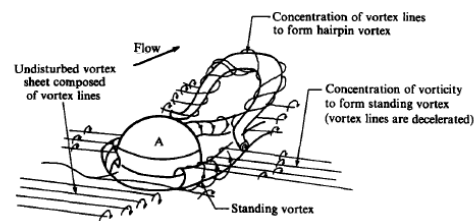


Figure 2.12: Hairpin representation. The formation process, as well as the standing vorteces are visible. From Acarlar and Smith (1987)

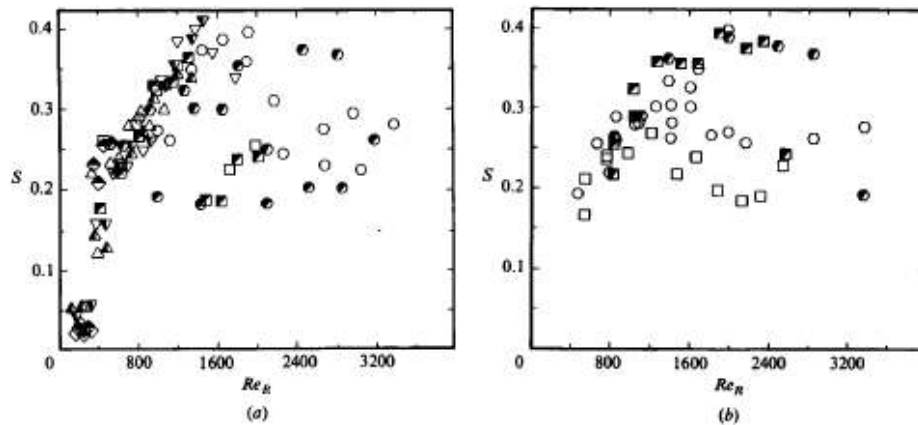


Figure 2.13: Strouhal number variation with Re_k : different symbols represent different radii, the full or empty filling stands for different hemispherical roughness and locations. From [Acarlar and Smith \(1987\)](#)

the pressure balance along these lines changes, and the reaction of the outer (potential) flow is to create the typical inward rotatory motion, which consequently generates the vortical structures. This phenomenon keeps on developing every time the hairpin vortex is discharged.

The downstream development of the vortices is studied by the authors, whose schematic evolution can be found in figure 2.14. They initially present a low angle of inclination from the surface, but the mutual interaction and induced velocity stretches the legs and causes the lift-up mechanism with about a 45° inclination. The stretching mechanism also causes vorticity growth in the core of the vortices. This process proceeds until the hairpin head exits the boundary layer, and curve backwards. Finally, for the purpose of this work it is valuable to mention the generation of secondary structures on the two sides of the hairpin vortex as it develops further downstream (see figure 2.15). The low momentum portion of the fluid that moves up due to the "primary" hairpin legs generates a shear layer which translates into the generation of two lateral vortical structures.

The last research that can be considered as traditional in the study of transition mechanism induced by a single element, concerns the phenomenon of the horseshoe vortex. This is broadly studied by [Baker \(1979\)](#), an experimental investigation on the characteristics of the vortex generating around cylindrical elements. It is one of the landmarks for the understanding of roughness induced transition. Centimeter-sized elements were placed in the test section of a low speed wind tunnel. Flow suction was applied to the wind tunnel wall boundary layers, in order to have a laminar boundary layer at the body location. The relative position between the element and the suction zone could be modified for the cylinder to have a diverse boundary layer profile. Pressure measurement and smoke flow visualization were exploited for the first part of this investigation. However, for the purpose of this thesis, it is far more important to report what has been accomplished by means of hot wire anemometry. The probe was placed just downstream the sides of the 6.35 cm element, in order to capture the oscillation of the horseshoe vortices. In fact, this part of the study focused primarily on the spectral analysis of the flow inside these steady structures, at 1 mm height from the wind tunnel wall. This test

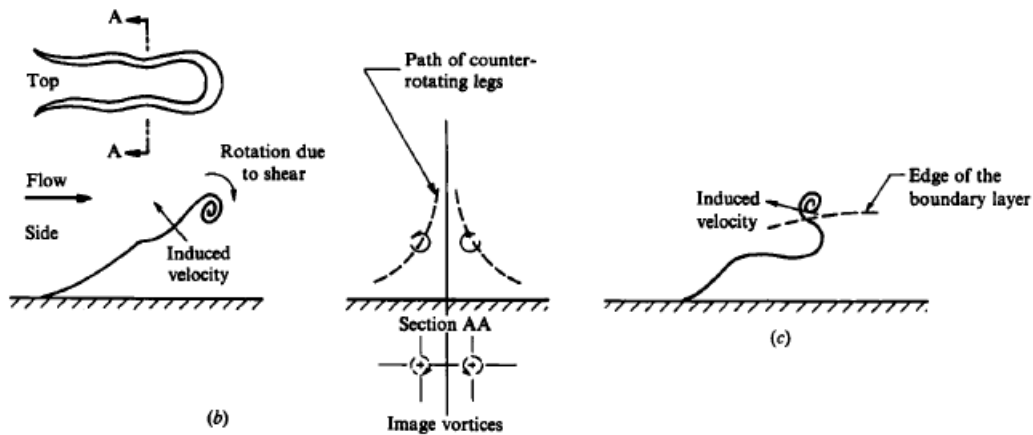


Figure 2.14: Scheme for the development of a hairpin vortex. Legs moving up from the surface (b) and tilting outside the BL. From Acarlar and Smith (1987)

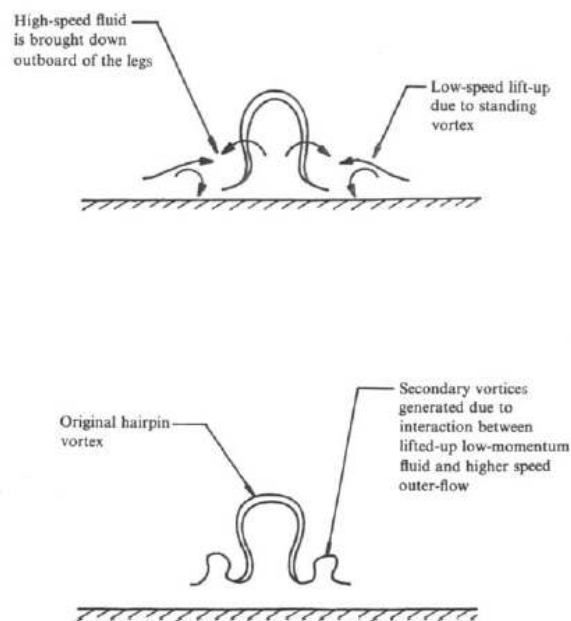


Figure 2.15: Secondary lateral vortices formation. From Acarlar and Smith (1987)

was carried out under the effects of several flow speed and the results obtained are strictly dependent on it. For a low speed condition, the horseshoe vortex was found to show a steady behaviour with no oscillation of sort. As the speed increased, the spectral analysis presented frequency peaks around the value of $Str = 0.26$, increase in parallel to the flow speed up to the high value of $Str = 0.4$. Once a certain level of speed was overcome, a turbulent behaviour was spotted. Figures 2.16 and 2.17 show the power spectral density (PSD) under the condition of $D/\delta^* = 33.8$ and $D/\delta^* = 34.2$, respectively, and $UD/\nu = 4720$ and $UD/\nu = 4780$. Although the conditions are pretty similar, the main peak frequency changes consistently. The smaller peaks visible in the figures are linked to the waveform reconstruction of the hot wire signal, and

are clearly harmonics of the main tone. Furthermore, Baker investigated if these oscillations were actually related to the physical oscillatory nature of the horseshoe vortex. He started by repeating a similar test with a streamlined and a splitter-plate equipped cylinder, in order to get rid of the shedding effects of the near wake. This way, he could understand if those tonal modes were related to the hairpin eddies or other shedding structures. Secondly, he analyzed the spectral response of the same flat plate model in absence of cylindrical body, in order to spot possible preexisting oscillating structures, i.e. responsive to the rotation of the wind tunnel blade. None of these tests identified another possible cause for those results. Therefore, the oscillatory nature of the horseshoe vortex was confirmed, together with the natural tonal modes. They were finally found as related to certain values of UD/ν and D/δ^* , capable of triggering this unstable response.

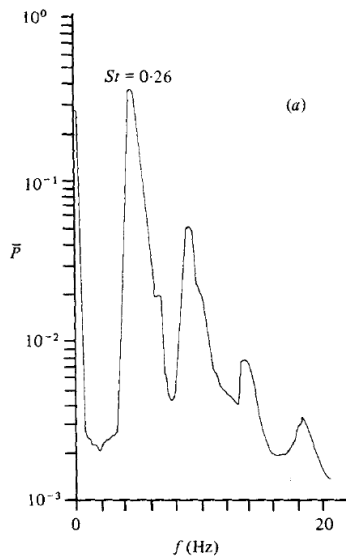


Figure 2.16: Horseshoe vortex PSD spectra, $x/D = -0.82$, $y/D = 0.063$, $z/D = 0$. $D/\delta^* = 33.8$ and $UD/\nu = 4720$. From Baker (1979)

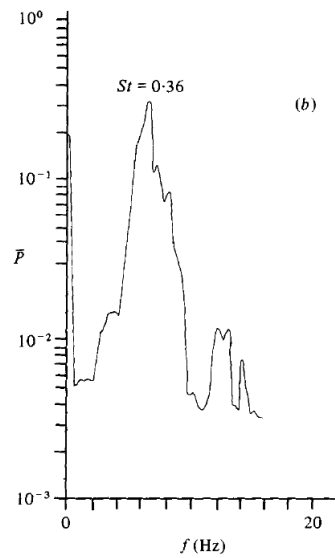


Figure 2.17: Horseshoe vortex PSD spectra, $x/D = -0.82$, $y/D = 0.063$, $z/D = 0$. $D/\delta^* = 34.2$ and $UD/\nu = 4780$. From Baker (1979)

2.3 Distributed Roughness Induced Transition

Before proceeding along the path of isolated roughness, it is important to go through a review of distributed roughness induced transition. Specifically, researches regarding spanwise arrays of roughness elements will be considered. In fact, most of the studies regarding discrete roughness in a swept wing boundary layer involve this type of roughness distribution, primarily used for the conditioning of the boundary layer and the control of the crossflow stationary

vortices behaviour. They have been exploited to study the receptivity and the instability growth of a swept wing boundary layer, under controlled conditions.

Reibert et al. (1996) performed experimental campaigns for hot wire measurement of stationary crossflow vortices. The $0.25\mu m$ polished surface generated nonuniform velocity disturbances, with the superimposition of many different modes, and was found inappropriate to evaluate single modes. The inclusion of an array of $6\mu m$ roughness elements ($Re_k = 0.1$) is able to generate fundamental modes that are in agreement with the given spacing between two of them. In other words, by placing the leading edge roughness element at a 12 mm distance from each other, the most unstable mode ($\lambda = 12mm$) is observed to develop into a growing disturbance. The same phenomenon occurred when forcing the flow with a 36 mm spaced array, with the $\lambda = 36mm$ mode triggered as the dominant one. They also reported the presence of main mode harmonics ($\lambda = 6mm$ and $\lambda = 4mm$ for the first case and $\lambda = 18mm$ and $\lambda = 12mm$ for the second case). Nevertheless, wavelengths larger than the spacing distance were never measured, meaning that this procedure is able to avoid their growth. These last observation gains importance in the article of Saric et al. (1998), where the forcing of the flow by a subcritically distributed array was applied to the boundary layer. It was observed that transition can be delayed, by spacing the elements with a distance that is shorter than the one exciting the most critical wavelength.

Other relevant researches around the receptivity process have been performed by David Tempelmann and coworkers. In these researches, they numerically investigated the receptivity mechanism in swept wing boundary layers, also by reproducing the experiments of the ASU team. They concluded that after increasing k roughly over the 10% of the displacement thickness, nonlinear receptivity effects must be taken into account (Tempelmann et al., 2012b), and confirmed that the receptivity is higher for surface roughness than for free stream turbulence (Tempelmann et al., 2012a). They compared the effects of vertical and streamwise freestream vorticity on the receptivity process, concluding the higher strength of the first (Tempelmann et al., 2011). Finally, further investigation around the predominance of steady or unsteady mode under different disturbances is studied by Schrader et al. (2009).

Following the work of the ASU group, Rizzetta et al. (2010) exploited DNS to investigate spanwise distribution of roughness elements on a 30° swept wing. Other than the study of the stability approach, the authors displayed some interesting results about the effects of differently shaped elements. According to figure 2.18, the shape of the elements strongly influences the velocity field aft the arrays, to an extent such that very different spanwise frequency spectra were linked to different shaped arrays. Diversely sized cylinders, parabolic bumps and 3D squares were used in this research. Some years later, Loiseau et al. (2015) showed that the wedges generated by a cylindrical element are much better sustained than the ones of a small bump, along the streamwise direction, confirming the sensitivity of this mechanism to the shape of the roughness elements.

Most of these researches take advantages of roughness elements (mainly cylinders), whose dimensions (and consequently Re_k) do not overcome the limit of the 'linear' range of receptivity; i.e. the amplitude of the stationary crossflow mode scales linearly with the elements height. Thus, it is possible to superimpose their disturbances of velocity to the main flow field (Kurz and Kloker, 2016). However, caution must be used when defining a 'linear' range of

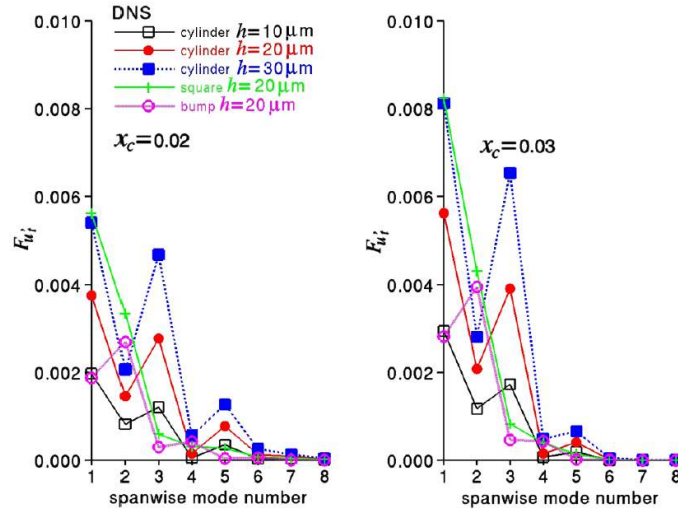


Figure 2.18: Spanwise frequency spectra. From Rizzetta et al. (2010)

receptivity. In fact, as shown by Kurz and Kloker (2014) the amplitude of the most amplified steady crossflow mode has a superlinear response with respect to the change in height of the spanwise roughness array. Hence, the growth in amplitude is steeper than a linear law, and the reason behind this result is not related to transient growth, as also confirmed by the authors. In the same piece of work the authors point out that a spanwise array of alternated hollows and protuberances (if exhibiting a zero spanwise mean) leads to a constant receptivity coefficient, thus a linear behaviour of the mode amplitude. This result appears extremely interesting, as it shows the importance of the flow blockage mechanism in the receptivity process.

In order to study a more complex roughness configuration, supposedly closer to a real condition of a wing, some researchers thought about possible variation to this topic. Placidi et al. (2016) experimentally contributed to this topic by investigating the case of two arrays of micron-sized roughness, placed 1% of the chord apart in the streamwise direction and staggered by 50% from each other spanwise. They found that the addition of the second row of elements slows down the growth of disturbance on a first stage. However, this does not lead to a delayed transition. Contrarily the second stage of transient growth was higher, causing an earlier transition. In the introduction to their work, Downs et al. (2008) summarized the variations in the transition mechanism under the effects of increasing disturbances and showed how to consequentially link: receptivity, primary mode growth, secondary growth mode, transient growth, bypass and breakdown, depending on the disturbance level. This has already been shown in figure 2.7. The authors investigated quasi random distributions of roughness in a flat plate characterized by different element heights. All the configurations ($Re_k = 164$, $Re_k = 227$ and $Re_k = 301$) displayed transient growth but only the $Re_k = 301$ case presented bypass transition. The conclusion of this work stated that Tollmien-Schlichting instabilities were not the cause of the transition, as another phenomenon was believed to be leading this process. The conflict between the dampening effect of steady flow structures and the unstabilizing growth of unsteady oscillation is pointed out as the key point for boundary layer transition due to a 3D roughness element. This conclusion was drawn based on the results

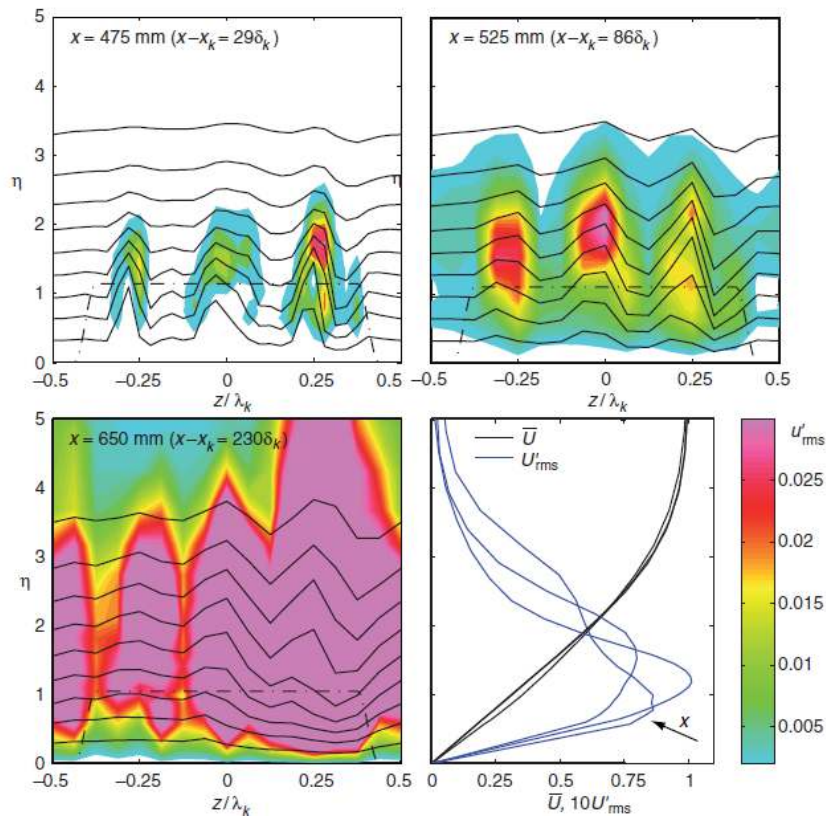


Figure 2.19: $Re_k = 301$: steady (increments of $0.1U_\infty$) and unsteady (colors) velocity contours. All the contours refer to the plot on the bottom right corner. From Downs et al. (2008)

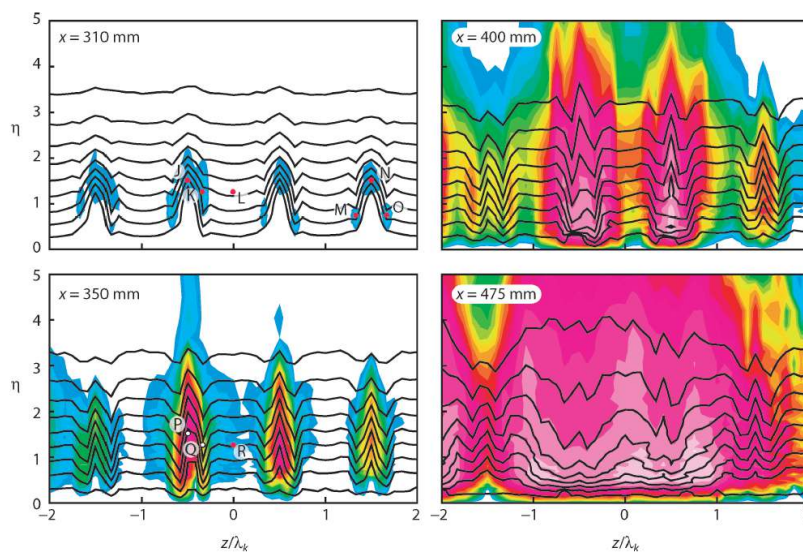


Figure 2.20: $Re_k = 334$: steady (increments of $0.1U_\infty$) and unsteady (exponentially distributed color levels) velocity contours. From Ergin and White (2006)

displayed on figure 2.19 and according to the findings of another important research from [Ergin and White \(2006\)](#). In fact, they carried out a research around the effects of a spanwise distributed roughness array in a flat plate boundary layer. The dimensions of the cylinders varied from moderate ($Re_k = 202$) to high ($Re_k = 334$) and their influence on transition was evaluated. They observed a Kelvin-Helmoltz instability mechanisms and the generation of an horseshoe vortex around the roughness element. Moreover, the temporal spectra are in good agreement with previous literature, as the dominant frequency of 650 Hz indicates a Strouhal number of 0.15. To be more specific about the aforementioned transition process involving steady and unsteady velocity fluctuations, an example of a supercritical condition is displayed in figure 2.20, where the unsteady fluctuation largely develop in the last frame. According to the authors of this work, when the fluctuations get too persistent and intense, the mean velocity fields loses its damping capability and transition takes place soon after the development of non-linear growth.

2.3.1 Isolated Roughness Induced Transition

This section is the final component of the literature review. It will describe those researches around isolated roughness transition that are the most relevant for the purpose of this work. These include both 2D and 3D boundary layers, with the latter on the second subsection.

Isolated Roughness in a 2D Boundary Layer

[Ye et al. \(2016b\)](#) investigated the flow behind four different isolated roughness elements by means of tomographic particle image velocimetry. The elements differ from each other because of their geometry shape: a cylinder, a 3D square, an hemisphere and a micro ramp. The experiment entailed a flat plate boundary layer and a supercritical Re_k value ($Re_k = 1170$ with the critical value placed between 455 and 682). Both a time-averaged and a instantaneous flow fields are shown. The tests were carried out with a 10 m/s speed of the wind tunnel and at a $h/\delta = 0.61$ position in the boundary layer. The flow topology of each element is observed and described, from the area in the strict vicinity of the element (featuring the already mentioned horseshoe and hairpin vortices) to the transition location. The first of these is shown in figure 2.21, where three different zy planes close to the roughness element ($x/h = 5, 14, 24$) are displayed. The picture displays the spatial organization of horseshoe pairs (HP), rear pairs (RP), tertiary pairs (TP), fourth pairs (FP), trailing-edge pairs (TRP), secondary pairs (SP). One could notice how the topology of the wake is extremely different from one geometry to another, with the presence of strong horseshoe vortex pairs when the roughness element has a blunt front shape.

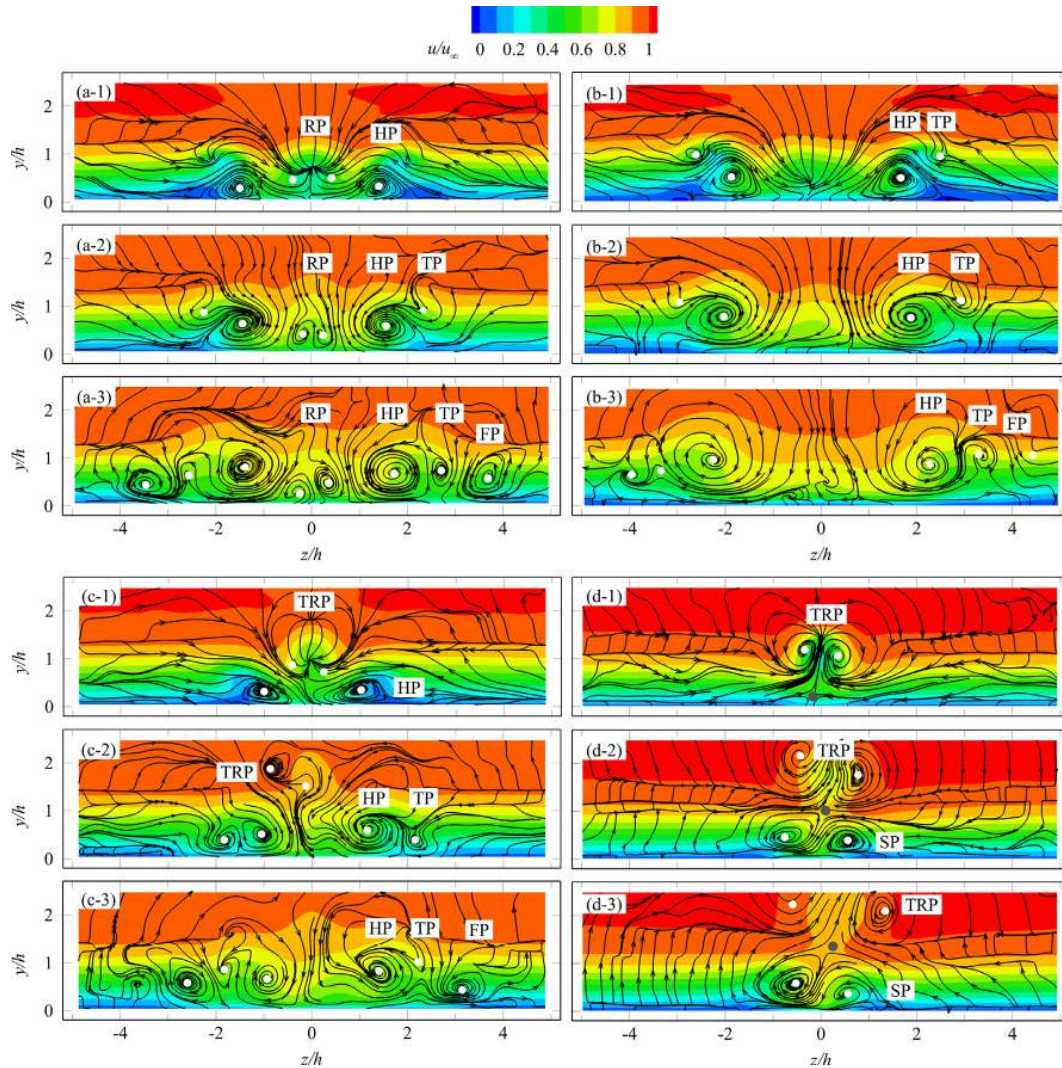


Figure 2.21: Streamlines of the in-plane velocity and time-averaged velocity contour of u/u_∞ : a) cylinder, b) square, c) hemisphere, d) micro-ramp. From Ye et al. (2016b)

The same results can be shown with another type of figure, namely: a conceptual sketch as figure 2.22. In both these images, the areas of low and high speed in the steady velocity field are put into relation to the vortical structures of the flow.

Other than the analysis of the time averaged flow field, time resolved tomographic PIV allowed the authors to investigate the instantaneous flow field and the generation of hairpin vortices aft the element. For the cylindrical roughness, this is shown in figure 2.23, where a schematic representation of the results can help understanding how the hairpin eddies relates to the transition process. The primary hairpin vortices (PHV) develop right after the element, in the region of the separated shear layer, whereas the leg-shaped secondary hairpin vortices (SHV) develop on their sides. The PHV start losing coherence at about $x/h = 20$, and develop into turbulent regime boundary layer streaks, whereas SHV experience a similar phenomenon at about $x/h = 30$. As this happens, new hairpin vortices develop. This way, the relation between the low velocities regions of the time-averaged field and the lateral spreading of

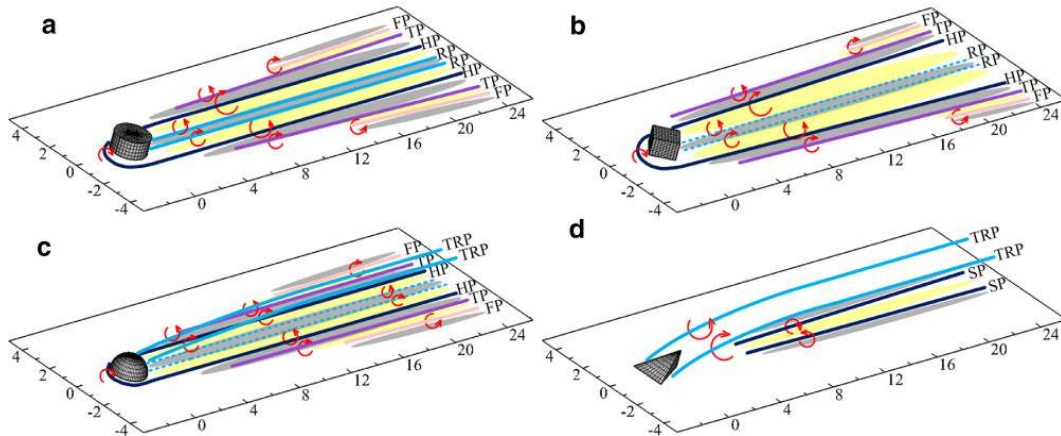


Figure 2.22: Wake topologies: lines represent streamwise vortices, grey and yellow areas represent low- and high-speed streaks respectively. From Ye et al. (2016b)

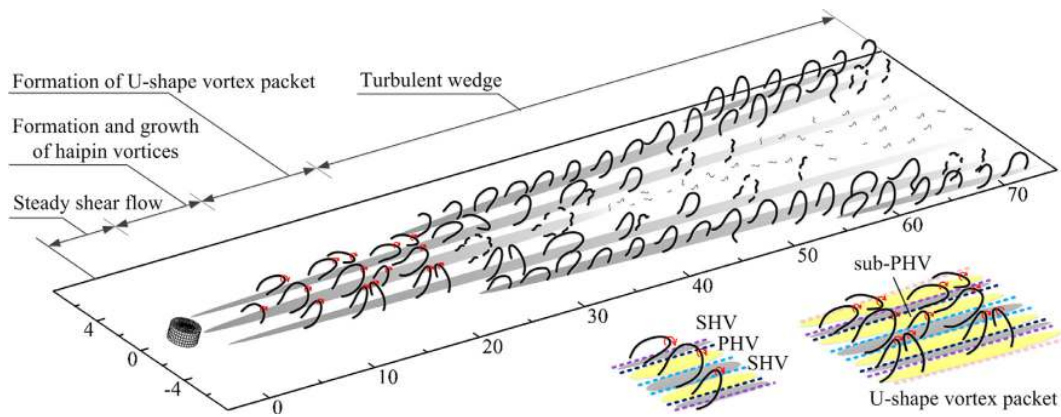


Figure 2.23: Conceptual representation of the wake formation of vortical structures. From Ye et al. (2016b)

turbulent wedge is displayed. In fact, the spanwise location of new hairpin vortices can be identified in the upwash motion regions caused by two adjacent streamwise vortices. These are low-speed regions according to the time-averaged field. In its downstream evolution, the turbulent streak develops new lateral low-speed regions. Therefore, new hairpin structures are generated, leading to the spreading of the wedge. Kuester and White (2016) and Chu and Goldstein (2012) reach similar conclusions, as the alternate low and high-speed streaks occurring on the sides of the turbulent wedges are identified as the leading mechanism for its spreading.

Another interesting data evaluation carried out by Ye et al. is displayed in figure 2.24. Following the work by Andersson et al. (2001), the amplitude (equation 2.2) of the velocity streaks is evaluated as a parameter for the identification of the flow properties downstream of the element. More specifically, when the amplitude is above $0.26U_\infty$ the instability related to the spanwise shear stresses are triggered, in a sinuous mode dominated condition. On the other hand, as the streaks amplitude grows above $0.37U_\infty$, the main phenomenon is the

varicose mode, generated by the three-dimensional layer instability.

$$Au(x) = \frac{1}{2} [\max_{yz}(u(x, y, z) - u_{bl}(x, y, z)) - \min_{yz}(u(x, y, z) - u_{bl}(x, y, z))] \quad (2.2)$$

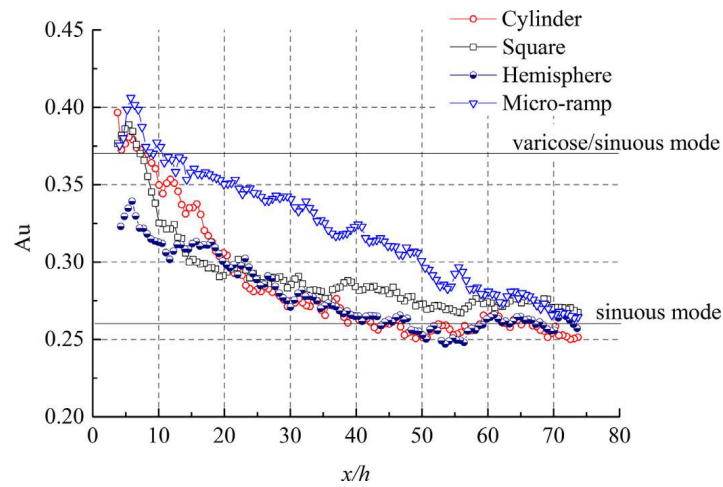


Figure 2.24: Streaks amplitude along streamwise coordinate. From [Ye et al. \(2016b\)](#)

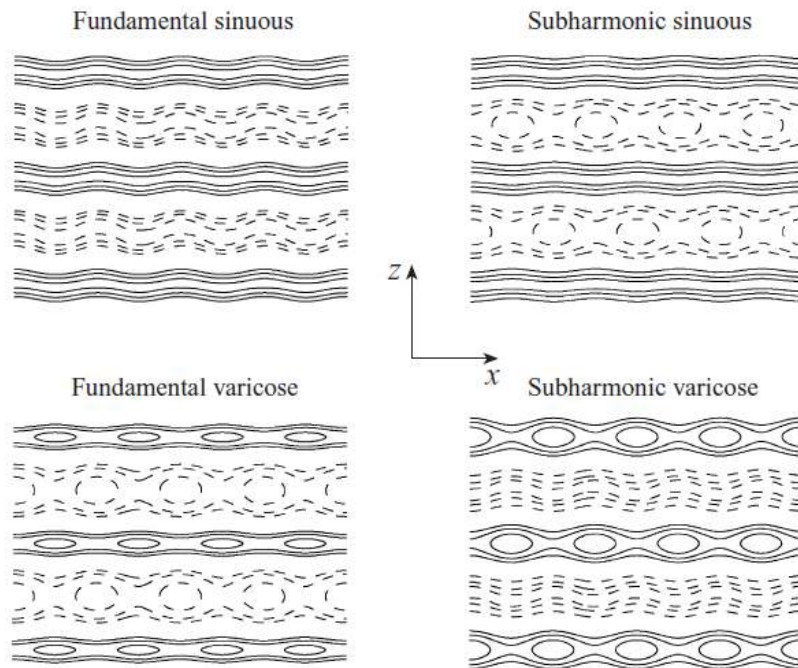


Figure 2.25: Instability modes along the xz plane. High-speed streaks: dashed lines. Low-speed streaks: solid lines. From [Andersson et al. \(2001\)](#)

Andersson et al. (2001) is an interesting piece of work for what concerns the streaks breakdown inside a boundary layer. More specifically, DNS are exploited to study the evolution of streamwise- aligned vortex structures. Particular attention is given of the lift-up mechanism, main cause of the velocity spanwise modulation in the mean flow. As explained by the authors, this condition may be related to the presence of inflection points in the main velocity, eventually leading to secondary instabilities and consequently to an early turbulent breakdown. Moreover, the aforementioned varicose or sinuous mode are illustrated in a visual manner by means of figure 2.25. These two terms refer to the geometrical distribution of the low speed streaks generation, indicated with solid lines in the pictures, whilst dashed lines refer to high speed regions.

It is of paramount importance for this research to accurately review the work from Loiseau et al. (2014). In this study, the authors investigate by means of DNS the effects of an isolated cylinder on a laminar boundary layer. They mainly focus on the characteristics of the low speed streaks creating aft the element, together with two pairs of low and high speed streaks on its sides. The aim is to investigate the types of instabilities generated by this phenomenon. Particularly, the study of varicose and sinuous modes is performed. The first is caused by the three dimensional shear layer aft the cylindrical element, whilst the sinuous mode resemble the Von Kármán instability and its related to the lateral shear layer. Moreover, a variation in the aspect ratio of the elements and in the Reynolds number is included in this study, as the effects of these two parameters are investigated. Throughout the whole set of tests, the displacement thickness and the boundary layer thickness are kept constant in order to isolate the effects of either the aspect ratio (named η in the reference) or Re . The latter is shown in figure 2.26 and 2.27, where the upper view and the side view are displayed. One can immediately notice how the the high Re condition presents way stronger gradients in the

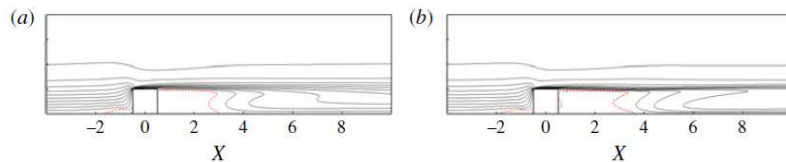


Figure 2.26: Symmetry plane view of the near wake under the effects of different Re : contours from $U = 0.1$ to $U = 0.99$. a) $(Re, \eta) = (600, 1)$, b) $(Re, \eta) = (1250, 1)$. From Loiseau et al. (2014)

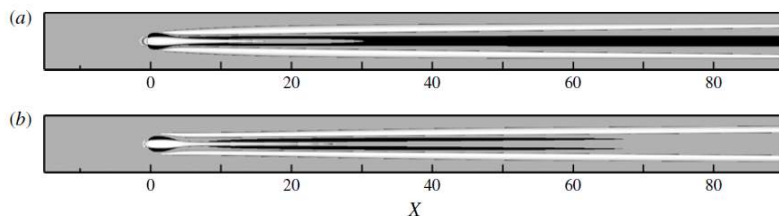


Figure 2.27: Top view of streaky structures aft the roughness element under the effects of different Re : white and black are respectively low- and high-speed streaks. a) $(Re, \eta) = (600, 1)$, b) $(Re, \eta) = (1250, 1)$. From Loiseau et al. (2014)

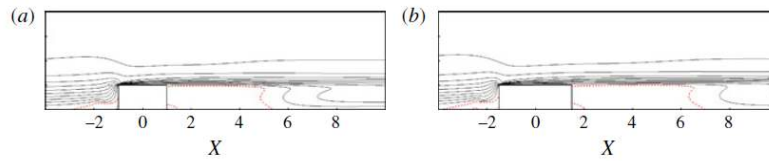


Figure 2.28: Symmetry plane view of the near wake under the effects of different η : contours from $U = 0.1$ to $U = 0.99$. a) $(Re, \eta) = (600, 2)$, b) $(Re, \eta) = (600, 3)$. From Loiseau et al. (2014)

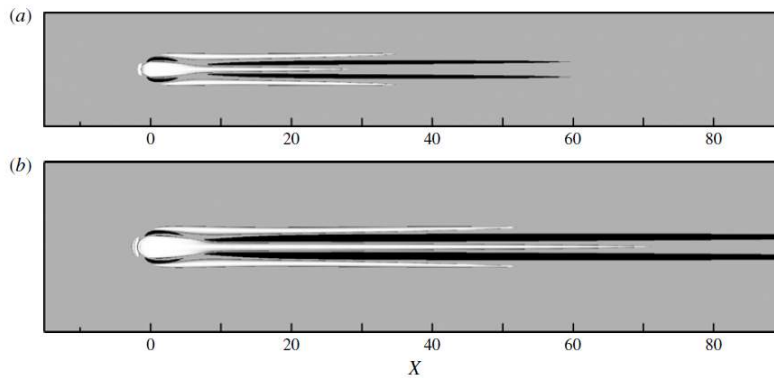


Figure 2.29: Top view of streaky structures aft the roughness element under the effects of different Re : white and black are respectively low- and high-speed streaks. a) $(Re, \eta) = (600, 2)$, b) $(Re, \eta) = (600, 3)$. From Loiseau et al. (2014)

streamwise evolution of the back-flow region (figure 2.26), as well as a long low-speed central region (figure 2.27) which forbids the merging of the high-speed streaks on its side (contrarily to the low Re condition).

A larger aspect ratio is expected to cause the accumulation of more vorticity in the wrapping mechanism occurring in the upstream side of the element: this should translate in stronger and more streamwise sustained vortical structures. Figure 2.29 seems to confirm this hypothesis. Nevertheless, the merging of the high-speed streaks is not observed any of the two cases, even if under the effect of a smaller diameter. Figure 2.28 shows a growth in the intensity and in the length of the backflow regions as the aspect ratio is increased, and so is the blockage effect caused by the element.

An extremely interesting aspect evaluated in this research is the effect of the aspect ratio on the development of different instability modes: varicose or sinuous. Figure 2.30 displays how a smaller aspect ratio (specifically $\eta \leq 1$) generates a perturbation scenario dominated by sinuous modes, whilst a $\eta \geq 2$ presents varicose instabilities. One must notice that this analysis has been focusing exclusively on the streamwise component of the velocity.

Sinuous modes are characterized by alternating positive and negatives speed structures, concentrated in the central zone of wake and with anti-symmetric behaviour with respect to the streamwise symmetry axis. Furthermore, the authors speculate around the idea that these

modes might receive energy from the strong velocity gradients acting spanwise and wall-normal in the shear layer region. The signal observed by a probe positioned in the near wake of the element is displayed in figure 2.31, with the right figure displaying the Fourier spectrum. One could immediately notice the strongly tonal behaviour, related to the shedding of the hairpin vortices shown in figure 2.32, by means of the λ_2 criterion. These eddies are the mechanism that leads to the tonal oscillation not only of the low-speed central region, but also of the other vortical structures. Varicose instabilities show the opposite symmetry behaviour with respect to the centerline of the low-speed streak, still they are considered to be linked to the transport of the shear layer gradients. Again, the Fourier spectrum and the hairpin visualization is shown in figure 2.34, with the signal from the probe in figure 2.33. However, it must be noticed that this time the velocity measured by the probe is the spanwise component.

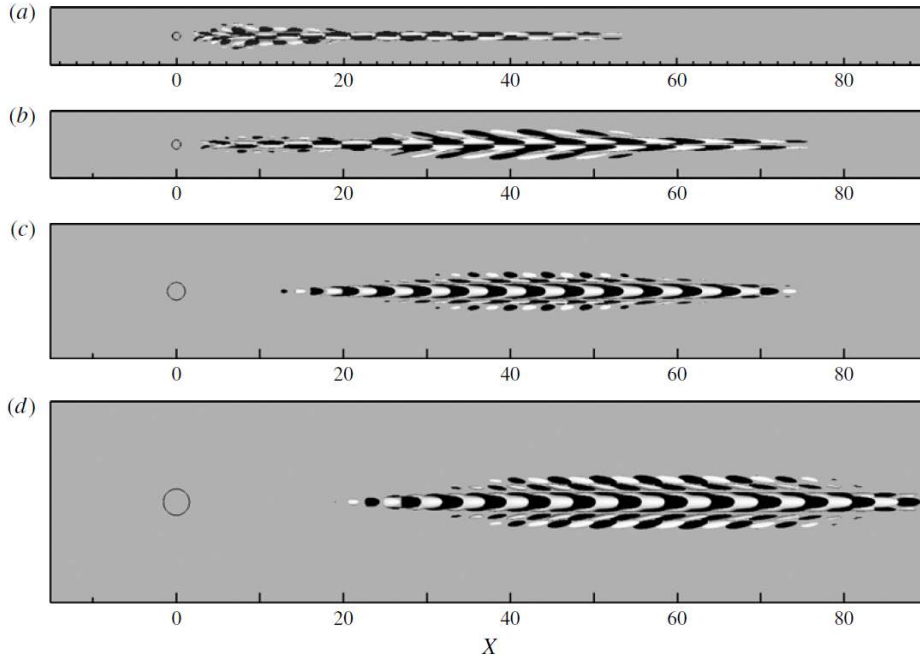


Figure 2.30: Main instability modes of the spanwise component of the velocity under the effect of different aspect ratio: a) $\eta = 0.85$, b) $\eta = 1$, c) $\eta = 2$, d) $\eta = 3$. From [Loiseau et al. \(2014\)](#)

Finally, the authors also report the transition diagram from [Doenhoff and Braslow \(1961\)](#) for the isolated roughness element (figure 2.35). The variation of the transition region (grey area) is modified by the variation of aspect ratio. The space below this area representing the sub-critical elements, causing no transition downstream of the roughness. All those elements whose representation lies above the grey zone present turbulence right aft the roughness, in an immediate transition scenario. In our research, these are the elements that will be called supercritical, not to be confused with the quasi-critical ones. In fact, this name will be given to those elements falling inside the grey zone. Their transitional characteristics may include the occurrence of transition at few diameters of distance from the element. However, it is possible they might undergo only strong perturbations, depending on other geometrical characteristics of the roughness.

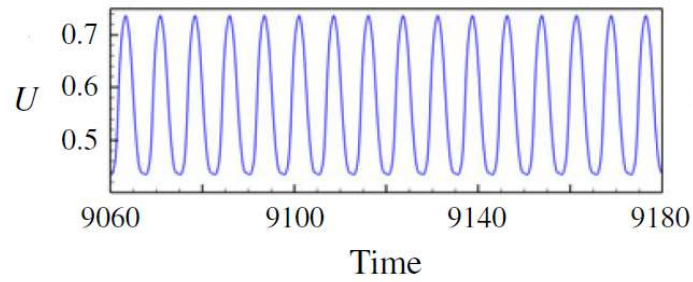


Figure 2.31: Flow velocity signal for a varicose instability dominated type of flow. From [Loiseau et al. \(2014\)](#)

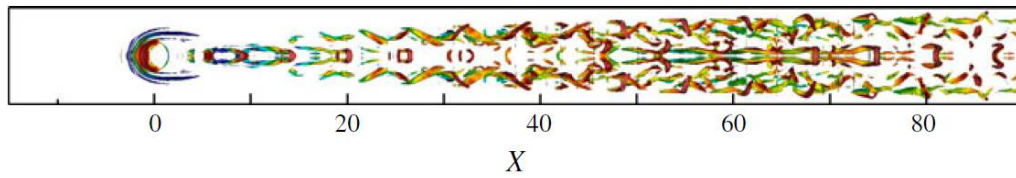


Figure 2.32: Lambda criterion visualization of hairpin vortex generation, in a varicose instability dominated type of flow. From [Loiseau et al. \(2014\)](#)

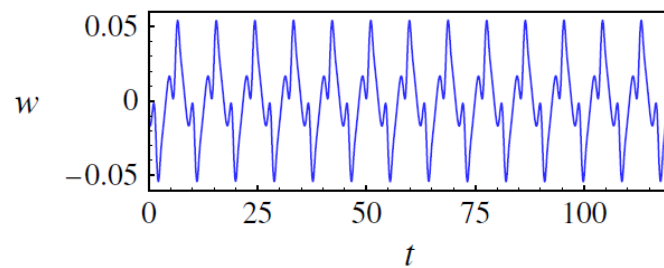


Figure 2.33: Flow velocity signal for a sinuous instability dominated type of flow. From [Loiseau et al. \(2014\)](#)

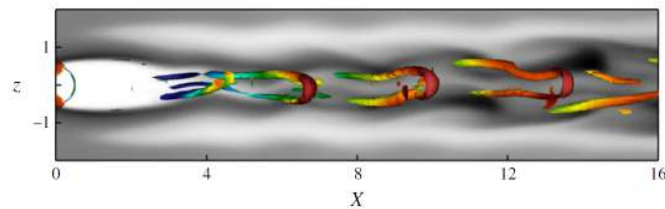


Figure 2.34: Lambda criterion visualization of hairpin vortex generation, in a sinuous instability dominated type of flow. From [Loiseau et al. \(2014\)](#)

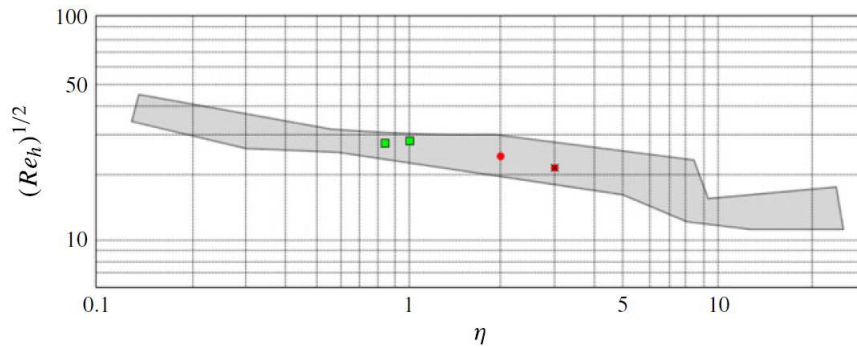


Figure 2.35: Reproduction of the transition diagram by Doenhoff and Braslow (1961), taken from Loiseau et al. (2014). Red and green markers respectively indicate varicose and sinuous instabilities limits.

To conclude the topic of varicose and sinuous perturbations, the work of Cherubini et al. (2013) can offer some interesting thoughts. The DNS study has a minimum k of 0.5, corresponding to a $Re_k = 25.1$ and maxima of $k = 1.5$ and $Re_k = 351.1$, whilst the diameter has been kept constant to 26. The first interesting results to be shown regards the behaviour of the streaky structures generated aft the elements, under the effects of differently sized bumps (figure 2.36). Specifically, a taller and a thinner element are compared ($k = 0.75$ on the left and $k = 1.5$ on the right) and three Reynolds number are shown. One could immediately notice something already confirmed by Loiseau et al. (2014): taller elements lead to a later merging of the two lateral high speed streaks and therefore disappearing of the low speed streak associated to the wake of the element. At the same time, higher Re conditions also delay in space the occurrence of this phenomenon and generates stronger streaky velocities.

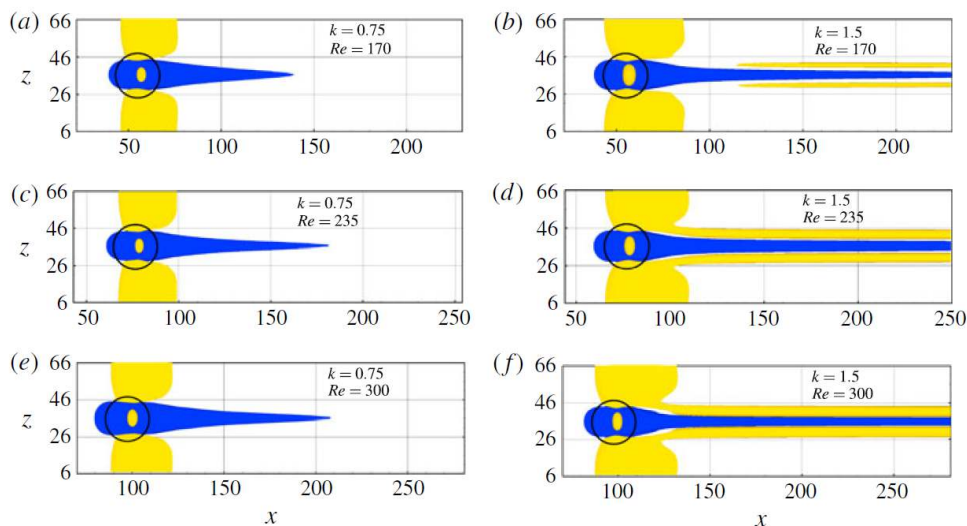


Figure 2.36: Streaks of positive (yellow) and negative (blue) velocity variation with respect to the average of the base flow. Reynolds values and heights reported on the figure. From Cherubini et al. (2013)

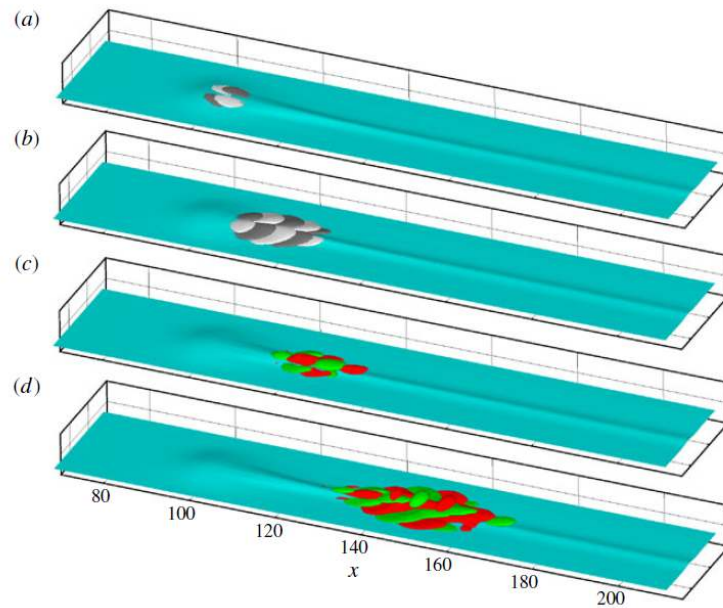


Figure 2.37: Evolution of varicose perturbation in time: a,b) streamwise vorticity perturbations, c,d) streamwise velocity perturbations. From Cherubini et al. (2013)

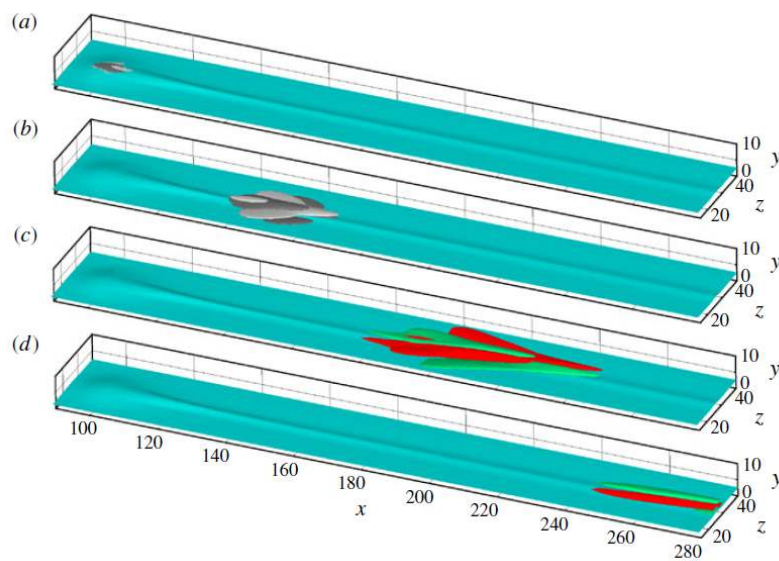


Figure 2.38: Evolution of sinuous perturbation in time: a,b) streamwise vorticity perturbations, c,d) streamwise velocity perturbations. From Cherubini et al. (2013)

As for the study of modes, investigations regarding the evolution of both varicose and sinuous perturbations are carried out. The results are shown in figure 2.37 and 2.38, where the selected roughness element and Reynolds number are the same: $Re_k = 300$ and $k = 1.5$. In the varicose disturbance evolution, the streamwise vorticity develops in the central region aft the element and their size "stretches" in the spanwise direction (black and white regions in the figures). This growth transports the base flow shear and generates streamwise velocity perturbation (green and red), which slowly grow in extension. In the sinuous mode evolution, the phenomenon is extremely similar, with the final "arrow" shape of the disturbances. However, it must be noticed the opposite type of symmetry displayed by the two graphs. The final velocity disturbances confirm the characteristics reported by [Loiseau et al. \(2014\)](#), but more interestingly the initial vorticity perturbations show the exact opposite trend: symmetric to the streamwise centerline for the sinuous and anti-symmetric for the varicose.

Isolated Roughness in a 3D Boundary Layer

One of the first pieces of work in which an investigation around isolated elements on a swept wing is carried out is [Radeztsky et al. \(1999\)](#). This publication contributed to the investigation of the boundary layer transition on the aforementioned ASU 45 degrees swept wing. The surface roughness was varied with three different polishment levels: painted, machine-polished and hand-polished surfaces. After having established the better transition performances (delayed transition location) of the hand-polished, they carried out different tests around the isolated roughness element. Firstly, flow visualization experiments were carried out: a $6\mu m$ height and 3.7 mm diameter roughness element was placed at $x/c = 0.23$. A single streak was clearly identifiable on the mainly laminar boundary layer, with the final edge placed at about $x/c = 0.40$. The streamwise position of this streak appeared to almost coincide with one of the crossflow vortices inside the natural boundary layer.

Flow visualization experiments included also the variation of roughness location effects. The same size was kept and the location was varied from $x/c = 0.005$ to $x/c = 0.045$, identifying the neutral stability point ($x/c = 0.02$) as the position of maximum influence on transition, as it is the point where the roughness triggers the earliest turbulent conditions. Just by moving the position 1.5% of chord upstream and 2.5% of chord downstream of the neutral point, the local transition position remains the same as the undisturbed case. This is visible in figure 2.39, whilst figure 2.40 shows the effects of different diameters and height for the same chord Reynolds number and roughness position. Thirdly, figure 2.41 shows the combined effects of Re_c and diameter. It can be concluded that the increase of height, diameter and Reynolds number all move transition upstream, but that there are disturbance conditions for which no relevant difference with the no-roughness scenario is identifiable.

It is worth mentioning a sentence from [Choudhari \(1994\)](#), who gives a physical explanation to the saturation in transition location when decreasing the element size under a certain level. In other words, below a given height of the roughness element, the decrease in dimension is no longer a beneficial action in terms of transition delay. The reasons are found in the domination of other external sources involving receptivity over the discrete roughness. This can be pointed out as an additional proof of the complexity of this topic, also due to the many factors involved and to their mutual interaction.

In the second part of Radeztsky et al. (1999), hot wire anemometry data have been obtained in order to evaluate the mean velocity profile evolution and the spectral content of the signal. Both of these are used for the identification of the principal crossflow mode and the study of its growth towards transition. Figure 2.42 show the evolution of the mean boundary layer velocity (\bar{u}/U_e), where the speed modulation generated by the roughness element is clear and evolves downstream until the local transition occurs. Only the case of the first oil flow visualization was considered ($6\mu\text{m}$ height, 3.7 mm diameter at $x/c = 0.23$). Finally, the author report the spectral analysis of the signal, with a power spectral density peak corresponding to the dominant crossflow mode ($\lambda = 9.5\text{ mm}$ and $\lambda_{CF} = 8\text{ mm}$, with the latter projected in the direction of the crossflow wave).

Some very interesting results could be found in the work of Brynjell-Rahkola et al. (2015).

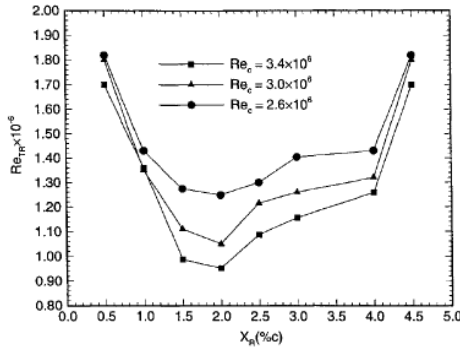


Figure 2.39: Transition Re vs. roughness position ($D=3.7\text{mm}$ and $k=6\mu\text{m}$). From Radeztsky et al. (1999)

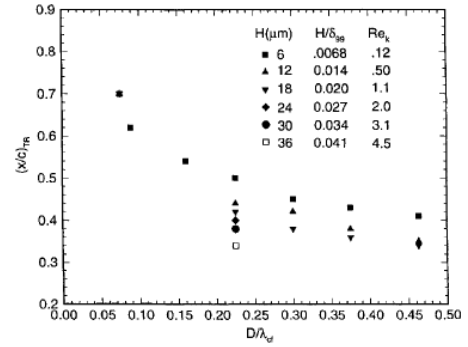


Figure 2.40: Transition location vs. roughness height and diameter ($x/c=0.023$ and $Re_c = 2.6 \times 10^6$). From Radeztsky et al. (1999)

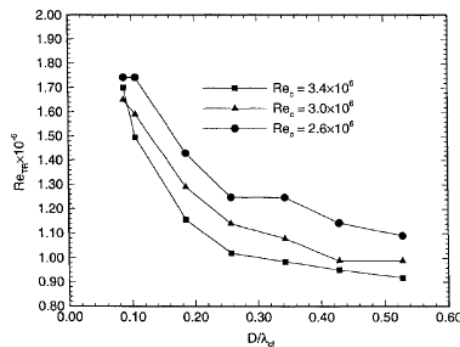


Figure 2.41: Transition Re vs. roughness diameter and Reynolds number ($x/c=0.023$). From Radeztsky et al. (1999)

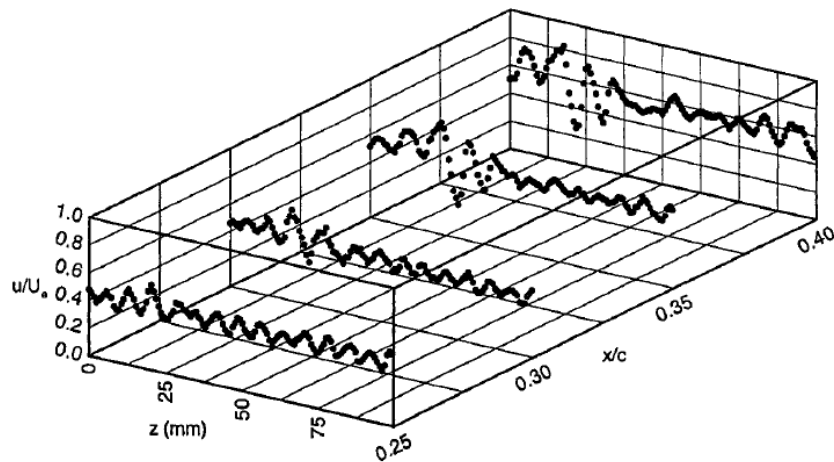


Figure 2.42: Spanwise hot-wire measurement of the streamwise velocity component ($y = y|\bar{u}/U_e = 0.5$, $k = 6\mu\text{m}$, $D = 3.7\text{mm}$, $x/c = 0.23$, $Re_c = 2.6 \times 10^6$). From Radeztsky et al. (1999)

The authors performed global stability analysis of the flow past an isolated roughness in a 3D boundary layer, by means of DNS. Two different non-dimensionalized heights were tested: $k = 0.8$ and $k = 1.1$, whose streamwise velocity and vorticity evolution is shown in figures 2.43 and 2.44. The first case did not lead to transition, while the downstream flow of the latter presents a transition mechanism to be associated to the typical crossflow vortex breakdown. In fact, the 50 most dominant eigenmodes are found to be unstable and related to the z -direction shear layer, as also in agreement with the results related to the breakdown of secondary instabilities in a crossflow dominated boundary layer (Serpieri and Kotsonis, 2016). In the near wake of the element, the eigenfunctions seem not be localized along the legs of the horseshoe vortex wrapping around it. Contrarily, they are found in the upper side shear layer of the wake, as shown in figure 2.46.



Figure 2.43: Evolution of the wake of a subcritical roughness element. From Brynjell-Rahkola et al. (2015)

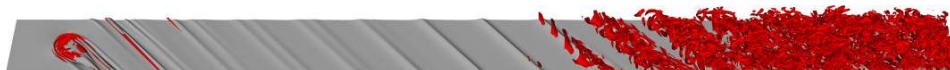


Figure 2.44: Evolution of the wake of a supercritical roughness element. From Brynjell-Rahkola et al. (2015)

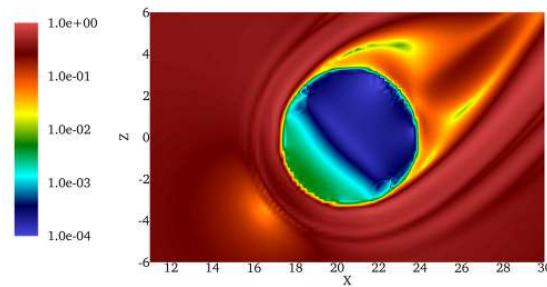


Figure 2.45: Upper view of the roughness element near wake: velocity magnitude ($y=0.4$). From Brynjell-Rahkola et al. (2015)

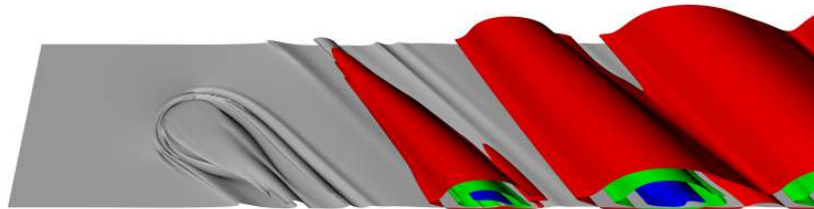


Figure 2.46: Eigenfunction of the most unstable mode in the supercritical roughness element. From Brynjell-Rahkola et al. (2015)

A final and interesting note about the flow topology shown in this paper regards the near wake. An upper view (figure 2.45) shows a strongly asymmetric shape, with a speed deficit wrapping around the element and "entering" into the wake region only from one of the two sides. This feature is to be kept into consideration for a comparison with the results obtained in this project.

In order to deeply understand the mechanisms leading to the growth of instabilities, a manipulated version of the linearized Navier–Stokes equations is exploited. This shows the relations between the growth rate of a given eigenmode and different terms of the energy. Among these, the relevant mechanisms are connected to the production term and the dissipation term. After the study of these energy components in the frequency domain, the authors speculate around the differences between low- k and the high- k cases, in this type of flows. On a general basis, they concluded that an high roughness element causes an unbalance in the terms of the energy equations, through the generation of strong perturbations. This unbalanced scenario forbids the decay of the disturbances, as it would instead be for a low height condition.

The work by Chernoray et al. (2005) is of high relevance with regards to isolated roughness disturbances in a crossflow dominated scenario. Furthermore, the experimental setup could be seen as quite similar to the one adopted in this thesis project. Hot wire anemometry was used to investigate the boundary layer under the condition of about 8.2 m/s freestream speed. An isolated asymmetric roughness element was used as vortex generator as shown in figure 2.47. It was placed at $0.3c$ (2.71 BL shape factor), the angle of attack was slightly negative (2°) and the flow on the suction side was tripped in order to avoid large scale separation

and instabilities affecting the flow on the measurement side. Furthermore, both a natural transition test and a forced scenario were reproduced. The latter consists in a blowing-suction mechanism forcing artificially the natural secondary disturbance frequency of the primary crossflow vortices, identified by the spectra analysis. This phase locking frequency was always kept at 210 Hz. The higher harmonics of this figure appears to be related to the non-linear interaction of the traveling and the stationary modes.

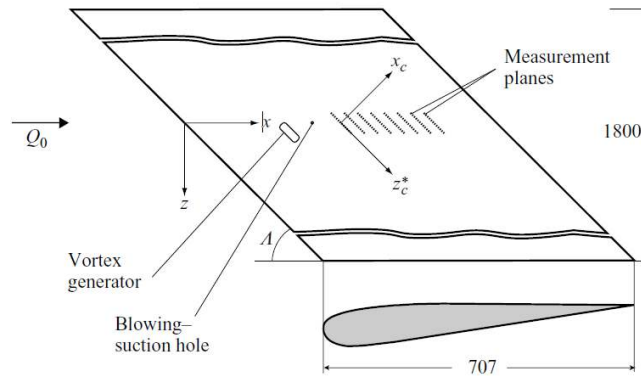


Figure 2.47: Experimenta scheme of the model. From [Chernoray et al. \(2005\)](#)

Aft the 35 mm roughness element one can notice one high speed streak in the central region, surrounded by two low speed streaks on its side. Figure 2.48 exactly displays these velocity streaks. The shape of the isosurfaces is very interesting for the sake of our research. The upper streak is linked to the vortex that is rotating against the natural crossflow vortices, whereas the lower one follows their rotation. These two vortical structures develops on the side of the element and evolves downstream, but with a totally different behaviour. It must be said that they might interact to a much larger extent for less elongated roughness elements (like the 8 mm circular one tested in the same study), which would scale down their sizes and the associated wavelength.

The phase locked measurement results are instead shown in figure 2.49, superimposed to the ones of the figure 2.48. The vortex packets on the upper side rotates against the natural crossflow vortices and leads to an evident dimensional growth of the low speed streak. However, the high speed region remains almost unchanged, as a probable result of the upward motion domination of that side of the roughness wake. Contrarily, the naturally-rotating vortex has an expanding high speed streak, and also shows a totally different shape of the low speed streak, with what appears to be a set of streaky structures.

The authors declare that the vortex supported by the crossflow develops secondary instabilities early, and it has a faster breakdown process. The phenomenon occurring in this case is the generation of z-mode secondary instabilities, whereas a y-mode is predominant in the unnaturally-rotating vortex. This latter is supposed to bring more stability to the vortical structure. Before concluding, it must be remembered that this experimental research does not seem to present any bypass transition mechanism, but only the generation of secondary disturbances eventually leading to transition.

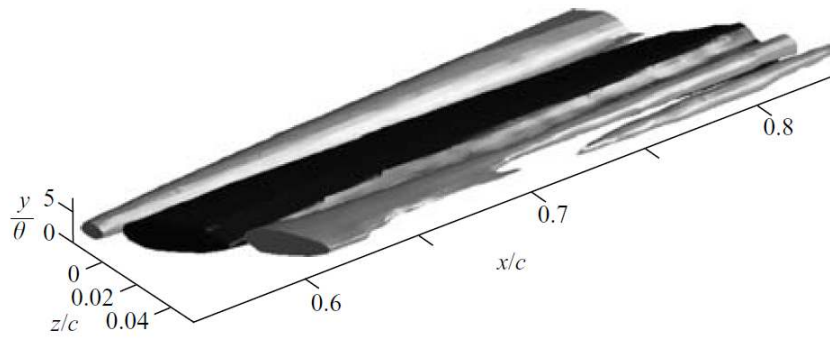


Figure 2.48: Stationary disturbances evolution: isosurfaces. From Chernoray et al. (2005)

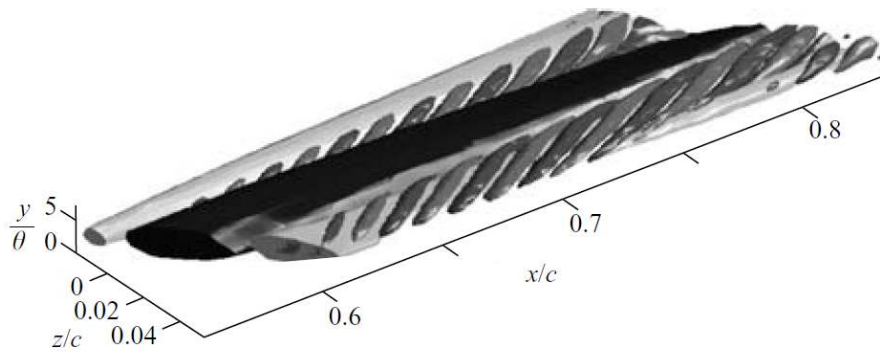


Figure 2.49: Forced perturbation modes. From Chernoray et al. (2005)

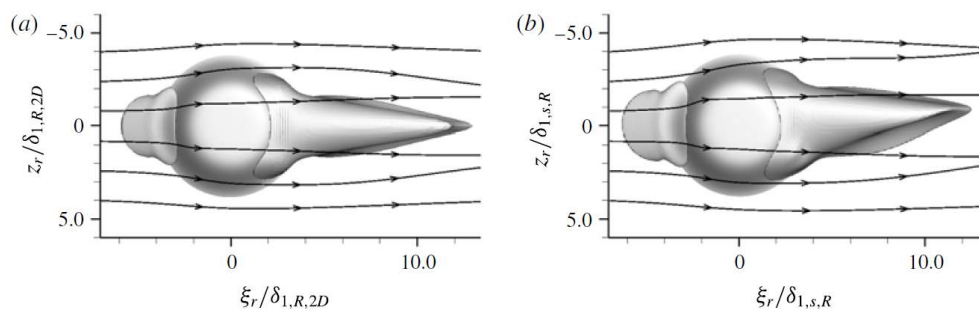


Figure 2.50: Backflow region in the near wake of the element, under the effects of a 2D and a 3D flow. The isosurface represents a $u = -1 \times 10^{-4}$. From Kurz and Kloker (2016)

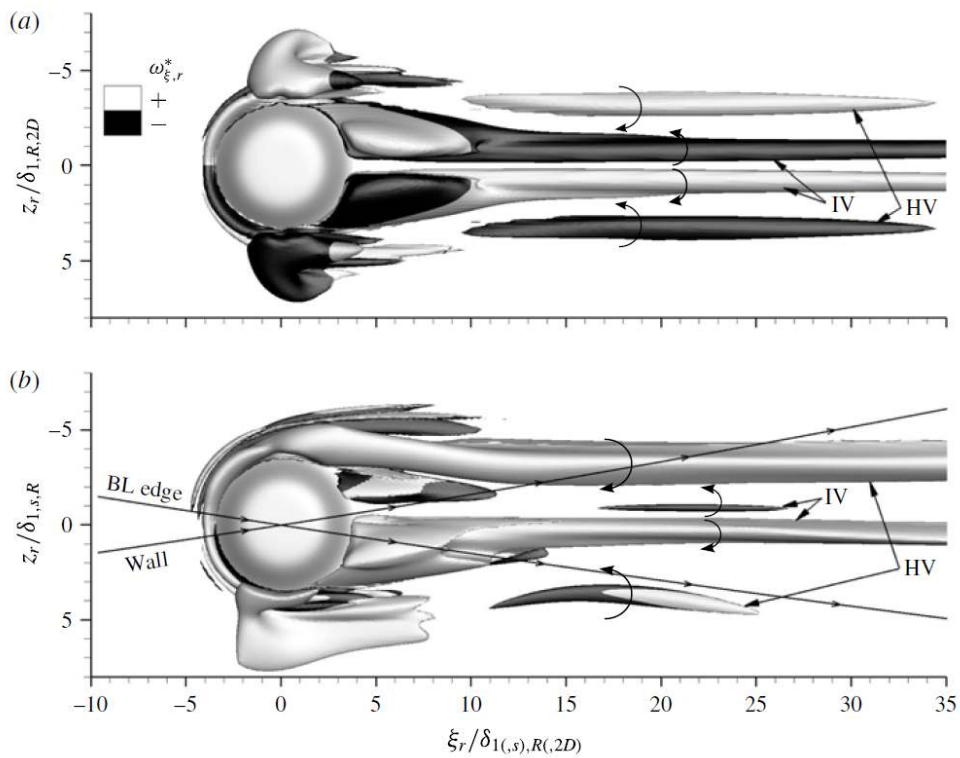


Figure 2.51: Isosurfaces of streamwise vorticity in the near wake of the element, under the effects of a 2D and a 3D flow. From Kurz and Kloker (2016)

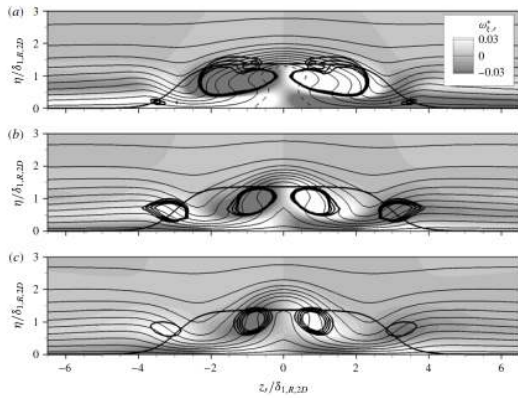


Figure 2.52: Two-dimensional flow: lambda criterion isocontours (lines) and shading of streamwise vorticity. From Kurz and Kloker (2016)

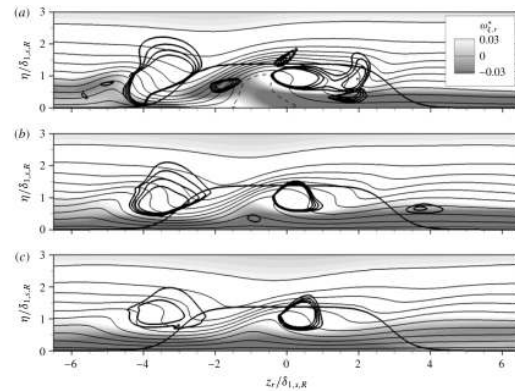


Figure 2.53: Three-dimensional flow: lambda criterion isocontours (lines) and shading of streamwise vorticity. From Kurz and Kloker (2016)

To conclude, the work of [Kurz and Kloker \(2016\)](#) is one of the most strictly related to the project of this thesis. A DNS investigation around transition induced by smoothed cylindrical roughness elements in a crossflow dominated boundary layer is presented. Different dimensions were tested by changing the non-dimensional height k and the roughness Reynolds number. In this research, the sweep angle was kept at 35° , the angle of attack at -6.1° . A suction type of flow disturbance was modeled upstream of the roughness element, capable of triggering the most amplified crossflow mode. Furthermore, the authors both investigated the transitory effects of both a crossflow dominated condition and a two-dimensional flow scenario, in order to compare them. This comparison was carried out by inserting in the two different boundary layers, the same roughness element, i.e. with the same Re_k and comparable flow conditions.

Figure 2.51 is the first result regarding the near wake comparison between the 2D and the 3D cases. The $k = 1.365$ and $Re_k = 487$ case is illustrated here, with a λ criterion visualization applied on the streamwise vorticity. Furthermore, figure 2.52 and 2.53 show the contour of streamwise velocity, isocontours of λ and the streamwise vorticity distribution. One can immediately notice that both scenarios display two main pairs of vortical structures: inner and horseshoe vortices, with the latter created as legs of the vorticity accumulation formed upstream the element. However, the crossflow dominated condition completely modifies the symmetry of the flow. This not is not only true in the different directions and inclinations of this structures. Other than this, the vortices (both inner and horseshoe) which rotates in the same direction as the crossflow natural ones are sustained by the flow, keeping on with the downstream development. On the other hand, the ones rotating in the other direction are

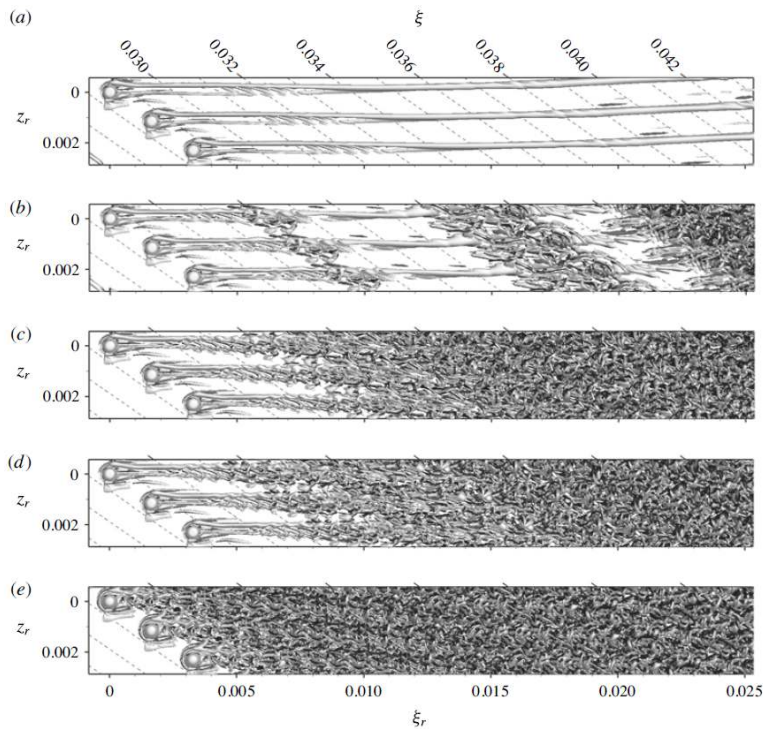


Figure 2.54: Snapshots of the wake evolution. From [Kurz and Kloker \(2016\)](#)

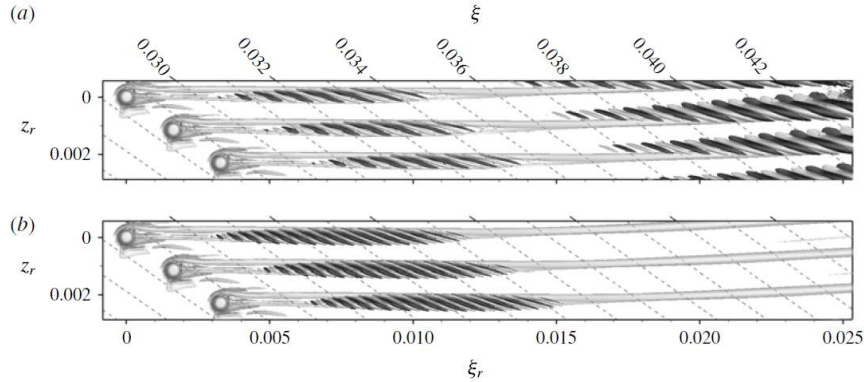


Figure 2.55: Global perturbation modes for $k = 1.5$ and $Re_k = 564$. From Kurz and Kloker (2016)

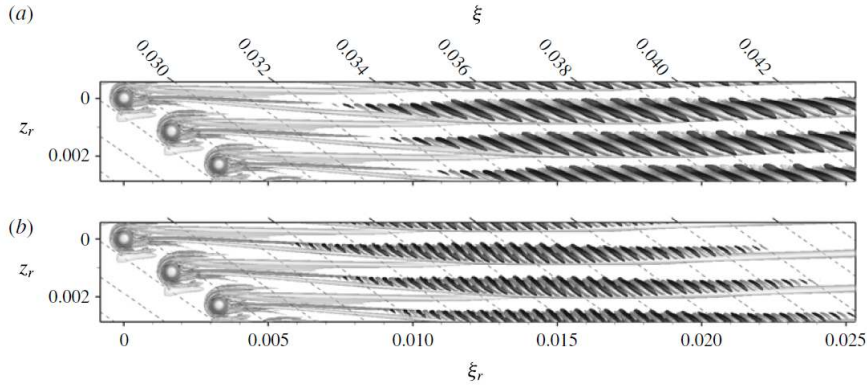


Figure 2.56: Global perturbation modes for $k = 2$ and $Re_k = 881$. From Kurz and Kloker (2016)

weakened early. Finally, figure 2.50 shows the recirculation zone downstream of the element, with the isosurfaces of a negative value of streamwise velocity for the two different cases. This is the final example of how these two cases display differences in the symmetry.

Another important part of the work from Kurz and Kloker is the evaluation of different transition scenarios, depending on the level of disturbances introduced by the roughness. For instance, figure 2.54-a presents the case of the not critical (called near critical by the authors) $Re_k = 487$ and $k = 1.375$, where the low amplitude noise introduced by the upstream artificial disturbance is not triggering transition. A localized growth related to the periodic impulses is identified, but immediately dampened out. Also the high amplitude noise of figure 2.54-b cannot yet develop a self sustained turbulence. When the Re_k is below the critical value, but high enough to sustain the naturally-rotating horseshoe vortex, the phenomenon displayed in figures 2.54-c and 2.54-d occur ($Re_k = 564$ and $k = 1.5$). These show transition happening downstream of the roughness element by means of a convective instability, without the inclusion of the noise generator. The $Re_k = 881$ and $k = 2$ condition consists of an immediate onset of transition behind the roughness element, due to a global instability behaviour of the flow (figure 2.54-e).

Finally, the last two elements are investigated by means of a global stability analysis. Figures 2.55 and 2.56 show the global modes of the two critical cases ($Re_k = 564$ and $Re_k = 881$, respectively), namely the real part of the streamwise velocity eigenfunction. The upper plot of figure 2.55 shows the mode associated to the lowest frequency and reports two region of high amplitude: along the naturally rotating inner vortex in the near wake and along the developed horseshoe vortex downstream. The second subfigure refers to the most amplified mode, with the the near wake phenomena and the absence of the downstream one. This may indicate that the near wake fluctuations and instabilities dominate this scenario. In fact, the part of the mode associated to secondary instabilities does not reach the threshold level of the isosurfaces. Also the images related to $Re_k = 881$ (figure 2.56) are showing the the lowest frequency mode and one of the most amplified ones. However, this time no difference between near wake and far wake behaviour is visible, and the region of global mode disturbances expands throughout the whole wake of the element.

2.4 Research questions, objectives and outline

After an overview of the past researches, it is important to define how this project relates to the available knowledge, putting it into context with the help of the research questions and goals. As previously mentioned in section 1, the main goal of this project is the analysis of the physical mechanisms behind the isolated roughness induced transition on a strongly three-dimensional boundary layer. More specifically, a 45° swept wing is tested. The effects of the two main dimensions are investigated, i.e. diameter and height of the roughness. The description of the turbulent status under the variation of these two parameters is tested, together with the effects of freestream speed. Several elements are selected for a broad study, and different techniques allows a thorough and complete investigation. To enter into the details, the research questions of this whole project are summarized in the following list:

- *What are the flow features generated aft of a isolated roughness element under the effects of a three dimensional boundary layer? And how do they interact with the crossflow component of the velocity?*
- *How does the variation in freestream speed, roughness height and roughness diameter influence these structures and the transition mechanism in this type of boundary layer?*

The final accomplishments obtained from this projects are a direct consequence of carrying out the research objectives. These are the steps to be taken towards the end of this research, and could be summarized in the following tasks:

- A selection of the relevant cases and geometries, based on both data from previous researches and a preliminary parametric study. These form the final experimental matrix, inclusive of a decision about how to exploit the different techniques among the selected cases.

- Preparation of the experimental campaign. This includes an accurate choice of the experiment parameters, instrumentation and setup. This point is strictly related to the previous one, as a proper trade-off between time management, selected cases and different techniques must be found.
- Experimental campaigns, carried out in different periods of time and based on different techniques.
- Analysis of the results. This a conspicuous part of the whole project, as it refers to the extraction of data and information from the experiments, and to the analysis and synthesis too. In other words, the data are extracted and consequently compared to each other and to literature, to understand and describe the physical mechanisms they rely on.
- Writing and completion of the research.

This thesis starts with chapters 1 and 2: the introduction to the project and the review of relevant past works, respectively. The latter is divided into sections, to better support the reader in the understanding of the different aspects involved in the topic. In the remainder of the report, the first chapter treats the methodology (3), i.e. all the experimental setups and techniques, other than the selected cases and their experimental and physical parameters. The largest is chapter 4, where all the results are displayed, together with their discussion. The chapter starts with a section dedicated to a parametric study, carried out with the use of infrared thermography and useful for a broad overview. The second part is extremely vast and dense in content. It treats the physical mechanisms, investigated in detail and depth, with the use of different experimental techniques. It starts with the analysis of the so-called *central element* ($U_\infty = 8m/s$, $D = 4mm$ and $k = 1.5mm$), which subsequently undergoes an increase and a decrease of all the three main parameters. These newly obtained cases are also investigated and included in the section. The final section of the chapter is dedicated to the effects of the aspect ratio outliers, which present unique characteristics, whose reasons and effects are described and studied. Finally, the conclusion and recommendations are to be found in chapter 5.

Chapter 3

Methodology

3.1 Experimental facilities

3.1.1 Wind tunnel and airfoil model

The experiments were carried out at the Low Speed Laboratory of Delft University of Technology, one of the facilities in use by the Aerodynamics Department of the Faculty of Aerospace Engineering. More specifically, the Low Turbulence Tunnel (LTT) was employed. This is a low turbulence subsonic wind tunnel, with a turbulence level varying from 0.002 to 0.1 depending on the setup of the seven anti-turbulence screens. It is a closed loop facility, with a 1.25 m tall, 1.8 m wide and 1.26 m long test section, and provided with a 17:1 contraction ratio.

The fiberglass swept wing model has an angle of sweep $\Lambda = 45^\circ$, a 1.27 m chord in the direction of the freestream velocity (c_X) and a 1.25 spanwise length (b), consequently it presents a 0.9 m chord in the direction normal to the leading edge (c_x). It is equipped with two rows of pressure taps, located at a quarter-span distance from the upper and lower wall of the wind tunnel. The airfoil is named 66018M3J, and consist of a modified version of the NACA 66018, whose details can be inferred from figures 3.1 and 3.2, and found in [Serpieri and Kotsonis \(2016\)](#). This airfol was specifically designed to avoid the amplification of any instability phenomena except the crossflow, i.e. to stop the growth of the Tollmien-Schlichting (TS) waves and the Görtler vortices. As explained in the reference, the latter are tackled by the absence of concavity. At the same time, the TS instability along the pressure side of the profile is dumped by the accelerating flow over a large part of the surface. This is linked to the favorable position of the pressure minimum for low angles of attack (α). More specifically, these features are valid for the pressure side of the model at the angle of attack adopted during this experimental study: $\alpha = 3^\circ$. Furthermore, this condition allowed to avoid the application of liners for the spanwise uniformity of the flow, required for the adoption of a 2.5 D hypothesis, and ensured a crossflow dominated transitional behavior of the boundary

layer.

The further attachment of a tripping band on the suction side of the model forced the flow to a turbulent regime. This prevented the occurrence of separation, whose possible unsteadiness might negatively affect the measurement on the pressure side. As for the location of the roughness elements, the main reason that lies behind the decision of 25% chord is related to the airfoil shape. This region corresponds to the end of the curved part of the wing model and the beginning of an almost flat surface, with the aforementioned optimal pressure distribution. Moreover, the absence of curvature represents an optimal condition for the laser illumination, needed for the PIV system. This roughness position also allows the author to refer to most of the previous research performed on flat plate, as the boundary layer shape factor at the element location is $H = 2.45$, close to the $H = 2.59$ of a flat plate.

In terms of operating speed, the selection of $U = 8\text{m/s}$, and therefore $Re_c \approx 6.5 \times 10^5$, for this research relied on a preliminary test campaign carried out at the LTT. It was found that the 8 m/s condition ensured all the aforementioned required flow features. Moreover, experiments confirmed the possibility to have a neat, clear and immediate flow visualization by using infrared thermographic techniques. Finally, three differently sized roughness elements ($D = 4\text{mm}$ and $k = 0.75\text{mm}$, $k = 1.5\text{mm}$, $k = 2.1\text{mm}$) appeared to trigger three diverse transition conditions. Therefore, it represented an optimal starting point towards the investigation of geometric effects on transition.

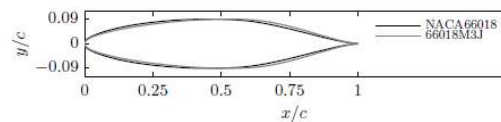


Figure 3.1: Comparison between NACA 66018 and 66018M3J airfoil. Profiles taken as perpendicular to the leading edge. From [Serpieri and Kotsonis \(2016\)](#)

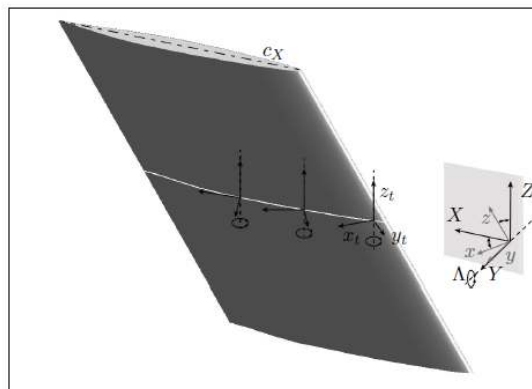


Figure 3.2: Airfoil model scheme with the representation of used reference systems. From [Serpieri and Kotsonis \(2016\)](#)

3.1.2 Coordinate system

The reference systems in use must be specified for sake of clarity, due to the complexity of the model. Figure 3.2 displays all of the three coordinate systems in relation to the swept wing model. The first to be assessed is the unswept XYZ , related to the set of velocities UVW , which adopt the subscript ∞ if related to freestream quantities. The plane XY runs parallel to the horizontal walls of the wind tunnel test section, with Y perpendicular to the leading edge of the wing. Z is perpendicular that plane. The swept reference system is such that $y = Y$ and the other two axes are rotate of $\Lambda = 45^\circ$ around it. Therefore, z runs parallel to the leading edge and x perpendicular to it. Finally, the local tangential system is composed by x_t, y_t and $z_t = Z$. The first two are respectively tangent and perpendicular to the projection of c_X on the model surface.

It is important to notify the peculiarities in the illustration of the data. In the HWA results, the plane along which the three dimensional boundary layer velocity is measured is zy_t . However, lowest value of the y_t axis is the coordinate at which the BL speed level fell below $\frac{1}{10}U_\infty$ in the undisturbed BL. At the same time the origin of the z axis presented in the plots is set along the X line passing through the roughness element, therefore at $Z = 0$ position. In fact, the XYZ coordinate system has its origin at the center of the roughness element.

3.2 Experimental techniques

3.2.1 Infrared thermography

Within this research, infrared therography has been largely exploited as flow visualization method to identify the local transitional behaviour of the flow disturbances generated by the roughness elements. It has been corroborated by previous researches as a reliable technique for the study of transition fronts (Grawunder et al., 2016) and as a quantitative measurement technique for the study of isolated roughness elements, specifically in hypersonic flow conditions (Avallone et al., 2016).

This technique relies on the thermodynamic principle of the heat transfer rate between the model surface and the boundary layer flow. This phenomenon is described by the Stanton number St :

$$St = \frac{q}{\rho u c_p \Delta T} \quad (3.1)$$

In equation 3.1, the term q represents the convected amount of heat and the denominator term is the total enthalpy exchange. Under the condition of a zero streamwise pressure gradient along the boundary layer, the Reynolds analogy 3.2 and the $Pr \approx 1$ conditions are fulfilled

(Grawunder et al., 2016).

$$\frac{St}{c_f} = \frac{1}{2} Pr^{-2/3} \quad (3.2)$$

Therefore, the proportionality between the skin friction coefficient c_f and the heat transfer q , lead to the possibility to derive the boundary layer flow regime from the surface temperature. The latter is linked to the heat transfer as suggested by equation 3.4, while the velocity gradient at the wall is proportional to the skin friction 3.3.

$$\tau = \mu \frac{\partial u}{\partial y}_{y=0} \quad (3.3)$$

$$q = -k \frac{\partial T}{\partial y}_{y=0} \quad (3.4)$$

Hence, an increase in velocity gradient at the wall, due to transition from laminar to turbulent, can be associated to a different behaviour in the heat exchange between the flow (i.e. the boundary layer) and the surface.

Specifically, this research made use of a steady and active infrared thermography technique. This is accomplished by uniformly and constantly heating the surface model by means of halogen lamps; whilst a sufficient amount of time is waited until the surface and the flow reach a thermal equilibrium and a steady state heat exchange occurs.

Carlomagno and de Luca (1998) reported the principles behind the measurement of boundary layer regimes by means of thermographic systems. Thermometers, such as thermocameras, compute the temperature of a given object by measuring its radiated electromagnetic energy. Planck's law characterizes this phenomenon, as the intensity of radiation for a given wavelength λ (monochromatic) and a fixed surface temperature T is:

$$E_\lambda = \frac{\epsilon_\lambda C_1}{\lambda^5 (e^{C_2/\lambda T} - 1)} \quad (3.5)$$

Equation 3.5 integrated throughout the whole spectrum corresponds to the Stefan-Boltzmann law:

$$E = \epsilon \delta T^4 \quad (3.6)$$

Although thermocameras are often associated to equation 3.6, they are not total-radiation radiometers; they actually cover only a small portion of the spectrum, the one related to a small band in the IR radiation range (Carlomagno and de Luca, 1998).

Experimental setup

The experiments performed during the preliminary experimental campaign allowed to understand the limits and potentiality of this technique for the flow visualization of the investigated phenomenon. More importantly, they have been used to rapidly identify the boundary layer regimes aft the roughness elements under the influence of different speeds, as already described. For the main experimental campaign a similar intention motivated the use of this technique; a large scale thermography campaign was carried out, in order to assess the effects of different roughness geometry on a first and visual stage. A schematic representation of this setup is displayed in figure 3.3, whereas details about this configuration are available from figures 3.4 and 3.5.

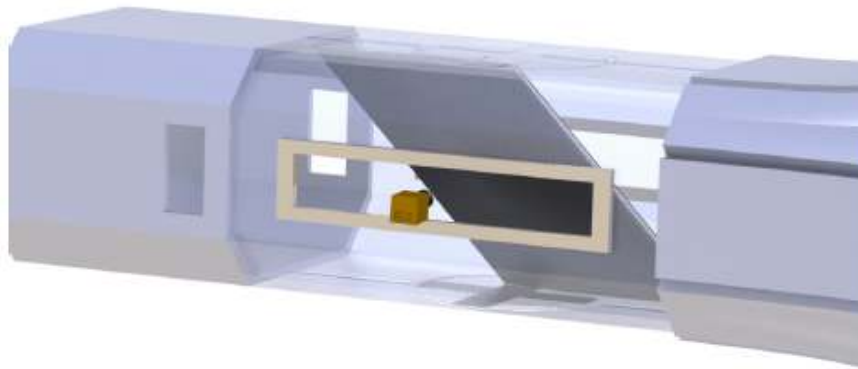


Figure 3.3: Schematic representation of the IR thermography experimental setup. From Serpieri et al. (2017)

Due to the immediate measurement response output, thermography was run in parallel to particle image velocimetry, both planar and tomographic. This aimed to monitor the actual flow phenomena in the region of PIV measurement. In other words, had an unexpected cause of perturbation accidentally entered the field of view of the PIV camera (such as residual accumulation of glue or scratches along the model), the thermocamera would have prevented the author to obtain jeopardize, therefore irrelevant data.

The thermocamera used in this research is an Optris PI 640, provided with a 640×480 pixel optical sensor, a $7.5 - 13 \mu\text{m}$ spectral range and an accuracy of $\pm 2^\circ \text{C}$. The field of view (FOV) of the test was $15^\circ \times 11^\circ$, related to the focal length 41.5 mm, and to the distance of approximately 0.9 m from the model. The six halogen lamps with 0.5 kW power were pointing towards the model as displayed in figure 3.6.

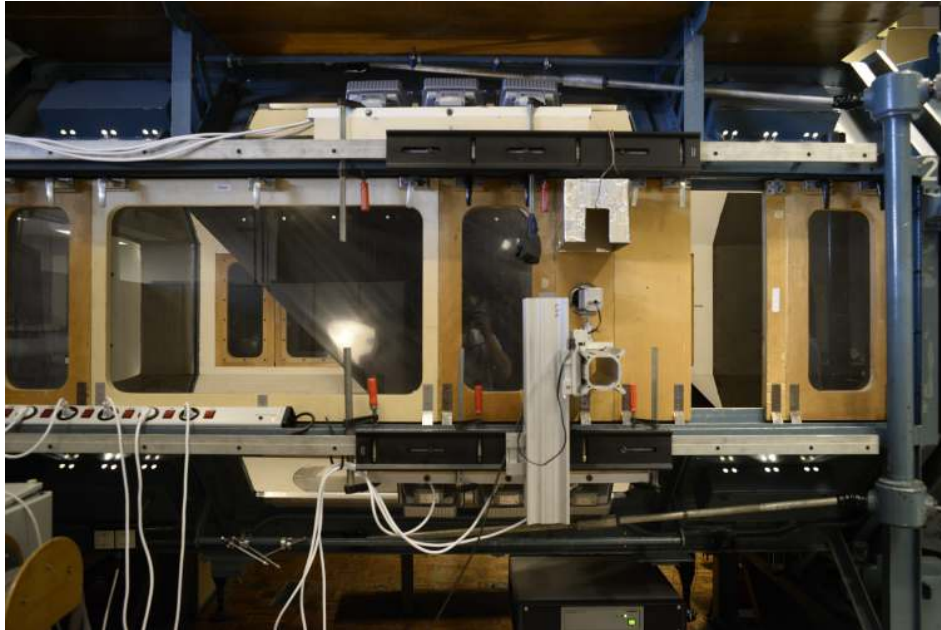


Figure 3.4: Experimental setup for the infrared thermography test



Figure 3.5: Close-up of the infrared camera setup



Figure 3.6: Illumination system for the infrared thermography experiment. View from inside the wind tunnel.

3.2.2 Hot wire anemometry

The hot wire anemometry (HWA) is a punctual velocity measurement technique largely used in the investigation of boundary layer phenomena, including isolated roughness induced transition (Radeztsky et al. (1999); Klebanoff et al. (1992)). It is performed by means of an electrically conductive wire, connected to a circuit and to a traverse system, in order to allow its movements towards the desired investigation positions. This technique is based on the interaction between the wire and the air flow. Without going deep into the operating principles, the Joule dissipation effect W and the heat exchange between the wire and the flow H are the two main terms for the thermal balance of the probe. In the hypothesis of static thermal equilibrium between the wire and the fluid:

$$H = W \tag{3.7}$$

The heat dissipated by Joule effect and the amount of heat exchanged by convection are proportional to the square of the measured voltage V^2 and to the Nusselt number, respectively.

For a forced convection regime, Nu can be rewritten as

$$Nu = \widetilde{C}_1 + \widetilde{C}_2 U^n \quad (3.8)$$

Which leads to:

$$V^2 = C_1 + C_2 U^n \quad (3.9)$$

Where U is the speed of the flow and n , C_1 and C_2 are parameters to be attained by means of an accurate calibration procedure. The last equation allow to assess the punctual flow velocity from the displayed voltage value of the electrical circuit.

Experimental setup

From figure 3.7 one can understand the experimental setup arranged for these tests, which is similar under many aspects to the one performed by [Serpieri and Kotsonis \(2016\)](#). The mechanic traverse system supports a Dantec Dynamics P15 single-wire probe, for the boundary layer investigation, together with a secondary probe placed outside the boundary layer for the contemporary measurement of the freestream conditions. The boundary layer probe had a standard micron-sized thickness and 1 mm length, and was connected to a TSI IFA-300 bridge. Being a single-wire set parallel to the Z axis, the velocity sensed was exclusively the summation of the binormal components, i.e. U and V . This results in the possibility to only display the total velocity $|U_{tot}| = \sqrt{U^2 + V^2}$, with a maximum calibration error between 0.5% and 0.9%. This velocity and its fluctuations will be reported in this thesis as U_{Avg}^{HWA} and U_{Std}^{HWA} , respectively.

As previously mentioned, the zero y_t position was set at 1/10 of the free stream velocity in the undisturbed boundary layer, during the preparatory routine before each measured zy_t plane. These were investigated at different streamwise positions, and the spatial resolution of the measurement varied according to the X station. Specifically, the further from the roughness element, the thicker the vortical structures inside the boundary layer. Moreover, the width of the turbulent wedge increased downstream. Hence, the resolution in both z and y_t , was selected according to the investigated roughness and distance from the origin. The y_t scanning was performed with 40 equally spaced measurements from the zero level to the outside of the boundary layer, with the latter clearly varying its value along the X axis. The z limits were selected in agreement with the previous measure and relying on the planar PIV data acquired (when available), with a variable resolution depending on the investigated case (never more than 1 mm between two z -positions). The sample frequency was set at 50 kHz, with a 20 kHz frequency lowpass filter and a acquisition time of 1 second per zy_t position.

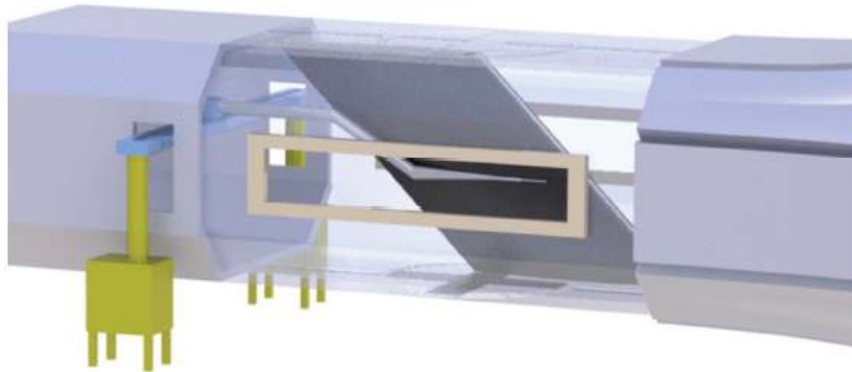


Figure 3.7: Schematic representation of the hot wire anemometry experimental setup. From Serpieri and Kotsonis (2016)

3.2.3 Particle image velocimetry

Particle image velocimetry (or PIV) is the main measurement technique for the goal of this research. It relies on the possibility to trace the position of light-scattering particles flowing in the air. This is performed by one or more CCD cameras, respectively for planar and three-dimensional PIV velocity measurement. The rest of the measurement system is composed by a seeding machine, whose main scope is to blow the proper amount of particles inside the wind tunnel flow, a software to coordinate the tools, and a laser lighting system. The last includes a pulsed laser source and a set of optical lenses (and a mirror) for the correct regulation of the light beam when it gets to the field of view of the camera. All these tools and settings are strictly intertwined among each other, such that an accurate experimental preparation is required for a successful outcome. The actual measure carried out by the cameras consist of two consecutive frames, separated by a microsecond-lasting time lapse. The position of the scattering particles at these two different instants slightly changes. At this point, the investigated flow field is separated in interrogation windows (normally between 24 to 48 pixel sized); and a cross correlation algorithm is applied to the two frames for each window. This generates a matrix of vectors showing the particles displacement distribution inside the FOV, and from the displacement and the time shift the software can compute the velocity field.

It must be mentioned that this section only describes the experimental setup for a planar PIV test. Moreover, this is the only PIV technique included in the core of this thesis. Nevertheless, a tomographic PIV experiments was also performed during the experimental campaign. Appendix A explains the reasons why tomo-PIV results were not included and how they were obtained, with a description of the experiments.

Experimental setup

Figure 3.8 displays a simplified scheme of the experimental setup exploited for PIV during this work, whereas actual pictures are visible in figures 3.9 and 3.10. These photographs report the combination of particle image velocimetry instrumentation with the Optris PI 640

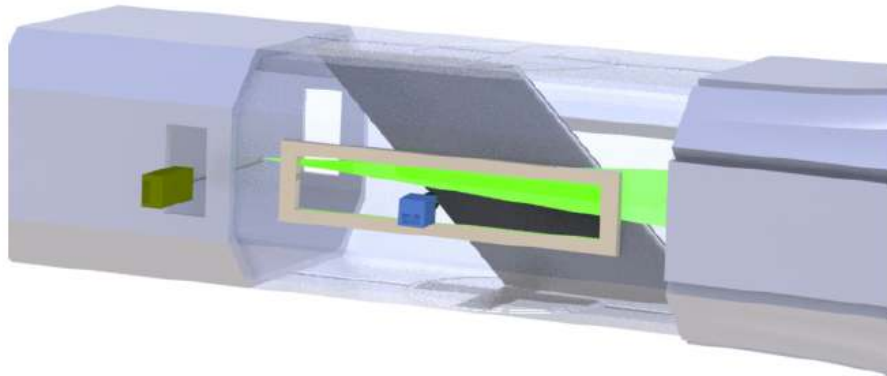


Figure 3.8: Schematic representation of the particle image velocimetry experimental setup. From Serpieri et al. (2017)



Figure 3.9: Close-up of the PIV setup: double camera arrangement for the

thermographic camera. The simultaneous measurements relies on the attempt to assess the presence of any disturbances on the measured field (or volume), before acquiring data by particle image velocimetry. In fact, the long post-processing of PIV data prevent the users from the identification of a failed experiment, within short amount of time. This expedient is believed to be worth becoming a standard procedure, especially for tomo-PIV measurements where the processing time may overtake the whole duration of a campaign.

The setup for these experiments entails a SAFEX fog generator with $1\mu\text{m}$ diameter particles and a Quantel Evergreen Nd:YAG laser. This is characterized by a double cavity, a 200 mJ pulse energy and a 532 nm wavelength λ . The laser light pointed at the direction of an optical mirror and was reflected through three lenses for the modification of the laser focus.



Figure 3.10: PIV laser sheet pointing at the investigation volume

The aim of these lenses was to generate a laser sheet illuminating the area downstream of the roughness element, parallel to the wing. For the last condition one must keep in mind that the wing surface is not completely flat, but presents a slight curvature. Two spherical lenses ($f = -75\text{mm}$ and $f = 125\text{mm}$) were exploited for the proper setting of the light focus, by changing the distance between them one could adjust the focal distance of the light and therefore its intensity distribution inside the investigated domain. Moreover, a cylindrical ($f = 150\text{mm}$) lens was added to control the inclination of the laser sheet with respect to the wing surface; and after setting them as parallel, it was used to modify its width in the wall parallel direction. Finally, the planar PIV light was running at a 1.5 mm distance from the wall and had an approximately 1 mm thickness.

A LaVision Imager Pro LX camera has been used. This is a 12 bit CCD camera equipped with a 16 MPixels sensor and a $7.4\mu\text{m}$ pixel dimension. A Nikon Micro-Nikkor objectives featuring a 200 mm focal length was included. The single camera was placed at a 0.9 m distance from the zone of investigation, resulting in a $135 \times 65\text{mm}^3$ field of view, with a numerical aperture of the cameras to $f_{\#} = 5.6$ and a magnification factor of 0.25. The total amount of data fields per run was set to 500, which was believed to be sufficient for a statistic evaluation of the phenomenon. The maximum acquisition frequency was mainly limited by the capabilities of the sensor-PTU system that could handle 1 Hz acquisition frequency. The time shift between two pulses was also changed according to the variable freestream speed: from $22\ \mu\text{s}$ to $30\ \mu\text{s}$, in order to keep the particle displacement inside the range of 12 to 18 pixels.

The velocities measured in this type of experiment lay in the plane of the laser sheet. In the field of view, these velocities correspond to the components along x_t and z_t , as the laser sheet runs tangent to the wing. Often, the measured velocity U_{Avg}^{PIV} is compared to U_{Avg}^{HWA} . This approximation is justified by the fact that the hot wire anemometry measure the vector sum of the velocities along x_t and y_t , with the latter being negligible inside a boundary layer.



Figure 3.11: Side view of the roughness elements ($D = 10mm$) attached to the wing model

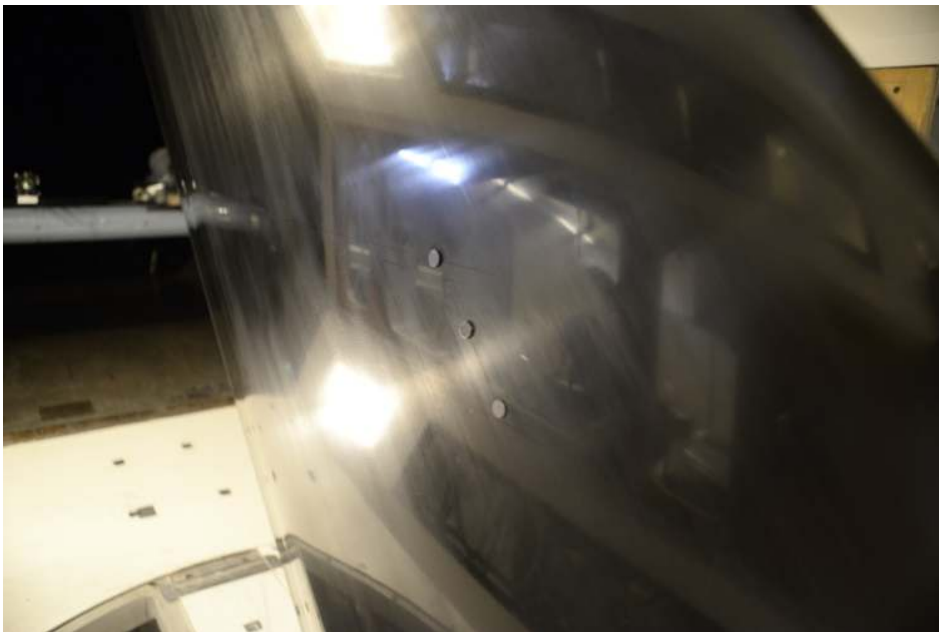


Figure 3.12: Front view of the roughness elements ($D = 10mm$) attached to the wing model

3.2.4 Roughness elements

The selection of the roughness element geometries came from the combination of experimental investigations and consideration deriving from literature. The aforementioned preliminary test performed with the first three roughness elements was needed to set a baseline for this research. After that, several new elements were produced in order to carry out a thorough investigation. The complete list of all the elements is represented by table 3.1.

	D=1.25 mm	D=2.5 mm	D=4 mm	D=6 mm	D=8 mm	D=10 mm
k=0.5 mm				X	X	X
k=0.75 mm			X			
k=1 mm				X	X	X
k=1.5 mm	X	X	X	X	X	X
k=2.1 mm			X			

Table 3.1: List of all the elements produced and tested during this project

This decision is based on the theories explained in section 2, according to which the fundamental parameter influencing the isolated roughness induced transition is Re_k (Tani, 1969). However, what can actually predict the transitional behavior of the boundary layer aft the roughness element is the relation between the Re_k and its relative critical value. This is known to scale with $k/D^{(2/5)}$, starting from the range 600-900, relative to the $k/D = 1$ condition (Ergin and White, 2006; Klebanoff et al., 1992, 1955).

By modifying either k or the freestream velocity one can investigate different types of transition scenarios. For instance, the growth of Re_k after an increase in k is steeper than the growth of the critical value of Re_k , as the latter scales with an exponential lower than unity. Hence, this is expected to move the phenomenon towards *more critical* conditions. However, this is not the only way to change how Re_k relates to its critical value. An increased diameter can move the critical Reynolds towards lower values and therefore making any experimental condition *more critical*. These are the concepts laying behind the decision of including new roughness elements with modified diameter. The specific selection of D values relied on the attempt to cover different ranges of criticality, combined with the feasibility of the manufacture and the possibility to compare results with available literature.

It must be reminded what was already mentioned in chapter 2, the three macro groups used in this report for the identification of the transition regime are: *sub-critical*, *quasi-critical* and *super-critical*. The first and the last groups are easy to explain, as they refer to the Re_k that respectively do not reach or completely overcome the critical Reynolds. The second group falls in the grey zone of figure 2.35, whose boundaries could be estimated with the aforementioned values 600-900 scaled with $k/D^{(2/5)}$. However, as pointed out in section 3.2.5, slight discrepancies might occur between the graphic and the equation.

The roughness elements were produced by cutting brass and copper rods of the desired diameters. A further polishing of the upper and lower circular surfaces was needed to remove imperfections and to bring the thickness uncertainty to a maximum of 0.05 mm. The whole surface was painted black in order to avoid reflections, which could be negatively affect the

PIV image recording to a large extent. The final results can be seen in figures 3.11 and 3.12, where all the elements were glued to the wing as shown in figure, adding a further ≈ 0.02 uncertainty to the thickness.

3.2.5 Experimental matrix

The experimental matrices are here reported for all the measurement techniques.

Infrared thermography

Infrared thermography was carried out for the elements displayed in table 3.1. Hence, all the elements displayed before were tested with this technique. However, the results for the smallest diameter element $D = 1.25m$, $k = 1.5mm$ will not be displayed, as the extreme size made the analysis of the images difficult. For each element, the velocity was varied from 6 m/s to 25 m/s, with steps of 0.5 m/s.

Hot wire anemometry

Each plane covered a range of y and z_t such to investigate the whole disturbance phenomenon. Hence, exclusively the X positions will be shown in the experimental matrix. Furthermore, the only investigated velocity was $U_\infty = 8m/s$ and it will not be mentioned in table 3.2.

	D=4 mm		D=10 mm	D=2.5 mm
X	k=0.75 mm	k=2.1 mm	k=1.5 mm	
6 mm	X	X	X	X
12 mm			X	X
18 mm			X	
24 mm	X	X	X	X
30 mm			X	
42 mm			X	X
54 mm		X	X	X
66 mm			X	
90 mm			X	X
114 mm			X	

Table 3.2: Hot wire anemometry experimental matrix

Particle image velocimetry

The PIV matrix is shown in table 3.3. For the elements that are subject of the deep analysis of section 4.2, a further scheme is shown. Table 3.4 reports the values of a nominal Re_k for all these scenarios, together with the estimation of a Re_k -range linked to the uncertainty in roughness height. In other words, the uncertainty in k due to its manufacturing translates in an uncertainty in the U_k . Therefore, the values of Re_k at the limits of this uncertainty range have been added. Moreover, the table includes the estimations of $Re_{k,critical}$, in order to understand their status or level of criticality, related to their aspect ratio. The estimation of transitory status has been obtained from the comparison of the nominal value of Re_k with the minimum and maximum value of critical Re_k , calculated according to section 3.2.4. It must be noticed that these parameters have been calculated, selecting $\nu = 1.51 \times 10^{-5}$, standard value of kinematic viscosity for air at $20^\circ C$. The author relied on a boundary layer solver code for the estimation of U_k , whose validity and reliability will be discussed later in section 4.1.2. Furthermore, another important parameter displayed in table 3.4 is the ratio k/δ_* , with the denominator being the displacement thickness of the boundary layer. This parameter quantifies the evolution of the boundary layer when encountering the disturbance. It is interesting to notice that the scaling of Reynolds critical with $k/D^{(2/5)}$ might cause two elements to be both in a super-critical condition, but present totally different ratios k/δ_* . At the same time two elements, with the same ratio might find themselves in totally different criticality status.

For sake of clarity, the definition of *central element* is reported and justified. This name is linked to the fact that $D = 4mm$, $k = 1.5mm$ is the starting point of this investigation. In fact, each of the three parameters (height, diameter and freestream speed) is first increased and then decreased, adding $3 \times 2 = 6$ cases to the deep investigation of section 4.2. Figure 3.13 can help understanding this concept: it is a schematic drawing of the central element (painted in red) and its variation with the three parameters. The arrows represent the freestream speed - the longer they are the higher the velocity.

	D=1.25 mm	D=2.5 mm	D=4 mm	D=6 mm	D=8 mm	D=10 mm
k=0.5 mm						X
k=0.75 mm			X			
k=1 mm						X
k=1.5 mm	X	X	X	X		X
k=2.1 mm			X			

Table 3.3: List of all the elements tested with PIV

		Ratio k/δ_*	Nominal Re_k	Range Re_k	Critical Re_k	Status
Central or Main	$U_\infty = 8m/s$ $D = 4mm$ $k = 1.5 mm$	1.53	592	547 - 637	405 - 608	Quasi
Change k	$U_\infty = 8m/s$ $D = 4mm$ $k = 0.75 mm$	0.77	170	143 - 204	307 - 461	Sub
	$U_\infty = 8m/s$ $D = 4mm$ $k = 2.1 mm$	2.15	973	937 - 1026	464 - 696	Super
Change U	$U_\infty = 6m/s$ $D = 4mm$ $k = 1.5 mm$	1.33	388	358 - 419	405 - 608	Sub
	$U_\infty = 12m/s$ $D = 4mm$ $k = 1.5mm$	1.88	1011	941 - 1080	405 - 608	Super
Change D	$U_\infty = 8m/s$ $D = 2.5mm$ $k = 1.5mm$	1.53	592	547 - 637	489 - 734	Quasi
	$U_\infty = 8m/s$ $D = 10mm$ $k = 1.5mm$	1.53	592	547 - 637	281 - 421	Super

Table 3.4: Transition regime of the main elements: nominal and critical Re_k

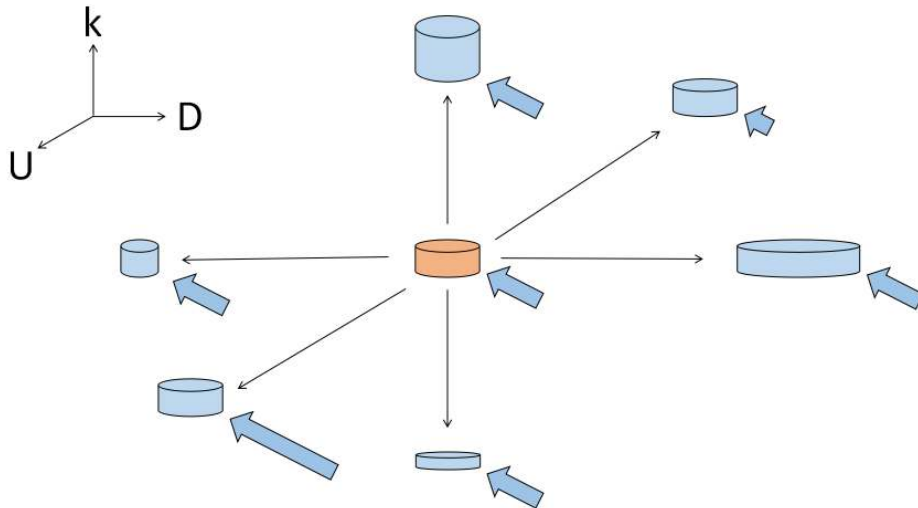


Figure 3.13: Schematic drawing of the element investigated in detail: the central element is painted in red

Chapter 4

Results

This chapter is divided in three main sections. The first part (4.1) is dedicated to a large parametric analysis performed with IR thermography. This is used as a baseline for the evaluation of the main experimental parameters (U_∞ , k and D) and their consequences on the transition scenario. Consequently, a large discussion regarding the effects of this three parameters is reported (4.2). This exploits all the different techniques in use, and provides a detailed description of all the phenomena involved in the isolated roughness induced transition for this three-dimensional BL. The third section (4.3) will report some results obtained from the aspect ratio outliers, and it will give the description and the justification for them.

4.1 Parametric Study of Transition with IR Thermography

4.1.1 The Turbulent Wedge Opening

The results from infrared thermography have been used for the broad investigation around the effects of the experimental parameters on the transition behaviour. The data obtained can be used as a flow-visualization technique, in order to characterize the different wakes and wedges generated by the elements. The generation and the evolution of the turbulent wedge has been topic of investigation for decades, with a milestone of this research in the work of [Schubauer and Klebanoff \(1955\)](#). In this early work, the authors were already able to identify the generation of turbulent wedges downstream isolated disturbance element on a wing. They stated that the half-angles observed always stayed in the vicinity of 10° , even though more recent authors such as [Chu and Goldstein \(2012\)](#) and [Zhong et al. \(2003\)](#) reported slightly lower values (down to 6°). The aspect that the most relate to this research is the distance between the roughness position and the origin of these wedges. Already in the work of [Schubauer and Klebanoff \(1955\)](#), it is stated that for a sufficiently small roughness disturbance, the wedge generation occurs further downstream of the element location. This is also confirmed by [Ye et al. \(2016a\)](#) by means of figure 4.1, where the weak initial perturbation

develops into the turbulent wedge at a certain distance from the micro-ramp. Moreover, they state that the mechanism of transition starts occurring with the spreading of this wedge. Therefore, the streamwise location at which the element wake assumes the characteristic of a turbulent wedge is strongly connected to the onset of transition.

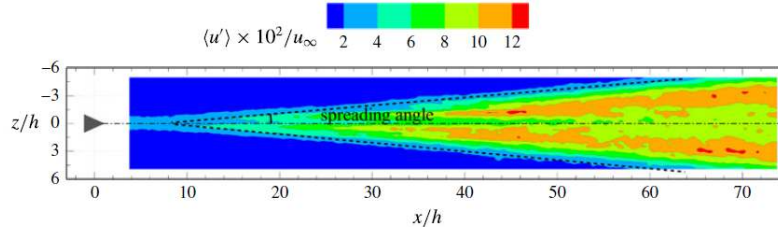


Figure 4.1: Spreading of the wedge angle and its streamwise velocity fluctuations (xz view). From Ye et al. (2016a)

However, it is not totally correct to define the position of wedge opening as the transition location. There might be some intermediate status before actual transition occurs. Hence, for a rigorous analysis, this thesis will refer to these X positions as "positions of *wedge opening*". Nonetheless, it must be said that these results are believed to represent an extremely valid and totally unambiguous method for the assessment and the comparison of different wakes. Finally, figure 4.2 shows an example of how a wedge opening appears. As also stated by Schubauer and Klebanoff (1955), the fully turbulent wedge has totally different size than the wake of the element in its vicinity. Figure 4.2 displays three elements with $D = 10\text{mm}$: a super-critical element, with the turbulent wedge occurring in the near wake of the cylinder, a quasi-critical and a sub-critical. The central element is characterized by the two initial HS vortices introducing a disturbance that after a certain X_{wo} develops in a turbulent wedge. The red lines identify the open wedge, and it is straightforward to discern the difference between their angle of aperture and the initial disturbance (black lines).

4.1.2 Thermographic Results

Effect of Element Height

Figures 4.3 and 4.4 show the variation of the wedge opening location when increasing the freestream speed of the wind tunnel. As stated in 2.2, the transitional behaviour of these phenomenon is highly critical (Tani (1969); Klebanoff et al. (1992)). For all the different elements, it only takes a slight increase in freestream velocity to go from a totally subcritical condition to a fully turbulent wedge starting right in front of the element. In fact, for speeds that are higher than 6 m/s (lowest speed tested), the absence of a marker means that the wake of the element simply does not open to a turbulent wedge within the field of view of the thermographic frame. Despite referring to different diameters, in both figures the effect of an increased height k is clear: a taller the element needs a lower speed to cause a transitional wedge. This is also totally expected, as the primary effect of an increased height is the increase of Re_k and therefore a more *critical* condition of transition.

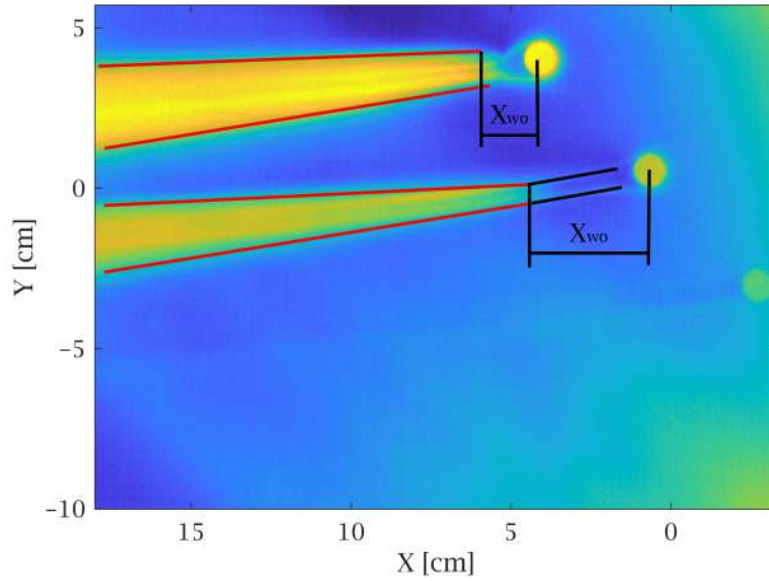


Figure 4.2: Visual legend for the thermography wedge opening. Red lines are the boundaries of a turbulent wedge. Black lines show the initial disturbance/horseshoe vortex traces.

It is now important to plot the X_{wo} variation when changing the Re_k related to each element: figures 4.5 and 4.6. From these plots a reorganization of the lines appears. Given two elements k_1 and k_2 the following statement is true:

$$if\ k_1 > k_2 \vee D_1 = D_2 \Rightarrow Re_{k,critical}^1 > Re_{k,critical}^2. \quad (4.1)$$

In other words, if the two elements have the same diameter, the taller element is related to a higher critical value of Re_k . Hence, given two elements under the effects of the same Re_k , the taller one would be farther away from a critical condition. The smaller of the two would be in a *more critical* status. Even though this might sound counter-intuitive, it may help reminding that a taller element would reach this Re_k condition with a way lower U_k (and U_∞). This is the reason behind the results of figures 4.5 and 4.6. For instance in figure 4.5, the tallest element is not even displaying a downstream onset of transitory effects for Re_k lower than 500. At the same value, the medium element has a convective form of transitional status, not yet arrived to an immediate tripping. Finally, the shortest one entered the region of immediate transition already at $Re_k = 400$.

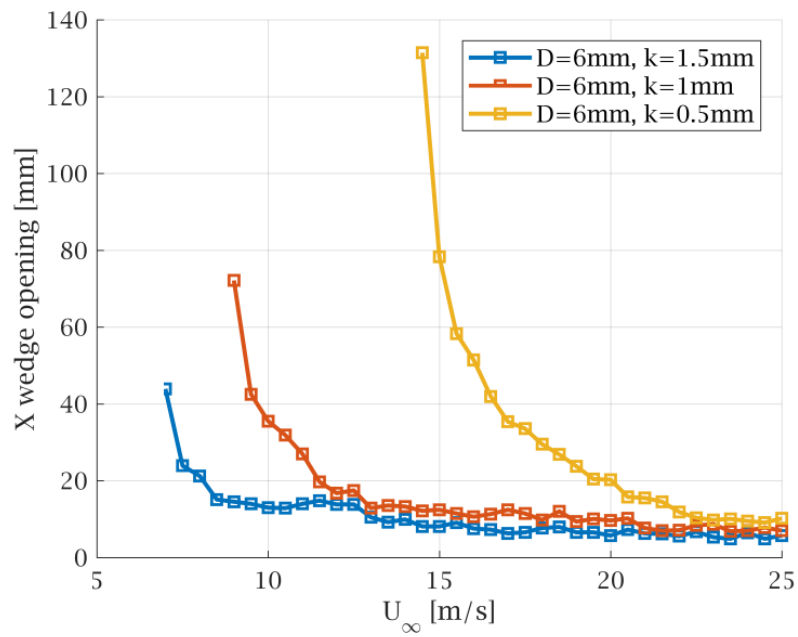


Figure 4.3: $D = 6mm$: position of wedge opening vs. freestream speed

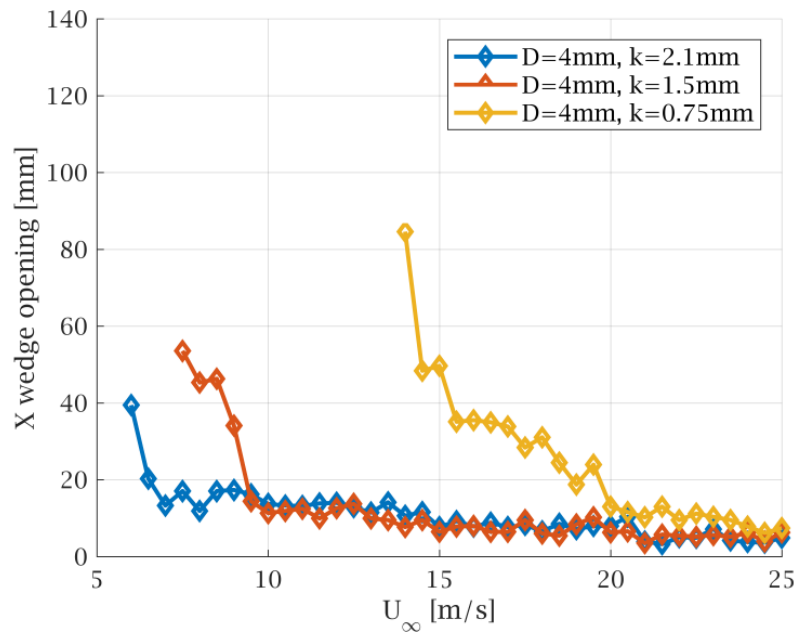


Figure 4.4: $D = 4mm$: position of wedge opening vs. freestream speed

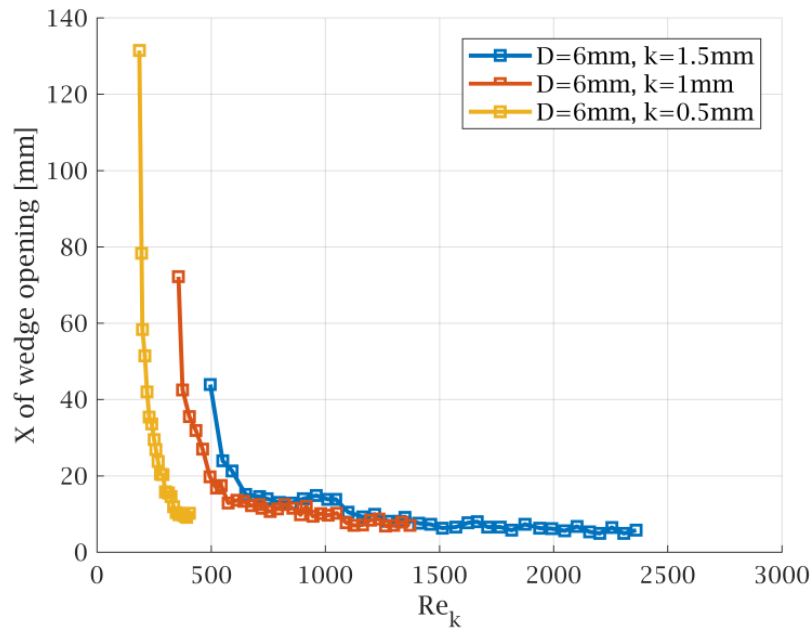


Figure 4.5: $D = 6mm$: position of wedge opening vs. Re_k

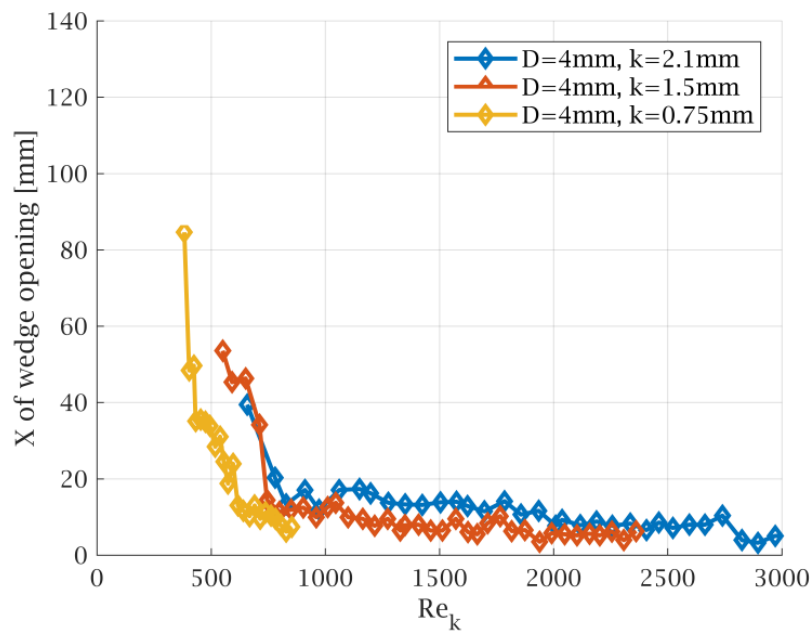


Figure 4.6: $D = 4mm$: position of wedge opening vs. Re_k

Effect of Element Diameter

The effect of a change in diameter follows a similar argument. In fact, it can be affirmed that:

$$\text{if } k_1 = k_2 \vee D_1 > D_2 \Rightarrow Re_{k,critical}^1 < Re_{k,critical}^2. \quad (4.2)$$

In words, if two elements feature the same height and are affected by the same Reynolds condition, the larger would be in a more critical condition. This is justified by the fact that the relative critical value of Re gets lower for an enlarged element. In this case there is no need to display the variation of freestream speed along the horizontal axis, as two elements with the same height and freestream velocity would necessarily have the same Re_k . The confirmation can be found in figure 4.7, where the elements all display the same height $k = 1.5mm$, and different diameters. It can be noticed that an decrease in diameter generally moves the transitory condition towards higher values of Re_k .

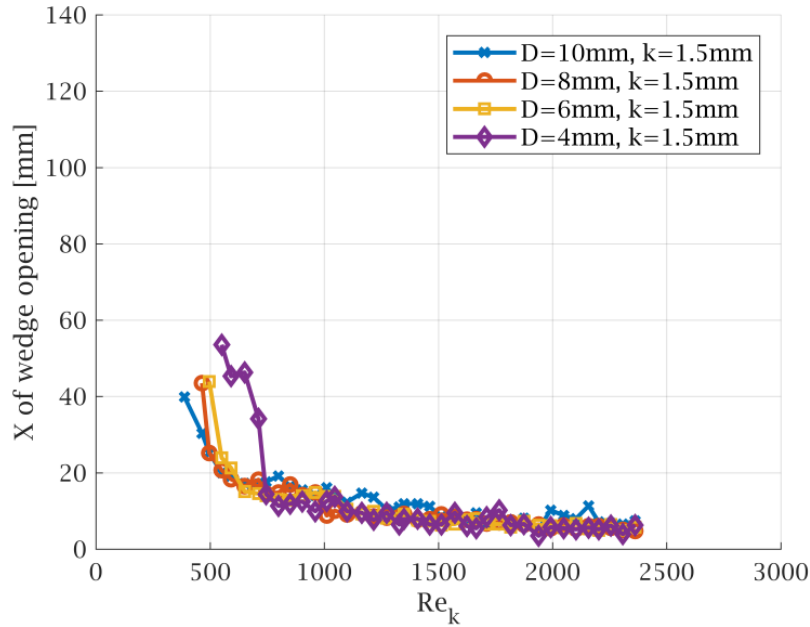


Figure 4.7: $k = 1.5mm$: position of wedge opening vs. Re_k

Estimation of Re_k

The validity of this investigation seems to be totally confirmed by figure 4.8, where the data for the roughness element $k = 0.75mm$, $D = 4mm$ and for the element $k = 1.5mm$, $D = 8mm$ merge. In fact, having the same aspect ratio, they must display the same condition, for any given Re_k value.

Finally, it is important to report that in order to calculate Re_k , the boundary layer profile at the roughness position must be known, or at least the speed U_k for that given element.

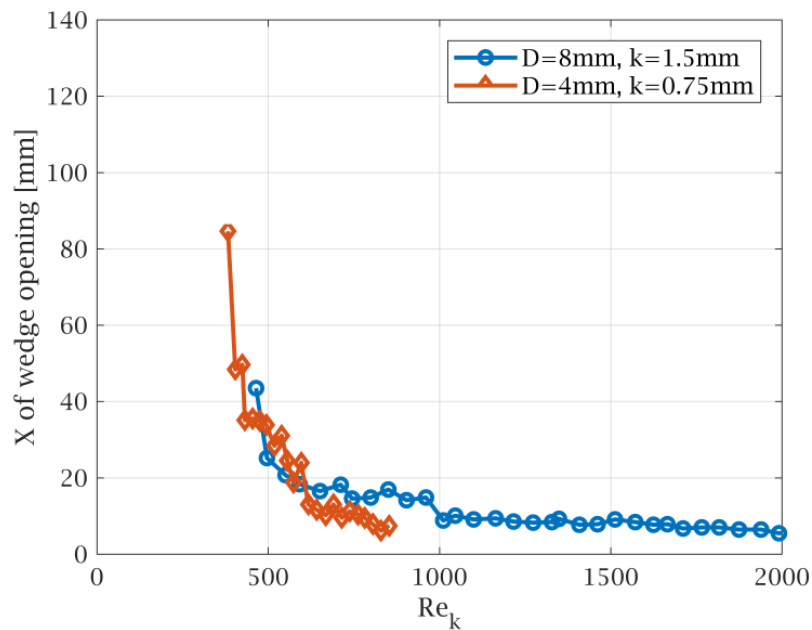


Figure 4.8: Matching of data for elements with same aspect ratio k/D

This might take a long time to be measured by means of exclusively experimental methods, i.e. by measuring the clean boundary layer profile. For instance, a hot wire anemometry measurement is fast and straightforward if needed for only one single freestream velocity condition. However, this data set required the measure of 39 different velocity profiles (from 6 m/s to 25 m/s with steps of 0.5 m/s). Therefore, the boundary layer profiles have been obtained by means of a Matlab[®] code solver available at the Department of Aerodynamics of TU Delft. The validity of this method is justified by the accuracy of this code in calculating the BL profile, whose example is shown in figure 4.9. Both the numerical boundary layer profile and the hot wire anemometry measurement are included in the plot (8 m/s freestream speed and $x/c=0.25$ position), showing the accuracy of the numerical solution. In the same figure, velocity profiles at the same position but different freestream speeds are added: 6 m/s, 12 m/s and 25 m/s.

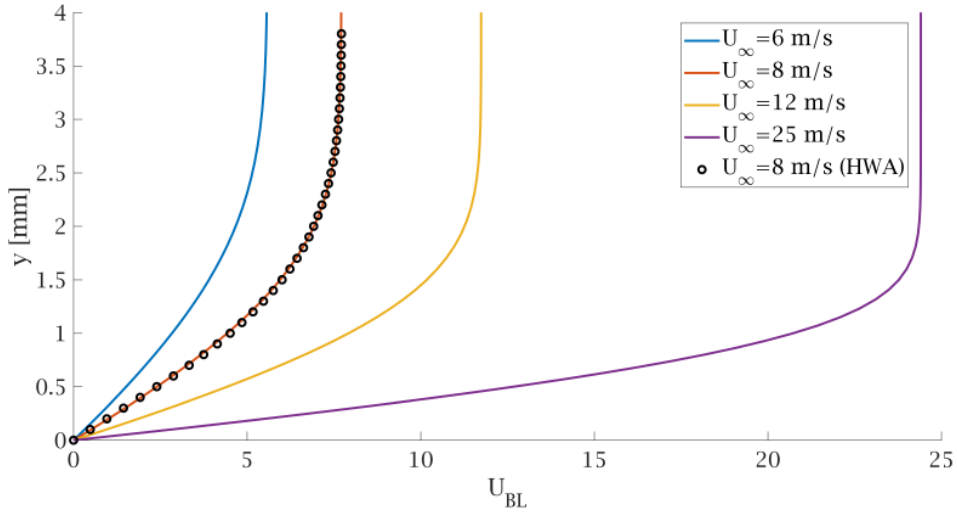


Figure 4.9: Boundary layer U profiles from the Matlab[®] code. The $U_\infty = 8\text{m/s}$ case is compared with the HWA results.

4.2 Flow Physics & Variation of Parameters

One of the purposes of this section is to display the results obtained with the different experimental techniques and to broadly describe the features of the flow, under the effects of different experimental parameters, such as k , D and freestream speed of the wind tunnel. Hence, this section will not only provide a thorough overview of the physical phenomena generated by this type of flow, but also include comparison between the cases. It is important to recall that the five roughness elements displayed in this section compose a *cross* in the k - D space. Moreover, the central element has been tested under the effects of two extra velocity conditions: $U = 6\text{m/s}$ and $U = 12\text{m/s}$. Some of the results rely on the undisturbed boundary layer fields (measured with PIV). Hence, the three time-averaged U fields are shown in appendix B, referring to the cases where no cylinder was introduced.

4.2.1 Central Element: $U = 8\text{ m/s}$, $D = 4\text{mm}$, $k = 1.5\text{ mm}$

This is the central element of the *cross*. It has been carefully selected during the preliminary thermographic campaign, as it appeared to display what will be called a *quasi-critical* condition. Regardless of all the several different nomenclatures used by the authors, the definitions used in this thesis work will now be provided. *Quasi-critical* is used to describe all those elements that can cause transition of the turbulent wedge after a certain distance from the element. They are not identified as *sub-critical*, i.e. whose introduced disturbances get dampened out and do not trigger transition, nor could be catalogued among the *super-critical* elements. The latter are defined as those ones whose transition is observed right after the element.

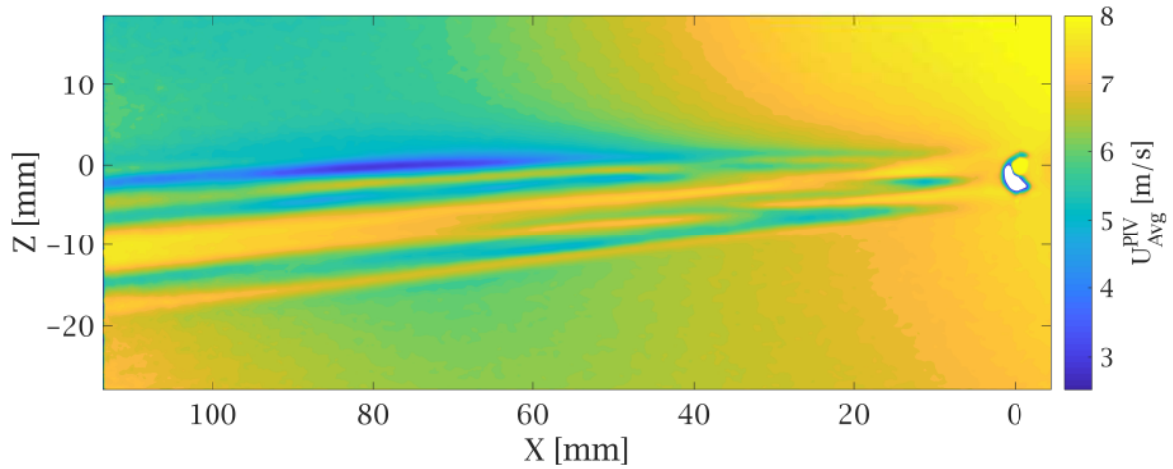


Figure 4.10: Central element: time averaged velocity field

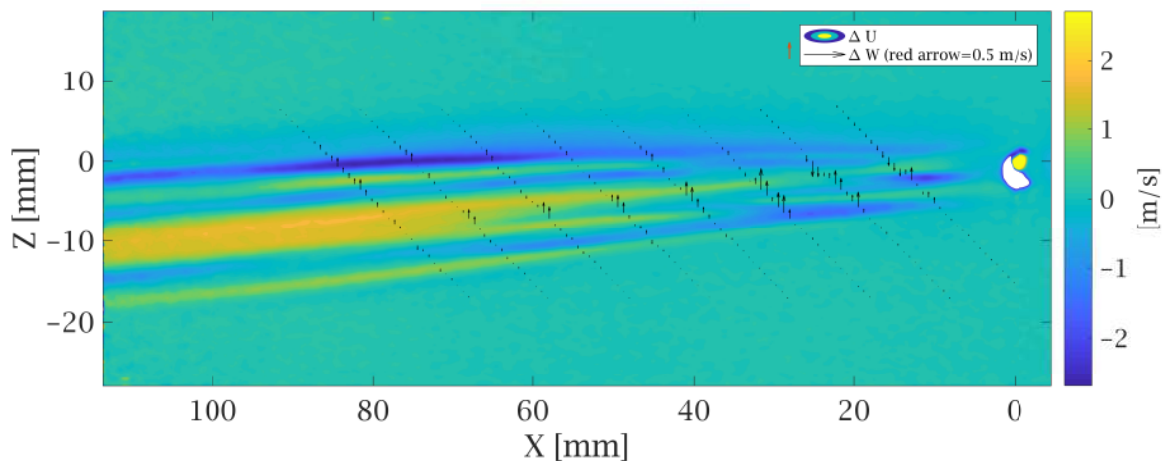


Figure 4.11: Central element: freestream and orthogonal velocity displacement from the clean BL

Averaged Velocity Field

Figure 4.10 shows the field of averaged velocity along the streamwise direction. The characteristic streaky behaviour is immediately visible. An alternation of high- and low-speed streaks occurs aft the roughness element, starting from the two high speed streaks wrapping around the element itself. These identify the two horseshoe vortices (also called HS vortices). Between these two high-speed streaks, a low-speed region appears, indicative of the wake behind the element. All these characteristics are visible in figures from 4.12 to 4.15, where the HWA results for the near wake range are shown. These zy planes of averaged velocity

help in understanding the shape of these high speed streaks and how they develop in the vicinity of the element. Before describing the rest of the velocity field, it must be reminded that these two horseshoe vortices happen to rotate in two different senses. As reminded by [Kurz and Kloker \(2016\)](#), the three-dimensional flow would have a different effect on these two structures as they develop downstream. In this specific case, the upper (lower) side of the PIV field and the right (left) side of the HWA planes figures are related to the counter-rotating (co-rotating) HS vortex. Low-speed streaks in the PIV image correspond to the low-speed *bumps* in the HWA planes. In fact, low-speed streaks are located where the up-wash mechanism pushes the low-momentum velocity from the wall region of the boundary layer towards its upper region. *Vice versa*, an high-speed streak corresponds to a high-momentum section of air blown towards the wall by the rotational movement of a vortex.

Continuing along the downstream direction, both for figure 4.10 and for figures 4.16-4.21, one could notice the beginning of a vortex cascade which lead to several extra streaks on the sides of the initial ones. Already at $X = 42mm$, four streaks of high speed could be identified in both measurement techniques. When proceeding further downstream, the first feature to be pointed out is a large and intense low speed streak running along the right side of what used to be the counter-rotating horseshoe vortex. This region of low-speed can reach down to the value of $\Delta U = -2.5m/s$, where the ΔU values are shown in figure 4.11 and correspond to the averaged velocities subtracted of the undisturbed boundary layer. By looking at figure 2.48, one can immediately recognize the presence of this low speed streak, which appear to have well defined size and strong intensity. Therefore, this phenomenon appears to be supported by the results from [Chernoray et al. \(2005\)](#). On the other side, one can observe a more intense cascade of streaks, just like the ones displayed in the reference. By the time the reader has reached this section, he/she might have already understood that the asymmetry of the flow is one of the main features of this experiment. This has consequences not only in this lastly mentioned difference between the two sides, but it also plays a role in many other aspects of the results.

Figure 4.11 has been added in order to tackle the slight curvature of the wing surface, which translate in a little difference in the distance from the wall of the PIV laser. Moreover, the combination of this lastly mentioned figure with figures 4.20 and 4.21 can help pointing out another interesting characteristic. In fact, as confirmed by past literature ([Kurz and Kloker, 2016](#)), all the vortex generated by the presence of the roughness element end up being either sustained or dampened out by the effect of the crossflow component of the boundary layer. Ultimately, this is likely to translate in a wake and a turbulent wedge that become increasingly dominated by the crossflow direction of rotation. As noticeable from figure 4.11 the arrows that display the ΔW component of the velocity (ΔW following the same explanation of ΔU) start in the near wake, with a distribution that appears to be perfectly relevant with two counter-rotating horseshoe vortices. Nevertheless, moving the attention towards the downstream W velocity, one could notice how the whole field is dominated by a flow which moves upwards. Finally, it is interesting to see how the streaky structures still preserve their periodicity and do not degenerate in a totally chaotic boundary layer.

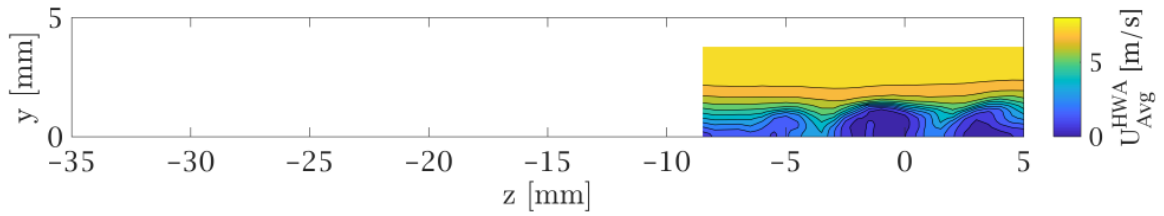


Figure 4.12: Central element: zy plane of time averaged velocity at $X = 6\text{ mm}$

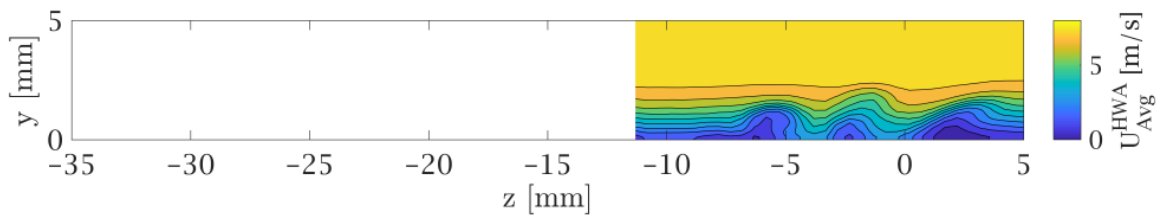


Figure 4.13: Central element: zy plane of time averaged velocity at $X = 12\text{ mm}$

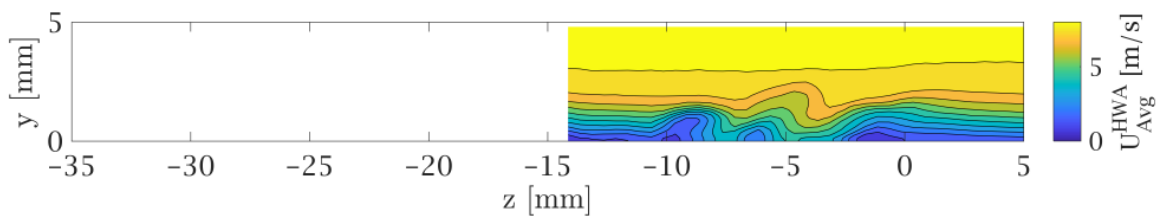


Figure 4.14: Central element: zy plane of time averaged velocity at $X = 18\text{ mm}$

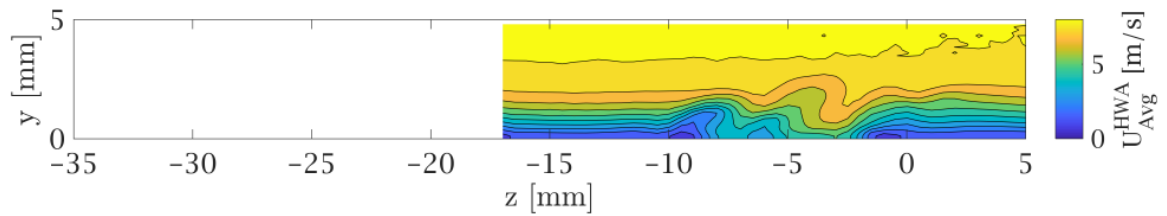


Figure 4.15: Central element: zy plane of time averaged velocity at $X = 24\text{mm}$

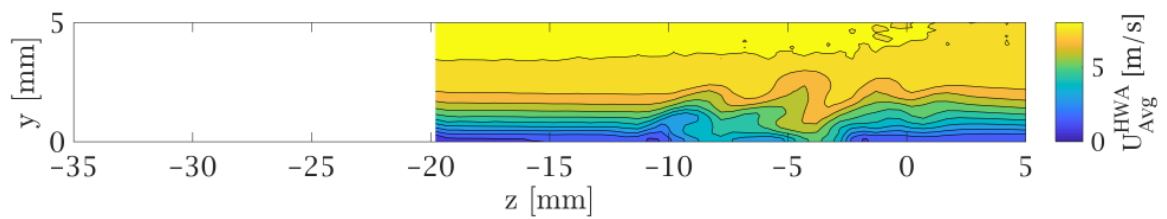


Figure 4.16: Central element: zy plane of time averaged velocity at $X = 30\text{mm}$

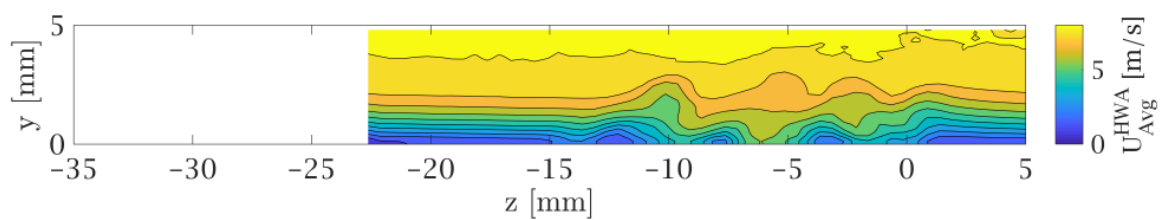


Figure 4.17: Central element: zy plane of time averaged velocity at $X = 42\text{mm}$

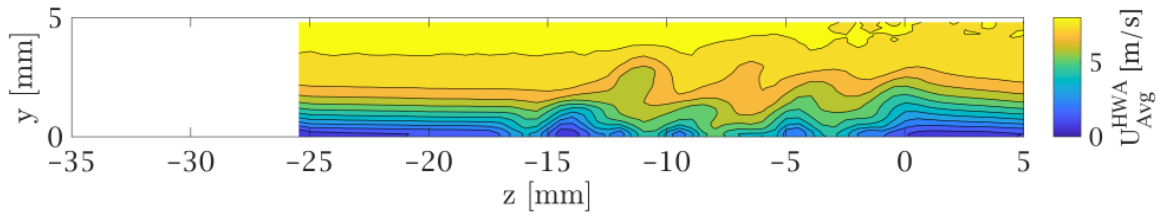


Figure 4.18: Central element: zy plane of time averaged velocity at $X = 54\text{mm}$.

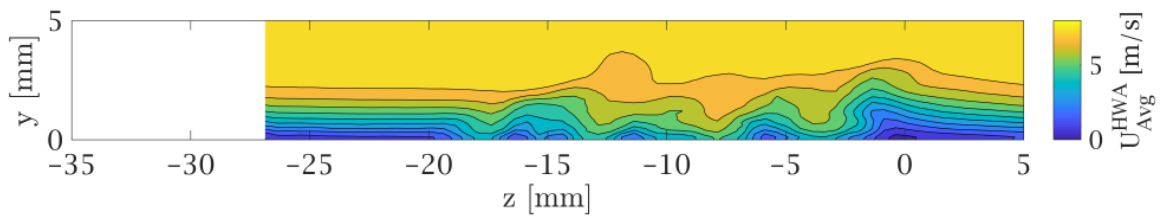


Figure 4.19: Central element: zy plane of time averaged velocity at $X = 66\text{mm}$.

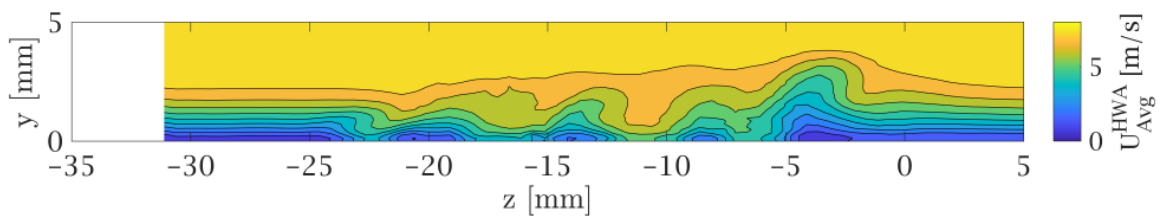


Figure 4.20: Central element: zy plane of time averaged velocity at $X = 90\text{mm}$.

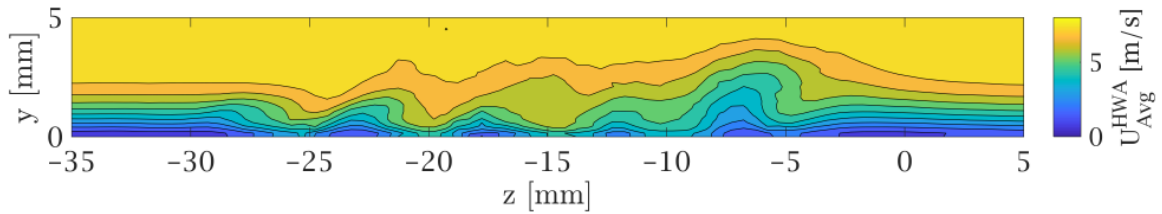


Figure 4.21: Central element: zy plane of time averaged velocity at $X = 114mm$

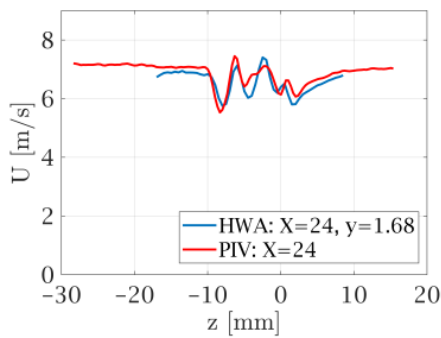


Figure 4.22: HWA and PIV comparison at $X = 24mm$: $y = 1.68mm$

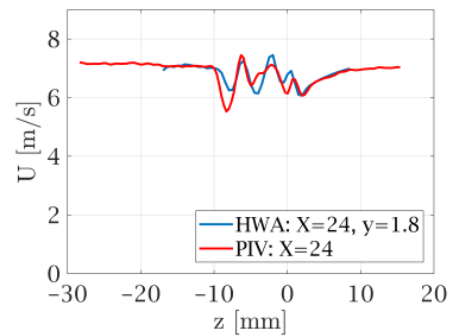


Figure 4.23: HWA and PIV comparison at $X = 24mm$: $y = 1.8mm$

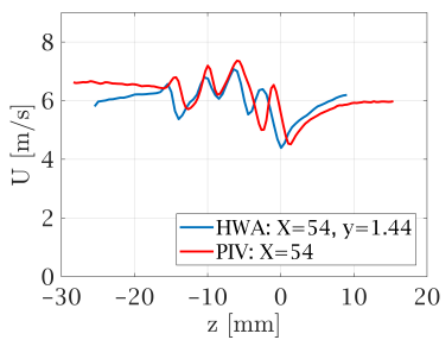


Figure 4.24: HWA and PIV comparison at $X = 54mm$: $y = 1.44mm$

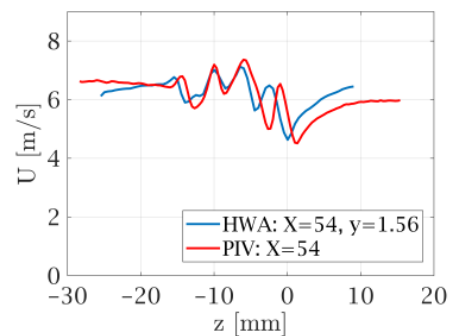


Figure 4.25: HWA and PIV comparison at $X = 54mm$: $y = 1.56mm$

Comparison between PIV and HWA

Figures 4.22 to 4.25 are used here in order to show to what extent the two techniques (HWA and PIV) provide comparable results. Their complementarity and the importance of combining them in order to have a clear picture of the phenomenon are confirmed here. As mentioned in chapter 3, the slight curvature of the wing surface affects the height at which the laser "cuts" the boundary layer, and the y position at which the two techniques match slightly varies along X .

As previously mentioned in chapter 3, another measurement has been carried out during the experimental campaign: tomographic particle image velocimetry. Some results for the central element are shown in appendix A, and it is very interesting to compare them with the results from this chapter.

Velocity Fluctuation Field

In combination with the averaged velocity field, the standard deviation (in time) of the velocity is displayed in figure 4.26. Once again, different behaviours are observed when comparing regions of the wake at different distances from the roughness element. In the near wake, three core regions of strong fluctuations dominate the field. Their position and intensity in the PIV measurement correspond to the ones displayed in figures from 4.27 to 4.31. These results are paramount for the understanding of the flow topology. As explained by [Loiseau et al. \(2014\)](#), the areas of strong instability are related to the three-dimensional shear generating around the element. This is the reason for which figure 4.30 shows peaks of time-fluctuations both in the center of the wake region and along the sides of the roughness elements, where already early authors ([Baker, 1979](#)) noticed the oscillatory nature of the flow, connected to the HS vortices.

Proceeding downstream, the first impression from the HWA results (from figure 4.32 to 4.34) might suggest a totally randomized shape and distribution of the oscillations. However, by observing figure 4.26, the fluctuations appear to reorganize themselves along the streaks related to the vortex cascade. As the observer continues moving the attention downstream, the final two planes of the HWA start displaying a more chaotic expansion of the field. Particularly, the final image (4.34) indicates an overall and intense growth of the oscillations, which was not observed in the previous planes.

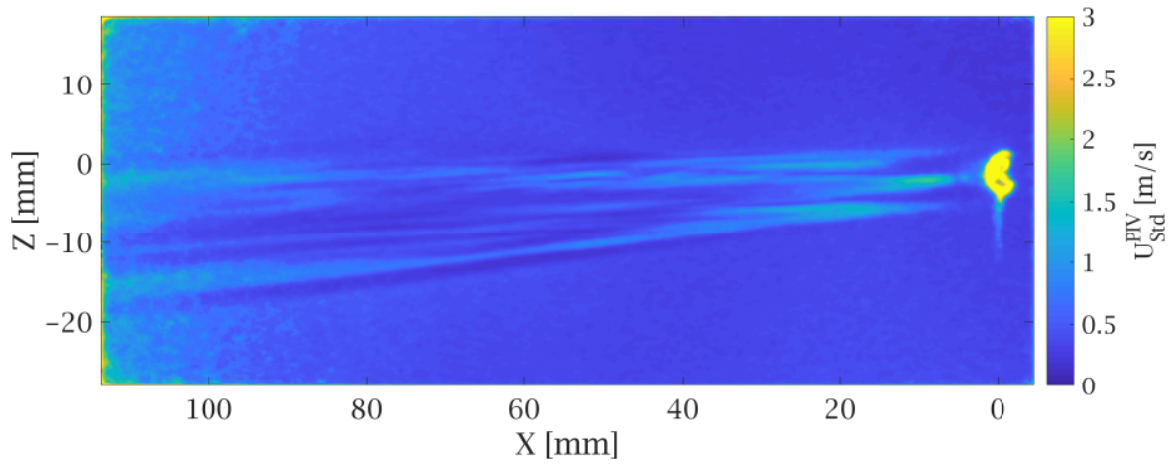


Figure 4.26: Central element: velocity fluctuations field

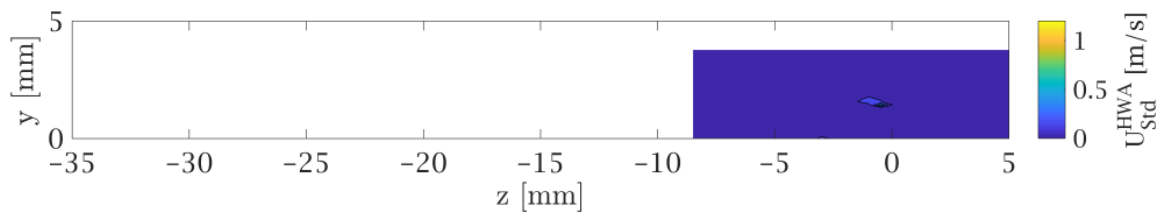


Figure 4.27: Central element: zy plane of velocity fluctuations at $X = 6mm$

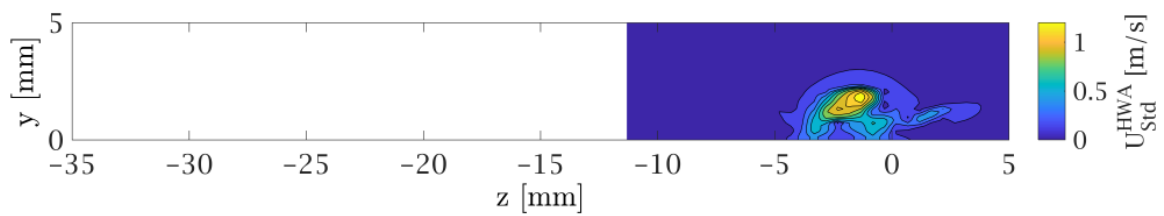


Figure 4.28: Central element: zy plane of velocity fluctuations at $X = 12mm$

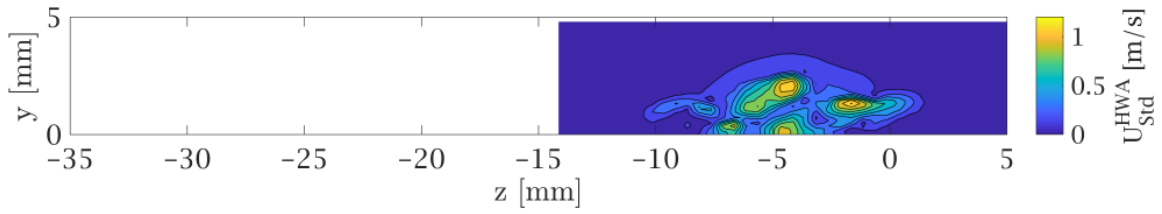


Figure 4.29: Central element: zy plane of velocity fluctuations at $X = 18\text{mm}$

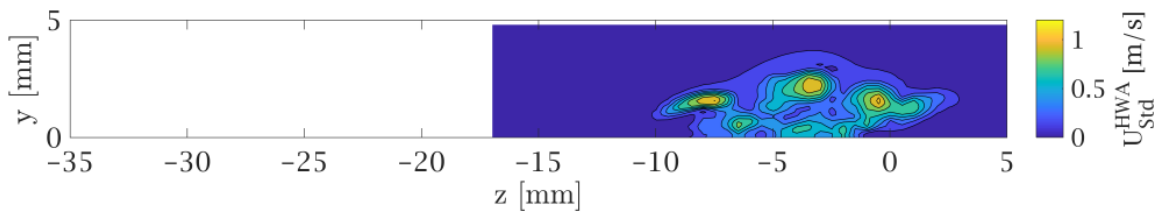


Figure 4.30: Central element: zy plane of velocity fluctuations at $X = 24\text{mm}$

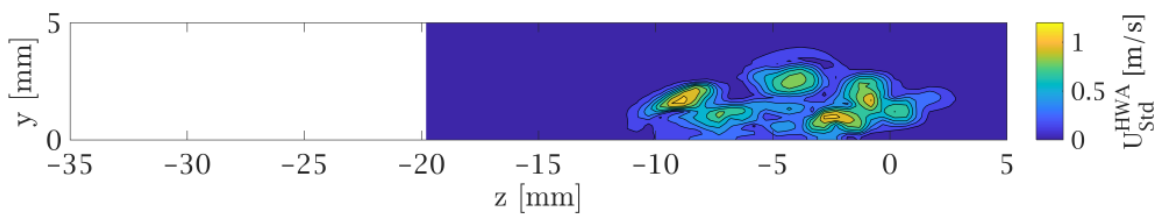


Figure 4.31: Central element: zy plane of velocity fluctuations at $X = 30\text{mm}$

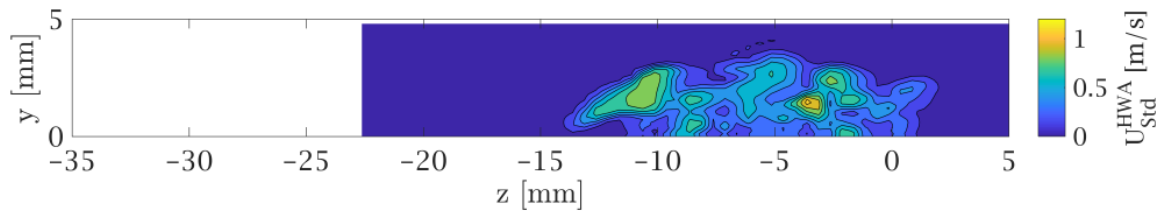


Figure 4.32: Central element: zy plane of velocity fluctuations at $X = 42\text{mm}$

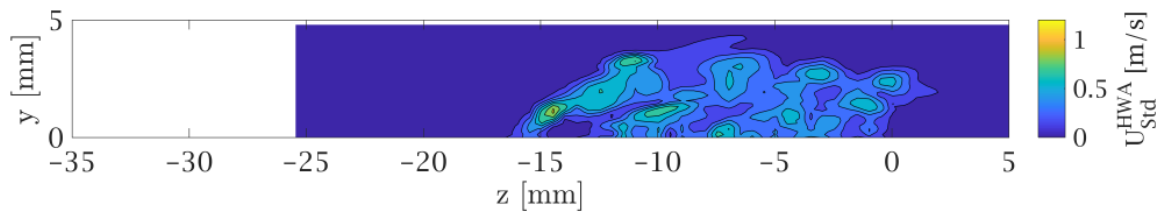


Figure 4.33: Central element: zy plane of velocity fluctuations at $X = 54\text{mm}$

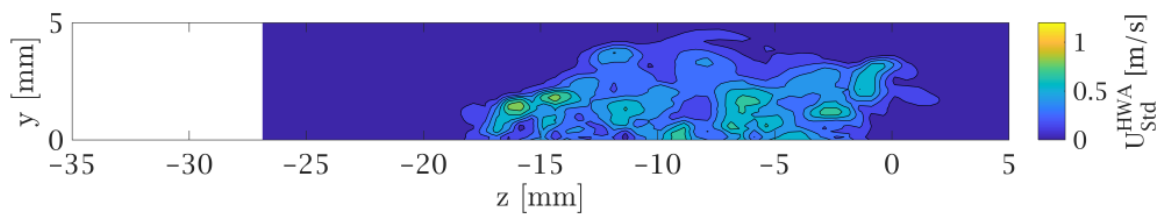


Figure 4.34: Central element: zy plane of velocity fluctuations at $X = 66\text{mm}$

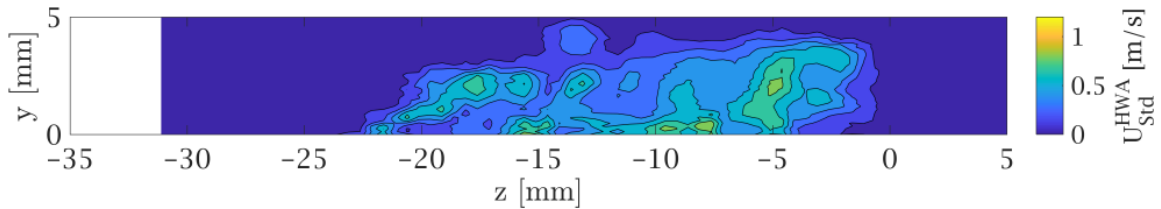


Figure 4.35: Central element: zy plane of velocity fluctuations at $X = 90mm$

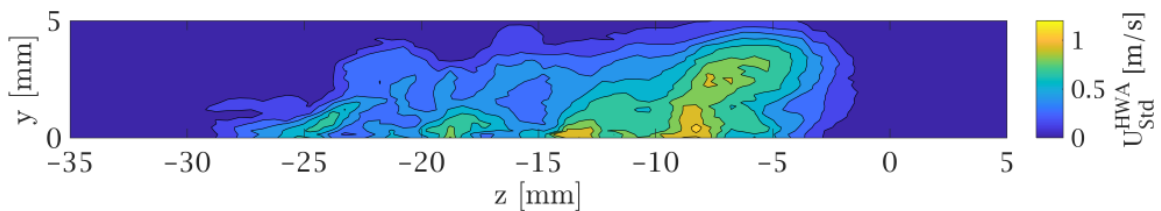


Figure 4.36: Central element: zy plane of velocity fluctuations at $X = 114mm$

Frequency Analysis

This type of analysis identifies some of the most important features of the investigated phenomenon. Among these, the strongly tonal behaviour of the HWA signal is displayed in figure 4.37. This figure shows how most of the energy (calculated as power spectral density and measured in decibel) is concentrated in a small band of frequencies. In the remainder of this report, it will be shown that the maximum tonal peak is always observed inside the band going from 500 Hz to 900 Hz, for every case investigated by HWA. The peaks that follows the main one are simply its harmonics (as their values are multiples of the fundamental one), and have been observed also by Baker (1979) and Loiseau et al. (2014). Furthermore, the red line in the plot is not to be confused with the blue line. The latter is the actual spectral analysis, the red plot is a representation of the band-pass filter (from 500 Hz to 900 Hz) that will be described later.

Baker (1979) observed a spectral analysis of the signal (see figures 2.16 and 2.17) which is similar to the one obtained in this experiment. Moreover, the values of Strouhal number are consistent with results from previous researches, at least for what concerns Str_k . In fact, it could be measured by means of the two formulae (4.3 and 4.4) described previously, referring to (Klebanoff et al. (1992)). The second formula leads to a value in agreement with the literature (see figures 2.10 and 2.13), whilst the parameter calculated with δ^* is lower than expected. One must notice that the Strouhal is always calculated on the plane $X = 24mm$,

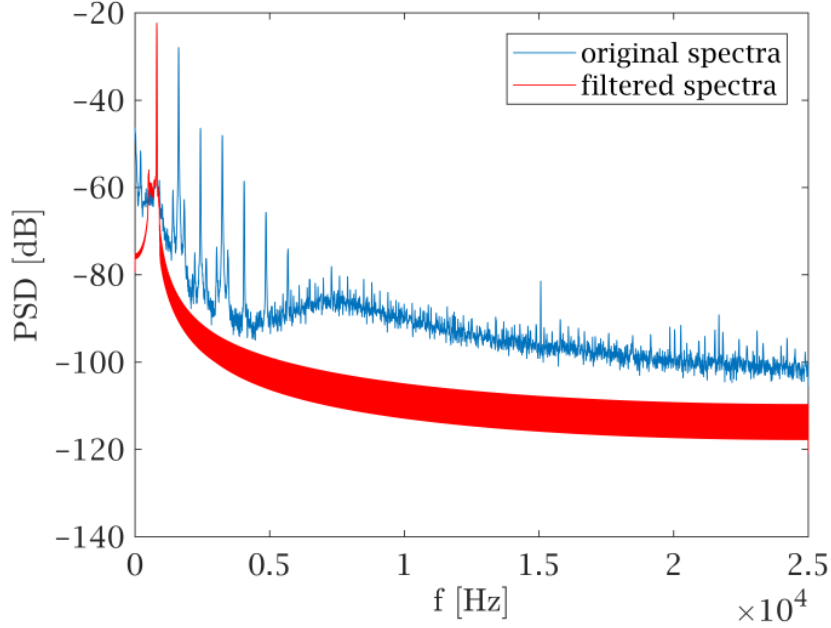


Figure 4.37: Example of a frequency spectrum and its filtering

at the $y = \delta_{0.99}/2$ position, for each of the element investigated with HWA. Finally, among all the z positions at this specific y height, the frequency associated to the maximum PSD was selected as reference frequency for the Strouhal number. This procedure is visible in figure 4.38, showing the spectra associated to every z position along the constant line $y = \delta_{0.99}/2$. This was carried out in order to maintain the same technique and keep the consistency of the calculation. The associated frequency and wavelength are $f = 790 \text{ Hz}$ and $\lambda = 7.39 \text{ mm}$.

$$Str_{\delta^*} = \frac{f\delta_k^*}{U_k} = 0.1285 \quad (4.3)$$

$$Str_k = \frac{fk}{U_k} = 0.1972 \quad (4.4)$$

Figure 4.38 is extremely useful to display the differences in frequency behaviour at different height inside the boundary layer, and also along the evolution of the wedge (increasing X , different yz planes). The tonal peaks seem to occur mainly in the vicinity of the regions with high fluctuations, as suggested by the comparison between figure 4.38 and figure 4.39. The latter presents only a restricted peak (PSD $> -40 \text{ dB}$) in the $f - z$ plot, as the z line exclusively slices the central area of high standard deviation of velocity. What is important to notice is the fact that the whole velocity field appears dominated by the same frequencies: all of the three peaks have their maximum energy in the range 787-800 Hz.

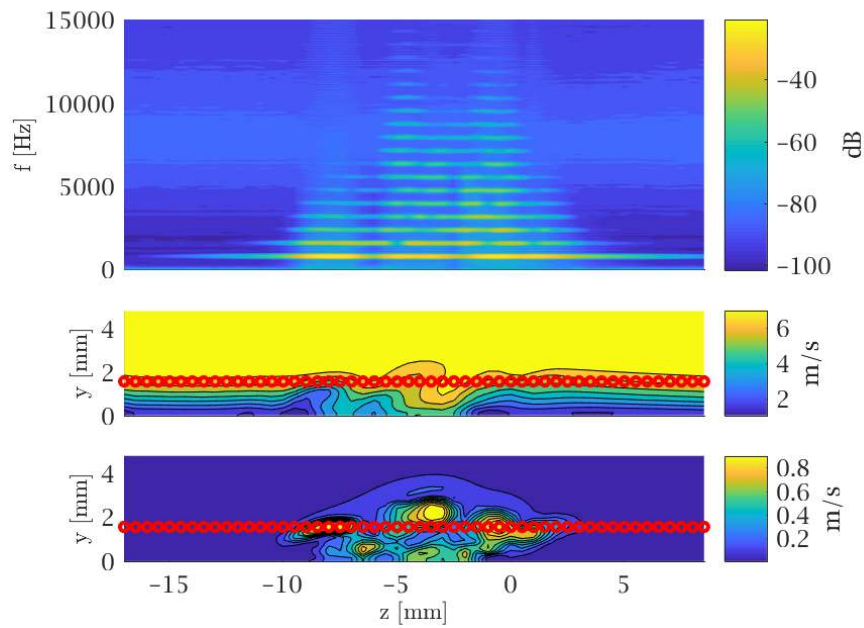


Figure 4.38: Central element, $X = 24mm$: frequency spectra along $y = \delta_{0.99}/2$

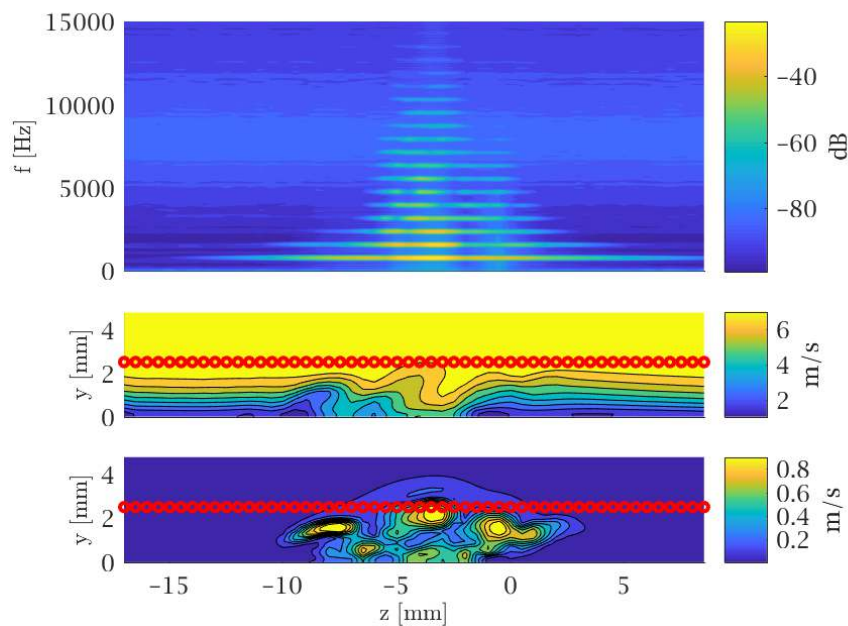


Figure 4.39: Central element, $X = 24mm$: frequency spectra along $y = 2.5mm$

The same typology of calculation and plot can be exploited for the actual evaluation of the transitional state of the flow. In other words, it is possible to understand whether the wake has reached a turbulent status, by plotting the frequency distribution along the $y = \delta_{0.99}/2$ line. Taking a look at figures from 4.40 to 4.43, the evolution of the spectra towards a

more turbulent state is evident. These figures show the frequency response at different X locations. The tonal behaviour leaves place to more distributed area of high PSD, that resemble the classic turbulent cascade spectrum. At $X = 54mm$ one may see the right side of the wake already facing some characteristics of the turbulent cascade. However, the strong tonal component of the spectra does not disappear until the last position $X = 114mm$. The left side of the wedge, instead show a tonal behaviour which tends to resist longer. This might be related to some type of sustaining effect that the crossflow dominated boundary layer has on this side. As a matter of fact, the left side correspond to the one connected to the horseshoe vortex that co-rotates with respect to to the natural crossflow vortices. This speculation is supported exclusively by some findings from [Kurz and Kloker \(2016\)](#), where all the vortices that rotate in the same direction as the natural CF are sustained, and they tend to increase as they evolve. However, along their downstream evolution, the two sides of the wedge generates secondary and tertiary vortices which rotate in other directions. The two HS are not the only ones playing a role in this phenomenon, therefore it is not correct to affirm that the early transition is only related to the HS rotation. Nevertheless, they appear to have slightly different behaviours, which is definitely linked to the three dimensionality of the natural boundary layer.

Another way to display both the tonal domination of the frequency spectra and the evolution of the flow towards an increasingly more turbulent condition, is the filtering of the signal with the aforementioned band-pass filter. After the filtering of the HWA signal, the values of standard deviation from the velocity are calculated again, including only the fluctuations related to that band. The lower frequency is set to 500 Hz and the higher to 900 Hz, the order of the filter is 20. From figures 4.44-4.48 one may draw the same conclusions already stated for the frequency contours. The signal is dominated by the tonal behaviour for a large part of the field. As the X position of the zy plane increases, more turbulent spectra are increasingly affected by the filter. In the near wake the passing band was including most of the high-PSD frequencies, therefore the fluctuation field appears almost unchanged (figure 4.44). In the far wake, its application removes a large part of the turbulent fluctuations. This is why the non-filtered fluctuations differ from the filtered ones for high X -positions.

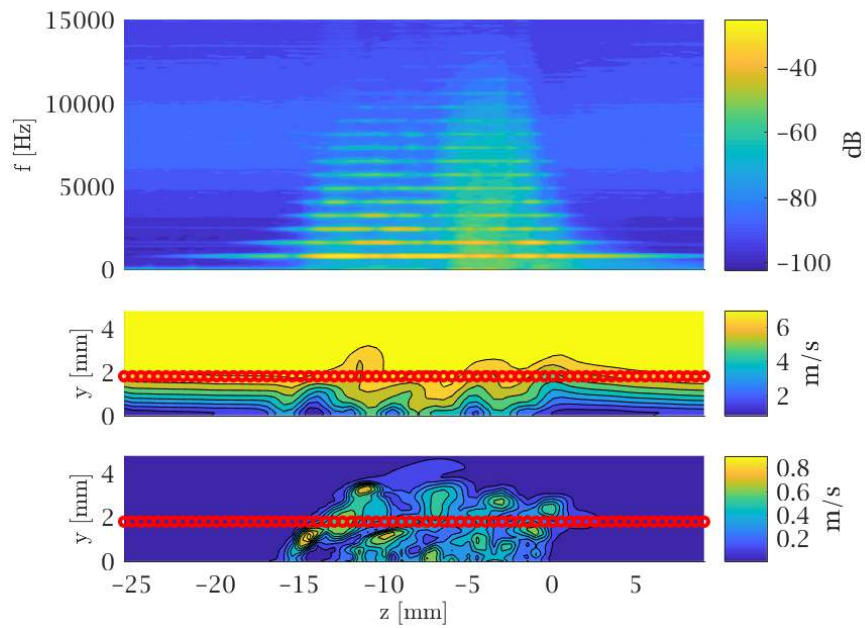


Figure 4.40: Central element, $X = 54mm$: frequency spectra along $y = \delta_{0.99}/2$

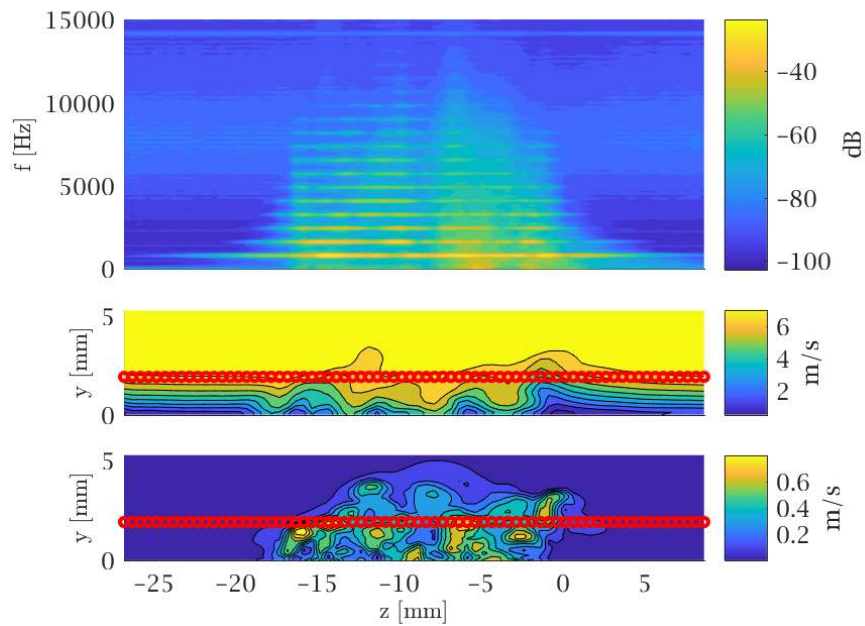


Figure 4.41: Central element, $X = 66mm$: frequency spectra along $y = \delta_{0.99}/2$

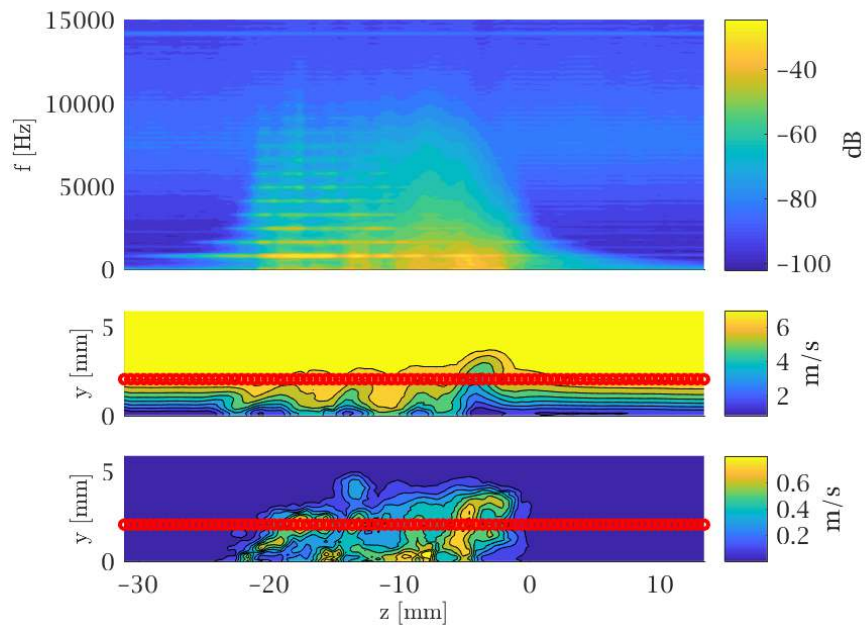


Figure 4.42: Central element, $X = 90mm$: frequency spectra along $y = \delta_{0.99}/2$

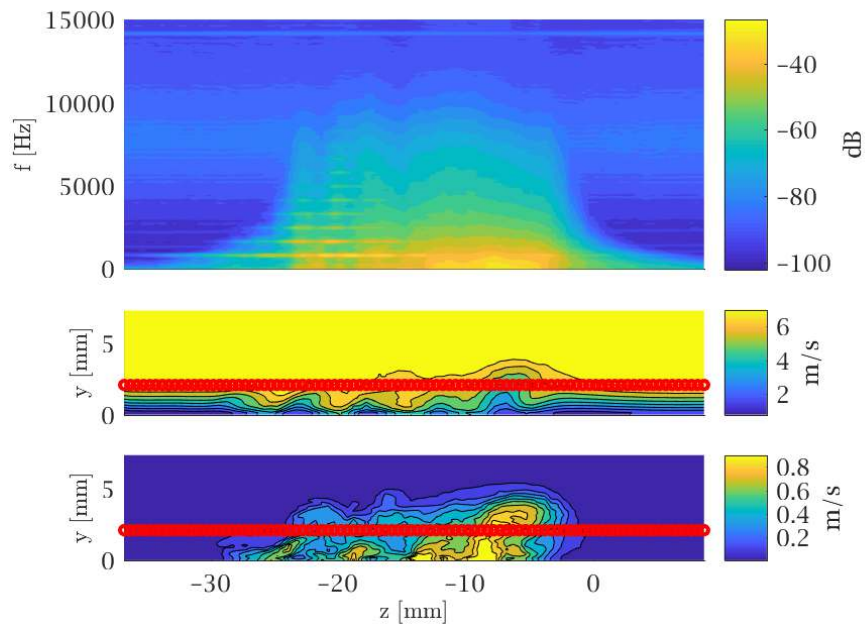


Figure 4.43: Central element, $X = 114mm$: frequency spectra along $y = \delta_{0.99}/2$

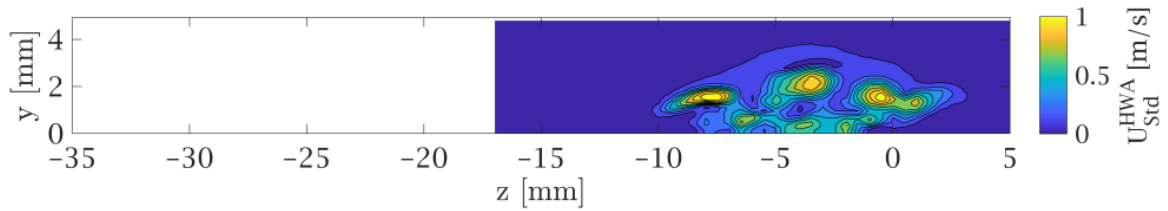


Figure 4.44: Central element: zy plane of filtered velocity fluctuations at $X = 24\text{mm}$

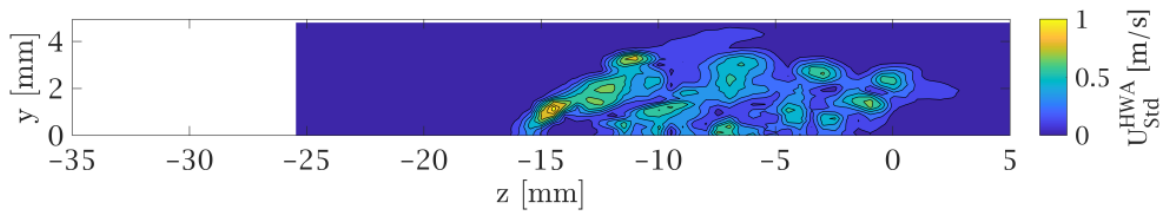


Figure 4.45: Central element: zy plane of filtered velocity fluctuations at $X = 54\text{mm}$

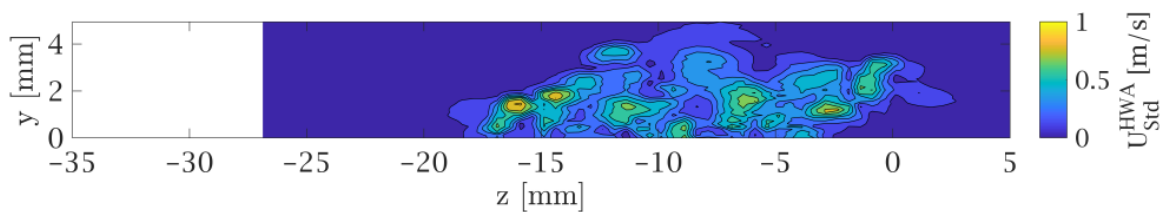


Figure 4.46: Central element: zy plane of filtered velocity fluctuations at $X = 66\text{mm}$

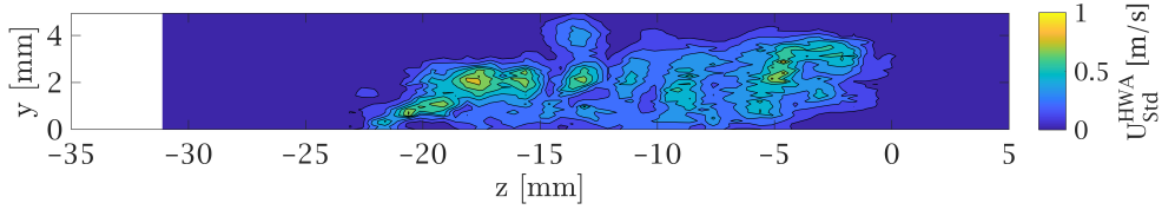


Figure 4.47: Central element: zy plane of filtered velocity fluctuations at $X = 90mm$

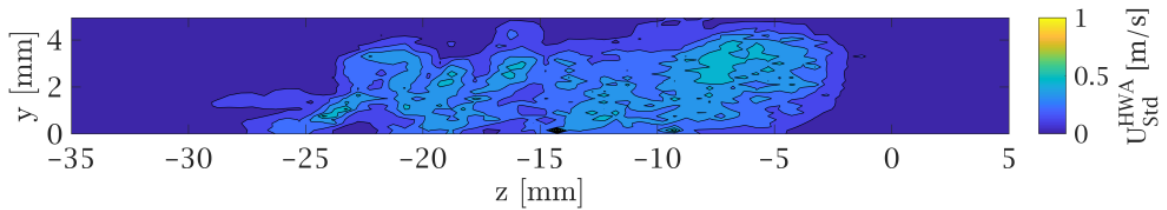


Figure 4.48: Central element: zy plane of filtered velocity fluctuations at $X = 114mm$

Analysis of the POD Modes

It has been already introduced how the velocity fluctuations and the tonal frequency spectra are concentrated in correspondance of three-dimensional shear layer. More specifically, in the upper part of the low-speed wake region and along the flanks. This is in agreement with the results from [Loiseau et al. \(2014\)](#), who also investigate the dominant mode when changing the aspect ratio of the element. As mentioned in chapter 2.3.1, varicose and sinuous modes are related to different instability mechanisms. To be more precise, the presence of a varicose pattern is explained by [Loiseau et al. \(2014\)](#) as an instability of the whole three-dimensional shear layer, that combined with the hairpin shedding in the near wake sustains a varicose modulation of the flow. The sinuous instability, instead, is linked to the "wiggling" of the central low-speed streak, caused by a mechanism similar to the Von Kármán vortices for a cylinder in a two-dimensional flow. The analysis of the spatial modes is carried out by means of a proper orthogonal decomposition, or POD ([Berkooz et al., 1993](#)). The result is a statistically based, spatial reconstruction of the disturbance fields generated by the roughness element. As the aspect ratio of the element is $k/D = 0.375$, which correspond to $\eta = D/k = 2.67$, this roughness is expected to generate a perturbation dominated by a varicose type of instability.

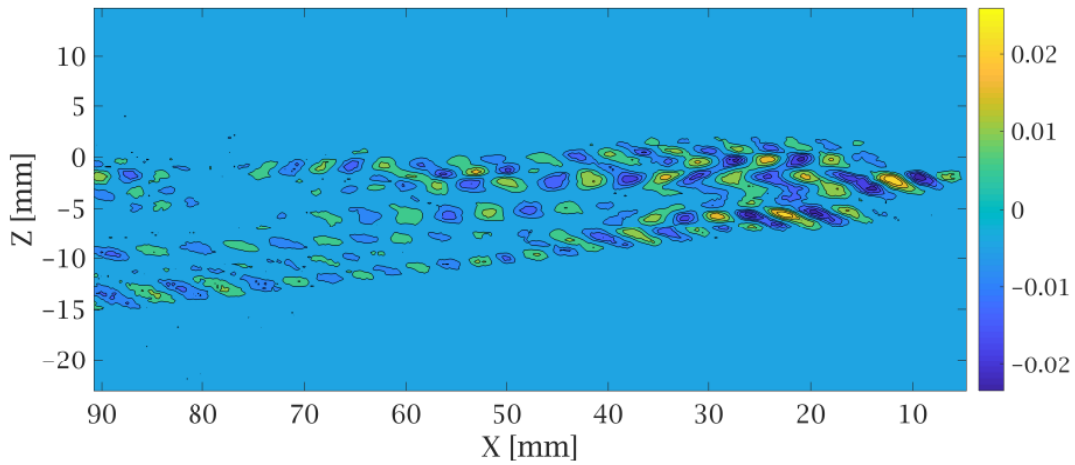


Figure 4.49: Central element: U component, POD mode 1

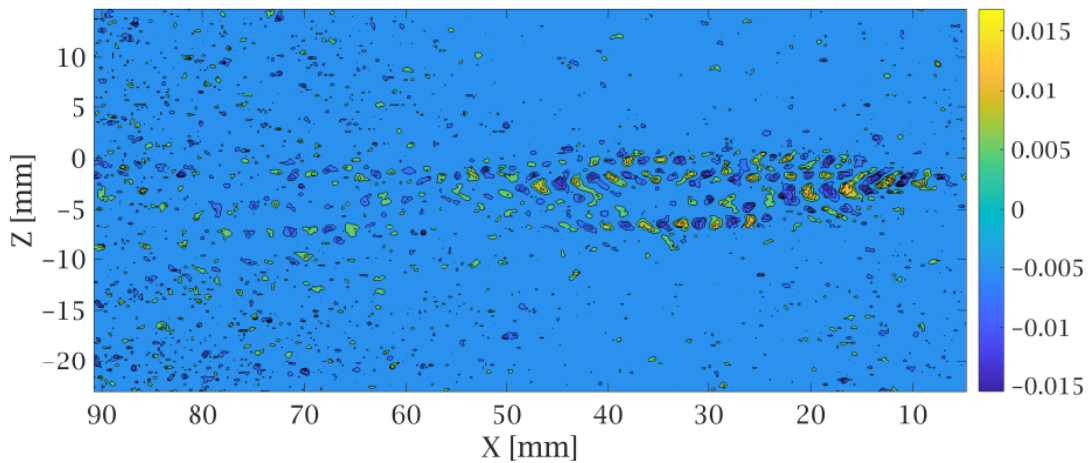


Figure 4.50: Central element: U component, POD mode 3

Figures 4.49 and 4.50 show the first two most dominant POD modes that are decoupled, referring to the U component of the velocity. The first thing to be noticed is the asymmetry of these fields. In fact, the structures have a symmetry axis tilted with respect to the X direction, and the identification of the mode type is not as easy as in a 2D boundary layer. Nevertheless, the resemblance with figure 2.30 (c) and (d) from [Loiseau et al. \(2014\)](#) is evident. The structures present short and compact spots, with smaller regions of opposite signs generating along the sides of the central main double-lines. Hence, a varicose perturbation is observed in this conditions, as expected. This means that the tonal shedding phenomenon is governed by the instability of the three-dimensional shear, with a specific attention to the upper-central part of the near wake.

What links these results with the data from the previous sections is the wavelength of the POD structures. For the most dominant POD mode, the eigenvalue distribution in the XZ

field present a wavelength that is comparable to the wavelength of the frequency used for the calculation of Str ($\lambda = 7.39mm$). Extracting the wavelength along a line that follows the path of the upper POD cascade, one obtains a value $\lambda \approx 6.8mm$. This is less than 10% difference from the one obtained with HWA. This correspondence is observed in all the cases with a dominant varicose perturbation, suggesting a common physical mechanism behind the tonal spectra in the frequency analysis and the most dominant eigenmode in the POD.

Comparison with previous literature is of fundamental importance for backing-up the discoveries of a research. Figure 4.51 is compared to figure 2.31, in order to display the high consistency in the results. The figure from literature show the velocity signal for a varicose dominated flow, measured in the center of the wake. Figure 4.51, instead was measured during this research, in the area of maximum fluctuations in the $X = 24mm$ plane. The similitude is macroscopic. Furthermore, by observing carefully, one could notice that all the maxima of figure 2.31 are sharp, as well as the minima of figure 4.51. At the same time, both the signals have the other extrema rounded, making the parallelism even more appropriate.

To conclude this section, the final comparison with [Loiseau et al. \(2014\)](#) refers to figure 2.32, where the lambda criterion shows the hairpin vortex generation. This instantaneous field is well comparable with the time series of Y -vorticity, shown in figures 4.52. The spatial organization of the instantaneous vorticity fields is similar in shape to the one from the reference. The author is aware that the figures display different quantities, but they both refer to an instantaneous time frame of the phenomenon. Both images show a curvy evolution of the flow, with a sequence of small bumpy structures.

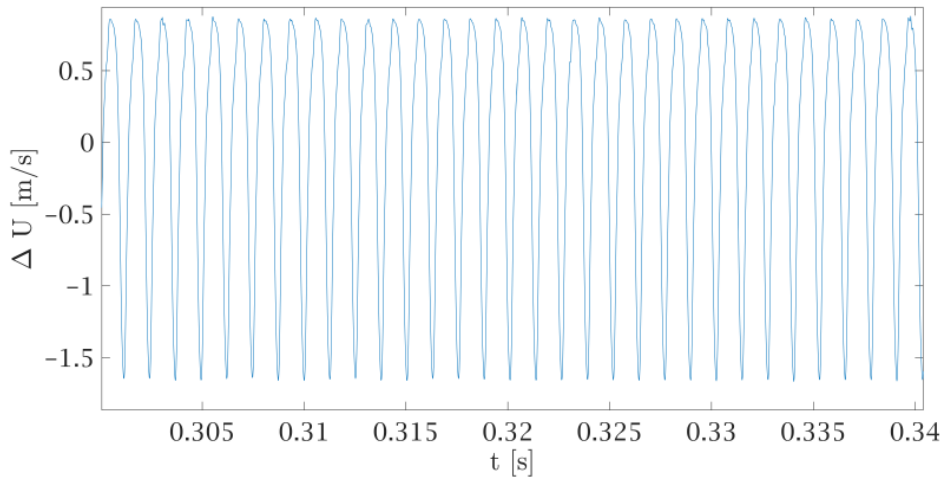


Figure 4.51: Central element: Recorded signal of HWA in the position of highest fluctuations

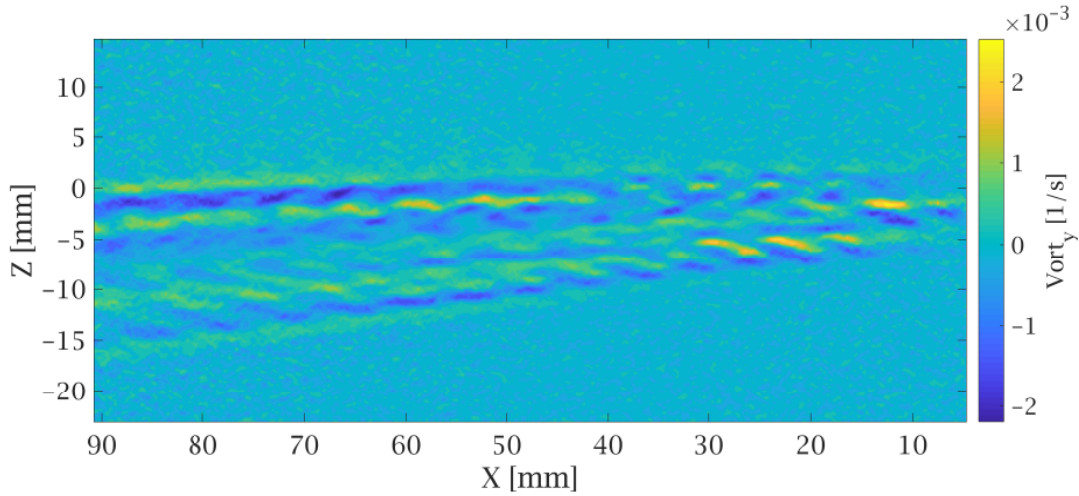


Figure 4.52: Central element: instantaneous Y -vorticity field

4.2.2 Effects of Height Variation

This section describes the effects that a variation of element height k causes on the flow features described in section 4.2.1. For this purpose, two extra elements are evaluated at the same Re_c (and freestream speed U_∞) as the main roughness element. The obtained results will be compared with the ones from the previous section, in order to identify how the change in k affects all the phenomena. The first of these two has a smaller height $k = 0.75\text{mm}$, half the thickness of the central element. As the flow condition did not change and neither did the diameter, this element is expected to present sub-critical behaviour. The tallest element is the $k = 2.1\text{mm}$, which according to table 3.4 is supposed to show super-critical characteristics.

A new type of graph will be shown, in addition to the ones already included in the previous sections. This simply consists in the extraction of metrics from the PIV fields. In order to understand how this metrics are obtained, figure 4.53 must be displayed.

This is the visual map, or simply an example of how the turbulent wedge borders are identified. After the roughness element, the quantities are extracted along lines inclined of 45° , at different distances X from the origin. For each z line, a simple equation is used in order to distinguish the inside of the wedge with the undisturbed boundary layer. Basically, given:

$$\Delta U_{norm} = \frac{\Delta U}{U_{clean}} \quad (4.5)$$

the first and the last z coordinate which satisfy equation 4.6 for each \bar{X} station are selected. These will be used as upper and lower border for the measure of W_w : the wedge z -thickness.

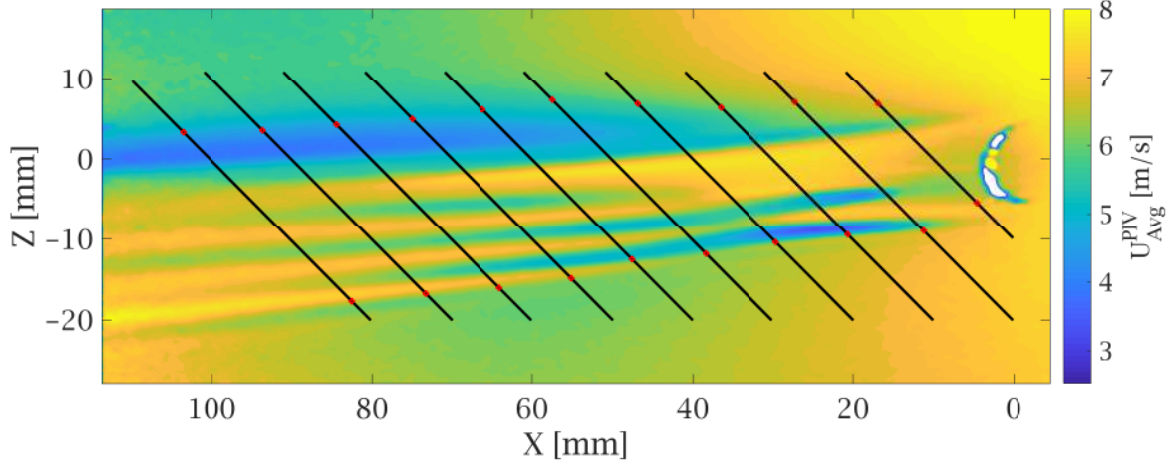


Figure 4.53: Visual map for the identification of the wedges

The metrics are extracted exclusively inside the domain of W_w .

$$|\Delta U_{norm}(z)|_{\bar{X}} > 0.15 \cdot \max |\Delta U_{norm}(z)|_{\bar{X}} \quad (4.6)$$

The two metrics are shown in equations 4.7 and 4.8. One consist in the integral of mean velocity displacement between the clean and the disturbed boundary layer. It shows how much the disturbed flow inside the wedge varies from the clean condition, and it will also be called *total velocity displacement* or simply *velocity displacement*. The second is an integration of velocity fluctuation inside the wedge. It is meant to show how the totality of the fluctuation caused by the element evolve along the wake, and it also named *total fluctuation*. Both this quantities have the size [$mm \times m/s$].

$$|\Delta U|_{TOT}(\bar{X}) = \int_W |\Delta U(\bar{X}, z)| dz \quad (4.7)$$

$$Std_{TOT}(\bar{X}) = \int_W Std(U(\bar{X}, z)) dz \quad (4.8)$$

Other than this quantities, the trend of the average value of $|\Delta U|$ and $Std(U)$ will be shown. This is obtained dividing equations 4.7 and 4.8 with the local length of the wedge W_w .

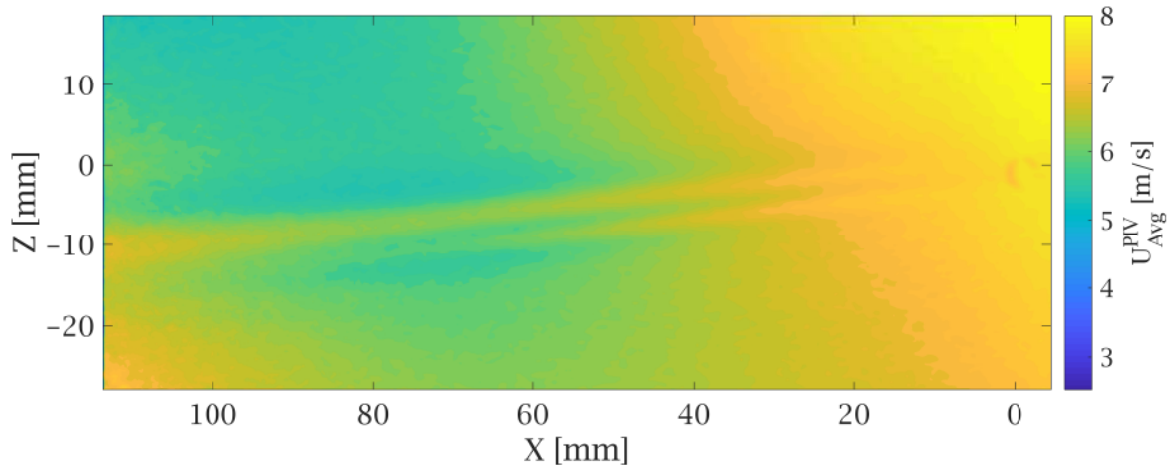


Figure 4.54: $D = 4mm$, $k = 0.75mm$: time averaged velocity field

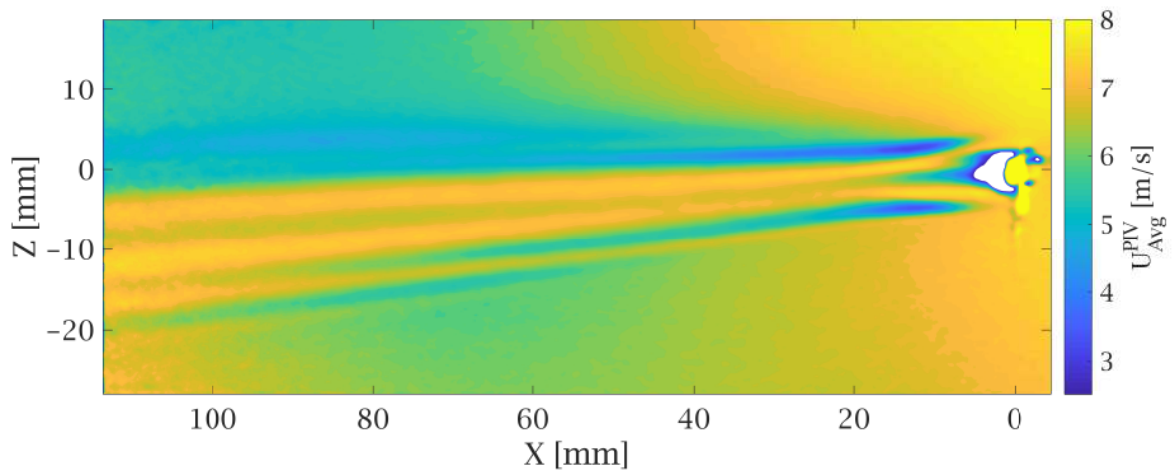


Figure 4.55: $D = 4mm$, $k = 2.1mm$: time averaged velocity field

Averaged Velocity Profile

Figures 4.54 and 4.55 show the U fields for the time-averaged velocities of $D = 4mm$ and height of $0.75mm$ and $2.1mm$, respectively. The first smaller element clearly display a sub-critical behaviour, without streaky structures developing aft the introduction of the disturbance. The sole presence of two weak high-speed streaks develop from the flanks of the element, eventually merging in a larger streak after about $X = 80mm$. The sub-critical nature of this element is even more evident in the HWA results. The wake of $k = 0.75mm$ is so weak in figure 4.56 that immediately gets dampened out in the following plane 4.59. This is

a totally different regime with respect to the one from figures 4.57 and 4.60.

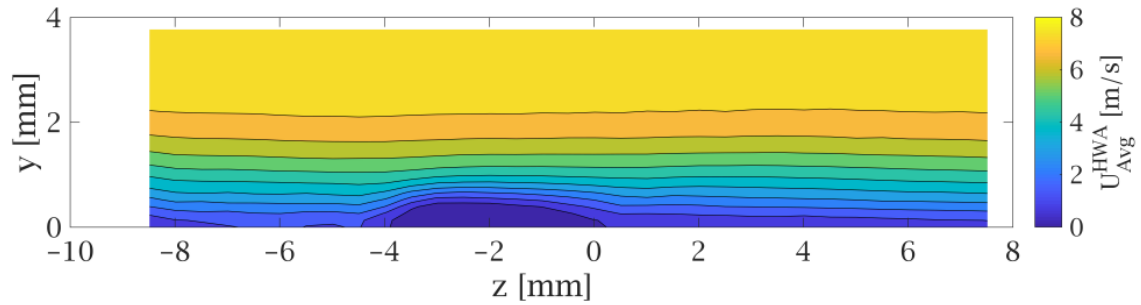


Figure 4.56: $k = 0.75mm$: zy plane of time averaged velocity at $X = 6mm$

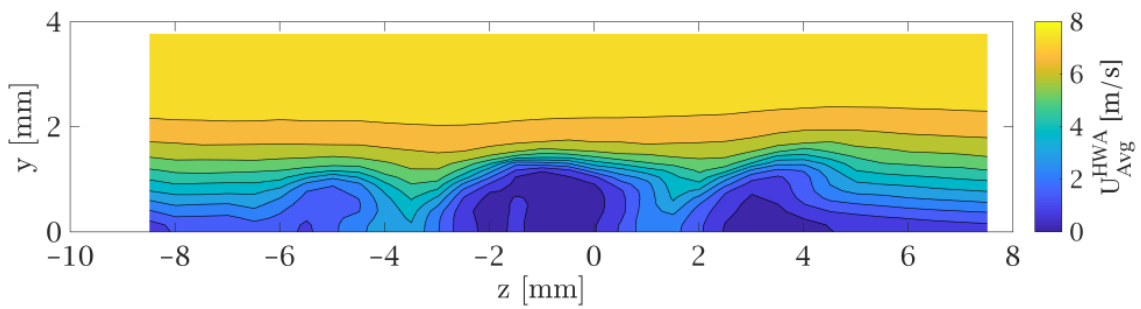


Figure 4.57: $k = 1.5mm$: zy plane of time averaged velocity at $X = 6mm$

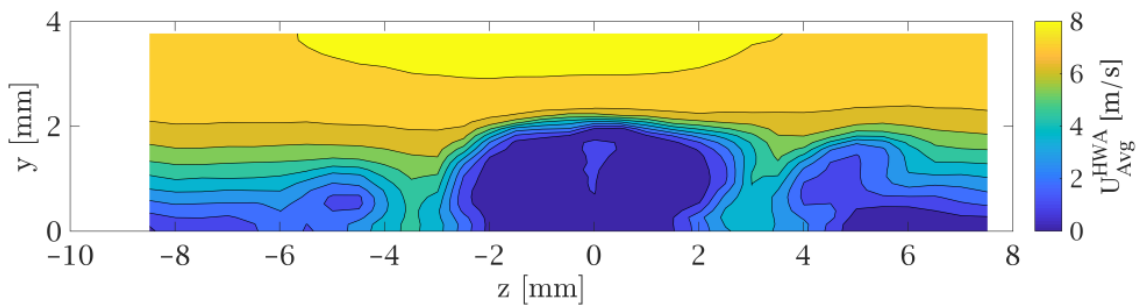


Figure 4.58: $k = 2.1mm$: zy plane of time averaged velocity at $X = 6mm$

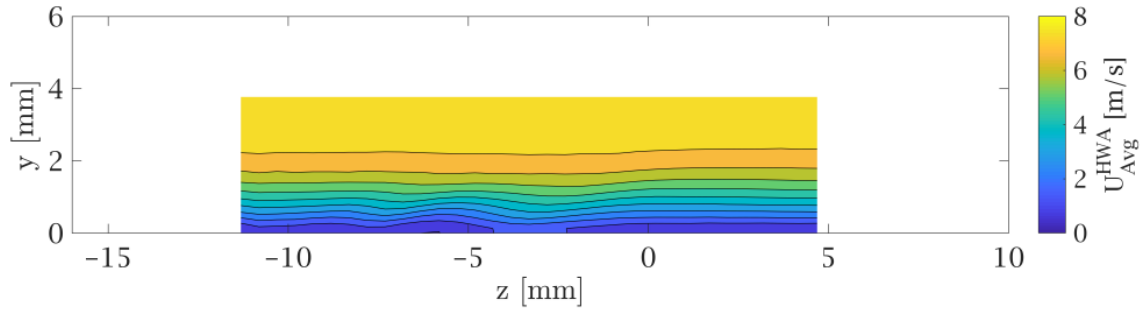


Figure 4.59: $k = 0.75\text{ mm}$: zy plane of time averaged velocity at $X = 24\text{ mm}$

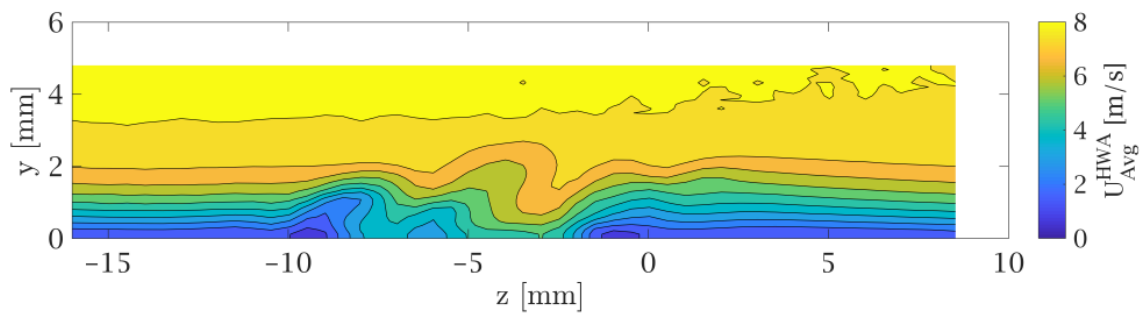


Figure 4.60: $k = 1.5\text{ mm}$: zy plane of time averaged velocity at $X = 24\text{ mm}$

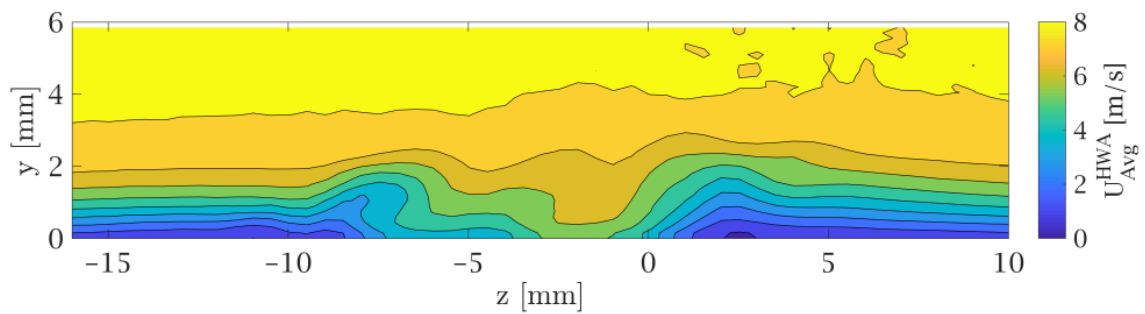


Figure 4.61: $k = 2.1\text{ mm}$: zy plane of time averaged velocity at $X = 24\text{ mm}$

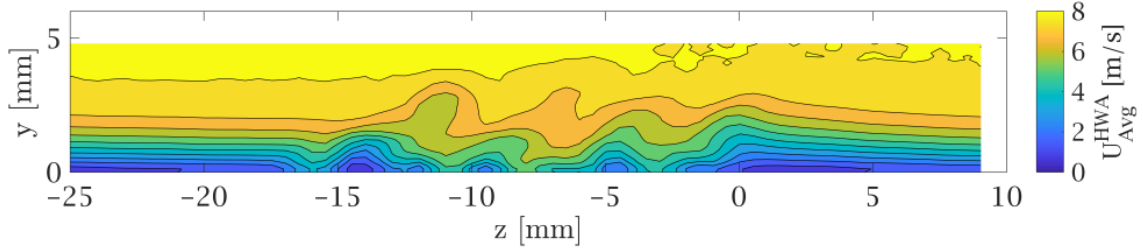


Figure 4.62: $k = 1.5mm$: zy plane of time averaged velocity at $X = 54mm$

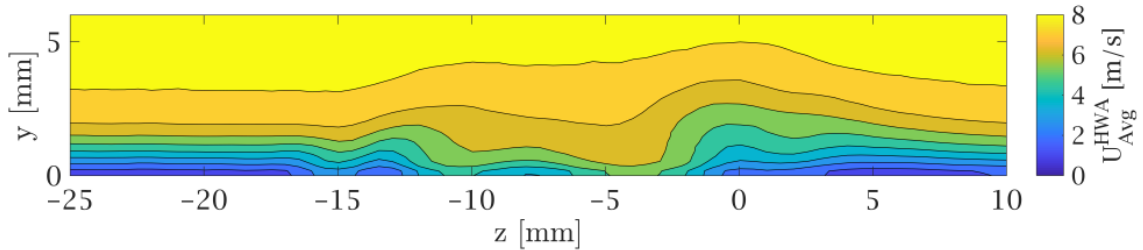


Figure 4.63: $k = 2.1mm$: zy plane of time averaged velocity at $X = 54mm$

The super-critical conditions related to the taller element are visible from figure 4.55. Once again, a different regime is displayed. The several streaks with almost the same size observed in the $k = 1.5mm$ case are substituted by only two pairs of large and well defined high- and low-speed streaks, starting immediately after the element. After that, smaller secondary streaks develop on the sides of these principals. This is visible from figures 4.61 and 4.63 other than from the PIV field. A much wider low-speed region develops in the vicinity of the element (figure 4.58), which afterwards turns into a well defined low-speed streak. The effects of the increased Re_k appears to be consistent with the results displayed by Cherubini et al. (2013) in figure 2.36: a higher k leads to stronger and better sustained streaky structures, delaying the merging of the two high speed streak and therefore the cancellation of the central low-speed zone.

Figure 4.64 and 4.65 show the evolution of the steady state metrics described in the beginning of this section. What can be immediately observed is the overall growth in velocity displacement when increasing k . This is completely expected, as the *criticality* of the element gets higher, and so does the intensity of the wake and the streaky structures. In terms of near wake, the super-critical element displays a peak at about $X = 18mm$. As the attention moves away from the low-speed region of the near wake, the function decreases and encounters a

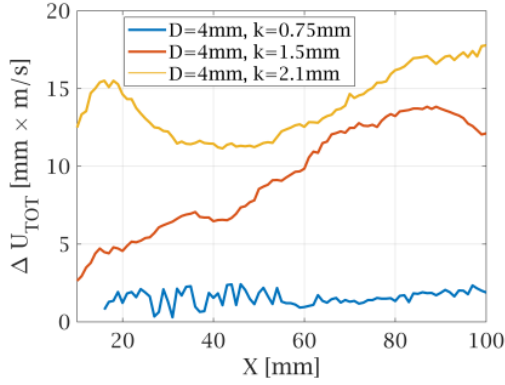


Figure 4.64: k variation: time averaged metrics

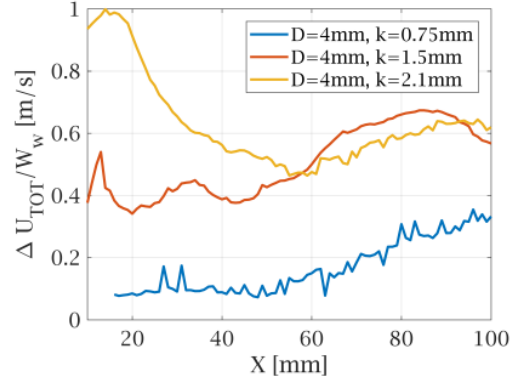


Figure 4.65: k variation: time averaged metrics (normalized)

flattening. Finally, it reaches new maximum after a second growth. The $k = 1.5mm$ element has a more monotonic increase, with the occurrence of a small bump at $X = 34mm$, in correspondence to the region where the streaky secondary structures start developing. Finally, after the maximum at $X = 88mm$, a slow decrease is mainly caused by the loss of intensity of the lowest-speed streak (visible in the top-left side of the PIV measure). The comparison between these two plots lead to a final interesting observation. Whilst the division by W_w does not change the proportions between $k = 1.5mm$ and $k = 2.1mm$ before $X = 50mm$, the same cannot be said for far wake. The two quantities reach a comparable magnitude throughout the whole final section of the plot, suggesting two different scenarios. The velocity displacement of the $k = 1.5mm$ case has the intensity of its ΔU streaks as the dominant mechanism for the growth of $|\Delta U|_{TOT}$. On the other hand, the increase in wedge width has a strong influence for the same quantity in the $k = 2.1mm$ condition, explaining the reason behind their similarity at high values of X .

Velocity Fluctuation Field

A similar comparison can be carried out with the velocity fluctuation fields 4.68 and 4.69. The low presence of fluctuations and the sub-critical conditions are evident in figure 4.68, as well as in figure 4.70, where the maximum level displayed is one order of magnitude lower than the other HWA figures. An interesting consideration may come from the observation of figures 4.72 and 4.74 and can be supported by the results from the time averaged PIV velocity field. In fact, the different regime observed for $k = 2.1mm$ also entails a lack of streaky behaviour. Three main zones of high fluctuations occur in proximity of the element (figure 4.69), where the intensity reaches the maximum in the whole field. After that, the distribution of fluctuations seems to spread uniformly in the XZ plane, with the exception of two lines running along the two main streaks of the time averaged field. Moreover, at $X = 54mm$ the shape of the fluctuation blob (4.74) starts assuming a shape similar to the right hand side of figure 4.36. The fluctuations start their zy uniform spreading much earlier than $k = 1.5mm$, suggesting an anticipated transition.

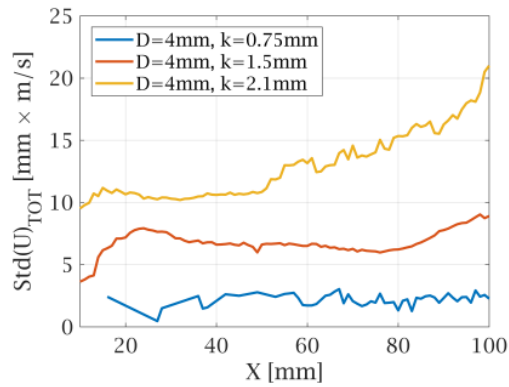


Figure 4.66: k variation: fluctuation metrics

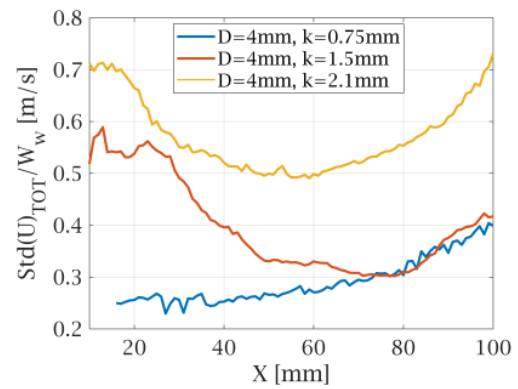


Figure 4.67: k variation: fluctuation metrics (normalized)

Figures 4.66 and 4.67 display the metrics related to the velocity fluctuations. Once again, a taller element leads to stronger fluctuation fields throughout the whole evolution of the wake. Hence, a *more turbulent* condition is linked to stronger fluctuations, as expected. The most interesting characteristic to point out is the presence of the peaks in the vicinity of the element for the figure 4.67. This might be related to the presence of strong concentration of fluctuations, due to a strongly unstable shear layer only for the quasi- and super-critical elements.

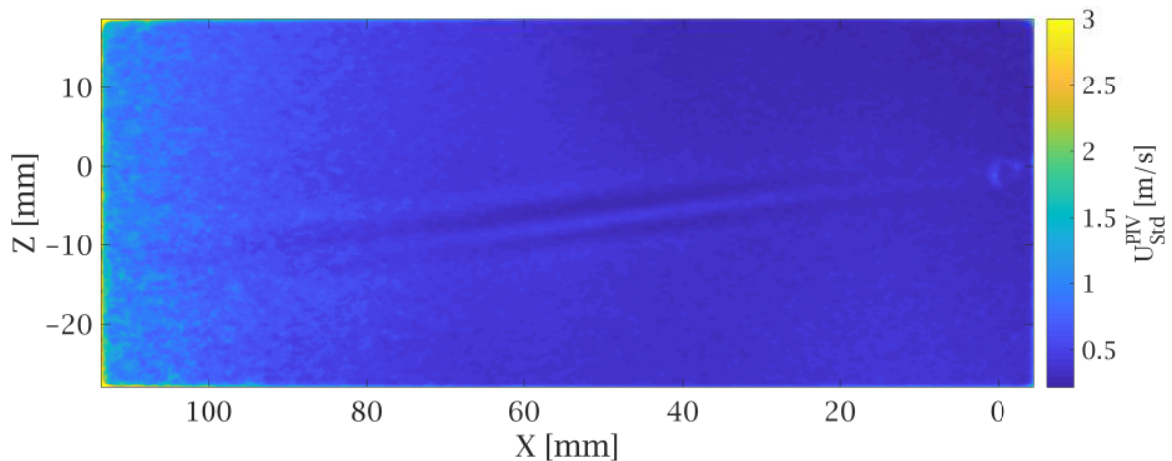


Figure 4.68: $D = 4\text{mm}$, $k = 0.75\text{mm}$: velocity fluctuations field.

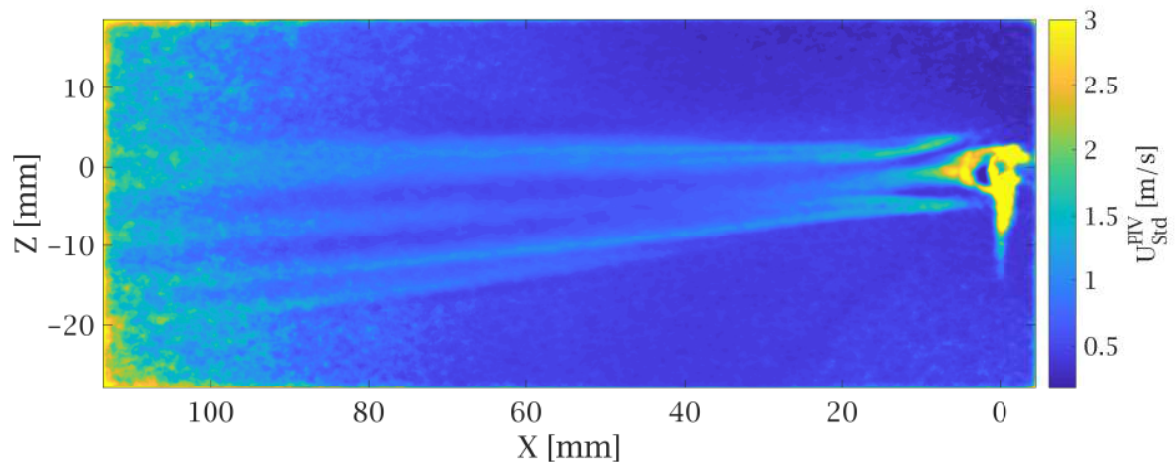


Figure 4.69: $D = 4mm$, $k = 2.1mm$: velocity fluctuations field.

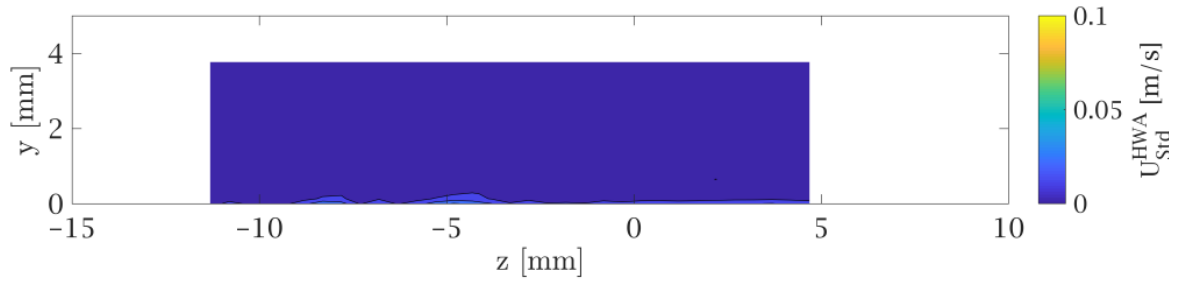


Figure 4.70: $k = 0.75\text{mm}$: zy plane of velocity fluctuations at $X = 24\text{mm}$

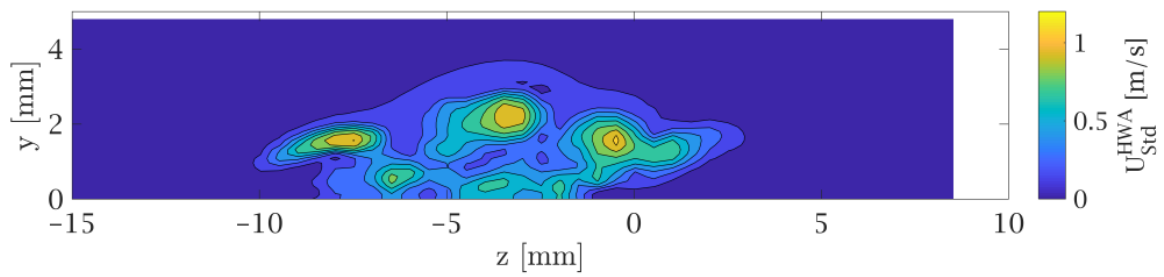


Figure 4.71: $k = 1.5\text{mm}$: zy plane of velocity fluctuations at $X = 24\text{mm}$

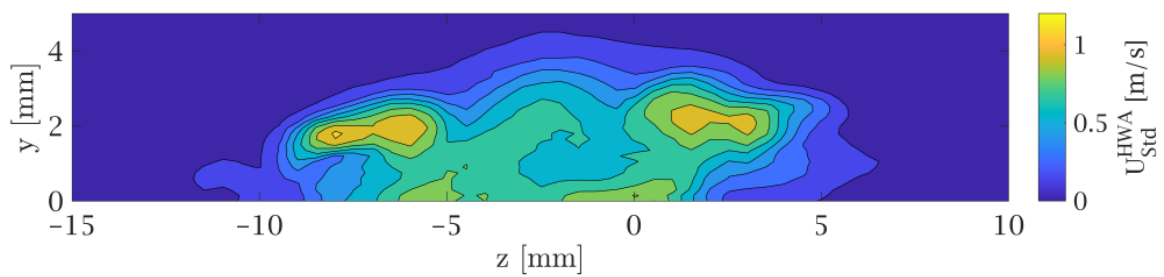


Figure 4.72: $k = 2.1\text{mm}$: zy plane of velocity fluctuations at $X = 24\text{mm}$

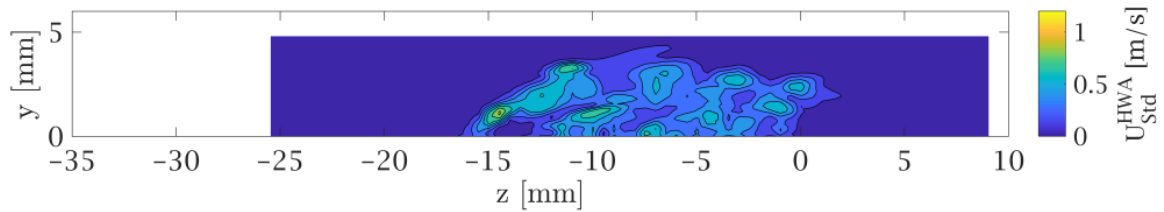


Figure 4.73: $k = 1.5mm$: zy plane of velocity fluctuations at $X = 54mm$

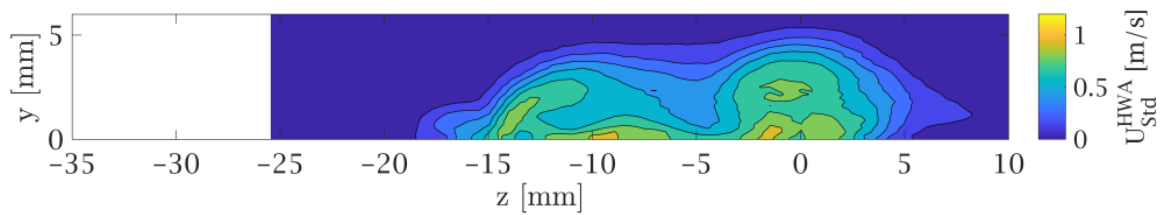


Figure 4.74: $k = 2.1mm$: zy plane of velocity fluctuations at $X = 54mm$

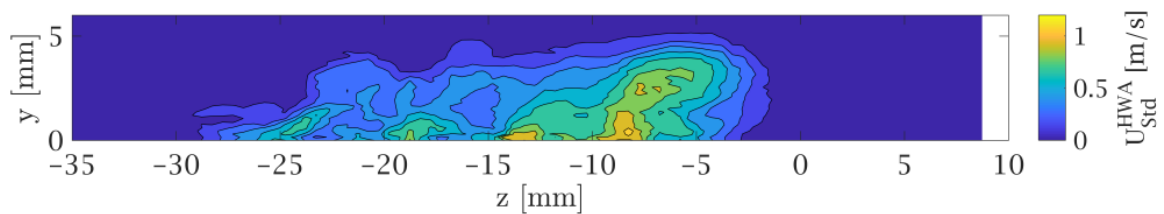


Figure 4.75: $k = 1.5mm$: zy plane of velocity fluctuations at $X = 114mm$

Frequency Analysis

Figure 4.76 show the frequency spectra related to $k = 2.1mm$, to be compared to figure 4.38 (from section 4.2.1). The tonal behaviour is still affecting the flow, with the characteristic

quantities corresponding to:

$$f = 801Hz \quad (4.9)$$

$$Str_{\delta^*} = 0.1112 \quad (4.10)$$

$$Str_k = 0.2389 \quad (4.11)$$

$$\lambda = 7.33mm \quad (4.12)$$

It must be noticed that all these quantities are obtained with the extraction of information along $y = \delta_{0.99}/2$, as explained previously.

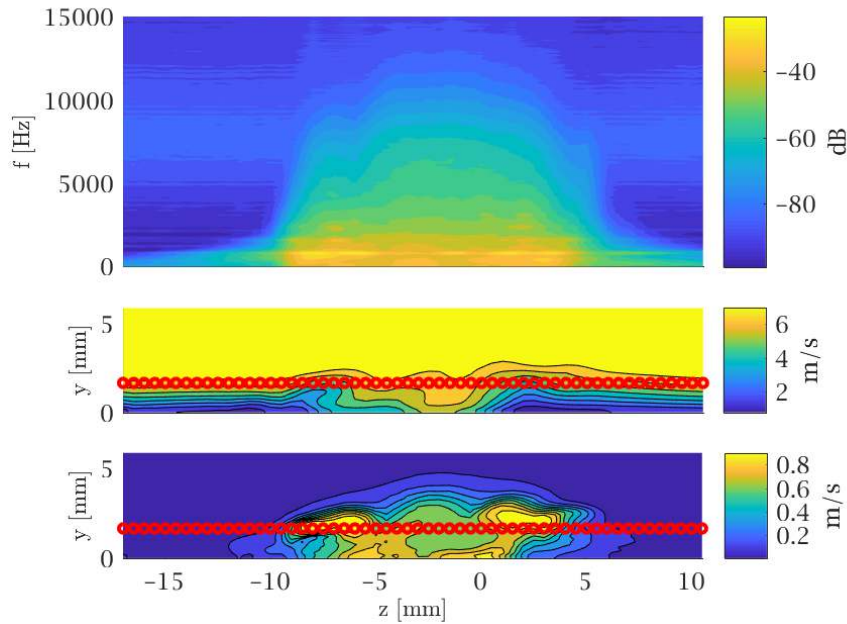


Figure 4.76: $D = 4mm$ and $k = 2.1mm$. $X = 24mm$: frequency spectra along $y = \delta_{0.99}/2$

Nevertheless, the earlier transition is eventually confirmed by the frequency analysis, as hinted by the shape of the fluctuation region in last paragraph. Figure 4.76 indicates a wedge almost totally dominated by turbulent spectra, extremely similar to what was observed at $X = 114mm$ for the $k = 1.5mm$ case (figure 4.43).

Analysis of the POD Modes

The analysis of the POD modes merely consist in evaluating figure 4.77, which shows the most dominant mode for the tall element condition. By comparing it with figure 4.49, the similar size of the structures is clear ($\lambda \approx 7.5mm$), as well as the concentration in the near wake of the element. The eigenmode is in the vicinity of the roughness cylinder, suggesting the presence of coherent structures and modal fluctuations exclusively before a totally turbulent wedge has developed.

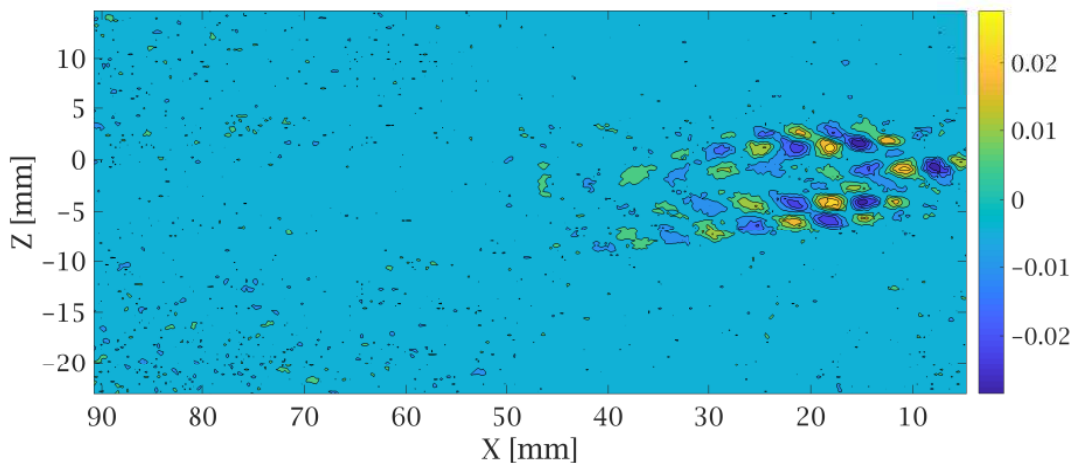


Figure 4.77: $D = 4mm, k = 2.1mm$: U component, POD mode 1

4.2.3 Effects of Freestream Velocity Variation

Just like in section 4.2.2, the effects of a different freestream velocity are investigated. The tested element is the central roughness cylinder, i.e. $D = 4mm, k = 1.5mm$. However, it was tested under the effects of 6 m/s and 12 m/s freestream speed, and the results are evaluated. It must be noticed that these scenarios are not provided with the same amount of results, as lacking of some measurement techniques used for the previous cases. The two investigated cases are expected to be placed in sub- and super-critical conditions, respectively. However, it must be pointed out that the $U_\infty = 6m/s$ condition lies exactly on the limit between the sub-critical area and the quasi-critical. In fact, a graphical observation of figure 2.35 would even identify it as quasi-critical.

Averaged Velocity Profile

By comparing figures 4.78 and 4.79 with figure 4.10, one can identify three different regimes of transition. Furthermore, some aspects are similar to section 4.2.2, suggesting analogies between the k and the U_∞ effects. Figure 4.78 depicts a similar scenario to the one from figure 4.54, with two high speed streaks slowly merging and the absence of secondary streaks. This result shows the sub-critical nature of the phenomenon. Nevertheless, table 3.4 predicts a

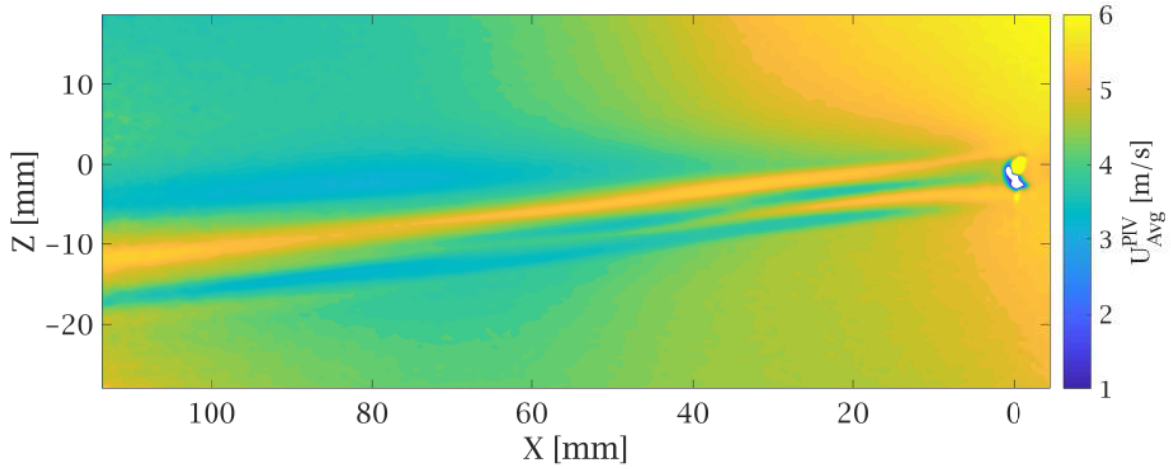


Figure 4.78: Central element at $U_\infty = 6\text{m/s}$: time averaged velocity field

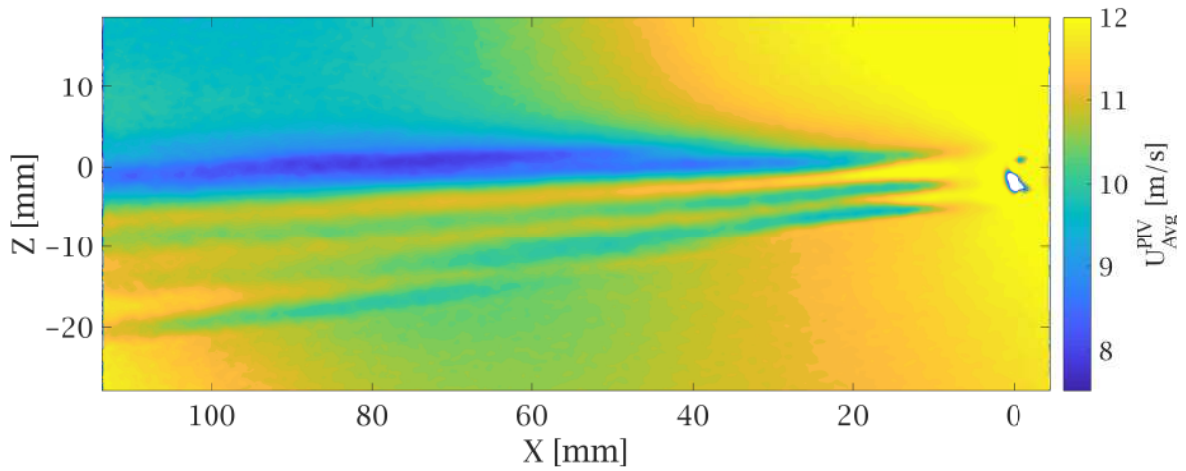


Figure 4.79: Central element at $U_\infty = 12\text{m/s}$: time averaged velocity field

condition that is closer to the quasi-critical state than $k = 0.75\text{mm}$, $D = 4\text{mm}$, $U_\infty = 8\text{m/s}$ is. This is totally confirmed, not only by the PIV contours, but also by figures 4.80 and 4.81. The latter show the presence of a bump in correspondence of the near wake, that was not observed in the $k = 0.75\text{mm}$, $D = 4\text{mm}$, $U_\infty = 8\text{m/s}$ case, and higher values of velocity displacement throughout the whole field. To conclude the analysis of the sub-critical condition, figure 2.27 from [Loiseau et al. \(2014\)](#) confirms that a lower freestream velocity is linked to a shorter central low-speed region. This appears to be confirmed by the comparison of figures 4.78 and 4.10, with the latter having the two high speed streaks merging at about $X = 65\text{mm}$ and $Z = -10\text{mm}$. On the other hand, the sub-critical case sees the low-speed

area fading away due to the disappearing of one of the two high speed streaks at about $X = 50\text{mm}$, $Z = -10\text{mm}$. Hence, the concepts of Loiseau et al. (2014) are confirmed by these results, but with a totally different dampening phenomena. The weakening of one high speed streak was not contemplated in Loiseau et al. (2014). This underline the complexity of the physics involved, linked to the three-dimensional boundary layer.

The super-critical scenario for an increased speed was expected to be even more critical than $k = 2.1\text{mm}$, according to the values of Re_k in table 3.4. This is not what can be deduced from figures 4.79 and 4.80. The case is still displaying some characteristics of the previous super-critical case: large streaks, a long lasting low-speed region in agreement with figure 2.27, and a large and intense low-speed region in the far wake and the right hand side of the wedge. However, qualitatively observing the turbulent wedge, it appears similar to an expanded version of figure 4.10, rather than a scenario comparable to the $k = 2.1\text{mm}$ case shown in section 4.2.2. In fact, the near wake region is the one with strong differences. Figure 4.55 shows a low-speed zone that develops right after the element and two large and intense low-speed streaks starting at 1 diameter distance from the roughness. These features are not present in the super-critical case related to $U_\infty = 12\text{m/s}$. This does not mean that $k = 1.5\text{mm}$, $D = 4\text{mm}$, $U_\infty = 12\text{m/s}$ is not a super-critical type of scenario, as predicted by the parameters from table 3.4. However, the results from this section seem to suggest that only part of the "full story" can be predicted with Re_k estimation. In other words, the use of Re_k and its estimated critical value works well for an approximate identification of the criticality. On the other hand, two elements being in the same transitional regime might present totally different physical phenomena. Hence, this suggests that other important parameters should be taken into account when working on the prediction of isolated roughness induced transition. For instance, $k = 1.5\text{mm}$, $D = 4\text{mm}$, $U_\infty = 12\text{m/s}$ is characterized by a ratio $k/\delta_* = 1.88$, which is almost exactly the mean value between 2.15 (measured for $k = 2.1\text{mm}$, $D = 4\text{mm}$ and $U_\infty = 8\text{m/s}$) and 1.53 (measured for $k = 1.5\text{mm}$, $D = 4\text{mm}$ and $U_\infty = 8\text{m/s}$). This could have been a relevant clue for predicting this scenario to have common characteristics with both the previous cases.

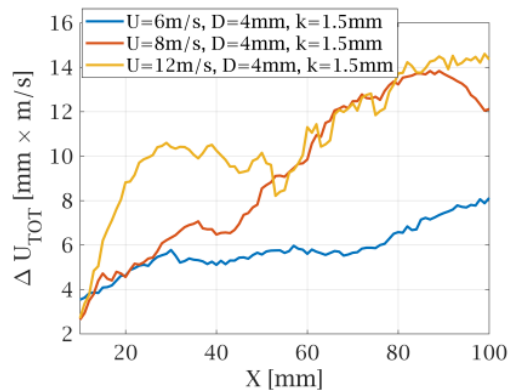


Figure 4.80: U variation: fluctuation metrics

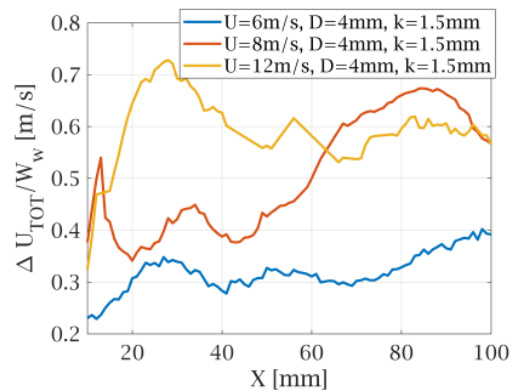


Figure 4.81: U variation: fluctuation metrics (normalized)

Velocity Fluctuation Field

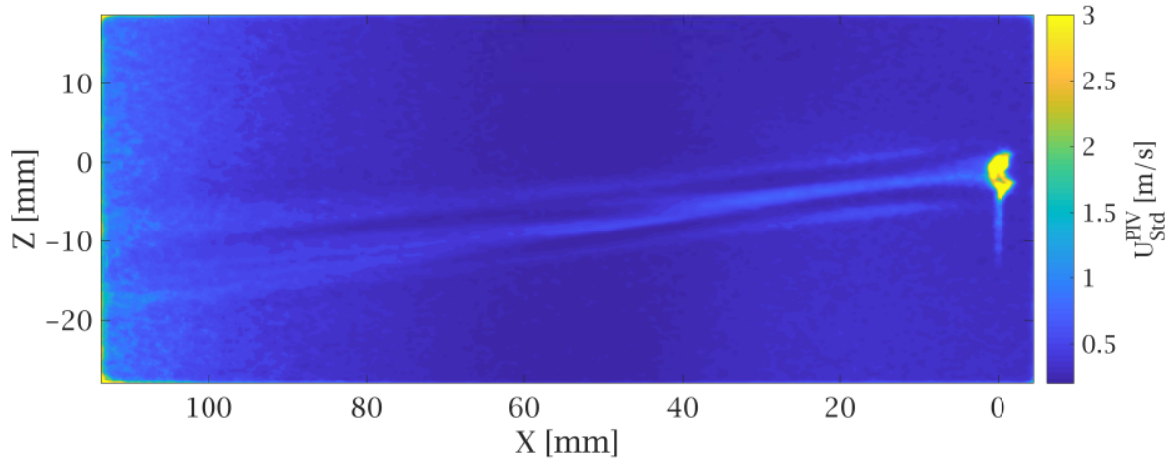


Figure 4.82: Central element at $U_\infty = 6\text{m/s}$: velocity fluctuations field

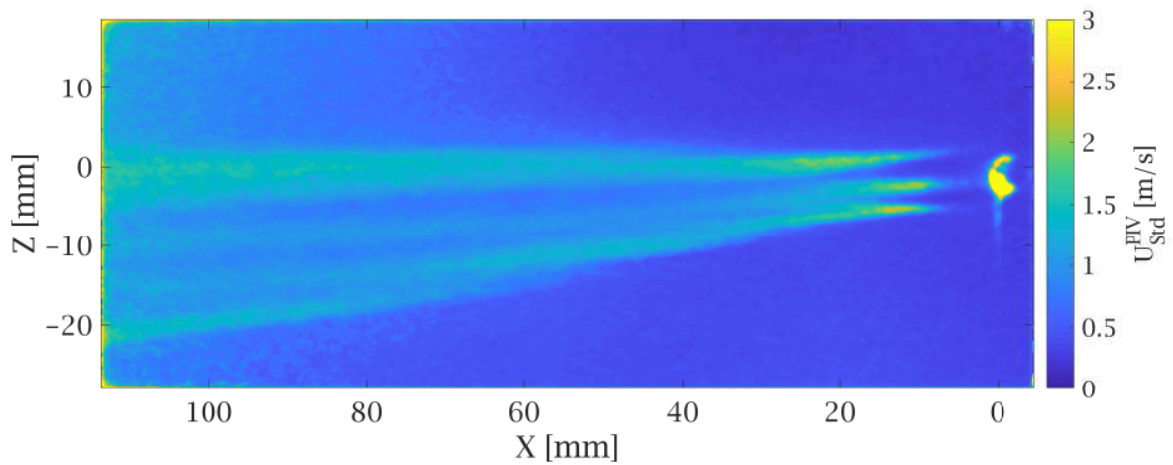


Figure 4.83: Central element at $U_\infty = 12\text{m/s}$: velocity fluctuations field

The fluctuation fields are shown in figures 4.82 and 4.83. Once again, figure 4.82 shows characteristics that could easily be linked to the $k = 0.75\text{mm}$ case. Low intensity in the fluctuations is observed throughout the whole field, with the strongest area concentrated along the central low-speed streak.

Just as the time averaged results, the fluctuation fields of the super-critical roughness has common characteristics both with $k = 1.5mm$, $D = 4mm$, $U_\infty = 8m/s$ and with $k = 2.1mm$, $D = 4mm$, $U_\infty = 8m/s$. This is very interesting, as its qualitative behaviour seems to be a compromise between the two phenomena, just like for the time-averaged velocity analysis. Three strong fluctuation cones generates aft the element, at about 1 diameter distance from the cylinder. Their shape and position does not differ from the quasi-critical condition of the the central element. Nevertheless, the growth and development of these high-fluctuation regions resemble the one observed for $k = 2.1mm$ in section 4.2.2. In fact, they do not display the streaky behaviour of $k = 1.5mm$, $D = 4mm$, neither the generation of secondary and tertiary streaks. Contrarily, these cones expand in space in a uniform distribution, with their two high-fluctuation lines running on the sides of the wedge. This type of behaviour has already been observed for $k = 2.1mm$, $D = 4mm$, $U = 8m/s$.

Analysis of the POD Modes

As for the study of the POD modes, another attempt is made to compare the super-critical case related to a high velocity (4.85) and the one due to a high k . The position and the distribution of this eigenmode is totally different with respect to the one of figure 4.77. These structures seem to concentrate only along the co-rotating horseshoe vortex, not in the whole shedding area as for the other case. On the other hand, the common point between them is the fact that they only develop downstream for a short distance, indicating the absence of coherent structures after $X = 50mm$. This might suggest that after the occurrence of transition, both cases loose the spatial coherency. Finally, what is interesting to notice is that the change in Reynolds does not seem to affect the wavelength of the reconstructed POD modes, as it keeps being comparable to the previous cases. The same can be said for figure 4.84, relative to 6 m/s as freestream speed. Here, the interesting note to point out is the similitude of this modal reconstruction to figures 2.55 and 2.49. Just like figure 4.85, it runs along a single HS vortex, but differently from the other case it only has a single row of elements and not a "double bubbled-line".

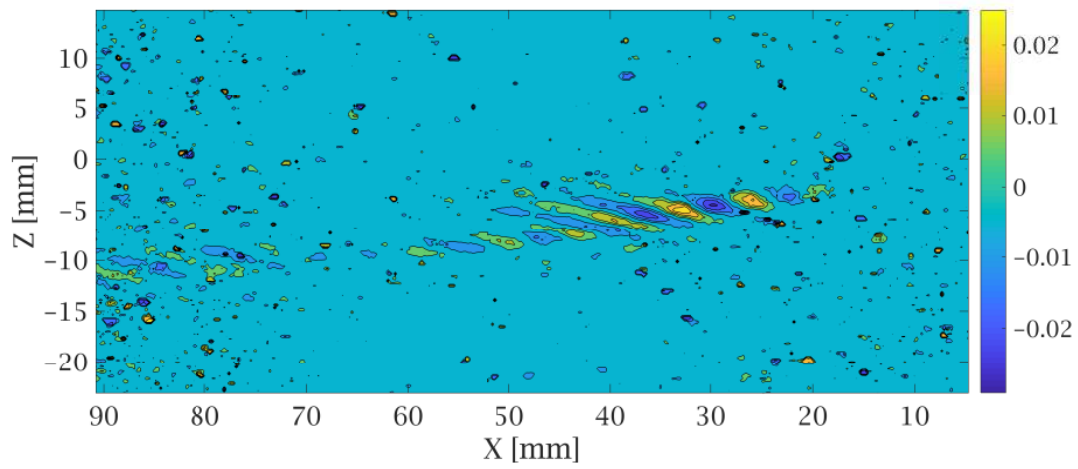


Figure 4.84: Central element at $U_\infty = 6 \text{ m/s}$: U POD mode 1

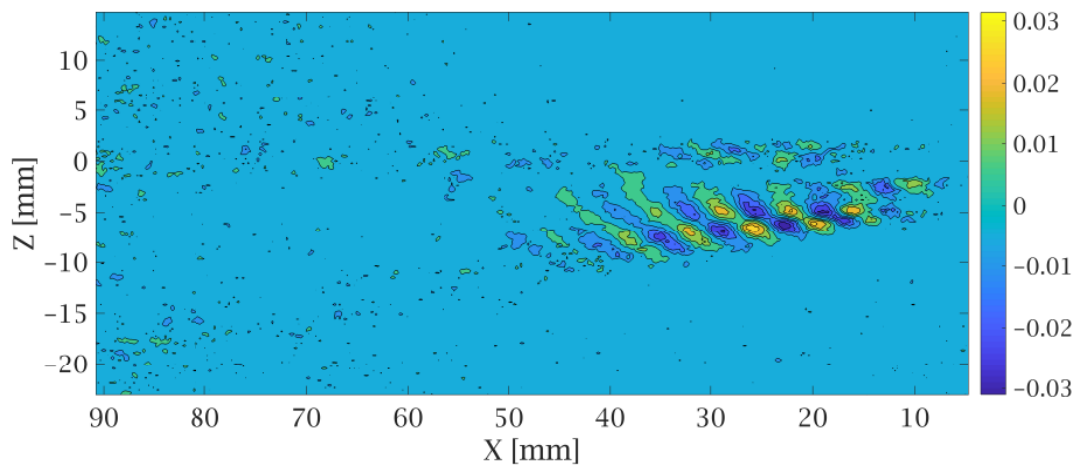


Figure 4.85: Central element at $U_\infty = 12 \text{ m/s}$: U POD mode 1

4.2.4 Effects of Diameter Variation

In this section, a variation of diameter is applied to the main central element, keeping the thickness and the freestream Reynolds number unchanged. Before the beginning of the analysis, considerations regarding table 3.4 are recalled. The $D = 2.5\text{mm}$ case is expected to be in a quasi-critical range, possibly in a less turbulent condition than the central element. The large diameter is predicted as a super-critical type of instability generator. The results are going to be compared with data from Cherubini et al. (2013) and Loiseau et al. (2014), both in terms of velocity distribution and analysis of the POD modes.

Averaged Velocity Profile

Figures 4.86 and 4.87 are suitable for analyzing the effects of different diameters on the time averaged velocity field, when compared to the main element. Figure 4.86 shows that when the diameter is decreased, the low-speed streak along the center of the wedge considerably decreases in length, with the two high-speed streaks merging already at about $10D$ distance from the element. This is backed-up by figure 2.29, where the larger cylinder generates a longer central streak. Once again, the complexity of the three-dimensional boundary layer makes the results display peculiar characteristics. Two high speed streaks develop soon after the merging of the originals, and are totally uneven in terms of intensity and size. This is emblematic of how the three-dimensionality changes the expected results: even when they appear to match the expectations, they do it with slight changes in phenomenology. Furthermore, the strong low-speed streak starts slowly appearing at $X = 20\text{mm}$ but never goes lower than 4 m/s . The same type of streak develops at about $X = 50\text{mm}$ for the central element.

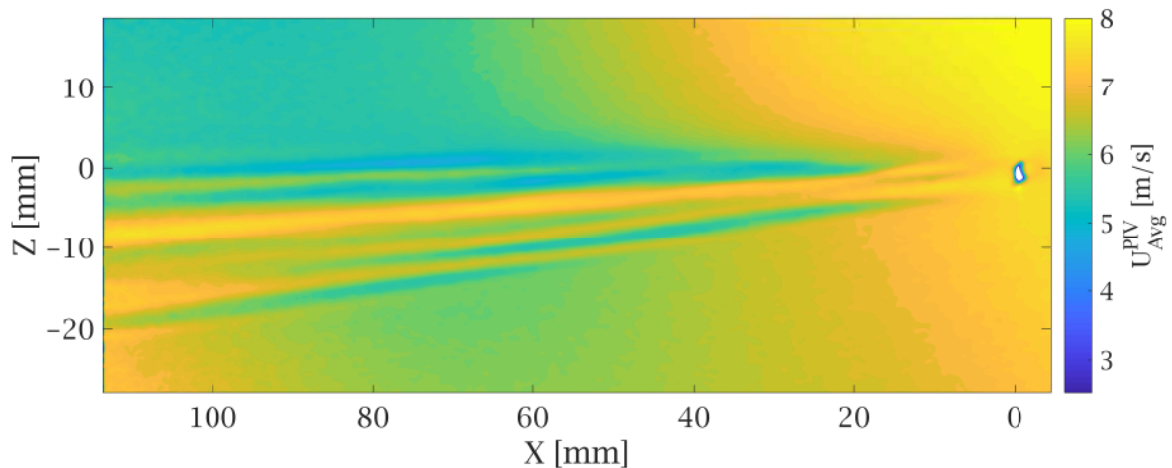


Figure 4.86: $D = 2.5\text{mm}$: time averaged velocity field

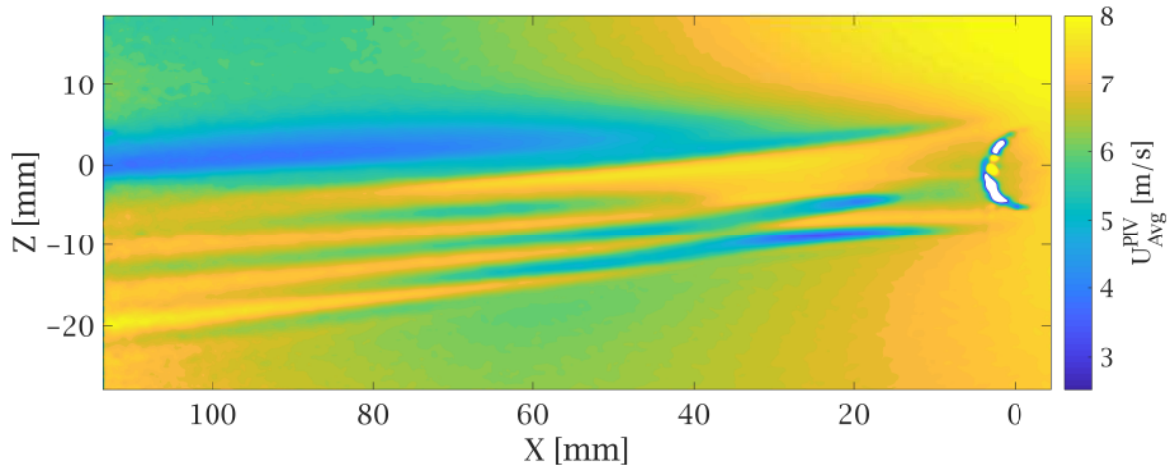


Figure 4.87: $D = 10\text{mm}$: time averaged velocity field

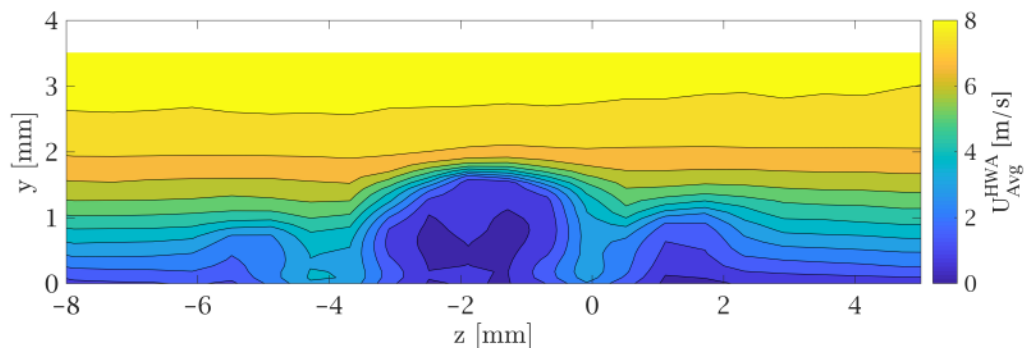


Figure 4.88: $D = 2.5\text{mm}$: zy plane of time averaged velocity at $X = 6\text{mm}$

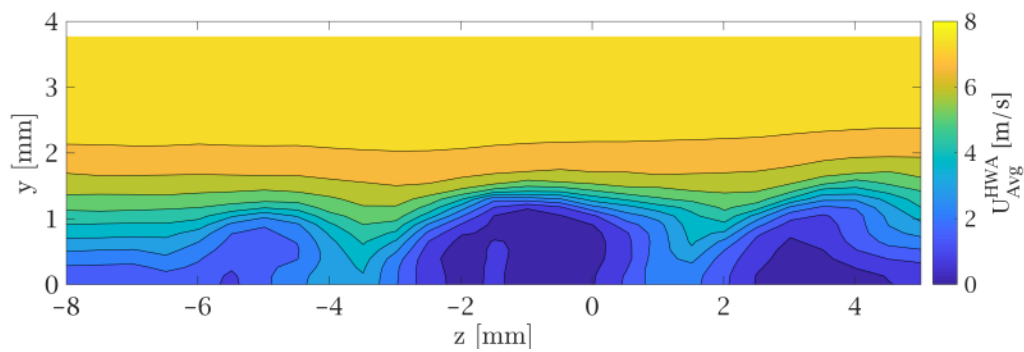


Figure 4.89: $D = 4\text{mm}$: zy plane of time averaged velocity at $X = 6\text{mm}$

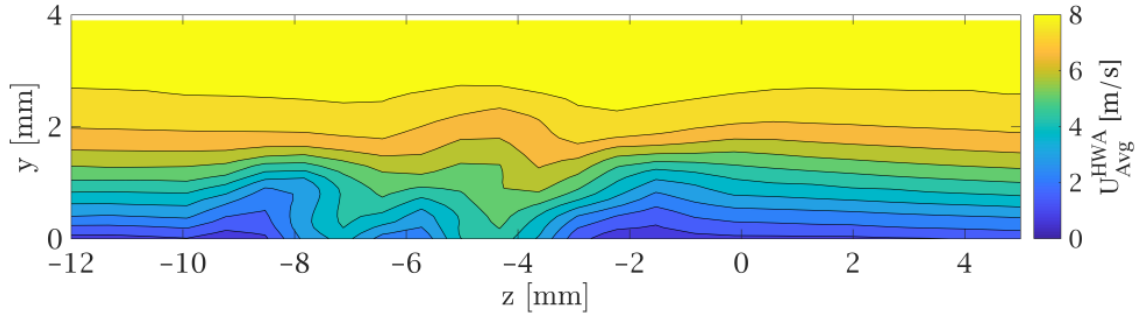


Figure 4.90: $D = 2.5mm$: zy plane of time averaged velocity at $X = 24mm$

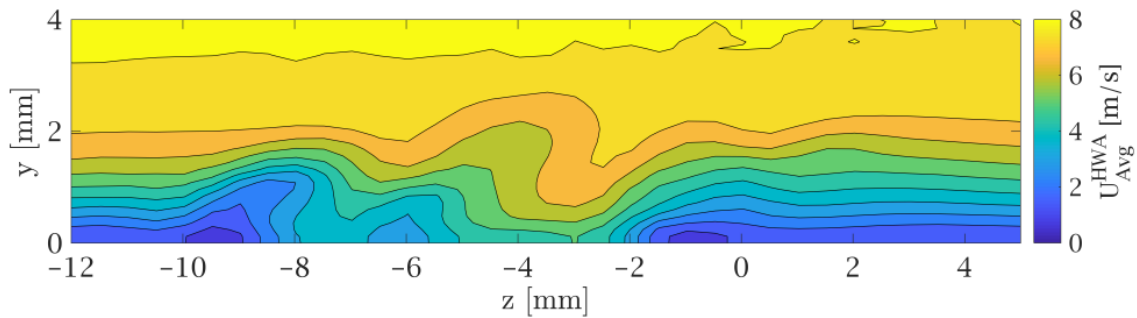


Figure 4.91: $D = 4mm$: zy plane of time averaged velocity at $X = 24mm$

Figures from 4.88 to 4.93 underline the similarities between the two quasi-critical scenarios. Especially for the first plane (figures 4.88 and 4.89), the near wake behaviour is qualitatively very similar, with variations in sizes mainly for the central low-speed region. Differences with regards to size, shape and intensity start developing at $X = 24mm$, where the $D = 4mm$ case shows a much more complex distribution. An extra hollow (high speed region) appears at $z = 0mm$ $y = 2.5mm$, developing into two low-speed bumps further downstream (4.91). In a different position, figure 4.90 sees a similar phenomenon happening at $z = -2.5mm$ $y = 1mm$. Finally, $X = 54mm$ underlines the difference between the two streaky structures, with a much larger number of peaks and hollows, for the case $D = 4mm$. Next to the main large low-speed peaks, new smaller velocity oscillations appear at low y , whereas the same is not observed for the smaller diameter.

As for the $D = 10mm$ condition, considerable differences are observed in the qualitative behaviour of the turbulent wedge. In the vicinity of the cylinder, the central low-speed region (shown at $X = 12mm$, figure 4.94) assumes the width of the element itself, being comparable in size. Furthermore, in the PIV image, the streaks are well defined and tend not to merge and disappear in their downstream evolution. This translates in the presence of few and well defined oscillations in the hot wire anemometry planes (figures from 4.95 to 4.98). The

presence of the small extra bumps identified for $D = 4\text{mm}$ is not shared with this scenario. Moreover, the PIV result shows a large high-speed streak generating right after the cylinder, which in the HWA correspond to the high-speed region entering deep down the inner part of the BL. This large region is visible at $z = 0\text{mm}$ for $X = 24\text{mm}$, and moves towards negative values of z as the flow evolves downstream.

Just like all the super-critical cases investigated so far, the steady state metric 4.99 shows higher values throughout the whole wake. The typical early bump is also observed, and no unexpected result appears. Furthermore, this plot contributes in showing the similarities between the two quasi-critical cases. Up to $X = 45\text{mm}$, the two plots displays comparable values, with a perfect matching between $X = 24\text{mm}$ and $X = 45\text{mm}$. In the second half of the graphs, the plot referring to main element encounters a steeper increase and overall higher displacement in velocity. This is expected due to the stronger disturbances introduced by the larger element.

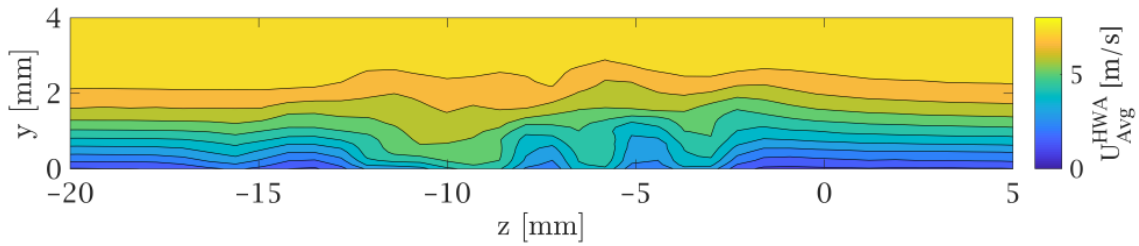


Figure 4.92: $D = 2.5\text{mm}$: zy plane of time averaged velocity at $X = 54\text{mm}$

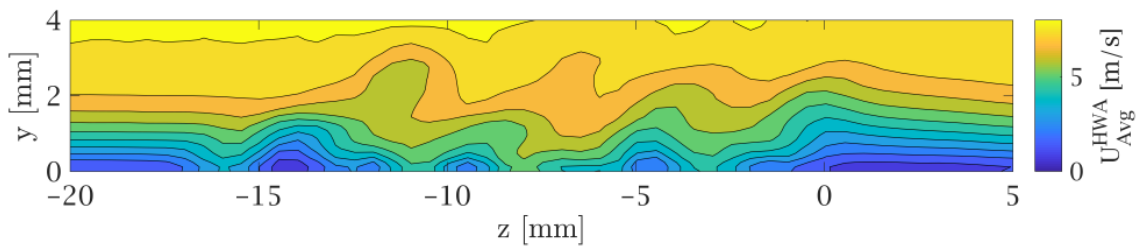


Figure 4.93: $D = 4\text{mm}$: zy plane of time averaged velocity at $X = 54\text{mm}$

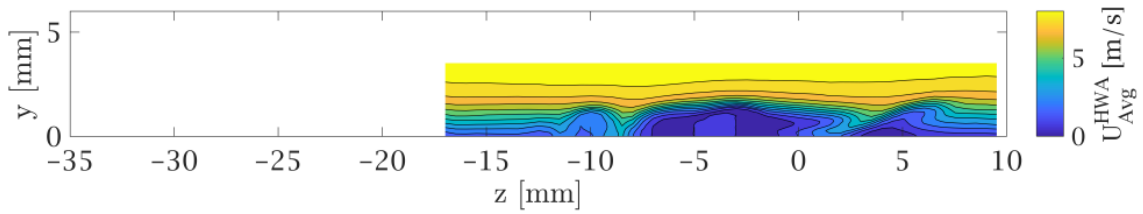


Figure 4.94: $D = 10\text{mm}$: zy plane of time averaged velocity at $X = 12\text{mm}$

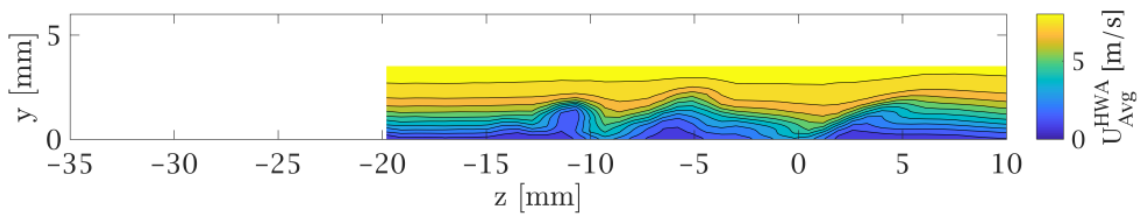


Figure 4.95: $D = 10\text{mm}$: zy plane of time averaged velocity at $X = 24\text{mm}$

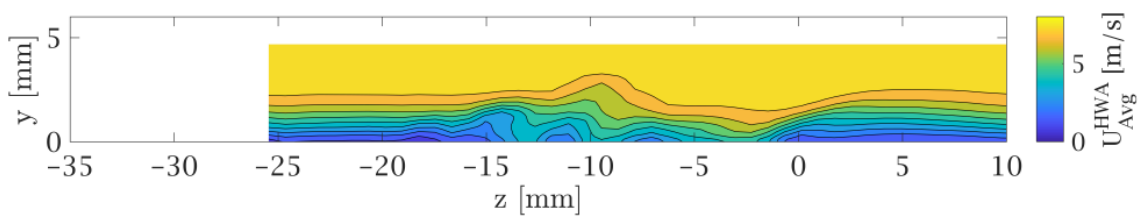


Figure 4.96: $D = 10\text{mm}$: zy plane of time averaged velocity at $X = 42\text{mm}$

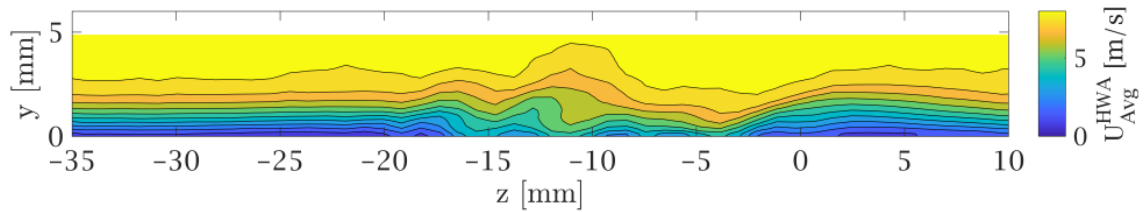


Figure 4.97: $D = 10\text{mm}$: zy plane of time averaged velocity at $X = 54\text{mm}$

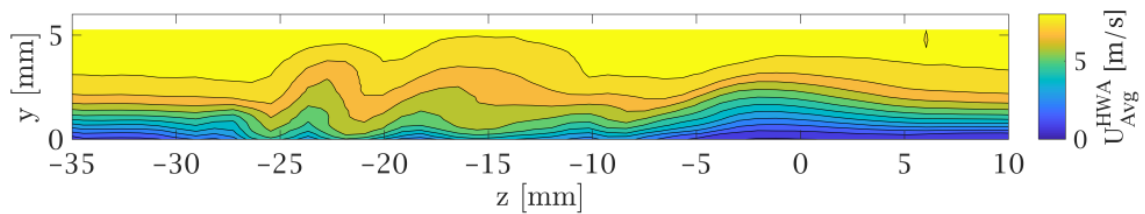


Figure 4.98: $D = 10\text{mm}$: zy plane of time averaged velocity at $X = 90\text{mm}$

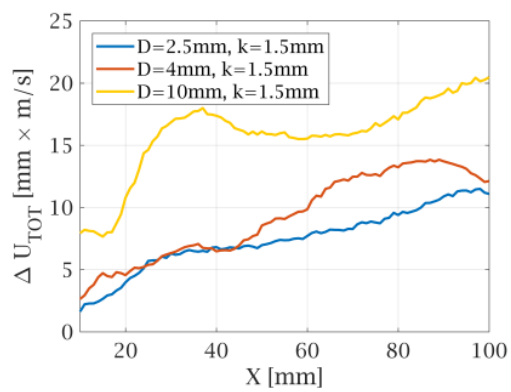


Figure 4.99: D variation: velocity displacement metrics

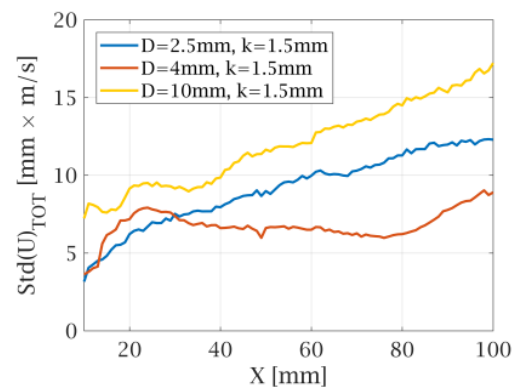


Figure 4.100: D variation: fluctuation metrics

Velocity Fluctuation Field

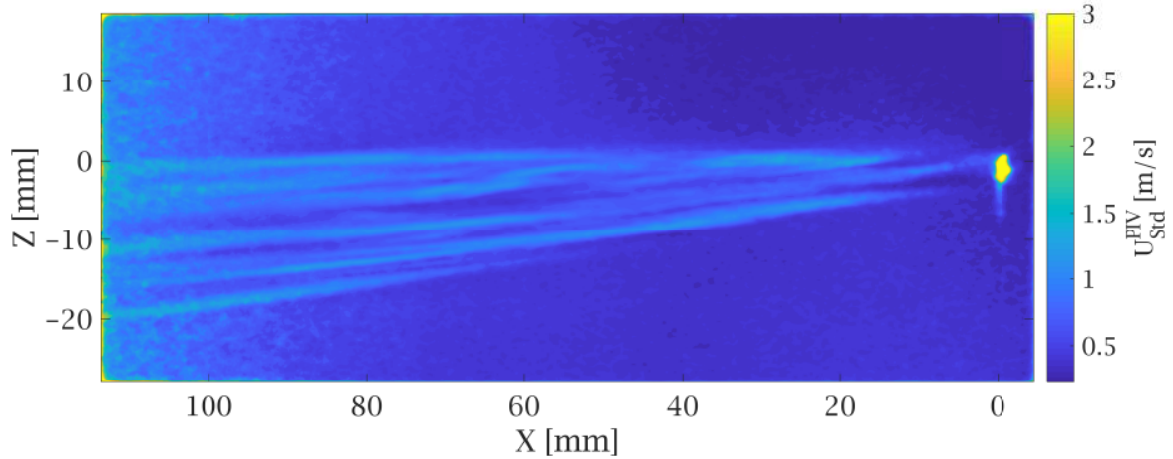


Figure 4.101: $D = 2.5mm$: velocity fluctuations field

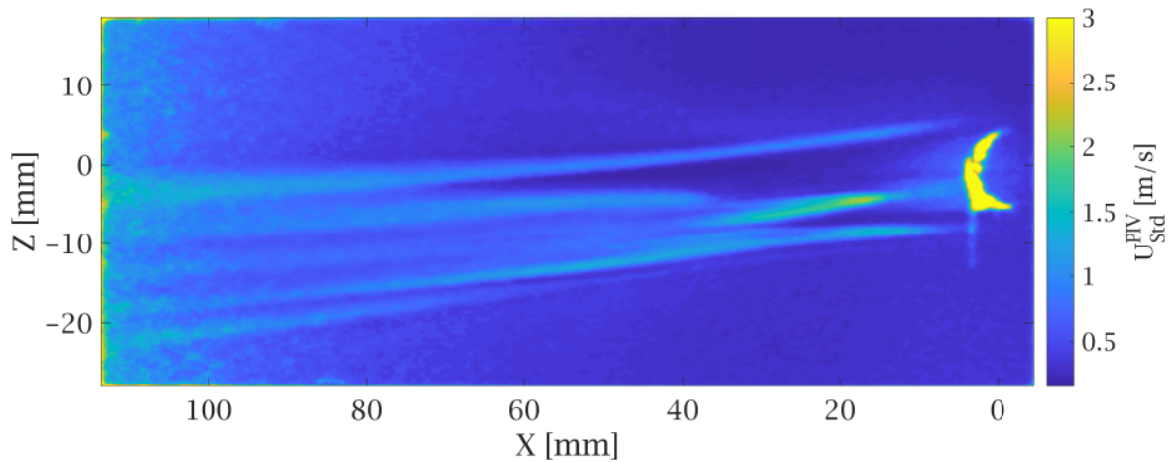


Figure 4.102: $D = 10mm$: velocity fluctuations field

In the fluctuation fields, the $D = 2.5mm$ 4.101 keeps displaying similarities with the central element. Once again, the high fluctuation cones start developing roughly at the element location, and grow into streaky structures which seem to follow the time averaged flow behaviour. Nevertheless, it appears that the evolution of the field does not encounter an overall decrease in intensity, as instead visible from figure 4.26 and even in figure 4.102. This peculiarity finds its confirmation in figure 4.100, where the results show an unexpected feature. One would expect the smallest diameter to display overall lower values of total fluctuations inside the wedge, but they actually overcome the trend of $D = 4mm$ for most of the turbulent wedge evolution. This is the first observation of a slightly unexpected outcome of this research.

In terms of total values of fluctuations 4.100, the $D = 10mm$ meets the expectations, with a growth that reminds the other super-critical elements. What is totally peculiar for this scenario is the distribution of these fluctuations in the XZ plane (see figure 4.102). As for the time averaged field, the fluctuation distribution is dominated by asymmetry, affecting the overall shape to a large extent. The large high speed streak is characterized by low fluctuations, whilst the highest values are observed in the region of "central" low-speed streak, at one diameter distance from the origin along X . This area is not strictly centered, as the asymmetry translates in a shifted wake too. Therefore its actual Z coordinate is about half a diameter lower than the center of the cylinder.

The analysis of the HWA data is left as final topic of this paragraph, as it seems to be crucial. As previously mentioned, the fluctuations can be dominated either by the instability of the three-dimensional shear layer all around the object, with a peak in the center of the wake, or by a lateral shear layer instability, leading to a Von Kármán vortex type of behaviour. According to [Loiseau et al. \(2014\)](#), larger diameters are associated to the first type of mechanism, leading to a varicose instability. On the other hand, the lower the η values are, the more a sinuous type of phenomenon is expected, with the shear layer developing along the flanks of the element as main region of instability. With this in mind, one might notice how the central element has three regions of high fluctuations for $X = 24mm$, two on the sides and one in the center of the wedge (figure 4.104). All of these three regions display similar sizes and values, as going from left to right, one encounters: 1.07 m/s, 1.04 m/s and 1.11 m/s on the local maxima on these regions. In the low diameter case (4.103) all the three regions have diminished size, with the central area having a considerably lower intensity (maximum 0.76 m/s) with respect to the right hand side (0.94 m/s). Finally, $D = 10mm$ sees the total domination of the central zone of fluctuation over the side regions (figure 4.105). The latter are less than half the size of the central one, and their maximum intensity is 1.1 m/s against the 1.26 of the central blob. As a general conclusion, an increased aspect ratio k/D slowly moves the fluctuation maximum from the upper-central region of the near wake to the regions along the cylinder flanks, with $D = 4mm$ being a compromise between these two scenarios.

To conclude, the $X = 54mm$ planes are visible in figures 4.106 to 4.108. The main observation would focus on the similarities between the two lower diameter cases, both showing local maxima randomly distributed all over the wedge. These correspond to streaks in the PIV field, as already mentioned when describing the characteristic of the central element 4.2.1. As expected, the $D = 10mm$ case shows a smoother distribution of the fluctuations over the wedge, which previously appeared as a consequence of a BL growing turbulent. All the considerations reported in this section must be kept in mind, as the different phenomena displayed later will rely on similar ideas.

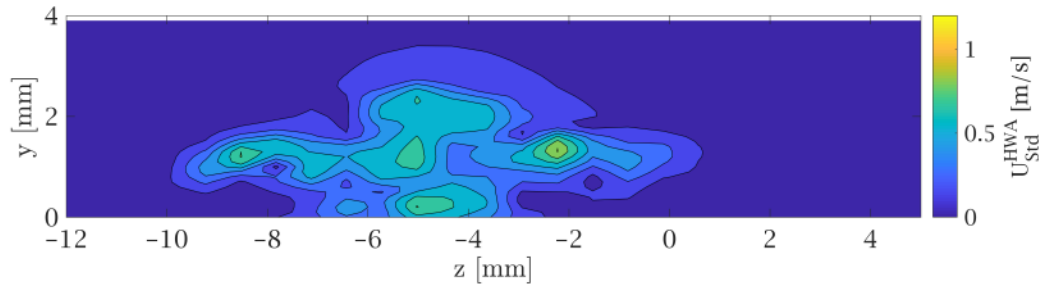


Figure 4.103: $D = 2.5mm$: zy plane of velocity fluctuations at $X = 24mm$

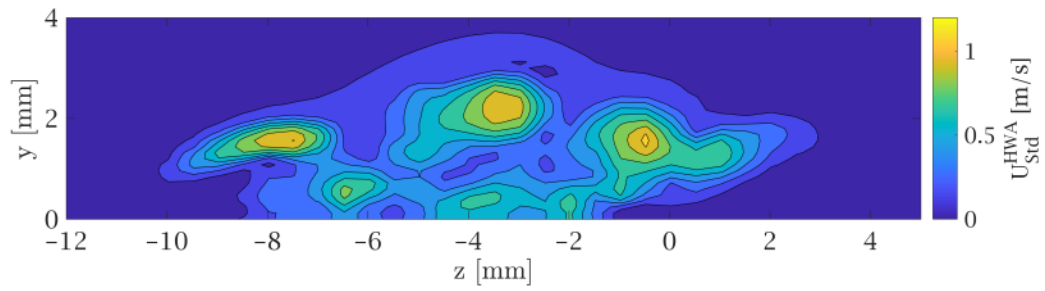


Figure 4.104: $D = 4mm$: zy plane of velocity fluctuations at $X = 24mm$

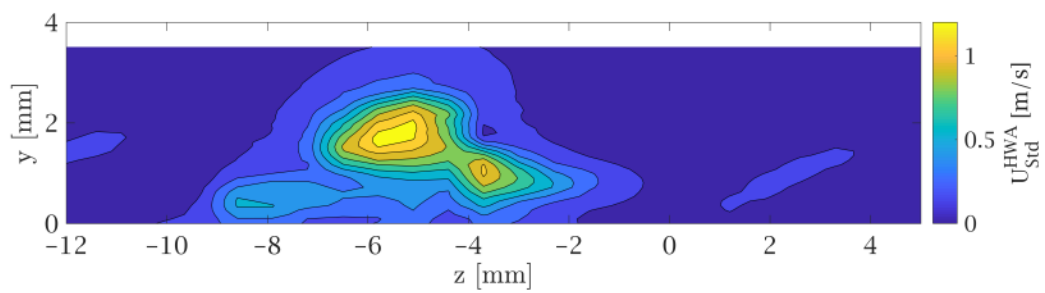


Figure 4.105: $D = 10mm$: zy plane of velocity fluctuations at $X = 24mm$

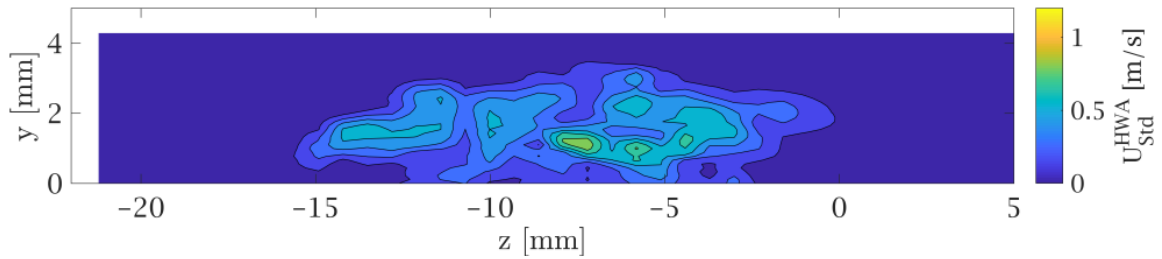


Figure 4.106: $D = 2.5\text{mm}$: zy plane of velocity fluctuations at $X = 54\text{mm}$

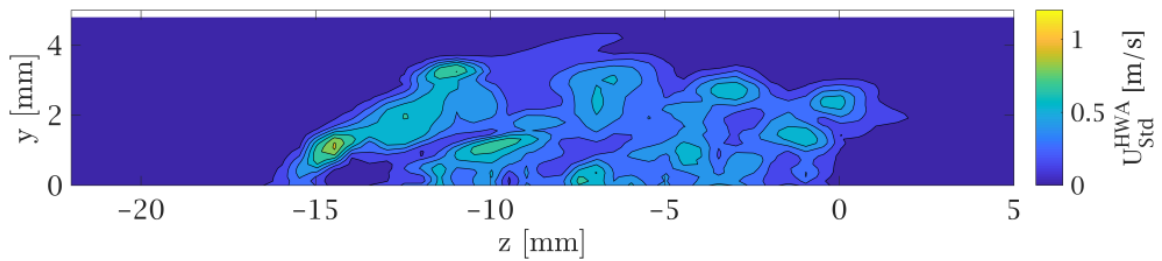


Figure 4.107: $D = 4\text{mm}$: zy plane of velocity fluctuations at $X = 54\text{mm}$

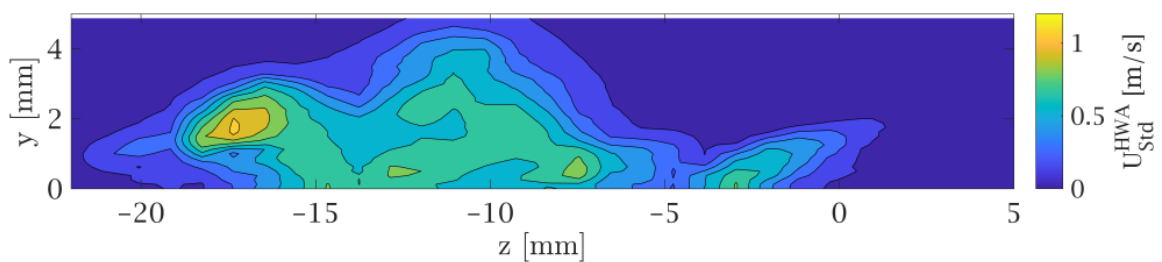


Figure 4.108: $D = 10\text{mm}$: zy plane of velocity fluctuations at $X = 54\text{mm}$

Frequency Analysis

Although $D = 2.5\text{mm}$ and $D = 10\text{mm}$ presented differences in the fluctuation peaks, the dominating frequency remains similar. In other words, the small diameter case has the main frequency always in the range 820-830 Hz, regardless of the position of investigation in the zy plane. In the same way, values around 600 Hz are the leading frequencies for $D = 10\text{mm}$. One must keep in mind that all these values are calculated at $X = 24\text{mm}$. Table 4.1 reports all the Strouhal numbers and dominating frequencies associated to $X = 24\text{mm}$ and $y = \delta_{0.99}$, as explained in section 4.2.1.

U=8 m/s, k=1.5 mm	f	Str_{δ^*}	Str_k
D=2.5 mm	827 Hz	0.1346	0.2064
D=4 mm	790 Hz	0.1285	0.1972
D=10 mm	616 Hz	0.1002	0.1538

Table 4.1: Frequencies and Strouhal numbers: variation of diameter

The outcome of the table is quite clear: an increased diameter leads to overall lower values of frequencies and Strouhal numbers. Once again, the Str_k values are in agreement with the ones displayed in figure 2.10 and 2.13.

Figure 4.109 shows the turbulent state of the wedge generated by $D = 10\text{mm}$ at 24 mm distance. This is the evidence needed for categorizing this scenario as a super-critical. At already a 2.4 diameter distance form the origin, the spectra show characteristics similar to the one of figure 4.42 (referring to $X = 90\text{mm}$ for the main element).

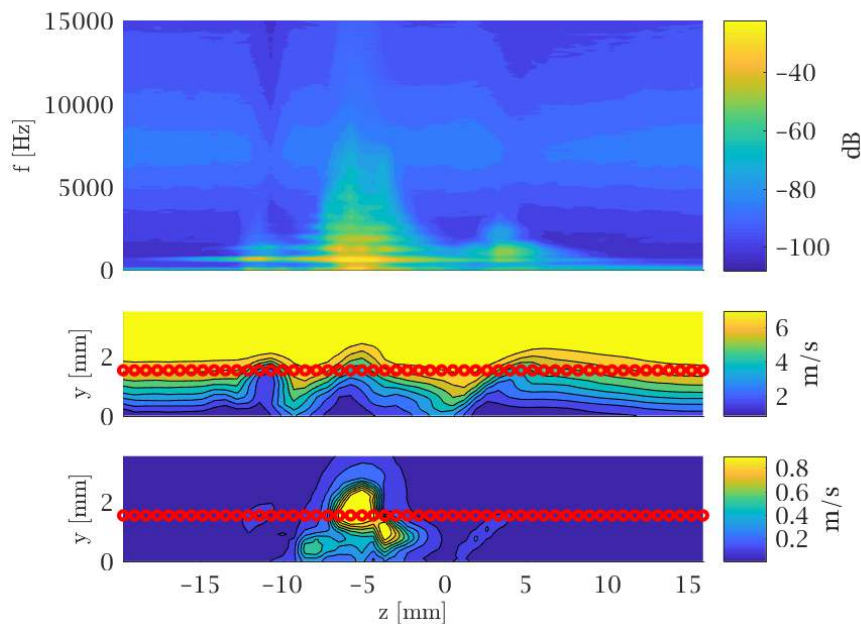


Figure 4.109: $D = 10\text{mm}$ and $k = 1.5\text{mm}$. $X = 24\text{mm}$: frequency spectra along $y = \delta_{0.99}/2$

Analysis of the POD Modes

The analysis of the instability modes under the effects of diverse aspect ratios is a core topic of the research from [Loiseau et al. \(2014\)](#). This has been largely mentioned in this report, and will be used as a comparison in this paragraph, together with [Cherubini et al. \(2013\)](#). The analysis of the fluctuation fields displayed the domination of the side shear instabilities when the diameter is small. The central shear was suggested as main mechanism for the large elements. This hinted what type of behaviour is expected from both these elements. According to [Loiseau et al. \(2014\)](#), an element whose η is below 1 should be totally dominated by sinuous instabilities, whilst $\eta > 2$ is the limit for a total varicose scenario. The already analyzed main element matches the expectations, with a varicose instability behaviour and $\eta = 2.67$. Therefore, the prediction of a varicose perturbation for $D = 10\text{mm}$ is expected to be confirmed.

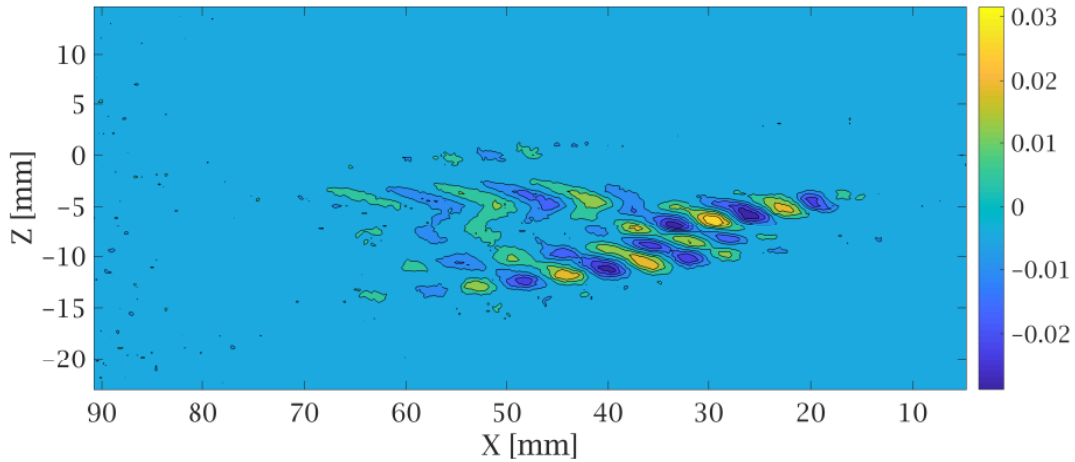


Figure 4.110: $D = 10\text{mm}$: U POD mode 1

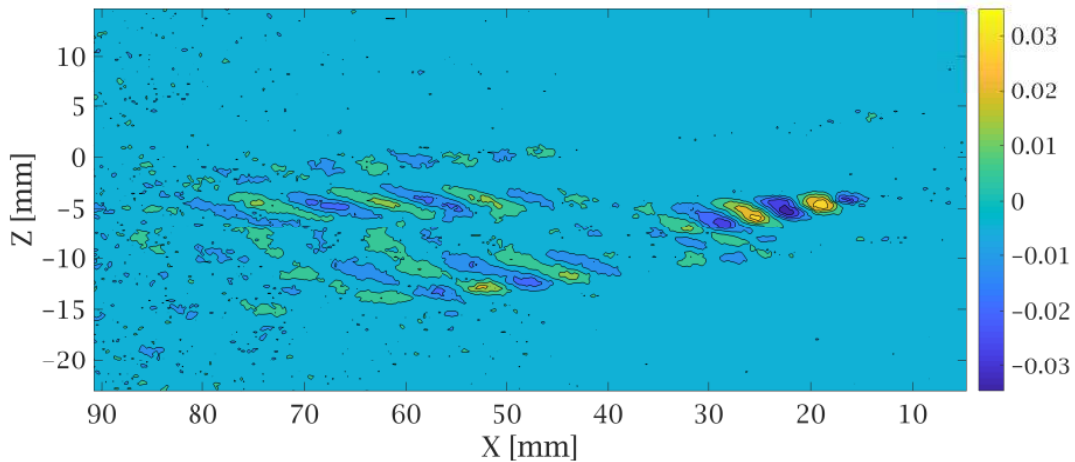


Figure 4.111: $D = 10\text{mm}$: U POD mode 3

As well as for most of the displayed data, it is not easy to compare the obtained results with previous literature, due to the three-dimensional BL and the asymmetric behaviour. This is valid especially for figures 4.110 and 4.111, where the two main decoupled POD modes are shown. The concepts of "varicose" and "sinuous" strongly rely on the symmetry identification, and the three-dimensional boundary layer makes this distinction difficult to assess. Nevertheless, there are characteristics of the POD modes that might still be compared to a 2D case. The distribution of the POD structures for $D = 10mm$ mainly focuses along the "central wake", in the proximity of the cylinder. For mode 1, it partially expands to the secondary low-speed streak, but starts fading away at about $X = 50mm$. Comparisons with figure 2.30 and figure 2.37 categorizes this as a varicose dominated scenario, with small compact elements along the center of the wedge.

Finally, the $D = 2.5mm$ condition has to be mentioned. Its value of η lies in a grey zone between 1 and 2 (1.67 to be precise), not directly mentioned by Loiseau et al. (2014) in figure 2.30. Its fluctuations in the HWA were mainly concentrated in the lateral areas of the wedge, coming from the flanks of the element. Moreover, the HWA time-signal of U (figure 4.112) recalls the shape of figure 2.33. However, it must be noticed that figure 2.33 referred to the w component of the velocity. Most of the hints seem to lead the prediction towards a sinuous instability, despite the aspect ratio not falling below $\eta = 1$. A further confirmation comes from figure 4.113. This has to be compared to figure 2.32. The figure appears to show a sinuous oscillation of the vorticity field, with elongated areas of high-vorticity assuming a curved shape.

The final confirmation comes from the POD modes (figures from 4.114 to 4.117). All these figures are discussed in their relationship to figures 2.30 and 2.38. With the exception of mode 5 (recalling a varicose shape), the most dominant POD modes assume a totally different shape and distribution. All the structures are much more elongated than the previous cases, and the seventh POD mode even resemble the "arrow shape" mentioned by Cherubini et al. (2013). The author declared that this shape is a feature of the sinuous instabilities. As mentioned before, the only valuable objection relies on the symmetry. The three-dimensionality of the BL does not allow to understand whether the symmetry is inverted with respect to the varicose case. In any case, the behaviour is totally different with respect to what was observed for larger diameters, and the shapes are undeniably closer to a sinuous rather than a varicose condition.

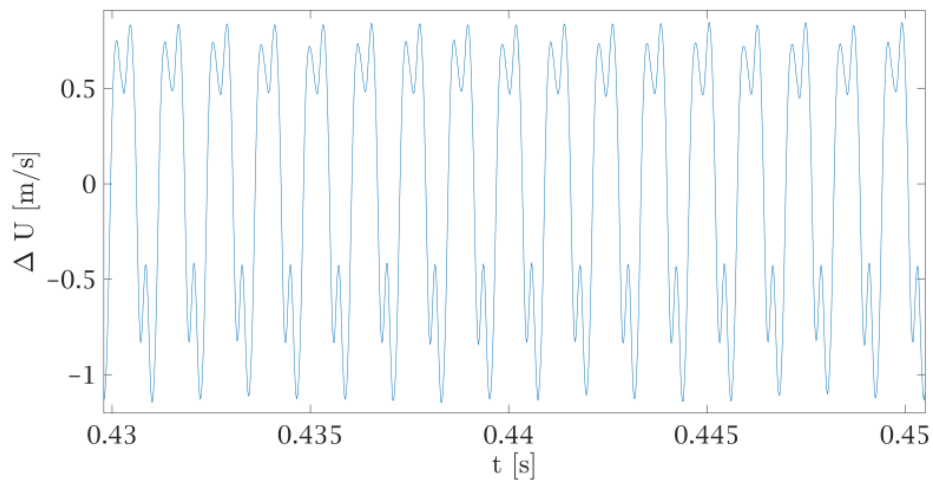


Figure 4.112: $D = 2.5\text{mm}$: Recorded signal of HWA in the position of highest fluctuations

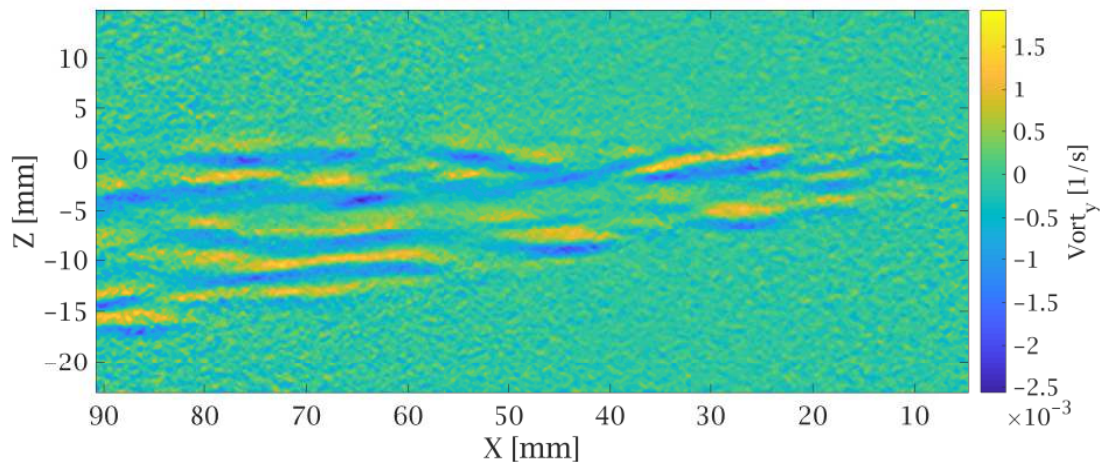


Figure 4.113: $D = 2.5\text{mm}$: instantaneous Y -vorticity field

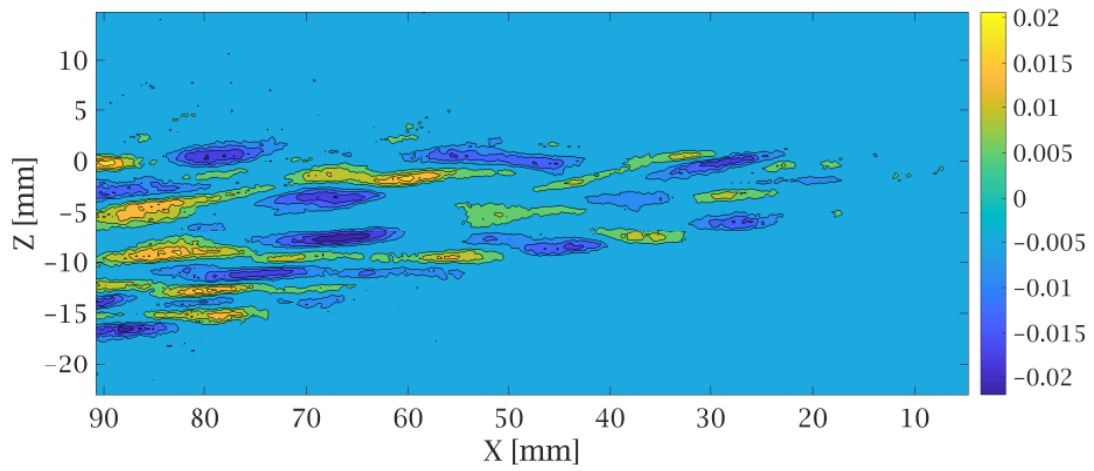


Figure 4.114: $D = 2.5\text{mm}$: U POD mode 1

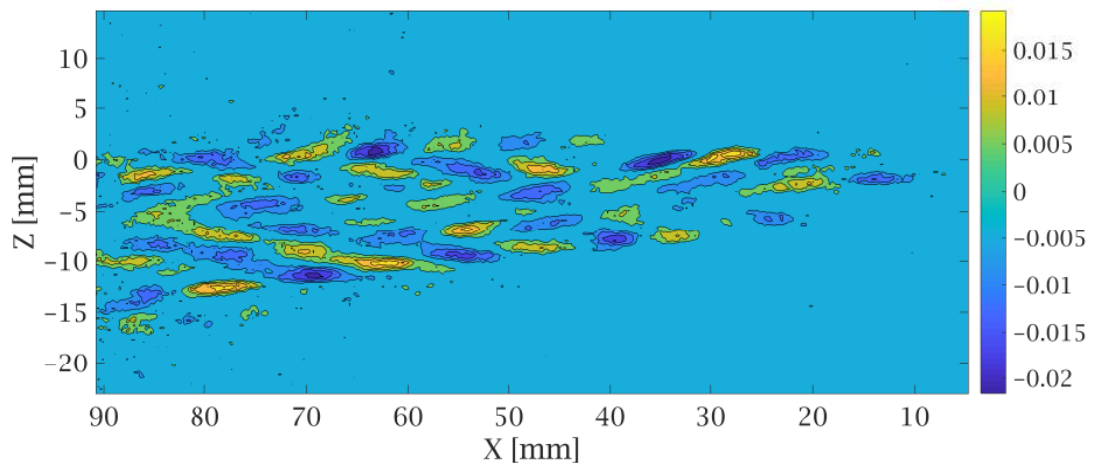


Figure 4.115: $D = 2.5\text{mm}$: U POD mode 3

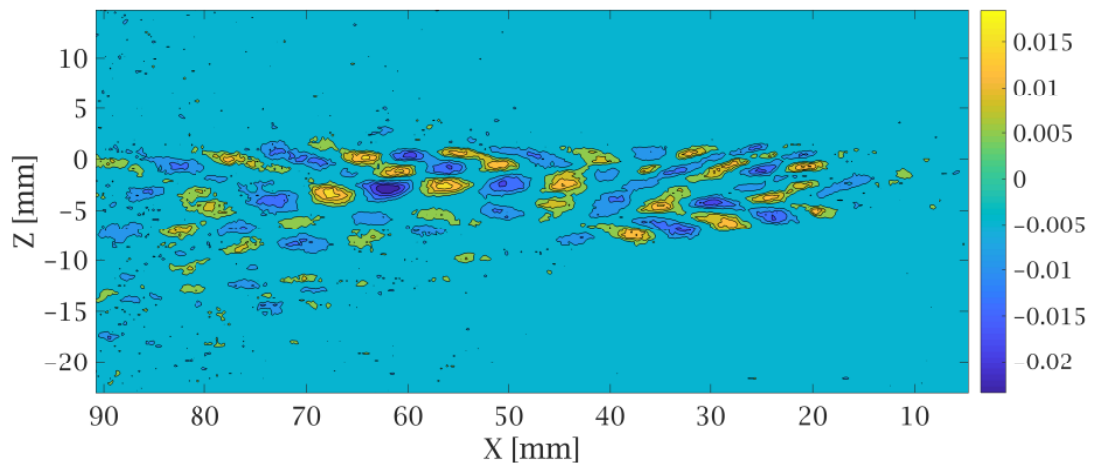


Figure 4.116: $D = 2.5\text{mm}$: U POD mode 5

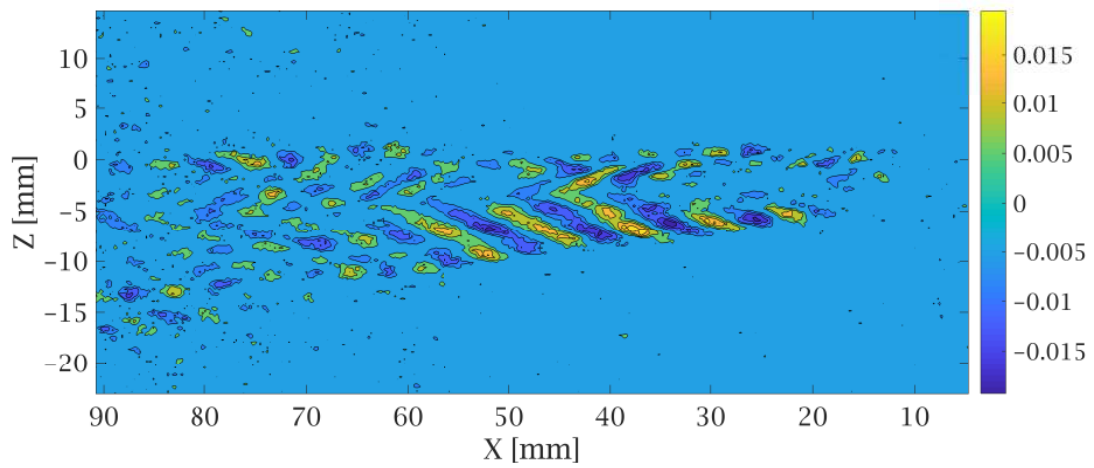


Figure 4.117: $D = 2.5\text{mm}$: U POD mode 7

4.3 Aspect Ratio Outliers

This section is dedicated to the analysis of those elements whose ratio k/D displays the highest and the lowest values. As already mentioned, peculiar flow characteristics have been found for a large value of aspect ratio, i.e. $D = 2.5mm$. Further observations will be dedicated to this case, in comparison with all the other elements. At the same time, the smallest values of aspect ratio also displayed some unexpected behaviour, verified with different techniques. Hence, a second section will concern the description of the elements with $D = 10mm$ and height equal to 1 mm and 0.5 mm, namely the smallest k/D considered in this project. Before these, an introduction will show how a large part of the metrics tends to have common characteristics, if scaled with proper parameters.

4.3.1 Scaling of the Metrics

The extraction of the metrics from particle image velocimetry has already been treated in the beginning of section 4.2.2. In terms of procedure for the data extraction of both the wedge width W_w and the metrics, the author refers to equations 4.6, 4.7 and 4.8. However, the variation of W_w along its downstream evolution has not been displayed so far. All the cases tested in this research are shown in figure 4.118 (except $D = 10mm$ and $k = 1mm/k = 0.5mm$), where the different trends of W_w are compared.

At first look, this figure might be confusing, but its purpose is soon to be explained. By combining some of the parameters already mentioned in this research, a new scaling parameter has been found (equation 4.13). By multiplying the wedge size with C_W , all the lines in figure 4.118 tend to merge in a single plot, as shown in figure 4.119 .

$$C_W = \left(\frac{k}{D}\right)^{\frac{2}{5}} \times \left(\frac{U_\infty}{Re_k}\right) \quad (4.13)$$

Three annotations must be made before proceeding. Firstly, it is curious how this new quantities change dimensions, having the same unit of measure as the metrics shown in chapter 4.2: $[mm \times m/s]$. Moreover, if one did not want to include scenarios with different velocities, but only those elements with the same $U_\infty = 8m/s$, the scaling parameter to be used would have been 4.14. Finally, all the lines seem to collapse into a graph that has an initial linear increase, and starts stabilizing around a constant value, after approximately $X = 50mm$.

$$C_{met} = \left(\frac{k}{D}\right)^{\frac{2}{5}} \times \left(\frac{1}{Re_k}\right) \quad (4.14)$$

The last two observations lead to a final note, regarding the velocity displacement metric for elements of same height and U_∞ and different D . After scaling these plots with parameter 4.14, figure 4.120 is obtained. What is interesting to notice, is that the plots merge into a linear trend approximately in the same range of X , where the scaled W_w flattened.

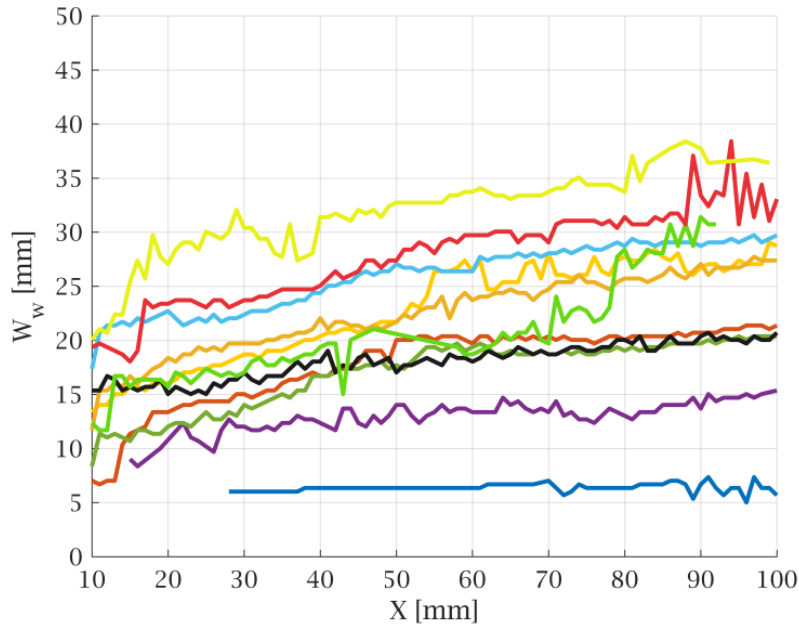


Figure 4.118: Wedge size along their downstream evolution. Legend on figure 4.119

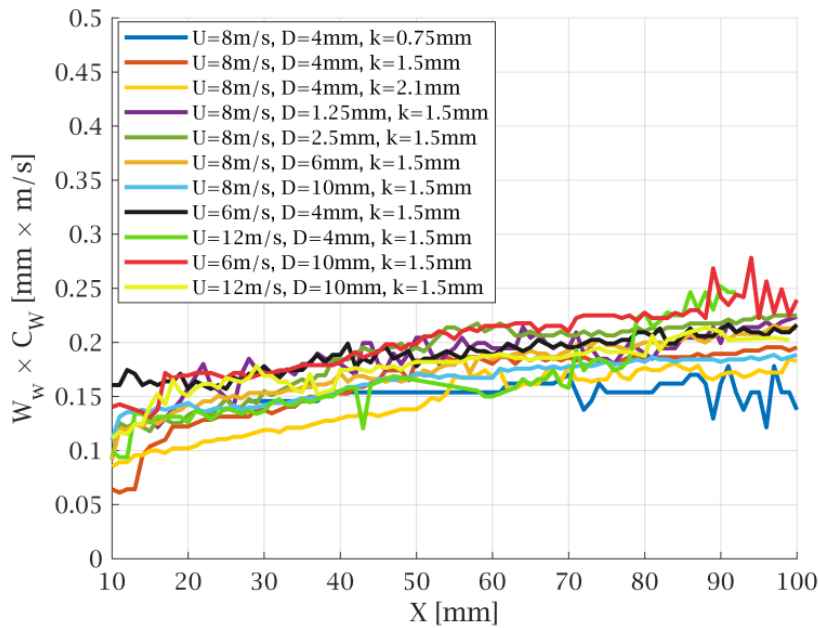


Figure 4.119: Wedge size along their downstream evolution, scaled with C_W

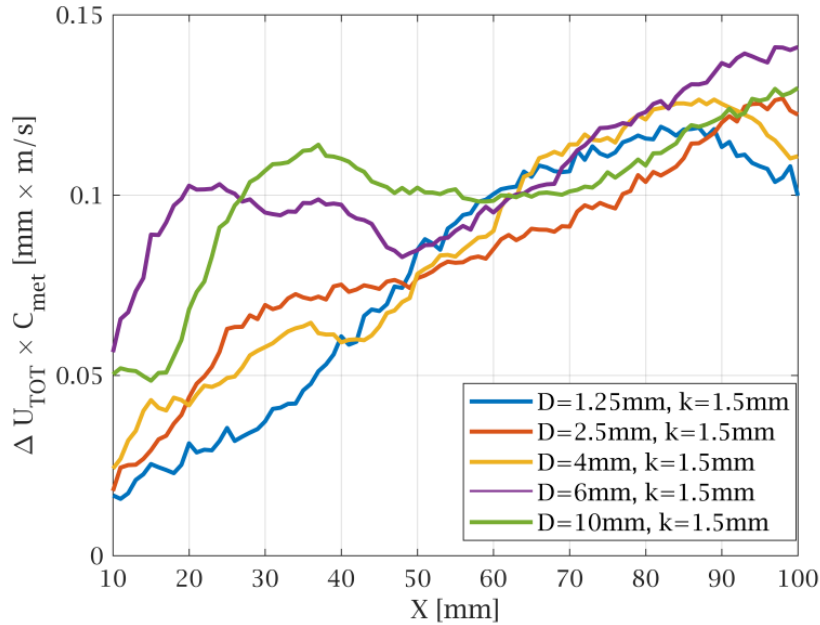


Figure 4.120: Velocity displacement metrics, scaled with C_{met}

4.3.2 Analysis of Sinuous Instability

The analysis of $D = 2.5mm$ has already been largely treated in section 4.2.4. The sinuous instability is what differentiates this element from the others. Moreover, the element seemed to display characteristics that are in common with the larger $D = 4mm$, which was partially expected as both quasi-critical roughness elements. Going deeper into the analysis of this element, C_{met} is applied also for the scaling of the total fluctuation metric (equation 4.8). This procedure is carried out for all those elements that displayed varicose perturbation as dominant mode, and for $D = 2.5mm$. Plotting all the scaled data in the same graph 4.121, one can immediately notice that all the varicose elements tend to have similar behaviour. The trends show a initial growth, whose peak is followed by a flattening (which for the case $D = 10mm$ is very short) and a final increase. The only exception is the sinuous instability scenario, whose fluctuations appear to grow monotonically and whose values are higher.

This is simply a further hint regarding the peculiarity of this case, but a stronger evidence is given by figure 4.122. The graph shows the wedge opening X position, already discussed in section 4.1: the two cases $D = 4mm$ and $D = 2.5mm$ are compared. Just like for figure 4.7, a smaller diameter is expected to face a turbulent condition at a higher speed. Figure 4.122 shows that this is true in terms of fully critical behaviour, i.e. when the turbulent wedge is right after the cylinder. The thinner element needs a Re_k that is roughly 500 units larger than the $D = 4mm$ in order to reach this state (when the X of opening reaches about 10mm). Nevertheless, the way in which the plot decreases towards a fully turbulent state is very different. When both the elements show the first presence of convective transition, the thinner element has a turbulent wedge closer to the origin. Nevertheless, its slope is lower,

with a much smoother and "less critical" behaviour.

This whole analysis is a further indication of how the topic is complex: with several aspects to be considered. The physics of the flow could considerably change and unexpected results could appear. Basically, different aspect ratios strongly affect the flow topology, influencing the way the flow structures interact. The sole fact that a thinner element leads to a sinuous mode is emblematic. Finally, the key for the understanding and predicting of the flow development relies in the study of the interaction between the flow realities in the vicinity of the element:

- the central low speed region, with the near low-speed wake and the shedding of the hairpin vortices
- the strong three-dimensional shear-layer, with the variable influence of either an upper or a lateral shear
- the horseshoe vortices, with their modulation of the base flow and the up-wash/down-wash motion

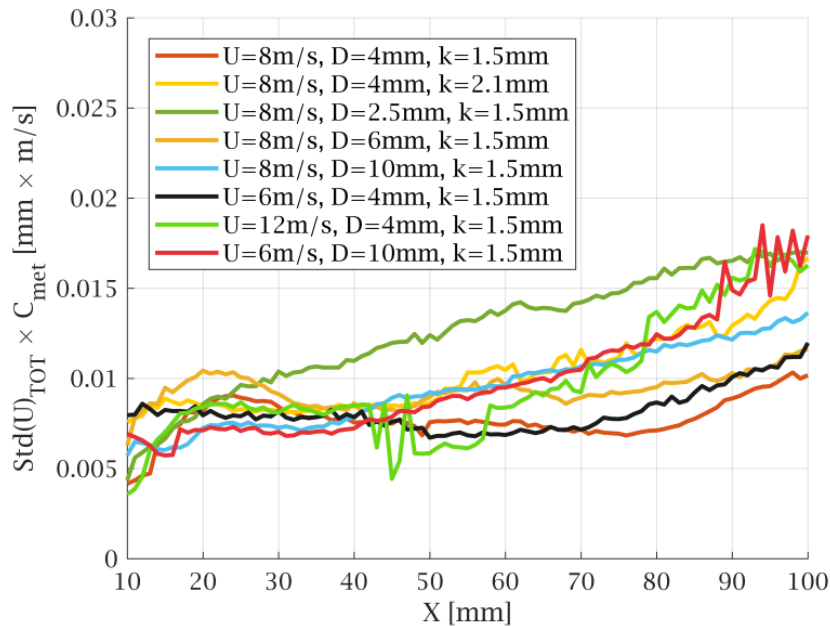


Figure 4.121: Fluctuation metrics of the elements displaying a POD mode structure (either varicose or sinuous), scaled with C_{met}

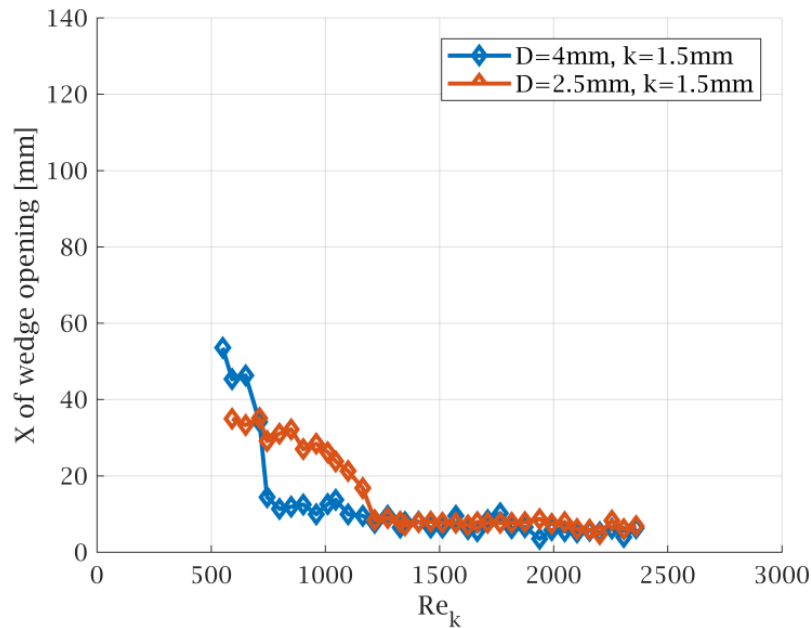


Figure 4.122: $D = 4mm, k = 1.5mm$ and $D = 2.5mm, k = 1.5mm$: position of wedge opening vs. Re_k

4.3.3 Analysis of Low Aspect Ratio k/D

The topics treated in this section represent another powerful statement to underline the complexity of the phenomenon, and to show how the flow structures might interact with each other in several different ways. The elements analyzed in this section are $D = 10mm, k = 1mm$ and $D = 10mm, k = 0.5mm$, characterized by extremely low aspect-ratios. These will also be compared with the largely discussed $D = 10mm, k = 1.5mm$. All these three elements are displayed in figure 4.123, where the wedge width evolution is plotted. The scaling described in section 4.3.1 is applied here, multiplying W_w with C_W . The results are depicted in figure 4.124: the merging of the data into almost a single line is not displayed by these cases.

As a further confirmation, the unique behaviour of these element is analyzed by means of infrared thermography as well. By looking at figure 4.126 and 4.125 one can notice a different trend with respect to the one shown in section 4.1. In figure 4.125, three elements with the same height ($k = 1mm$), and different diameters present the exact same criticality level at each Re_k , merging into a single line. This is different from we have seen for $k = 1.5mm$ (figure 4.7) and it is not exactly expected. More peculiarly, figure 4.126 shows the $k = 0.5mm$ elements being characterized by the opposite trend with respect to the one seen in figure 4.7. At a given Re_k , the most critically transitional element is the thinnest ($D = 6mm$), whilst the largest ($D = 10mm$) element is in a less critical scenario. According to these data, an increased diameter results in a beneficial effects in terms of delaying transition. In other words, a larger diameter is not connected to more critical scenarios, for this specific examples.

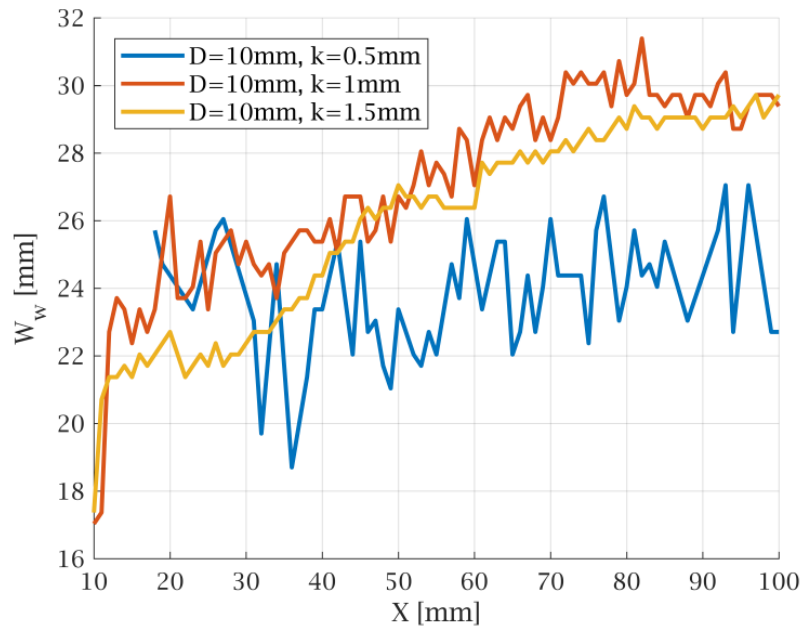


Figure 4.123: Wedge size along their downstream evolution, for elements with $D = 10\text{mm}$.

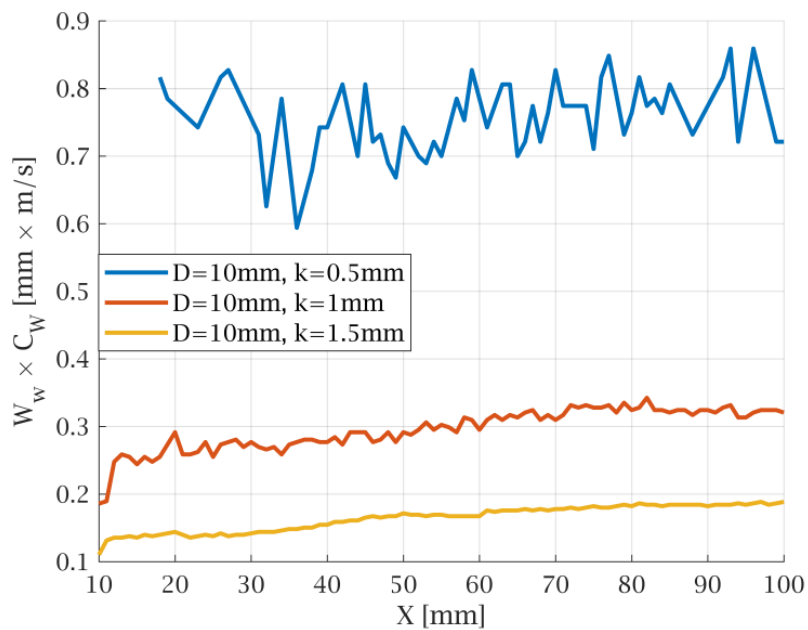


Figure 4.124: Wedge size along their downstream evolution scaled with C_W , for elements with $D = 10\text{mm}$.

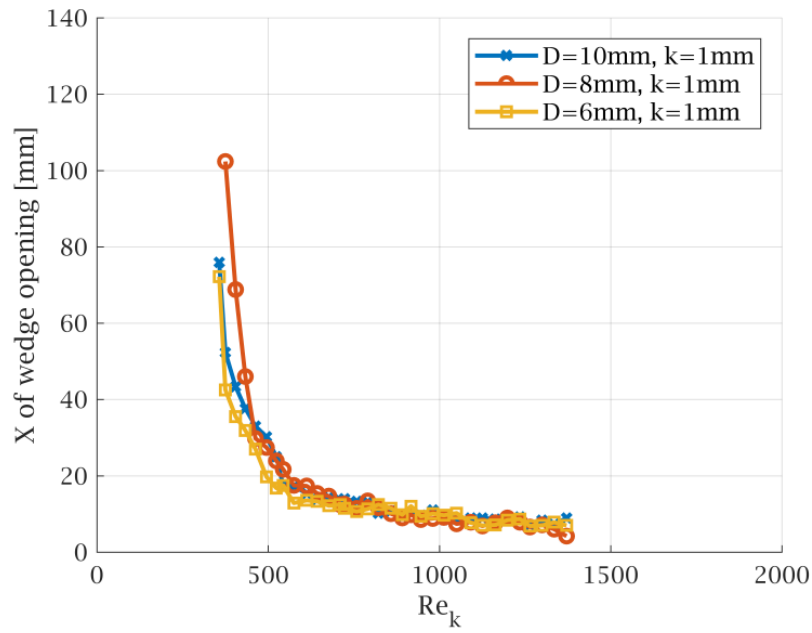


Figure 4.125: $k = 1\text{mm}$, different diameters: position of wedge opening vs. Re_k

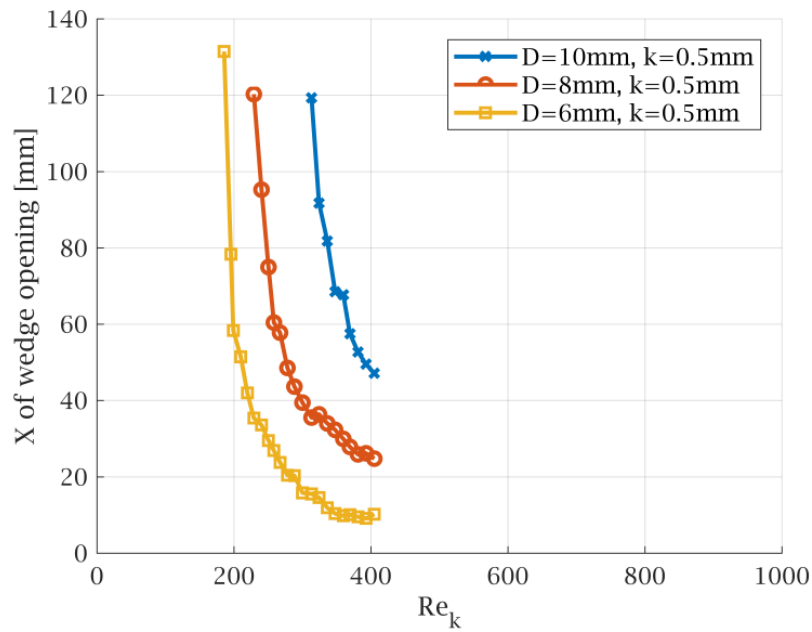


Figure 4.126: $k = 0.5\text{mm}$, different diameters: position of wedge opening vs. Re_k

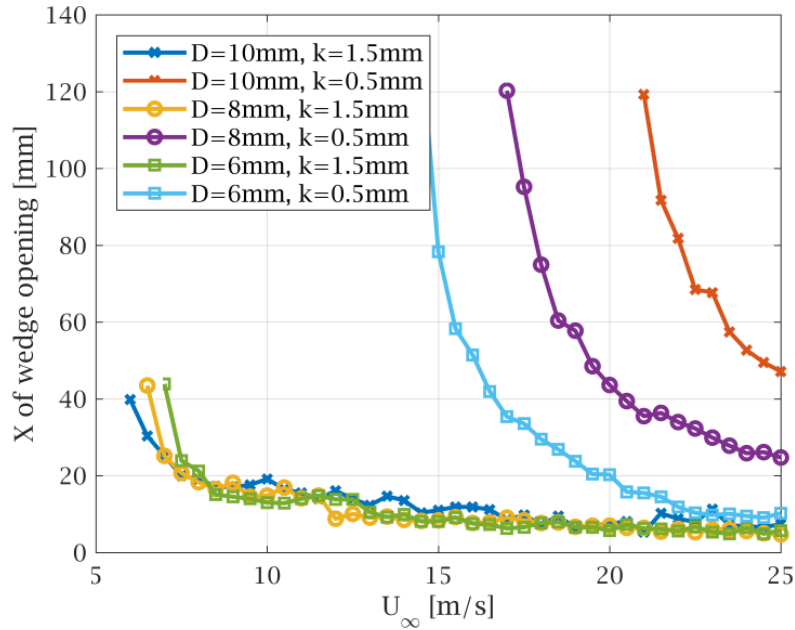


Figure 4.127: $k = 0.5\text{mm}$ and $k = 1.5\text{mm}$, different diameters: position of wedge opening vs. U_∞

It has already been mentioned that several different phenomena play a role in this transition mechanism, and their physical interaction might change considerably under the effects of different experimental parameters. With this concept in mind, a possible explanation for the unexpected beneficial effect of a larger diameter could be pursued. Normally, an increased diameter is related to a stronger wake, hence a larger and more intensely low-speed region aft the cylinder. This phenomenon is combined with stronger shear stresses, and leads to stronger instabilities of the flow near the element. As previously described, these instabilities can translate into a varicose "pulsation" of the low-speed central streak or into a sinuous oscillation, both transmitted to all the flow structures. These disturbances have a strong influence on the horseshoe vortices too, and eventually participate to the occurrence of a turbulent wedge, and to the onset of transition. All of this appears confirmed for the "tall" elements, investigated so far ($k = 1.5\text{mm}$).

Nevertheless, it might be possible that an increase in diameter is not sufficient to trigger critical perturbations for elements with an extremely low k (such as 0.5mm). In other words, increasing the diameter might cause a larger wake or a slightly stronger oscillation, but these premises are not strong enough for a worsening of the transition scenario. On the other hand, a larger diameter have undeniably beneficial effect on the transition scenario: a larger separation between the two horseshoe vortices. There is a possibility that for low- k elements, the merging of the two HS vortices is the dominant mechanism and the main cause of the turbulent wedge opening. This would explain why the benefits of two distant vortices prevaricate over the disadvantages of slightly stronger instabilities in the near wake. These ideas appear to be supported by figure 4.128, where the two high-speed streaks for $k = 0.5\text{mm}$ seem to never merge, following heir almost parallel paths. Finally, the comparison between figure 4.129 and figure 4.130 clarifies this theory. In figure 4.129, three elements with $D = 6\text{mm}$ are shown.

The lowest one is the $k = 0.5\text{mm}$, just like for figure 4.130, where the elements have a 10 millimeter diameter. First of all, it could be noticed how the merging of the two streaks sets the onset for the opening of the wedge, just like stated before. Furthermore, the position where this phenomenon occurs is almost the same, for the two elements with $k = 0.5\text{mm}$. What is totally in agreement with the previous observations is that the $D = 6\text{mm}$ elements are displayed at a 15 m/s freestream speed, while the velocity for $D = 10\text{mm}$ was 22.5 m/s. Hence, despite the considerably higher speed, the larger element vortices merge at the same distance as the thinner cylinder.

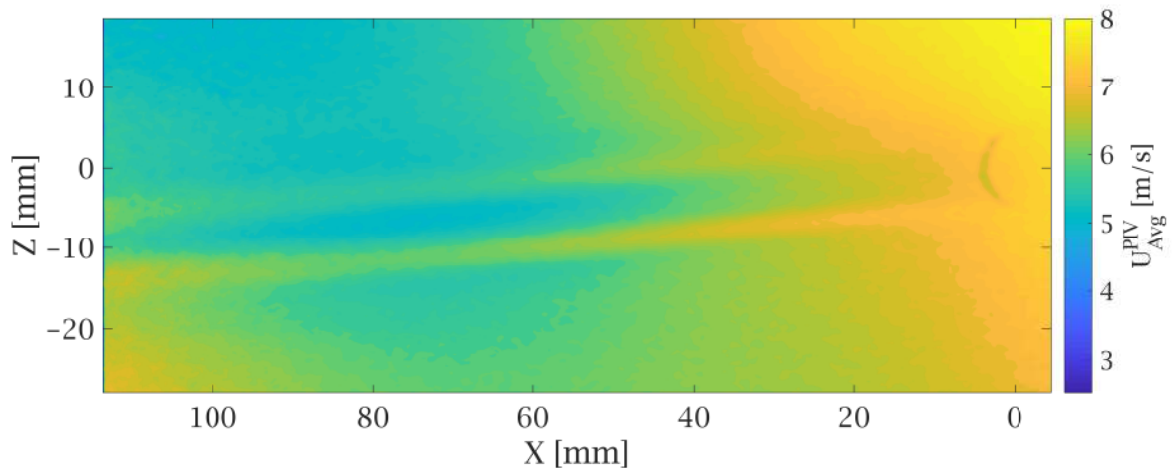


Figure 4.128: $D = 10\text{mm}$, $k = 0.5\text{mm}$, $U_{\infty} = 8\text{m/s}$: U time averaged field.

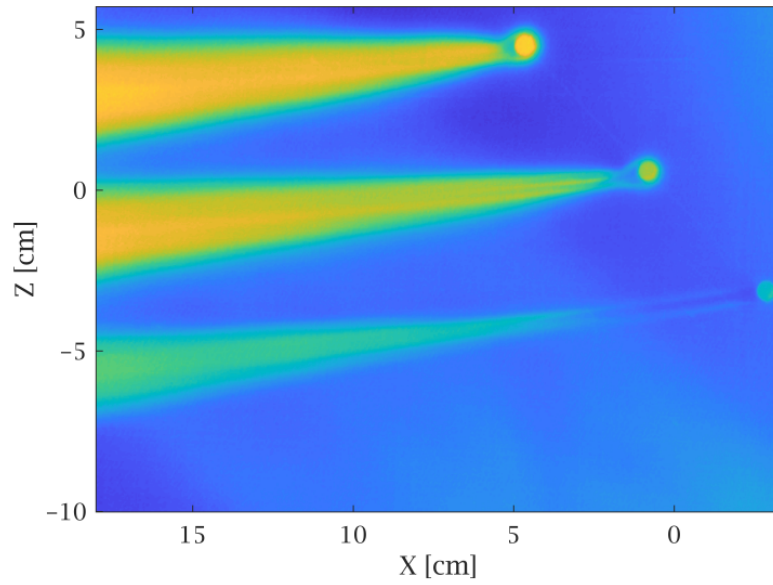


Figure 4.129: $D = 6mm$ and $U_{\infty} = 15m/s$

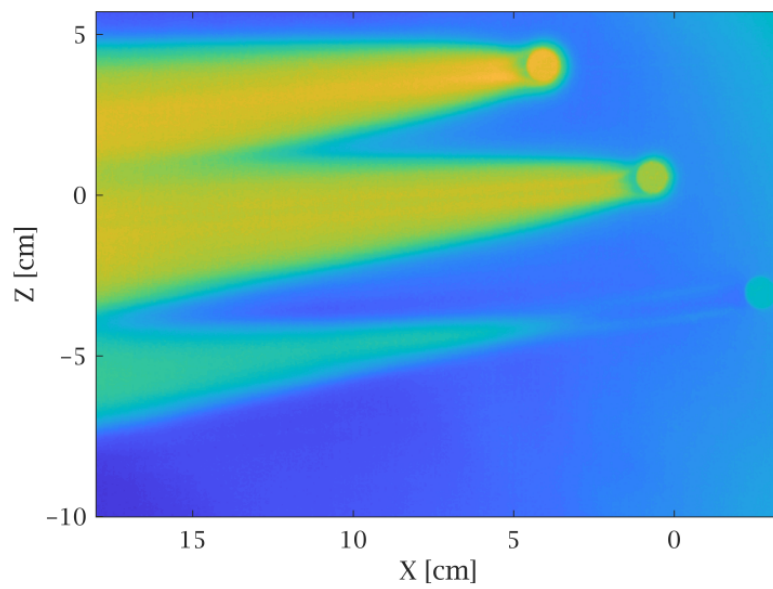


Figure 4.130: $D = 10mm$ and $U_{\infty} = 22.5m/s$

Chapter 5

Conclusions and Recommendations

The aim of this thesis was to investigate the effects of an isolated roughness element on the boundary layer transition of a 45° swept wing. This crossflow dominated boundary layer was perturbed with the introduction of cylindrical roughness elements. The attention was focused on the physical features of the flow. The description of the flow topology covered several aspects of the phenomenon - from the near wake structures to the development of a fully turbulent wedge. Moreover, the analysis included the changes in flow characteristics, under the effects of different experimental parameters. These experimental parameters are: the freestream speed, the height and the diameter of the cylindrical elements. In order to achieve this goal, different experimental techniques were used, during multiple wind tunnel campaigns. The tests were carried out at the Low Speed Wind Tunnel of Delft University of Technology, and the model was a 45° swept wing model designed by [Serpieri and Kotsonis \(2016\)](#). The combination of infrared thermography, particle image velocimetry and hot wire anemometry allowed to have diverse perspectives and data, whose complementarity was precious for the deep understanding of the phenomena.

5.1 Conclusions

What emerged from the research is in partial agreement with the results of previous studies. The flow aft the element is characterized by a wedge of perturbed flow, where high- and low-speed streaks alternate. The way these streaky structures develop strongly depends on the geometrical parameters and the velocity of the freestream flow. Generally, an extremely sub-critical element only sees the shedding of two weak horseshoe vortices, whose intensity is not strong enough to modulate a streaky behaviour. A quasi-critical element is characterized by the alternate sequence of streaks, with strong three-dimensional features, due to the influence of the crossflow component. This translates into a total asymmetry of the flow, affecting every aspect of the phenomenon. The super-critical behaviour was observed for scenarios where the speed, the height or the diameter grew enough to trigger boundary layer transition in the

strict vicinity of the element. The velocity fluctuations mostly followed the organization of the turbulent wedge streaks, and in the near wake they were mainly concentrated in correspondence of the regions of strong shears. All these flow characteristics considerably changed with the three parameters. A large part of the discussion is dedicated to the assessment of these changes, and to the physical reasons behind them.

A tonal frequency spectra was observed for all the cases that were not neatly sub-critical, with a frequency and a Strouhal number increasing with the diameter of the element. The tonal behaviour concentrated inside the region of strong velocity fluctuations, relating it to the instability generated by the three-dimensional shear layer. These instabilities could assume the shape of a varicose or a sinuous perturbation, with the latter being related to shallower roughness elements (higher aspect ratio k/D). The analysis and the comparison of these two type of instabilities were performed, with the support of previous researches.

The prediction of the critical status (i.e. sub-, quasi- or super-critical) by means of the comparison between Re_k and critical Re_k is a good approximate method for most of the investigated cases. In fact, the cases where the aspect ratio does not fall below 0.15 and does not overcome 0.6, perfectly matches with this prediction strategy, largely used by previous researches. However, the phenomena appeared to be extremely complex, and the interaction between the different flow structures to be consistently dependent on other parameters, such as the ratios k/D and k/δ_* . The assessment of Re_k alone does not result to be sufficient for a specific prediction of the flow phenomena, other parameters need to be taken into consideration. When the aspect ratio reached outlier levels, and the interaction between the near wake structures changed drastically, partially unexpected results were observed. These included delayed transitory effects and different instability mechanisms.

Overall, the aim of the research was achieved to a good extent. The studied phenomenon is of complex nature, and this must be taken into account when applying this topic to a practical level. These roughness elements might not only represent unexpected accumulations over a wing, but also parts of the design. The design and production of rivets, screws and junctions might use some of the concepts discussed in this report. The pursuit of an optimal solution might need a deep analysis of the flow physics, with specific test acting towards a less generic prediction.

5.2 Recommendations

The recommendations must focus around those elements with extreme aspect ratios. The physical phenomena involved in those scenarios deserve to be studied further, in order to fully understand them. A better comprehension of these cases might lead to an optimal exploitation of these data on a practical basis. This means that both large and small aspect ratios are valuable topics to be treated more deeply. Another broad parametric study might be needed; this time, with several new elements all displaying k/D values in the vicinity of 0.1. On the other hand, large aspect ratio elements should be mainly studied in regards to their triggering of sinuous instabilities, with a thorough focus on how this influences all

the aspects of the flow. Moreover, the three-dimensional nature has been proven to be a paramount characteristic of the flow, and totally deserves attention. A possible interesting analysis would consist in reproducing on an experimental environment the work by [Kurz and Kloker \(2016\)](#): a two-dimensional and a three-dimensional flow compared. The two experiments would have comparable parameters and setups, in order to isolate the effects of the perpendicular component of the boundary layer. Finally, the next studies might want to try to isolate the effects of the non-dimensional parameters involved, trying to keep all the others constant (k/D , Re_k or k/δ_*).

The combination of different techniques allowed to have a complete view of the phenomenon, passing from a parametric general study to a detailed measurement on a specific aspect of the phenomenon. For this reason, this type of approach is believed to have solid potential for investigations of flow topology. Nevertheless, a possible further development of this research could pass from a deep tomographic PIV analysis, as suggested in appendix A. Even better, a time-resolved tomographic PIV would be able to complete the picture, adding a three-dimensional data resolved in space and time, at least on part of the field.

Bibliography

- M. Acarlar and C. Smith. A study of hairpin vortices in a laminar boundary layer. part 1. hairpin vortices generated by a hemisphere protuberance. *Journal of Fluid Mechanics*, 175: 1–41, 1987.
- P. Andersson, L. Brandt, A. Bottaro, and D. S. Henningson. On the breakdown of boundary layer streaks. *Journal of Fluid Mechanics*, 428:29–60, 2001.
- F. Avallone, F. Schrijer, and G. Cardone. Infrared thermography of transition due to isolated roughness elements in hypersonic flows. *Physics of Fluids*, 28(2):024106, 2016.
- C. Baker. The laminar horseshoe vortex. *Journal of fluid mechanics*, 95(02):347–367, 1979.
- G. Berkooz, P. Holmes, and J. L. Lumley. The proper orthogonal decomposition in the analysis of turbulent flows. *Annual review of fluid mechanics*, 25(1):539–575, 1993.
- H. Bippes. Basic experiments on transition in three-dimensional boundary layers dominated by crossflow instability. *Progress in aerospace sciences*, 35(4):363–412, 1999.
- M. Brynjell-Rahkola, P. Schlatter, A. Hanifi, and D. S. Henningson. Global stability analysis of a roughness wake in a falkner–skan–cooke boundary layer. *Procedia IUTAM*, 14:192–200, 2015.
- G. M. Carlomagno and L. de Luca. Infrared thermography for flow visualization and heat transfer measurements. In *International Conference on Engineering Education*, 1998.
- A. Carpenter, W. Saric, and H. Reed. Laminar flow control on a swept wing with distributed roughness. In *26th AIAA Applied Aerodynamics Conference*, page 7335, 2008.
- V. G. Chernoray, A. V. Dovgal, V. V. Kozlov, and L. Loefdahl. Experiments on secondary instability of streamwise vortices in a swept-wing boundary layer. *Journal of Fluid Mechanics*, 534:295–325, 2005.
- S. Cherubini, M. De Tullio, P. De Palma, and G. Pascazio. Transient growth in the flow past a three-dimensional smooth roughness element. *Journal of Fluid Mechanics*, 724:642–670, 2013.
- M. Choudhari. Roughness-induced generation of crossflow vortices in three-dimensional boundary layers. *Theoretical and Computational Fluid Dynamics*, 6(1):1–30, 1994.

- J. Chu and D. Goldstein. Investigation of turbulent wedge spreading mechanism with comparison to turbulent spots. In *50th AIAA Aerospace Sciences Meeting including the New Horizons Forum and Aerospace Exposition*, page 751, 2012.
- V. Citro, P. Luchini, F. Giannetti, and F. Auteri. Boundary-layer flows past an hemispherical roughness element: Dns, global stability and sensitivity analysis. *Procedia IUTAM*, 14:173–181, 2015.
- H. Deyhle and H. Bippes. Disturbance growth in an unstable three-dimensional boundary layer and its dependence on environmental conditions. *Journal of Fluid Mechanics*, 316: 73–113, 1996.
- A. v. Doenhoff and A. Braslow. The effect of distributed surface roughness on laminar airfoil. *Boundary Layer and Flow Control*, 2:657–681, 1961.
- R. S. Downs, E. B. White, and N. A. Denissen. Transient growth and transition induced by random distributed roughness. *AIAA journal*, 46(2):451–462, 2008.
- F. G. Ergin and E. B. White. Unsteady and transitional flows behind roughness elements. *AIAA journal*, 44(11):2504–2514, 2006.
- M. Grawunder, R. Reiß, and C. Breitsamter. Thermographic transition detection for low-speed wind-tunnel experiments. *AIAA Journal*, 2016.
- J. Green. Laminar flow control-back to the future? In *38th Fluid Dynamics Conference and Exhibit*, page 3738, 2008.
- D. S. Henningson, A. Lundbladh, and A. V. Johansson. A mechanism for bypass transition from localized disturbances in wall-bounded shear flows. *Journal of Fluid Mechanics*, 250: 169–207, 1993.
- P. Klebanoff, G. Schubauer, and K. Tidstrom. Measurements of the effect of 2-dimensional and 3-dimensional roughness elements on boundary-layer transition, 1955.
- P. Klebanoff, W. Cleveland, and K. Tidstrom. On the evolution of a turbulent boundary layer induced by a three-dimensional roughness element. *Journal of Fluid Mechanics*, 237: 101–187, 1992.
- M. S. Kuester and E. B. White. Structure of turbulent wedges created by isolated surface roughness. *Experiments in Fluids*, 57(4):1–13, 2016.
- H. B. Kurz and M. J. Kloker. Receptivity of a swept-wing boundary layer to micron-sized discrete roughness elements. *Journal of Fluid Mechanics*, 755:62, 2014.
- H. B. Kurz and M. J. Kloker. Mechanisms of flow tripping by discrete roughness elements in a swept-wing boundary layer. *Journal of Fluid Mechanics*, 796:158–194, 2016.
- J.-C. Loiseau, J.-C. Robinet, S. Cherubini, and E. Leriche. Investigation of the roughness-induced transition: global stability analyses and direct numerical simulations. *Journal of Fluid Mechanics*, 760:175–211, 2014.

- J.-C. Loiseau, S. Cherubini, J.-C. Robinet, and E. Leriche. Influence of the shape on the roughness-induced transition. In *Instability and Control of Massively Separated Flows*, pages 123–128. Springer, 2015.
- M. Malik, F. Li, and C.-L. Chang. Crossflow disturbances in three-dimensional boundary layers: nonlinear development, wave interaction and secondary instability. *Journal of Fluid Mechanics*, 268:1–36, 1994.
- M. Mochizuki. Smoke observation on boundary layer transition caused by a spherical roughness element. *Journal of the Physical Society of Japan*, 16(5):995–1008, 1961.
- M. Morkovin, E. Reshotko, and T. Herbert. Transition in open flow systems—a reassessment. *Bull. Am. Phys. Soc*, 39(9):1882, 1994.
- M. V. Morkovin. On the many faces of transition. In *Viscous drag reduction*, pages 1–31. Springer, 1969.
- M. Placidi, E. van Bokhorst, and C. J. Atkin. On the effect of discrete roughness on the growth of crossflow instability in very low turbulence environment. *AIAA Aviation*, pages 13–17, 2016.
- L. Prandtl. in verhandlungen des dritten internationalen mathematiker-kongresses in heidelberg 1904. A. Krazer, ed., Teubner, Leipzig, Germany, 1905.
- R. H. Radeztsky, M. S. Reibert, and W. S. Saric. Effect of isolated micron-sized roughness on transition in swept-wing flows. *AIAA journal*, 37(11):1370–1377, 1999.
- J. A. Redford, N. D. Sandham, and G. T. Roberts. Compressibility effects on boundary-layer transition induced by an isolated roughness element. *AIAA journal*, 48(12):2818–2830, 2010.
- M. Reibert, W. Saric, R. Carrillo, Jr, and K. Chapman. Experiments in nonlinear saturation of stationary crossflow vortices in a swept-wing boundary layer. In *34th Aerospace Sciences Meeting and Exhibit*, page 184, 1996.
- E. Reshotko and A. Tumin. Role of transient growth in roughness-induced transition. *AIAA journal*, 42(4):766–770, 2004.
- D. P. Rizzetta, M. R. Visbal, H. L. Reed, and W. S. Saric. Direct numerical simulation of discrete roughness on a swept-wing leading edge. *AIAA journal*, 48(11):2660–2673, 2010.
- W. Saric, R. Carrillo, Jr, and M. Reibert. Leading-edge roughness as a transition control mechanism. In *36th AIAA Aerospace Sciences Meeting and Exhibit*, page 781, 1998.
- W. S. Saric, H. L. Reed, and E. B. White. Stability and transition of three-dimensional boundary layers. *Annual Review of Fluid Mechanics*, 35(1):413–440, 2003.
- W. S. Saric, A. L. Carpenter, and H. L. Reed. Passive control of transition in three-dimensional boundary layers, with emphasis on discrete roughness elements. *Philosophical Transactions of the Royal Society of London A: Mathematical, Physical and Engineering Sciences*, 369(1940):1352–1364, 2011.

- L.-U. Schrader, L. Brandt, and D. S. Henningson. Receptivity mechanisms in three-dimensional boundary-layer flows. *Journal of Fluid Mechanics*, 618:209–241, 2009.
- G. B. Schubauer and P. S. Klebanoff. Contributions on the mechanics of boundary-layer transition. *NACA Technical Note*, 1955.
- J. Serpieri and M. Kotsonis. Three-dimensional organisation of primary and secondary cross-flow instability. *Journal of Fluid Mechanics*, 799:200–245, 2016.
- J. Serpieri, S. Y. Venkata, and M. Kotsonis. Towards laminar flow control on swept wings with ac-dbd plasma actuators as active roughness. In *55th AIAA Aerospace Sciences Meeting*, page 1459, 2017.
- S. Suryanarayanan, D. B. Goldstein, G. L. Brown, A. R. Berger, and E. B. White. On the mechanics and control of boundary layer transition induced by discrete roughness elements. In *55th AIAA Aerospace Sciences Meeting*, page 0307, 2017.
- I. Tani. Boundary-layer transition. *Annual Review of Fluid Mechanics*, 1(1):169–196, 1969.
- I. Tani, H. Komoda, Y. Komatsu, and M. Iuchi. *Boundary-layer transition by isolated roughness*. Aeronautical Research Institute, 1962.
- D. Tempelmann, L.-U. Schrader, A. Hanifi, L. Brandt, and D. Henningson. Numerical study of boundary-layer receptivity on a swept wing. In *6th AIAA Theoretical Fluid Mechanics Conference*, page 3294, 2011.
- D. Tempelmann, A. Hanifi, and D. S. Henningson. Swept-wing boundary-layer receptivity. *Journal of Fluid Mechanics*, 700:490–501, 2012a.
- D. Tempelmann, L.-U. Schrader, A. Hanifi, L. Brandt, and D. S. Henningson. Swept wing boundary-layer receptivity to localized surface roughness. *Journal of Fluid Mechanics*, 711:516–544, 2012b.
- E. White, W. Saric, R. Gladden, and P. Gabet. Stages of swept-wing transition. In *39th Aerospace Sciences Meeting and Exhibit*, page 271, 2001.
- Q. Ye, F. F. Schrijer, and F. Scarano. Boundary layer transition mechanisms behind a micro-ramp. *Journal of Fluid Mechanics*, 793:132–161, 2016a.
- Q. Ye, F. F. Schrijer, and F. Scarano. Geometry effect of isolated roughness on boundary layer transition investigated by tomographic piv. *International Journal of Heat and Fluid Flow*, 61:31–44, 2016b.
- S. Zhong, T. Chong, and H. Hodson. A comparison of spreading angles of turbulent wedges in velocity and thermal boundary layers. *American Society of Mechanical Engineers. Journal of Fluids Engineering*, 125(2):267–274, 2003.

Appendix A

Tomographic PIV

This appendix is fully dedicated to the tomographic PIV experiments performed during this project. After the description of the methodology, some results will be shown and shortly discussed. These have not been included in the main flow of the thesis, as a deep analysis of the other three techniques (combined) was preferred for several reasons. Among these one can name: differentiation of the type of data, time-resolution of the HWA, vastness of results for the IR thermography and time consumption of the tomo-PIV processing. This experiment represents the *icing on the cake* for this thesis. Moreover, it is a valid argument to display how the combination of planar PIV and HWA was a valid replacement of the tomo-PIV results. Finally, this indicates a very interesting step to be taken, for further improvements of this work.

A.1 Methodology

The tomographic PIV experimental setup keeps several characteristics of the planar tests. The seeder and the laser system in use are the same as described in section 3. With the differences of two cylindrical lenses ($f = -100mm$ and $f = 200mm$), instead of a single one and a laser light sheet extended from 0.5 mm to 4.5 mm along the wall normal direction (measures took place at 30 % of the chord). In total, four cameras have been exploited for this test, at a distance of about 1.1 m, and a three dimensional FOV of $80 \times 50 \times 4mm^3$. This is obtained by setting the numerical aperture of the cameras to $f_{\#} = 5.6$ and including an innovative component. Additionally to the objectives used in the planar PIV setup, four Kenko 2×TELEPLUS PRO 300 DGX teleconverters were joined to the cameras. These are conversion lenses for the amplification of the magnification factor M, which raises from 0.25 to 0.4, for this specific case. The time-lapse between the pulses and the number of frames is unchanged. Figures A.1 and A.2, display the setup for this experiment. As noticeable, the four cameras are included of the tomographic sensor, for the live recording of the flow. In this case, this is even more crucial, as the time consuming processing forbids a rapid control

of the acquired images. In the following sections, two different cases will be shown, and the results will mainly be compared to the planar PIV and HWA fields already discussed.



Figure A.1: Tomographic PIV setup, inclusive of the thermographic camera

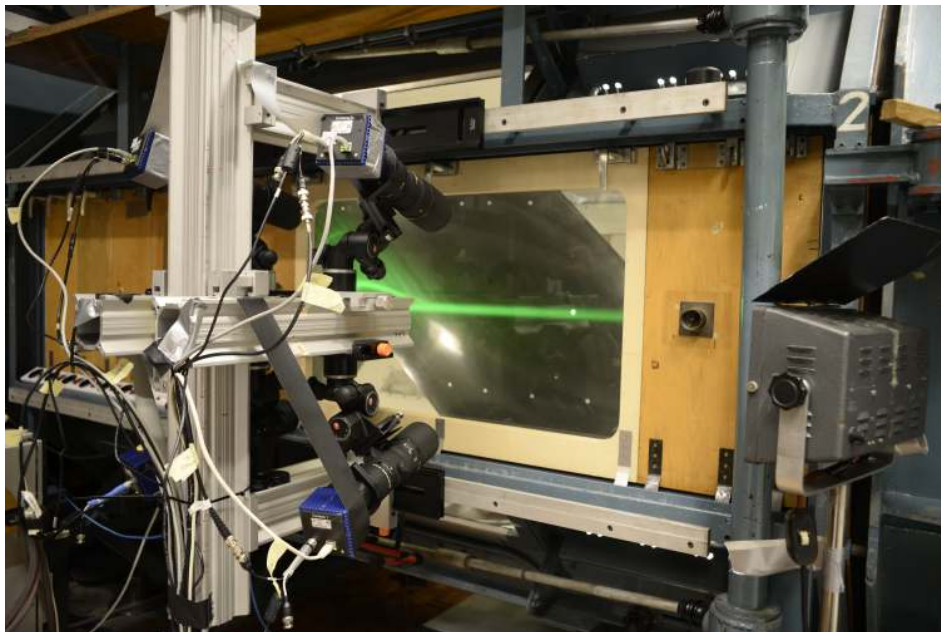


Figure A.2: Tomographic PIV setup. In the background the laser sheet along the FOV

A.2 Results

Both the cases displayed in the next subsection by means of figures from A.7 to ?? do not add a large quantity of extra information to the data displayed in the core of the thesis. Nevertheless, they confirm that a combination of planar PIV and HWA can provide with a valid volumetric investigation of the boundary layer. Moreover time resolved HWA fields can be obtained, with a very high resolution. The longitudinal planes resemble the planar PIV field shown chapter 4.2 with the only difference in the slightly lower y -position where the tomo-PIV results appear to match with the planar. This suggests the need of further work towards correcting the origin location in the three dimensional tomo-PIV field. However, this is beyond the purposes of this section, whose aim is to serve as a support for the data in the main part of the thesis and to give a hint on possible improvements. In fact, tomographic PIV allows to work on three-dimensional and spatially-resolved data, with the possibility to include analysis on the X -vorticity, and to display three-dimensional structures.

A.2.1 Central Element: $U = 8 \text{ m/s}$, $D = 4\text{mm}$, $k = 1.5 \text{ mm}$

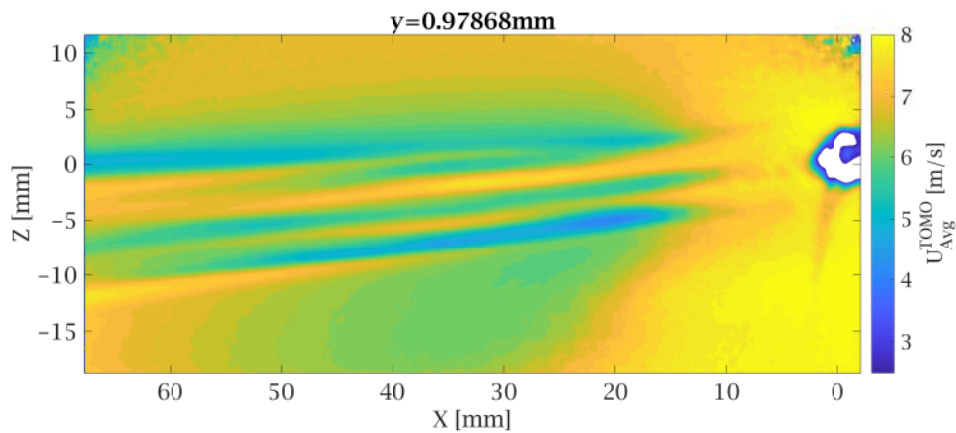


Figure A.3: Tomographic PIV results: wall parallel planes for $U = 8\text{m/s}$, $D = 4\text{mm}$, $k = 1.5\text{mm}$, $y = 0.98\text{mm}$

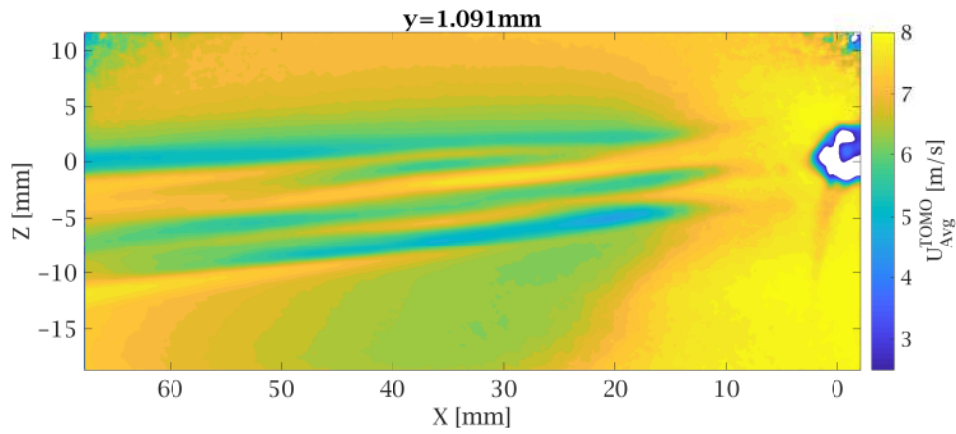


Figure A.4: Tomographic PIV results: wall parallel planes for $U = 8\text{m/s}$, $D = 4\text{mm}$, $k = 1.5\text{mm}$, $y = 1.09\text{mm}$

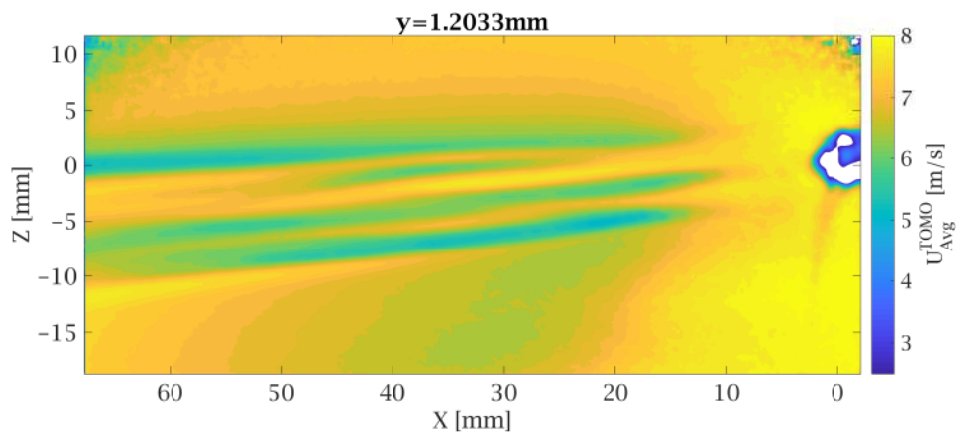


Figure A.5: Tomographic PIV results: wall parallel planes for $U = 8\text{m/s}$, $D = 4\text{mm}$, $k = 1.5\text{mm}$, $y = 1.2\text{mm}$

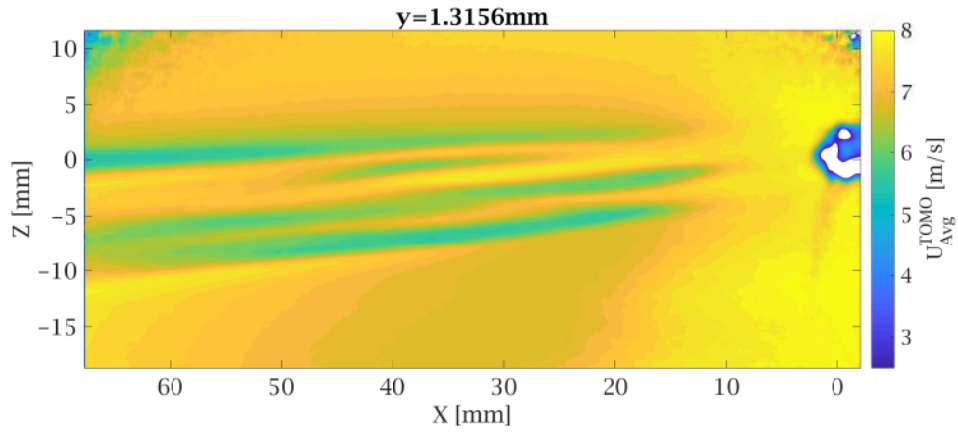


Figure A.6: Tomographic PIV results: wall parallel planes for $U = 8$ m/s, $D = 4$ mm, $k = 1.5$ mm, $y = 1.32$ mm

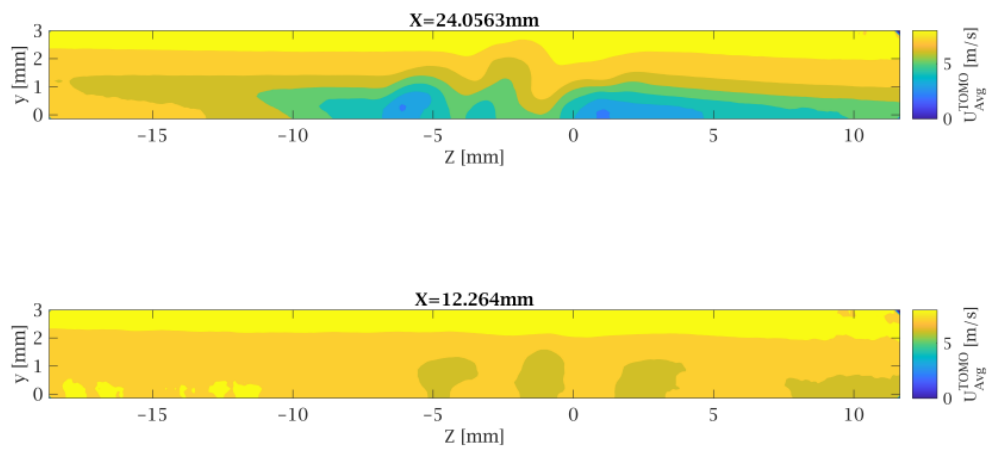


Figure A.7: Tomographic PIV results: wall normal planes for $U = 8$ m/s, $D = 4$ mm, $k = 1.5$ mm

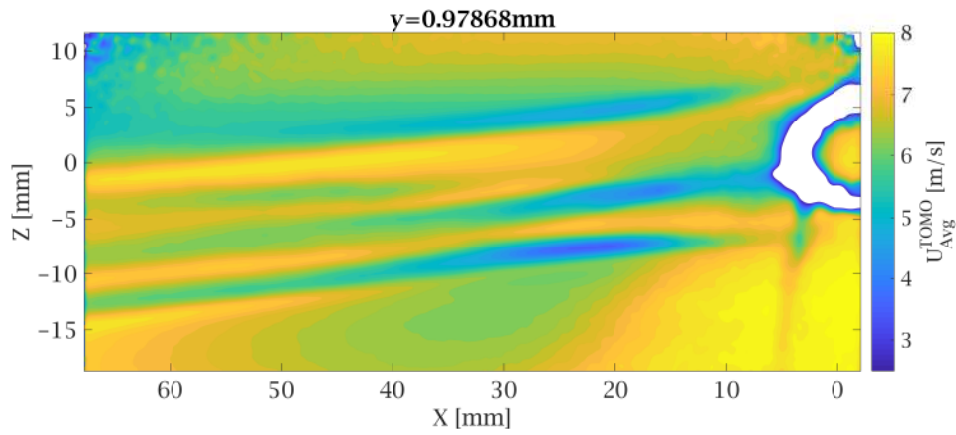
A.2.2 Diameter increase: $U = 8 \text{ m/s}$, $D = 10\text{mm}$, $k = 1.5 \text{ mm}$ 

Figure A.8: Tomographic PIV results: wall parallel planes for $U = 8\text{m/s}$, $D = 10\text{mm}$, $k = 1.5\text{mm}$, $y = 0.98\text{mm}$

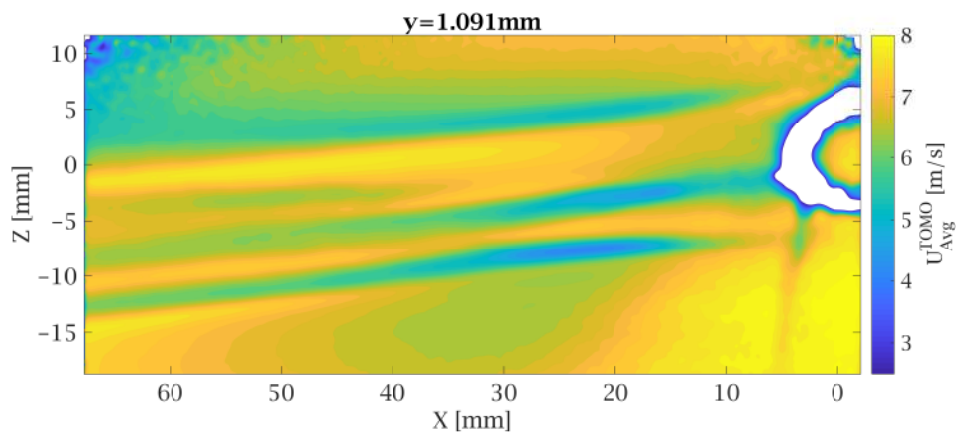


Figure A.9: Tomographic PIV results: wall parallel planes for $U = 8\text{m/s}$, $D = 10\text{mm}$, $k = 1.5\text{mm}$, $y = 1.09\text{mm}$

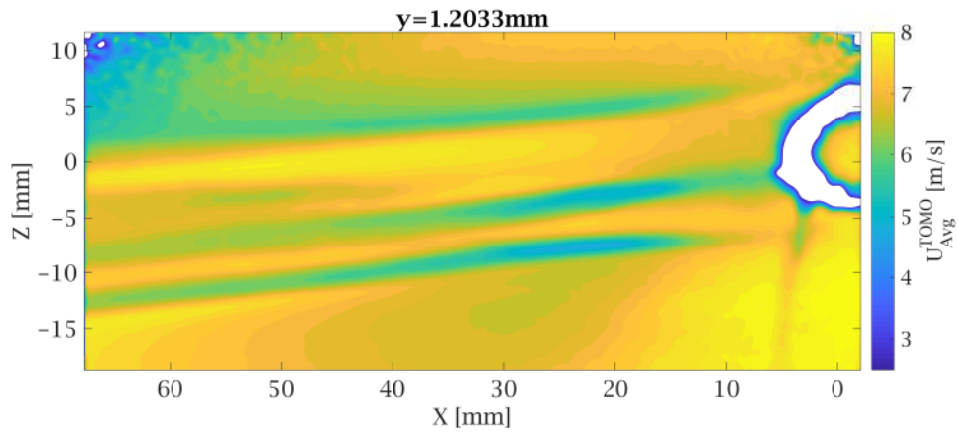


Figure A.10: Tomographic PIV results: wall parallel planes for $U = 8\text{m/s}$, $D = 10\text{mm}$, $k = 1.5\text{mm}$, $y = 1.2\text{mm}$

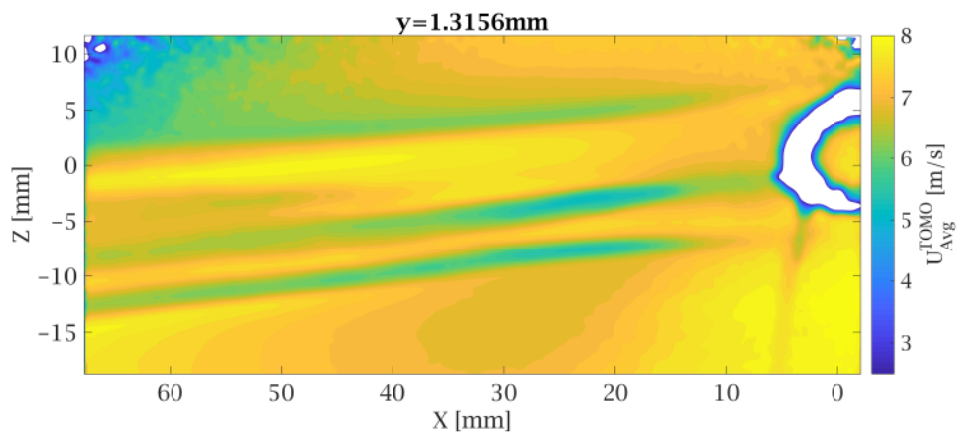


Figure A.11: Tomographic PIV results: wall parallel planes for $U = 8\text{m/s}$, $D = 10\text{mm}$, $k = 1.5\text{mm}$, $y = 1.32\text{mm}$

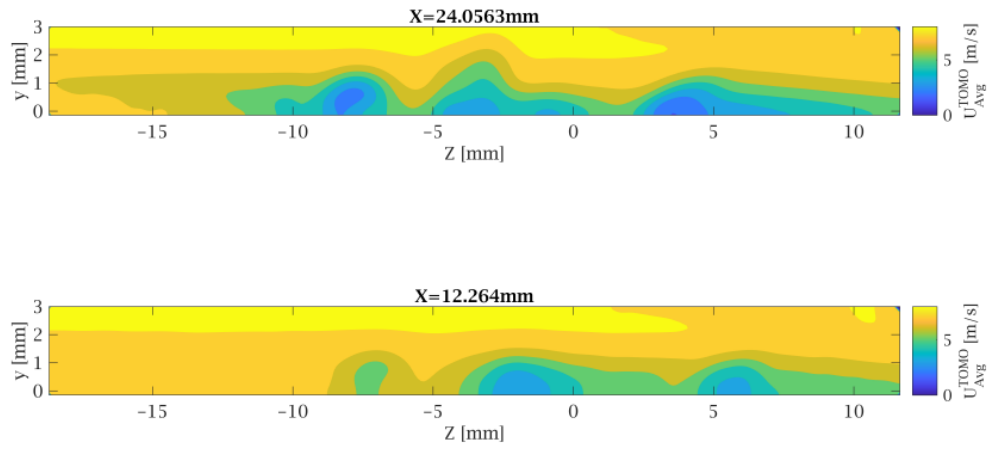


Figure A.12: Tomographic PIV results: wall normal planes for $U = 8\text{m/s}$, $D = 10\text{mm}$, $k = 1.5\text{mm}$

Appendix B

Clean Boundary Layers

In this section, three pictures are displayed. They show the clean boundary layers for the three freestream velocities treated in chapter 4.2. The term "clean" stands for undisturbed, i.e. measured without the presence of the roughness elements.

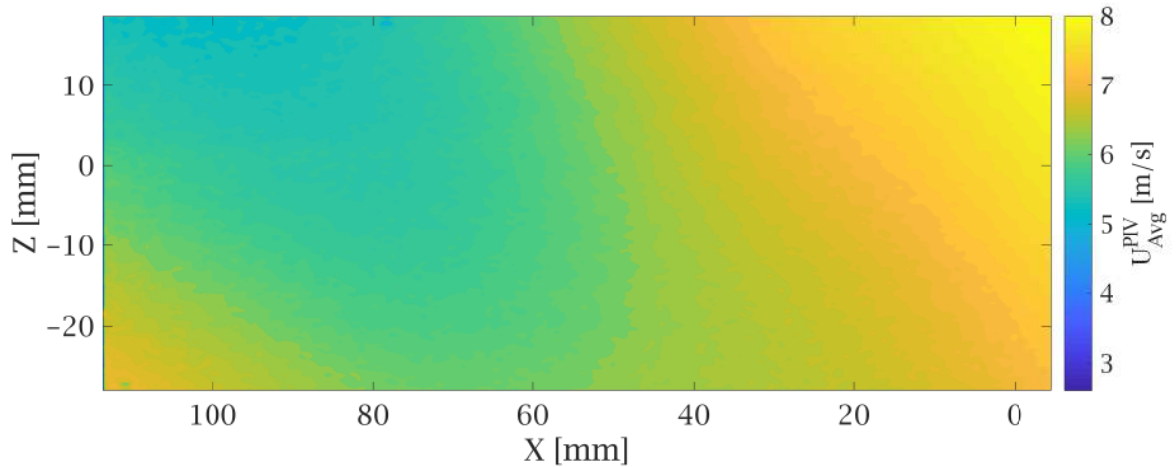


Figure B.1: $U_{\infty} = 8m/s$: clean boundary layer

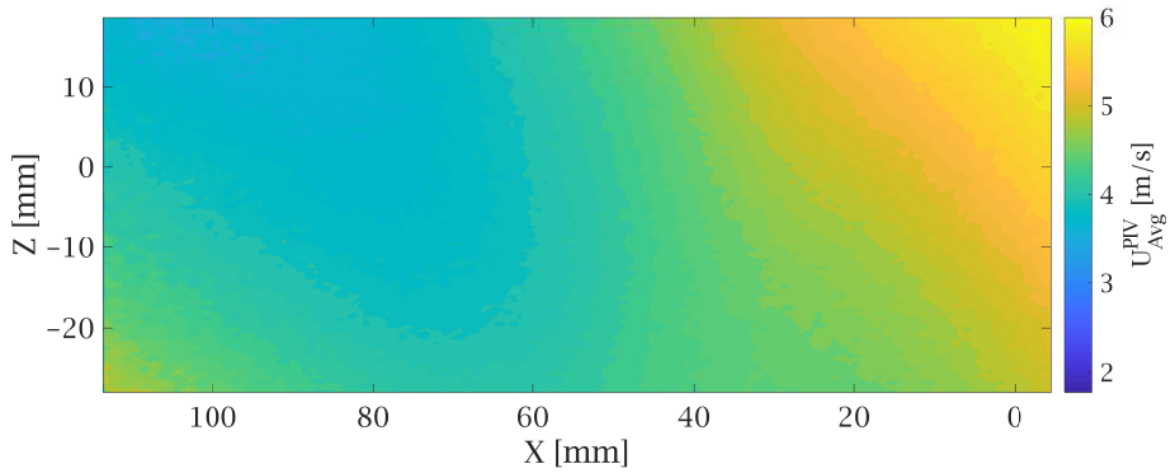


Figure B.2: $U_{\infty} = 6m/s$: clean boundary layer

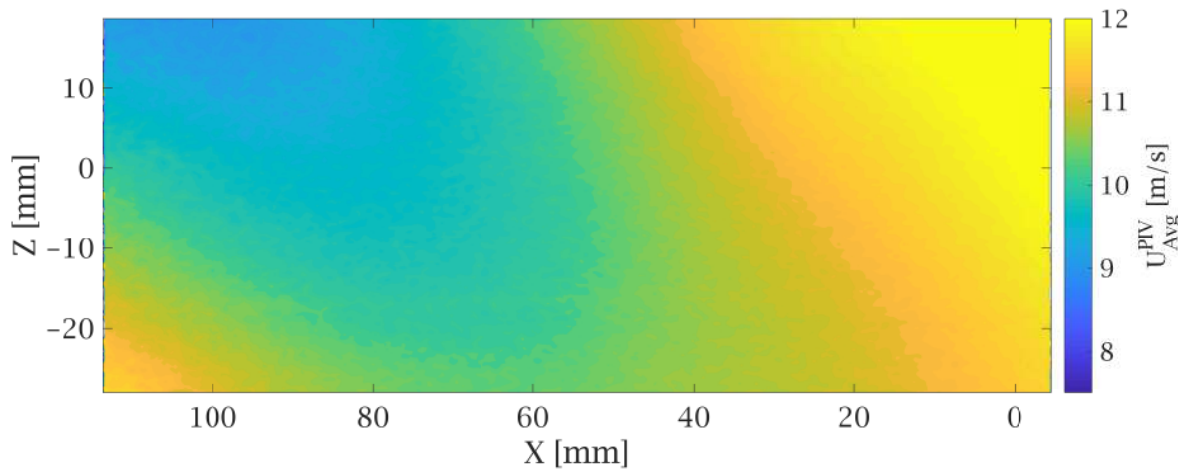


Figure B.3: $U_{\infty} = 12m/s$: clean boundary layer

